HLH

DOE/ER-0046/13
Vol. 1

# Damage Analysis and Fundamental Studies

Quarterly Progress Report
January-March 1983

May 1983

**U.S. Department of Energy**
Office of Energy Research
Office of Fusion Energy
Washington, DC 20545

NOTICE



Printed in the United States of America
Available from
National Technical Information Service
U.S. Department of Commerce
5285 Port Royal Road
Springfield, VA 22161

NTIS price codes
Printed copy: A10
Microfiche copy: A01

DOE/ER-0046/13
UC-20,20c
Vol. 1

# Damage Analysis and Fundamental Studies

Quarterly Progress Report
January-March 1983

**May 1983**

**U.S. Department of Energy**
Office of Energy Research
Office of Fusion Energy
Washington, DC 20545

# FOREWORD

This report is the twenty-first in a series of Quarterly Technical Progress Reports on *Damage Analysis and Fundamental Studies* (DAFS), which is one element of the Fusion Reactor Materials Program, conducted in support of the Magnetic Fusion Energy Program of the U.S. Department of Energy (DOE). The first eight reports in this series were numbered DOE/ET-0065/1 through 8. Other elements of the Fusion Materials Program are:

- Alloy Development for Irradiation Performance (ADIP)
- Plasma-Materials Interaction (PMI)
- Special Purpose Materials (SPM).

The DAFS program element is a national effort composed of contributions from a number of National Laboratories and other government laboratories, universities, and industrial laboratories. It was organized by the Materials and Radiation Effects Branch, DOE/Office of Fusion Energy, and a Task Group on *Damage Analysis and Fundamental Studies,* which operates under the auspices of that branch. The purpose of this series of reports is to provide a working technical record of that effort for the use of the program participants, the fusion energy program in general, and the DOE.

This report is organized along topical lines in parallel to a Program Plan of the same title so that activities and accomplishments may be followed readily, relative to that Program Plan. Thus, the work of a given laboratory may appear throughout the report. Note that a new chapter has been added on Reduced Activation Materials to accommodate work on a topic not included in the early program plan. The Contents is annotated for the convenience of the reader.

This report has been compiled and edited under the guidance of the Chairman of the Task Group on *Damage Analysis and Fundamental Studies,* D. G. Doran, Hanford Engineering Development Laboratory (HEDL). His efforts, those of the supporting staff of HEDL, and the many persons who made technical contributions are gratefully acknowledged. T. C. Reuther, Materials and Radiation Effects Branch, is the DOE counterpart to the Task Group Chairman and has responsibility for the DAFS program within DOE.

G. M. Haas, Chief
Reactor Technologies Branch
Office of Fusion Energy

CONTENTS

CONTENTS (Cont'd)

CONTENTS (Cont'd)

CONTENTS (Cont'd)

## FIGURES

FIGURES (Cont'd)

FIGURES (Cont'd)



CHAPTER 4

1. Grain Boundary Chemistry, Hydrogen Embrittlement and Stress Corrosion Behavior of HT9 (PNL)

FIGURES (Cont'd)

# TABLES

TABLES (Cont'd)

# CHAPTER 1

# IRRADIATION TEST FACILITIES

## RTNS-II IRRADIATIONS AND OPERATIONS

C.M. Logan and D. W. Heikkinen
Lawrence Livermore National Laboratory

### 1.0 Objective

The objectives of this work are operation of RTNS-II (a 14-MeV neutron source facility), machine development, and support of the experimental program that utilizes this facility. Experimenter services include dosimetry, handling, scheduling, coordination, and reporting. RTNS-II is dedicated to materials research for the fusion power program. Its primary use is to aid in the development of models of high-energy neutron effects. Such models are needed in interpreting and projecting to the fusion environment, engineering data obtained in other spectra.

### 2.0 Summary

Irradiations were performed for 21 different experimenters during this quarter. Dedication of the new modular building took place on February 9, 1983. Fourteen Japanese cherry trees were presented to RTNS-II as a gift from the Japanese scientists. The second U.S.-Japan Steering Committee meeting was held on February 9-11, 1983. Due to problems with the rotating target, approximately two and one-half weeks of unscheduled outage occurred. Work has started to prepare the right machine for initial operation.

### 3.0 Program

Title: RTNS-II Operations (WZJ-16)
Principal Investigator: C. M. Logan
Affiliation: Lawrence Livermore National Laboratory

### 4.0 Relevant DAFs Program Plan Task/Subtask

TASK II.A.2,3,4.
TASK II.B.3,4
TASK II.C.1,2,6,11,18.

## 5.0 Irradiation - C. M. Logan, D. W. Heikkinen and M. W. Guinan

During this quarter, irradiations (both dedicated and add-on) were done for the following people.

| Experimenter | P or A* | Sample Irradiated |
|---|---|---|
| D. Nethaway (LLNL) | P | $^{239}Pu$, $^{238}U$ and $^{235}U$ - measure the fission yields. |
| N. Yoshida (Kyushu)<br>H. Takahashi (Hokkaido)<br>Y. Shimomura (Hiroshima)<br>S. Morozumi (Tohoku)<br>A. Kohyama (Tokyo)<br>S. Ishino (Tokyo)<br>C. Kinoshita (Kyushu)<br>E. Kuramoto (Kyushu)<br>N. Igata (Tokyo)<br>K. Kamada (Nagoya)<br>M. Doyama (Tokyo)<br>S. Kitajima (Kyushu)<br>E. R. Bradley (PNL) | P | Pure metals, pure alloys, practical alloys, semiconductors and oxides to study the effect of cascade damage structure on microstructural evolution at 200 and 400°C. Using TEM, positron annihilation, tensilite test and FIM. |
| J. Fowler (LANL) | P | MACOR - changes in electrical and mechanical properties. |
| T. Norris (LANL) | P | $^{241}Am$ and $^{243}Am$ - measure the (n,2n) cross sections. |
| R. Hopper (LLNL) | A | $^{235}U$ and optical materials - etched fission fragment tracks in optical materials for surface treatment. |
| Y. Ogawa (Nagoya) | A | Al alloys - activation analysis |
| C. Ichihara (Kyoto) | A | MgO - measure the absorption of light for dosimetry. |
| P. Hahn (Vienna) | A | Nb-Ti - measure fluxoid pinning strength of superconductors. |

5.0 (continued)

| Experimenter | P or A | Sample Irradiated |
|---|---|---|
| N. Yoshida (Kyushu) | A | Si,Cu,Ni,Mo,Al-4%Cu,Al-4%Cu-0.2%Sn and Al(TEM) Al,SUS 316, Fe, Mo (positron annihilation) Cu (tensile test) |

*P = primary, A = Add-on

5.1 RTNS-II Status - C. M. Logan and D. W. Heikkinen

Installation of two Balzers pumps, replacing the horizontal pumps (Sargeant Welch), was completed on the left machine.

A team of operations, mechanical and electronic personnel, have started preparing the right machine for operation. The accelerator column has already been installed.

A differential pump line started leaking which caused the target rotor-stator to make contact. The failure of the line was caused by fatigue. It took approximately two and one half weeks to fix the problem.

The joint U.S.-Japan Steering Committee approved ten new experiments for RTNS-II in the meeting held February 9-11, 1983.

6.0 Future Work

Irradiations will be continued for J. Fowler (LANL), N. Yoshida (Kyushu), Y. Ogawa (Nagoya) and R. Hopper (LLNL) during the next quarter. An irradiation for H. Heinisch (HEDL) with N. Yoshida (Kyushu), K. Miyahara (Tokyo), A. Kohyama (Tokyo), S. Kitajima (Kushu), N. Igata (Tokyo), C. Kinoshita (Kyushu), S. Ishino (Tokyo), K. Abe (Tohoku), M. Dohyama (Tokyo), H. Takahashi (Hokkaido), M. Kiritani (Hokkaido) and E. Kuramoto (Kyushu) are tentatively scheduled early in the next quarter. Also during this period, irradiations for C. Logan (LLNL), C. Ichihara (Kyoto) and P. Hahn (Vienna) will be made. Later in the quarter, T. Okada (Osaka) is tentatively scheduled.

## 6.1 Publications

"The RTNS-II Fusion Neutron Facility for Materials Damage Studies," D. W. Heikkinen and C. M. Logan, to be presented at the 7th Symposium on Ion Sources and Ion Assisted Technology and the 4th International Conference on Ion and Plasma Assisted Techniques, Kyoto Japan, September 12-16, 1983. UCRL 88830

## LIGHT ION ACCELERATOR FACILITY TO STUDY THE EFFECTS OF INTERSTITIAL HELIUM AND HYDROGEN ATOMS ON MICROSTRUCTURAL EVOLUTION IN SELF-ION IRRADIATED NICKEL

D.B. Bullen, G.L. Kulcinski, and R.A. Dodd (University of Wisconsin)

### 1.0 Objectives

The objectives of this work are to study the effects of interstitial hydrogen and helium atoms on microstructural evolution in self-ion irradiated nickel utilizing the recently completed Light Ion Accelerator Facility. This study will also utilize the cross-section sample preparation technique[1] to study the effects of dose, dose rate, and injected interstitials.

### 2.0 Summary

Initial experiments have been completed to characterize the phase space properties of the beam as it leaves the accelerator. Subsequent irradiations of annealed nickel foils with $He^+$ and $H^+$ beams at 700 keV were completed to determine maximum operating parameters of the system. Results of each test are tabulated.

### 3.0 Program

Title: Radiation Effects to Reactor Materials
Principal Investigators: G.L. Kulcinski and R.A. Dodd
Affiliation: University of Wisconsin

### 4.0 Relevant DAFS Program Task/Subtask

Subtask II.C.2.1 Effects of Helium on Microstructural Evolution
Subtask II.C.3.2 Effects of Hydrogen on Microstructural Evolution

## 5.0 Accomplishments and Status

The Light Ion Accelerator Facility, shown schematically in Fig. 1, consists of a 700 kV electrostatic accelerator, beam focusing and analyzing equipment, a vacuum system and a specimen holder/heater. Characteristics of the beams produced with the accelerator were obtained utilizing an emittance measuring device[2] which continuously samples the phase space area occupied by the beam. The results of these measurements are summarized in Table 1. The emittance for the contour containing 90% of the beam decreases as the accelerating potential increases for both $H^+$ and $He^+$ beams. This increase is expected since higher accelerating voltages reduce space-charge effects. We used the measured emittances in transport calculations through beam handling components of the accelerator system.

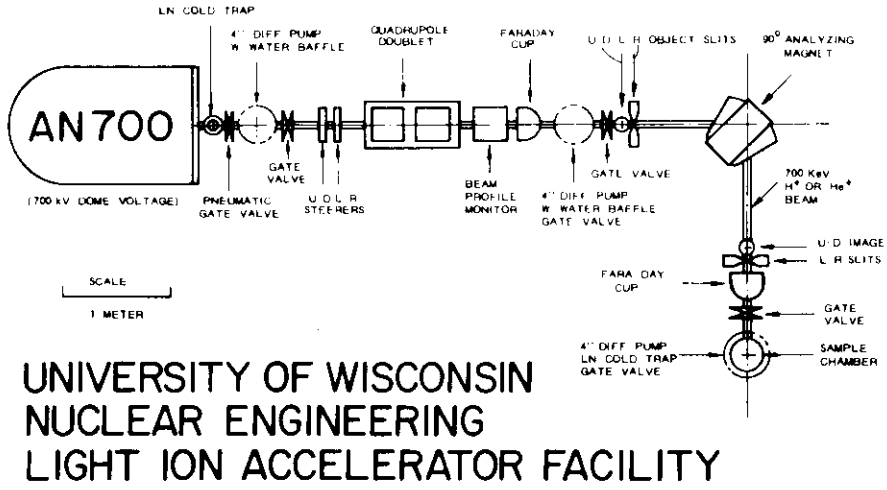


FIGURE 1. Schematic of the University of Wisconsin Light Ion Accelerator Facility, Which Includes a 700-kV Electrostatic Accelerator, and a 90° Analyzing Magnet with a Mass-Energy Product of 3.4 amu·MeV/$Z^2$.

TABLE 1

SUMMARY OF EMITTANCE CHARACTERISTICS FOR AN700 ACCELERATOR

| Dome Voltage (kV) | Ion | Beam Current (μA) | Emittance (90% Contour) ($\pi$ mm mrad $MeV^{1/2}$) |
|---|---|---|---|
| 700 | $H^+$ | 5 | 2.62 |
| 500 | $H^+$ | 4 | 2.81 |
| 200 | $H^+$ | 4 | 6.32 |
| 700 | $He^+$ | 5 | 3.92 |
| 500 | $He^+$ | 8 | 4.19 |

Initial irradiations of annealed nickel foils and a sample of 316 stainless steel were completed to study the maximum, steady-state operating conditions of the system. Samples were irradiated at room temperature to study the maximum temperature rise due to beam heating. Irradiations were completed to fluences of 1-5 x $10^{18}$ ions/$cm^2$. A summary of the initial irradiation parameters is given in Table 2.

The temperature change due to beam heating varied as a function of beam species and sample. For the $He^+$ beam at 700 keV on nickel foils the temperature rise at a maximum flux of 5.21 x $10^{14}$ $He^+$ ions/$cm^2$-sec was 275°C. Irradiations at a flux of 1.75 x $10^{14}$ $He^+/cm^2$-sec yielded a temperature rise of 225°C. An irradiation of 316 stainless steel was completed to determine the effect of sample properties on beam heating. As can be noted in Table 2, the beam heating in 316 SS for a flux of 4.90 x $10^{14}$ $He^+$ ions/$cm^2$-sec was 550°C. The hydrogen ion irradiations yielded a similar beam heating effect for nickel irradiated at fluxes of ~ 5 x $10^{14}$ $H_3^+$ ions/$cm^2$-sec. It should be noted that due to source tuning characteristics, the prevalent beam species produced in the r.f. source for hydrogen was $H_3^+$. Variation in source tuning parameters and gas pressure should allow subsequent irradiations with dominant beams of $H^+$ or $H_2^+$.

TABLE 2

IRRADIATION PARAMETERS SUMMARY

| Beam Species | Energy (keV) | Flux (ion/cm$^2$-sec) | Sample | $\Delta$T (°C) | Fluence (ion/cm$^2$) |
|---|---|---|---|---|---|
| $He^+$ | 700 | $5.21 \times 10^{14}$ | Ni | 275 | $2 \times 10^{18}$ |
| $He^+$ | 700 | $4.90 \times 10^{14}$ | 316 SS | 550 | $2 \times 10^{18}$ |
| $He^+$ | 700 | $1.75 \times 10^{14}$ | Ni | 225 | $1 \times 10^{18}$ |
| $H_3^+$ | 750 | $4.79 \times 10^{14}$ | Ni | 175 | $5 \times 10^{18}$ |
| $H_3^+$ | 750 | $5.56 \times 10^{14}$ | Ni | 175 | $2 \times 10^{18}$ |
| $H_3^+$ | 750 | $6.67 \times 10^{14}$ | Ni | 225 | $1 \times 10^{18}$ |

Preinjection irradiations will be completed at lower fluxes to reduce the effects of beam heating. Sample temperatures will be controlled to within ±5°C utilizing the sample heater.

## 6.0 References


1. J.B. Whitley, Ph.D. Thesis, University of Wisconsin, Madison, WI (1978).
2. L.L. Ames, Nuclear Instruments and Methods, 151, 363 (1978).


## 7.0 Future Work

Samples of nickel, 316 stainless steel and binary nickel alloys will be injected with hydrogen and helium atoms and subsequently irradiated with 14 MeV $Ni^{3+}$ ions to produce displacement damage. Cross-section sample preparation techniques will be utilized to study the effects of dose, dose rate and injected interstitials on microstructural evolution and phase stability.

## 8.0 Publications

1. D.B. Bullen, J.H. Billen, and G.L. Kulcinski, "The Effect of Preinjected Gas Atoms on Depth Dependent Damage in Self-Ion Irradiated Nickel," to be published IEEE Transactions on Nuclear Science, (April 1983).

## INTENSE TITANIUM ION BEAM FOR RADIATION DAMAGE STUDIES

J.H. Billen, G.L. Kulcinski, and R.A. Dodd (University of Wisconsin)

### 1.0 Objective

The objective of this work is to develop an intense source of titanium ions for injection into a tandem accelerator to allow self-ion irradiation of titanium and titanium alloys.

### 2.0 Summary

A beam of $TiH^-$ ions suitable for heavy-ion irradiation studies utilizing a tandem accelerator has been developed and characterized. Beam currents and emittances are presented with estimated operating lifetimes of sputter cathodes.

### 3.0 Program

Title: Radiation Effects to Reactor Materials
Principal Investigators: G.L. Kulcinski and R.A. Dodd
Affiliation: University of Wisconsin

### 4.0 Relevant DAFS Program Plan Task/Subtask

Subtask II.C.3.2 Effect of Hydrogen on Microstructural Evolution

### 5.0 Accomplishments and Status

We have used the ion source SNICS[1,2] (Source of Negative Ions by Cesium Sputtering) for a number of years to produce several microampere beams of $Al_2^-$, $Cu^-$ and $Ni^-$. These ions are accelerated to the high voltage terminal of a model EN electrostatic tandem accelerator where they are stripped in $N_2$ gas to form a beam of positive ions. After further acceleration as positive ions

the ~ 15-MeV beam irradiates a metal specimen in an ultrahigh vacuum environment. To avoid possible contamination of the specimen by injected interstitial atoms of the beam species one usually prefers to irradiate the specimen with ions of the specimen material, so-called self-ion irradiation.

Recent interest in studying radiation damage in titanium persuaded us to attempt to make a beam of titanium negative ions. An earlier attempt to produce $Ti^-$ ions by sputtering pure titanium in SNICS was unsuccessful. The electron affinity of Ti is not well determined and may not even be positive, so this result was not unexpected. An alternative approach is to produce a molecular negative ion such as $TiH^-$. For a tandem electrostatic accelerator a $TiH^-$ beam is equally as satisfactory as the monatomic ion itself. Stripping in the charge exchange canal of the high voltage terminal results in a monatomic positive ion with 98% of the energy of the $TiH^-$ ion and produces a negligible degradation in the transverse emittance of the beam.

Billquist and Yntema[3] at the Argonne National Laboratory (ANL), have experimented with a cathode made of hydrogen-loaded Ti in the ANL version of SNICS. They were able to produce a 2-μA beam of $TiH^-$ using an early version of the SNICS geometry. However, the Wisconsin SNICS has been modified to enhance beam output based upon recent calculations of the intensity and emittance for the sputter source, and one could expect a substantial improvement of the 2-μA beam obtained at ANL. Billquist supplied us with a 6.4 mm long x 6.4 mm diameter pill of Ti loaded with hydrogen to a Ti:H ratio of approximately 1:1. This pill was press-fitted into an aluminum sputter cathod for use in the Wisconsin SNICS.

We have produced a 21-μA beam of $TiH^-$ by bombarding the cathode with ~ 4 keV $Cs^+$ ions. This beam intensity is 5-6 times that ordinarily injected into the EN tandem accelerator to obtain damage rates of a few dpa/hour in the specimen. The measured beam emittance was 9.1 π and 6.5 π mm mrad $MeV^{1/2}$ for 90% and 80% of the beam, respectively. These figures compare favorably to the ~ 8 π mm mrad $MeV^{1/2}$ acceptance of the accelerator. In addition to the $TiH^-$ beam

the source produces simultaneously over 100-μA of $H^-$. We have run the $TiH^-$ beam continuously for 8 hours. Based upon experience with other cathode materials we expect lifetimes for a hydrogen-loaded titanium cathode in excess of 10 days.

## 6.0 References


1. G.A. Caskey, R.A. Douglas, H.T. Richards, and H.V. Smith, Jr., Nucl. Instrum. and Meth., 157, 1 (1978).

2. J.H. Billen, Proc. 6th Conf. on the Application of Accelerators in Research and Industry (Denton, Texas, 1980) in IEEE Trans. Nucl. Sci., NS-28, 1535 (1981).

3. P.J. Billquist, private communication.


## 7.0 Future Work

Further measurements of current and emittance will be completed over the lifetime of the sputter cathode for the $TiH^-$ beam. Irradiations of titanium specimens utilizing the tandem accelerator will be completed to confirm the applicability of this beam to heavy-ion irradiation studies.

# C H A P T E R  2

## DOSIMETRY AND DAMAGE PARAMETERS

## FISSION REACTOR DOSIMETRY - HFIR - CTR31, 32, 34, and 35

L. R. Greenwood (Argonne National Laboratory)

### 1.0 Objective

To characterize neutron irradiation facilities in terms of neutron flux, spectra, and damage parameters (DPA, gas production, transmutation) and to measure these exposure parameters during fusion materials irradiations.

### 2.0 Summary

Results are summarized for four separate irradiations in HFIR, designated CTR-31, 32, 34, and 35. The neutron fluxes and energy spectra agree quite well between the runs. Small corrections have been made to the CTR32 reaction rates due to improved burnup calculations. Helium production in nickel and stainless steel is being revised slightly according to new neutron cross section evaluations for $^{59}Ni$. The status of all other experiments is summarized in Table 1.

### 3.0 Program

Title: Dosimetry and Damage Analysis

Principal Investigator: L. R. Greenwood

Affiliation: Argonne National Laboratory

### 4.0 Relevant DAFS Program Plan Task/Subtasks

Task II.A.1 Fission Reactor Dosimetry

TABLE 1

STATUS OF DOSIMETRY EXPERIMENTS

| | Facility/Experiment | Status/Comments |
|---|---|---|
| ORR | - MFE 1 | Completed 12/79 |
| | - MFE 2 | Completed 06/81 |
| | - MFE 4A1 | Completed 12/81 |
| | - MFE 4A2 | Completed 11/82 |
| | - MFE 4B | Samples Expected 04/83 |
| | - MFE 4C | Irradiation in Progress |
| | - TBC 07 | Completed 07/80 |
| | - TRIO-Test | Completed 07/82 |
| | - TRIO-1 | Irradiation in Progress |
| HFIR | - CTR 32 | Completed 04/82 |
| | - CTR 31, 34, 35 | Completed 04/83 |
| | - CTR 30 | Irradiation in Progress |
| | - T1, RB1, CTR39 | Samples Received 03/83 |
| | - T2, T3 | Irradiations in Progress |
| | - RB2, RB3 | Irradiations in Progress |
| | - CTR 40-45 | Samples Sent 10/82 |
| Omega West | - Spectral Analysis | Completed 10/80 |
| | - HEDL1 | Completed 05/81 |
| FBR II | - X287 | Completed 09/81 |
| IPNS | - Spectral Analysis | Completed 01/82 |
| | - LANL1 (Hurley) | Completed 06/82 |
| | - Hurley | Completed 02/83 |
| | - Coltman | Irradiation in Progress |

## 5.0 Accomplishments and Status

Measurements and calculations have been completed for four separate irradiations in the High Flux Isotopes Reactor (HFIR) at Oak Ridge National Laboratory. The irradiation histories are, as follows:

| Experiment | Dates | Power (MWD) |
|---|---|---|
| CTR31 | 10-03-80 to 05-25-81 | 21,853 |
| CTR32 | 08-17-80 to 12-12-80 | 10,863 |
| CTR34, 35 | 12-24-81 to 04-17-82 | 10,614 |

Results from CTR32 were reported previously (L. R. Greenwood, Damage Analysis and Fundamental Studies, Quarterly Progress Report, DOE/ER-0046/9, pp. 32-40, 1982). However, slight revisions have been made in activation and helium production rates according to new nuclear data.

Radiometric and helium accumulation dosimeters were located at eight different vertical heights in each experimental assembly, either at the top or bottom of each level. All samples were gamma counted at ANL and then sent to Rockwell International for helium analysis.

The radiometric dosimetry results are listed in Tables 2 and 3. Burnup corrections are required for all of the reactions and these are typically 5-10% for the fast reactions but as high as 20-50% for thermal reactions. These corrections can be checked in several ways. In the case of thermal reactions, a simple iterative technique provides a unique reaction rate since the reaction in question is responsible for the burnup of the target nuclei. Once the thermal flux is known, it can then be used to estimate the much smaller corrections for the threshold reactions. Since the flux spectrum is apparently quite constant in HFIR, we can check the final results by demanding internal consistency within each run and between different runs. In the case of $^{58}Fe(n,\gamma)^{59}Fe$, corrections must be made for the burnin of $^{58}Fe$ from both $^{56}Fe$ and $^{57}Fe$. Corrections for $^{54}Fe(n,p)$ and $^{55}Mn(n,2n)$ are hampered by the lack of any cross section measurements on $^{54}Mn$ (<10 b). Excellent consistency is obtained for both reactions if we assume a $^{54}Mn$ thermal cross sections of about 5 b. The $^{58}Fe(n,\gamma)$ and $^{63}Cu(n,\alpha)$ reaction rates have been adjusted slightly from the rates published previously (CTR32) according to these new

TABLE 2

THERMAL ACTIVATION MEASUREMENTS IN HFIR
(Values corrected for burnup and normalized to 100 MW; uncertainty ±2% )

| Height, cm | $\sigma\phi$ (atom/atom-s) | | | | | | |
|---|---|---|---|---|---|---|---|
| | $^{59}Co(n,\gamma)(10^{-8})$ | | | | $^{58}Fe(n,\gamma)(10^{-9})$ | | |
| | 31 | 32 | 34 | 35 | 32 | 34 | 35 |
| 20.8 | 3.64 | 4.18 | -- | -- | 1.26 | -- | -- |
| 18.8 | -- | -- | 4.35 | 4.50 | -- | 1.28 | 1.30 |
| 16.7 | -- | -- | -- | -- | 1.35 | -- | -- |
| 12.5 | 5.56 | 5.55 | 5.56 | 5.64 | 1.67 | -- | 1.59 |
| 6.3 | -- | -- | 6.68 | 6.63 | -- | 1.95 | 1.92 |
| 4.2 | 7.10 | 7.21 | -- | -- | 2.08 | -- | -- |
| -3.1 | -- | -- | 6.72 | 6.35 | -- | 1.93 | -- |
| -4.2 | 6.67 | 7.28 | -- | -- | 2.10 | -- | -- |
| -8.3 | -- | -- | -- | -- | 1.82 | -- | -- |
| -9.4 | -- | -- | 5.92 | 5.94 | -- | 1.68 | 1.74 |
| -12.5 | 5.63 | 5.76 | -- | -- | 1.70 | -- | -- |
| -15.6 | -- | -- | 5.11 | 5.07 | -- | 1.48 | 1.46 |
| -20.8 | 4.28 | 4.22 | -- | -- | 1.20 | -- | -- |
| -21.9 | -- | -- | 3.67 | 3.69 | -- | 1.09 | 1.09 |

| | $^{93}Nb(n,\gamma)(10^{-9})$ | |
|---|---|---|
| | 31 | 32 |
| 20.8 | 1.63 | 1.73 |
| 12.5 | 2.46 | 2.43 |
| 8.3 | -- | 2.78 |
| 4.2 | 3.04 | 3.05 |
| 0.0 | 3.26 | -- |
| -4.2 | 3.02 | 3.08 |
| -12.5 | 2.46 | 2.49 |
| -20.8 | 1.73 | 1.67 |
| -25.0 | -- | 1.43 |

TABLE 3

THRESHOLD ACTIVATION MEASUREMENTS IN HFIR
(Values corrected for burnup and normalized to 100 MW; uncertainty ±2%)

| Height, cm | $\sigma\phi$ (atom/atom-s) | | | | | | |
|---|---|---|---|---|---|---|---|
| | $^{54}Fe(n,p)(10^{-11})$ | | | | $^{46}Ti(n,p)(10^{-12})$ | | |
| | 31 | 32 | 34 | 35 | 31 | 32 | 34 |
| 20.8 | 3.94 | 4.13 | -- | -- | 5.86 | -- | -- |
| 18.8 | -- | -- | 4.79 | 4.58 | -- | -- | 6.82 |
| 16.7 | -- | 5.22 | -- | -- | -- | -- | -- |
| 12.5 | 5.81 | 6.44 | -- | 6.08 | 9.02 | 9.43 | -- |
| 6.3 | -- | -- | 6.82 | 6.85 | -- | -- | 9.81 |
| 4.2 | 6.43 | 6.99 | -- | -- | 10.16 | 10.46 | -- |
| 0.0 | -- | -- | -- | -- | -- | 10.34 | -- |
| -3.1 | -- | -- | 7.13 | -- | -- | -- | 10.54 |
| -4.2 | 6.95 | 6.86 | -- | -- | 10.98 | 10.23 | -- |
| -8.3 | -- | 6.77 | -- | -- | -- | -- | -- |
| -9.4 | -- | -- | 6.62 | 6.58 | -- | -- | 9.69 |
| -12.5 | 5.85 | 6.08 | -- | -- | 9.16 | 8.89 | -- |
| -15.6 | -- | -- | 5.19 | 5.41 | -- | -- | 7.60 |
| -16.7 | -- | -- | -- | -- | -- | 7.28 | -- |
| -20.8 | 3.94 | 3.86 | -- | -- | 5.98 | 5.66 | -- |
| -21.9 | -- | -- | 3.69 | 3.82 | -- | -- | 5.28 |

| Height, cm | $^{55}Mn(n,2n)(10^{-13})$ | | | | $^{63}Cu(n,\alpha)(10^{-13})$ | |
|---|---|---|---|---|---|---|
| | 31 | 32 | 34 | 35 | 31 | 32 |
| 20.8 | 1.18 | 1.23 | -- | -- | 2.73 | 3.22 |
| 18.8 | -- | -- | 1.50 | 1.35 | -- | -- |
| 12.5 | 1.74 | 1.94 | 1.75 | 1.78 | 4.44 | 4.65 |
| 6.3 | -- | -- | 2.02 | 2.06 | -- | -- |
| 4.2 | 1.94 | 2.13 | -- | -- | 6.50 | 5.18 |
| 0.0 | -- | -- | 2.07 | -- | 6.01 | -- |
| -3.1 | -- | -- | 2.08 | -- | -- | -- |
| -4.2 | 2.02 | 2.10 | -- | -- | 5.94 | 5.18 |
| -9.4 | -- | -- | 1.93 | 2.14 | -- | -- |
| -12.5 | 1.87 | 1.83 | -- | -- | 5.00 | 5.42 |
| -15.6 | -- | -- | 1.59 | 1.61 | -- | -- |
| -20.8 | 1.26 | 1.23 | -- | -- | 3.20 | 2.98 |
| -21.9 | -- | -- | 1.10 | 1.15 | -- | -- |

burnup calculations. The $^{58}Fe(n,\gamma)$ values are about 4% lower and the $^{63}Cu(n,\alpha)$ values about 7% higher than reported previously for CTR32. Some of the values reported for $^{63}Cu(n,\alpha)^{60}Co$ appear to be inconsistent, although the reasons for these differences are not understood. Random cobalt impurities could explain the problem; however, overall the cobalt impurity level should be less than 0.1 ppm.

Activation rates for threshold reactions from all four runs are compared in Fig. 1. As can be seen, the consistency is excellent demonstrating the repeatability of the neutron flux and spectrum in HFIR. The maximum activation rates are listed below, as determined by a least-squares fit to the data in Table 2.

| Reaction | Midplane Activation Rate(atom/atom-s) | | | |
|---|---|---|---|---|
| | CTR31 | CTR32 | CTR34 | CTR35 |
| $^{58}Fe(n,\gamma)^{59}Fe(10^{-9})$ | -- | 2.04 | 1.94 | 1.92 |
| $^{59}Co(n,\gamma)^{60}Co(10^{-8})$ | 6.87 | 7.12 | 6.72 | 6.57 |
| $^{54}Fe(n,p)^{54}Mn(10^{-11})$ | 6.83 | 7.22 | 7.16 | 7.17 |
| $^{46}Ti(n,p)^{46}Sc(10^{-11})$ | 1.08 | 1.05 | 1.05 | -- |
| $^{63}Cu(n,\alpha)^{60}Co(10^{-13})$ | 6.13 | 5.51 | -- | -- |
| $^{55}Mn(n,2n)^{54}Mn(10^{-13})$ | 2.05 | 2.18 | 2.08 | 2.22 |
| $^{93}Nb(n,\gamma)^{94}Nb(10^{-9})$ | 3.05 | 3.06 | -- | -- |

These data were used with the computer code STAYSL to adjust the neutron flux spectrum calculated by Kam and Swanks.[1] The adjusted flux and fluence values are listed in Table 4. The last column of fluxes is the average for all four runs. The run-to-run scatter from the average is only ±5%; however, there does appear to be real differences in the thermal flux level. Differences in the fuel cycle and variations in shielding by the experimental assemblies can of course perturb the thermal flux. The flux spectra adjusted by STAYSL are all quite similar and are represented by Fig. 2.

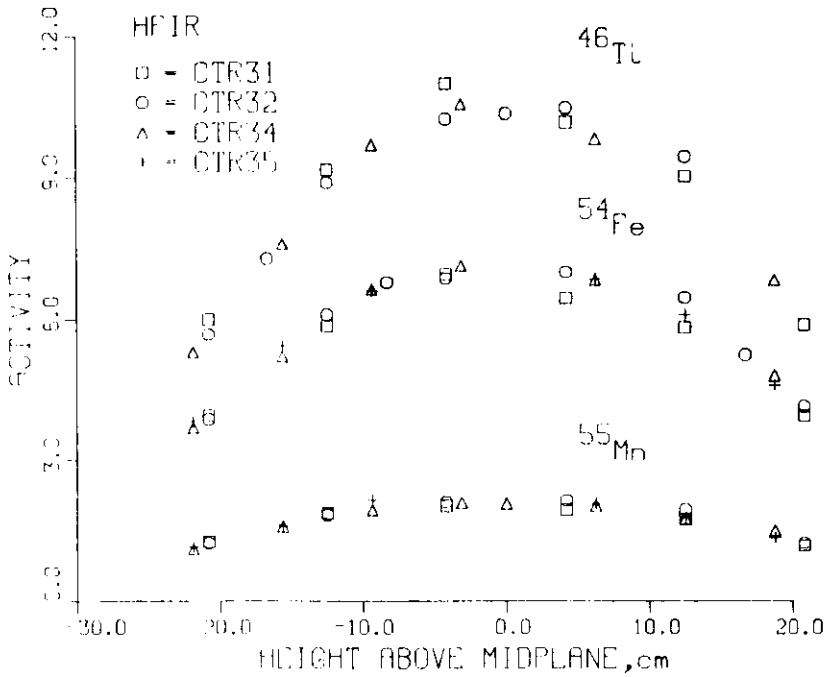


FIGURE 1. Relative Activation Rates Shown as a Function of Height Above Midplane for the $^{46}Ti(n,p)^{46}Sc$, $^{54}Fe(n,p)^{54}Mn$, and $^{55}Mn$ Reactions. Four irradiations are compared in HFIR-CTR31, 32, 34, and 35.

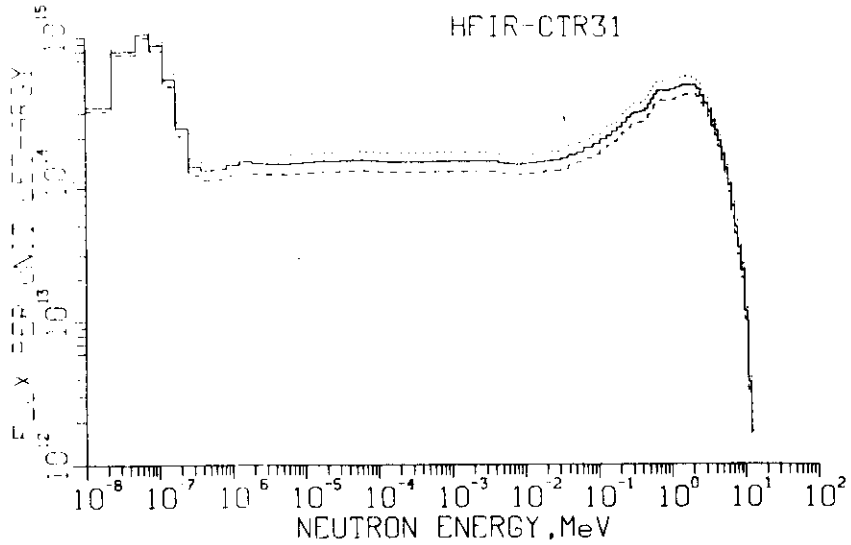


FIGURE 2. Adjusted Neutron Spectrum Shown for the HFIR-CTR31 Irradiation. This spectrum is nearly identical for the CTR32, 34, and 35 irradiations. Flux per unit lethargy is energy times flux. The dotted and dashed lines represent one standard deviation; however, uncertainties are highly correlated.

TABLE 4

MIDPLANE NEUTRON FLUXES AND FLUENCES MEASURED IN HFIR
(Values normalized to 100 MW; uncertainty ±5-10%)

| Energy, MeV | Flux, x $10^{15}$ n/cm$^2$-s | | | | |
|---|---|---|---|---|---|
| | CTR31 | CTR32 | CTR34 | CTR35 | Average |
| Total | 4.95 | 5.10 | 4.87 | 4.77 | 4.92 |
| Thermal (<.5 eV) | 2.04 | 2.11 | 1.99 | 1.94 | 2.02 |
| >0.11 | 1.29 | 1.34 | 1.30 | 1.28 | 1.30 |
| 0.5 eV - 0.11 | 1.62 | 1.65 | 1.59 | 1.55 | 1.60 |
| 0.11 - 1 | 0.643 | 0.655 | 0.629 | 0.617 | 0.636 |
| 1 - 5 | 0.598 | 0.630 | 0.616 | 0.610 | 0.614 |
| 5 - 10 | 0.051 | 0.051 | 0.050 | 0.049 | 0.050 |
| 10 - 20 | 0.0016 | 0.0016 | 0.0016 | 0.0016 | 0.0016 |

| | Fluence, x $10^{22}$ n/cm$^2$ | | | |
|---|---|---|---|---|
| | CTR31 | CTR32 | CTR34 | CTR35 |
| Total | 9.34 | 4.78 | 4.47 | 4.38 |
| Thermal (<.5 eV) | 3.84 | 1.98 | 1.82 | 1.78 |
| >0.11 | 2.45 | 1.26 | 1.19 | 1.17 |
| 0.5 eV - 0.11 | 3.06 | 1.55 | 1.45 | 1.42 |
| 0.11 - 1 | 1.21 | 0.614 | 0.577 | 0.565 |
| 1 - 5 | 1.13 | 0.590 | 0.564 | 0.560 |
| 5 - 10 | 0.097 | 0.048 | 0.045 | 0.045 |
| 10 - 20 | 0.0031 | 0.0015 | 0.0014 | 0.0014 |

Flux gradients were deduced from the activities in Tables 2 and 3, as shown in Fig. 1. All of the data for each reaction and run were fitted to a quadratic function by the least-squares method. The average fits for each reaction are listed in Table 5. The linear term b is quite insignificant, confirming that the maximum flux is centered within ±1 cm of midplane for all reactions. The quadratic term c is very nearly the same for all reactions; however, the thermal gradient is slightly flatter than the fast gradient, as might be expected. This spectral difference is less than 2% over ±20 cm of interest. The flux gradients in Table 5 were determined by averaging the thermal and fast gradient coefficients. Displacement damage and gas production would also be expected to follow the same gradients except for helium production in nickel which is a two-step thermal reaction. Work on these gradients is now in progress.

TABLE 5

FLUX AND ACTIVITY GRADIENTS FOR HFIR
[Least-squares fit to data in Tables 2 - 3
$f(z) = a[1 + bz + cz^2]$, z = height (cm)]

| Reaction | a | $b(10^{-3})$ | $c(10^{-3})$ |
|---|---|---|---|
| $^{59}Co(n,\gamma)^{60}Co$ | $6.82 \times 10^{-8}$ | -0.365 | -0.968 |
| $^{58}Fe(n,\gamma)^{59}Fe$ | $1.97 \times 10^{-9}$ | +0.066 | -0.944 |
| $^{54}Fe(n,p)^{54}Mn$ | $7.10 \times 10^{-11}$ | +0.284 | -0.994 |
| $^{46}Ti(n,p)^{46}Sc$ | $1.06 \times 10^{-11}$ | +0.841 | -0.995 |
| $^{55}Mn(n,2n)^{54}Mn$ | $2.13 \times 10^{-13}$ | +0.147 | -0.974 |

| Flux ($n/cm^2$-s) | a | $b(10^{-3})$ | $c(10^{-3})$ |
|---|---|---|---|
| Thermal (<.5 eV) | $2.02 \times 10^{15}$ | -0.150 | -0.956 |
| Fast (>0.1 MeV) | $1.30 \times 10^{15}$ | +0.563 | -0.995 |
| Total | $4.92 \times 10^{15}$ | +0.195 | -0.975 |

## 6.0 References

1. F. B. K. Kam and J. H. Swanks, Neutron Flux Spectrum in the HFIR Target Region, ORNL-TM-3322 (1971).

## 7.0 Future Work

Helium and displacement calculations are now in progress for all four irradiations. Helium values are being reevaluated in terms of new cross section evaluations for $^{59}Ni$. Dosimeters are now being analyzed for the T1, T2, RB1, and CTR-39 irradiations in HFIR.

## 8.0 Publications

None.

## MEASUREMENT OF THE $^{27}Al(n,2n)^{26}Al$ CROSS SECTION NEAR THRESHOLD

R. K. Smither and L. R. Greenwood (Argonne National Laboratory)

### 1.0 Objective

To develop the use of the (n,2n) reaction in aluminum as a useful dosimetry reaction for fusion reactor neutrons.

### 2.0 Summary

The cross section of the $^{27}Al(n,2n)^{26}Al$ reaction near threshold is needed to evaluate the possibility of using this reaction as a dosimetry tool for fusion reactor neutrons. The (n,2n) reaction in Al splits into two parts. The first part leads to the formation of $^{26}Al$ in the $5^+$ ground state while the second part of the cross section leads to the formation of $^{26}Al$ in the $0^+$ isomeric at 228 keV. These two reaction channels can be separated by their quite different decay patterns. The threshold energies (lab) for neutrons for these two reactions are 13.542 MeV and 13.778 MeV, respectively. This makes these two reactions particularly sensitive monitors of the energy distribution of the neutrons produced in a fusion reactor and it may be possible to measure plasma ion temperatures by comparing these (n,2n) reaction rates with the Al(n,p) and Al(n,$\alpha$) reaction rates which vary much more slowly at these neutron energies. Very little experimental work has been done on the (n,2n) cross section in Al so measurements near threshold are essential for the evaluation of this dosimetry technique.

## 3.0 Program

Title: Dosimetry and Damage Analysis

Principal Investigator: L. R. Greenwood

Affiliation: Argonne National Laboratory

## 4.0 Relevant DAFS Program Plan Task/Subtasks

Task II.A.2. Higher Energy Neutron Dosimetry.

Task II.A.7. MFR Dosimetry.

## 5.0 Accomplishments and Status

The cross section for the production of the $0^+$ isomeric state at 228 keV in $^{26}Al$ from the reaction $^{27}Al(n,2n)^{26}Al$ was measured at neutron energies of 14.6 to 14.8 MeV. All previous measurements[1] were for neutron energies above 16 MeV so these measurements represent the first work at near threshold neutron energies. The measured cross sections are much lower than one would expect if the reaction is assumed to form the $0^+$ iosmeric state directly and suggest that most of the observed cross section for this reaction results in the formation of the first $1^+$ state at 1057.8 keV which then beta-decays 100% to the $0^+$ state. If this is true, then it effectively raises the Q-value for this reaction by 830 keV and the neutron threshold energy in the lab frame of reference is raised to 14.639 MeV. This changes the interpretation of the dosimetry data obtained with this reaction making it sensitive to a slightly higher energy region of the neutron spectrum. The near threshold measurements made by R. K. Smither and L. R. Greenwood[2] for the components of the Al(n,2n)

cross section that populates the $5^+$ ground state was also much lower than would be expected if the recation is assumed to form the $5^+$ ground state directly. Theory and experiment agree much better if one assumes that most of the yield near threshold is associated with the formation of the first $3^+$ state at 416.9 keV in $^{26}Al$. This $3^+$ state decays to the $5^+$ ground state 100% of the time. If all of the production of the $5^+$ state by neutron energies near threshold is through the $3^+$ state, the Q-value of this reaction channel will be raised by 417 keV.

The previous experiments of R. K. Smither and L. R. Greenwood[2] did not completely rule out the direct formation of the $5^+$ ground state by a small component of the (n,2n) reaction. Further experiments are planned with near threshold neutrons to resolve this question.

## 5.1 Cross Section Measurements for $^{27}Al(n,2n)^{26}Al$ for Near Threshold Neutron Energies

The Q-value of the (n,2n) reaction in aluminum is such that the threshold neutron energy falls within the energy range of neutrons produced in fusion reactors. The reaction is therefore a potentially useful dosimetry reaction for monitoring the plasma ion temperatures. This cross section separates naturally into two partial cross sections. One part produces the $5^+$ ground state of $^{26}Al$, while the second part produces the $0^+$ isomeric state at 228 keV. These two levels decay in quite different ways allowing their separation through dosimetry measurements. The $5^+$ ground state decays (99%) through the $2^+$, 1808.6 keV state of $^{26}Mg$ and can be monitored by observing the 1808.6 keV gamma ray. The $0^+$ isomeric state decays directly to the $0^+$ ground

state of $^{26}Mg$ (see Fig. 1) and is monitored by observing the 511 keV annihilation radiation associated with the positron production. The $5^+$ ground state decay also produces positrons, but the life-times of the two states is so different that no real interference occurs. Basically this means that the (n,2n) reaction produces two reaction channels whose cross sections vary rapidly with neutron energy in the energy range appropriate for fusion reactors. When these reaction rates are compared with the observed reaction rates for the $^{27}Al(n,p)^{27}Mg$ and $^{27}Al(n,\alpha)^{24}Na$ reactions or other dosimetry reactions where the neutron cross section is varying quite slowly in this neutron energy region, then considerable information about the energy spectrum of the fusion-produced neutrons is obtained. This procedure is illustrated in Fig. 2 where the near threshold cross sections of these two (n,2n) reactions are compared to typical fusion neutron energy spectra. The two neutron cross section curves are calculated assuming a simple evaporation model that leads directly to either the $5^+$ ground state or the $0^+$ isomeric state. The relatively slowly varying cross section for the (n,p) and (n,$\alpha$) reactions is also shown in Fig. 2. The comparison of either (n,2n) reaction rate to one of the slowly varying reactions will give a plasma ion temperature. Figure 3 is a plot of the normalized ratio of the production of the $5^+$ ground state through the (n,2n) reaction to the production of $^{24}Na$ through the (n,p) reaction. The even more rapidly rising ratio of the production of the $0^+$ isomeric state to the (n,p) is also shown. The dashed curve is normalized production ratio for $^{58}Ni(n,2n)/^{58}Ni(n,p)$ which is typical for most other dosimetry materials where the threshold energy for the (n,2n) reaction does not fall in the fusion energy region. The ratios are normalized to one for ion temperatures approaching zero.

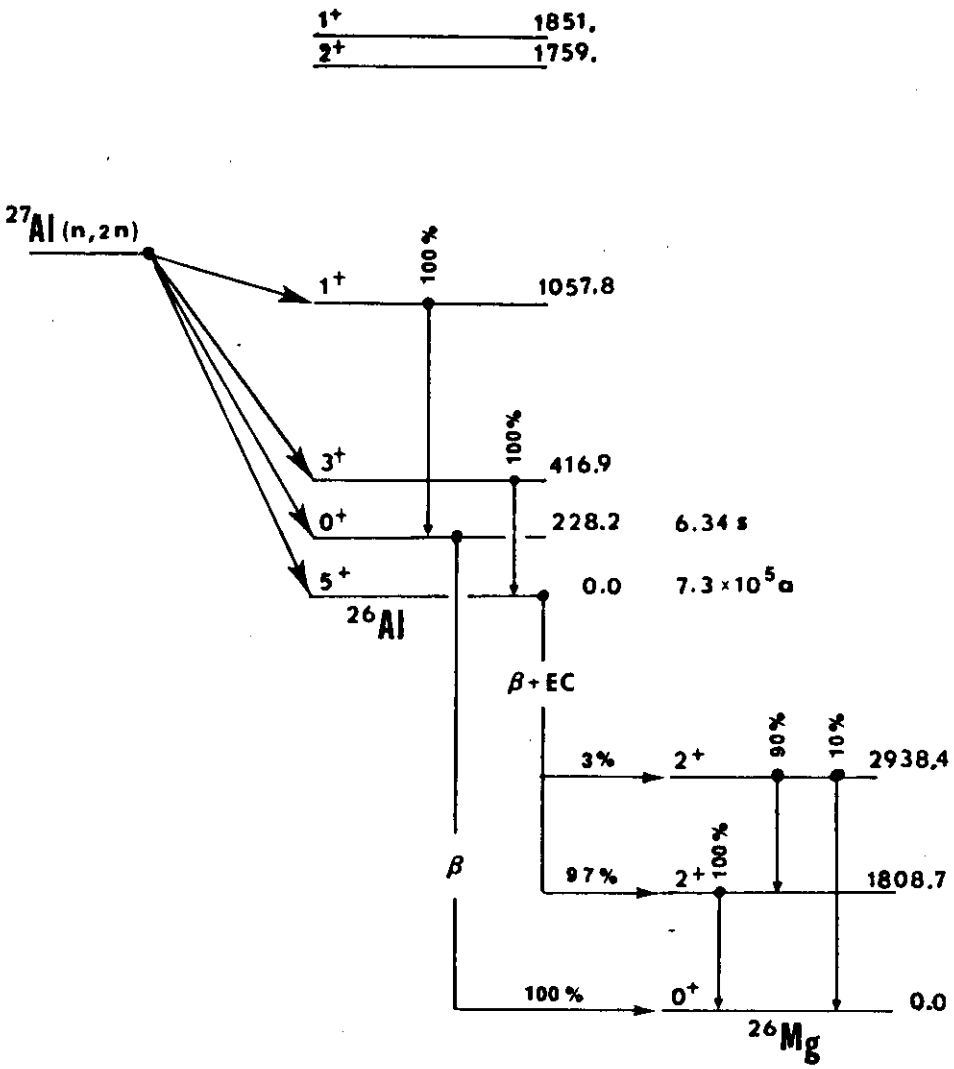


FIGURE 1. $^{27}Al(n,2n)$ Population of States in $^{26}Al$ Followed by Decay to $^{26}Mg$.

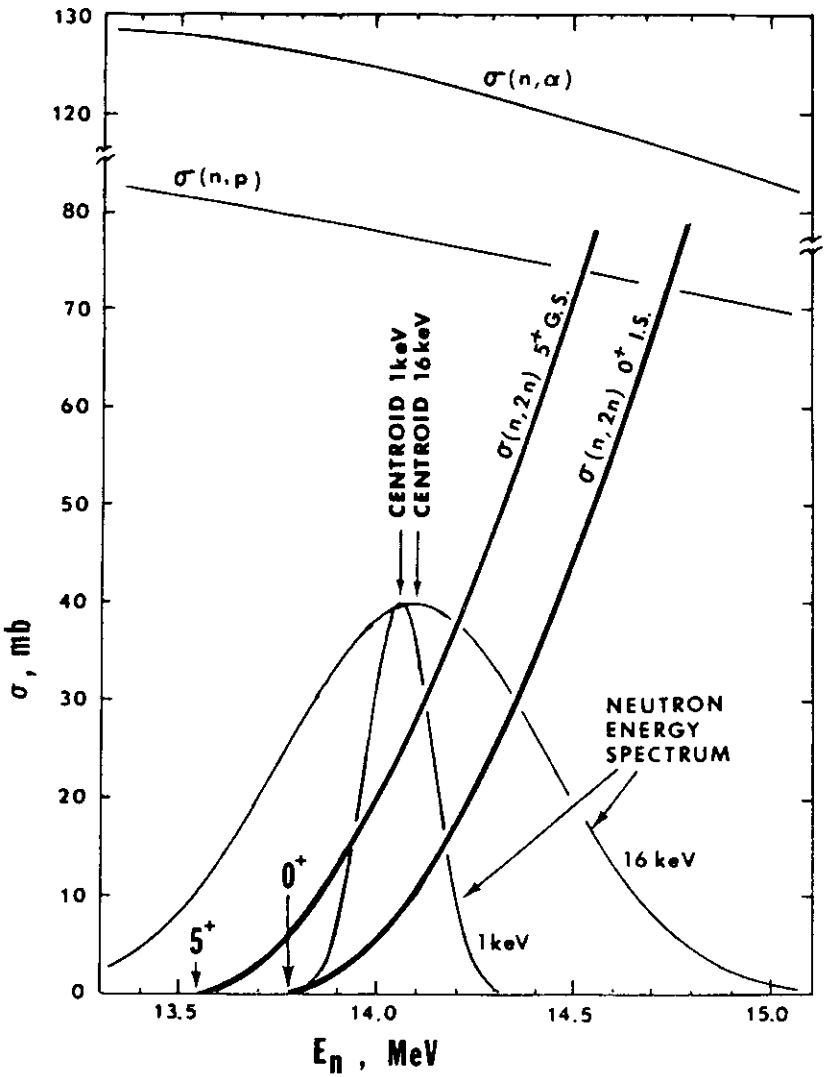


FIGURE 2. Comparison of (n,2n) Cross Section (Theoretical) for the Production of the $5^+$ Ground State and the $0^+$ Isomeric State at 228 keV with Neutron Energy Distributions Associated with 1 keV and 16 keV, for D-T Plasmas.

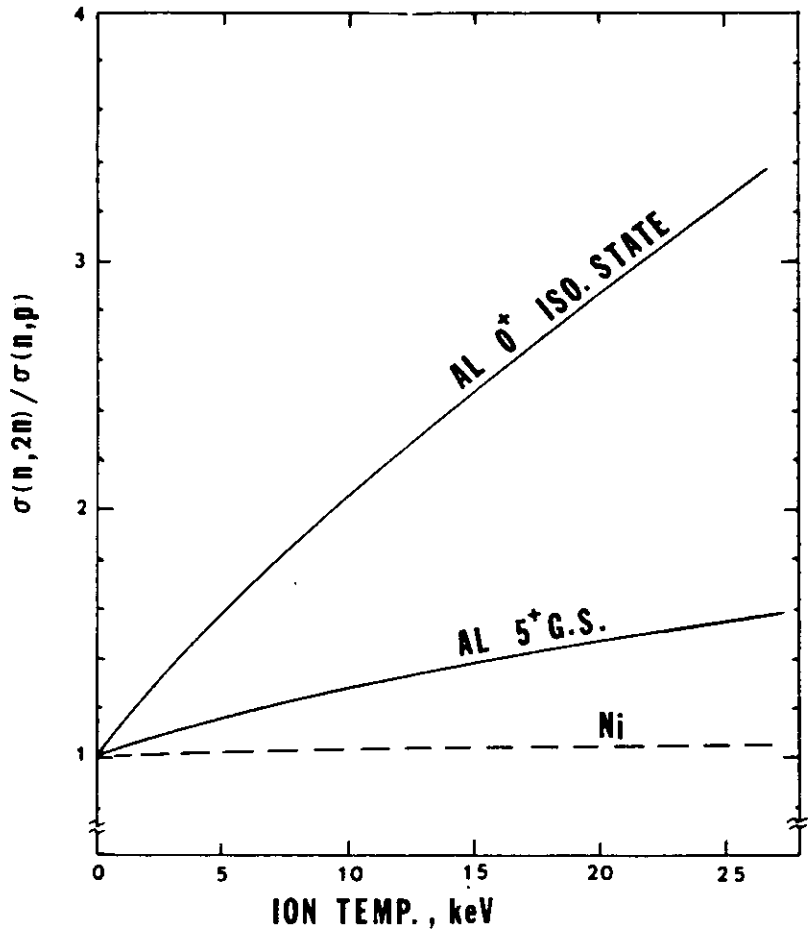


FIGURE 3. Normalized Ration of the (n,2n) Cross Section to the (n,p) Cross Section for the Production of the $5^+$ Ground State and the $0^+$ Isomeric State (Solid Lines) and the Normalized Ratio of (n,2n)/(n,p) for $^{58}Ni$.

The near threshold cross section measurements of Smither and Greenwood[2] of the $5^+$ ground state are shown in Fig. 4. The long-dashed curve is the theoretical calculation that assumes all of the near threshold cross section forms the $5^+$ ground state directly. The only adjustable parameter is the nuclear temperature. The value of this parameter is taken as the same as found to be appropriate for similar nuclei. The fit to the data is very poor. The solid curve is a similar calculation where one assumes that all of the threshold yield proceeds through the direct production of the $3^+$ ground state at 416.9 keV. In this case the theoretical curve fits the data very nicely. The short-dashed curve is a second calculation of the cross section based on the direct production of the $5^+$ ground state using a less likely value for the nuclear temperature. It does not fit the data very well, but is not completely ruled out by the data. New experiments are planned using neutron energies in the 13.8 to 14.4 MeV range to clear up this uncertainty. These new experiments will make use of the RTNS-II neutron generator at LLL as did the earlier experiments.

The cross section measurements of G. S. Mani, et al.[1] for the production of the $0^+$ isomeric state are plotted in Fig. 5 as squares. The lowest energy neutron used in these experiments was 16.2 MeV, but already at these energies the yield was well below the expected yield as indicated by the long-dashed curve. The two short-dashed curves are attempts to fit the data by varying the nuclear temperature. Neither of these attempts fit the data in an acceptable manner. The solid curve assumes that all the cross section near threshold for this reaction channel is associated with the direct production of the $1^+$ state at 1057.8 keV. This curve fits the data very well. Although strongly suggestive,

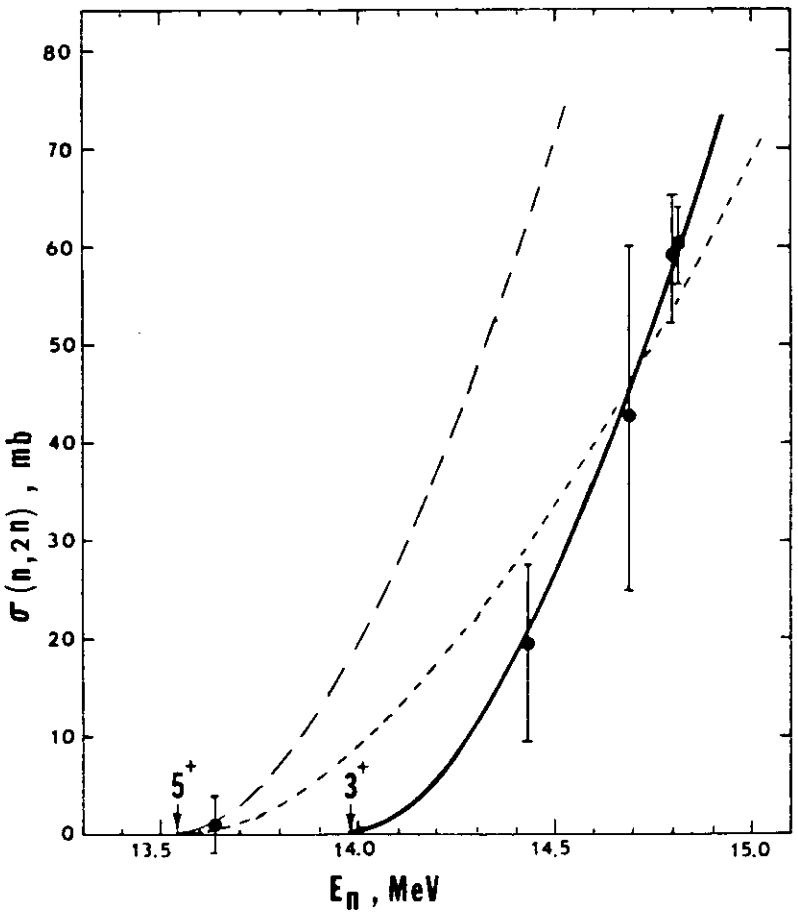


FIGURE 4. Comparison of Theoretical (n,2n) Cross Sections with the Data of Reference 2.

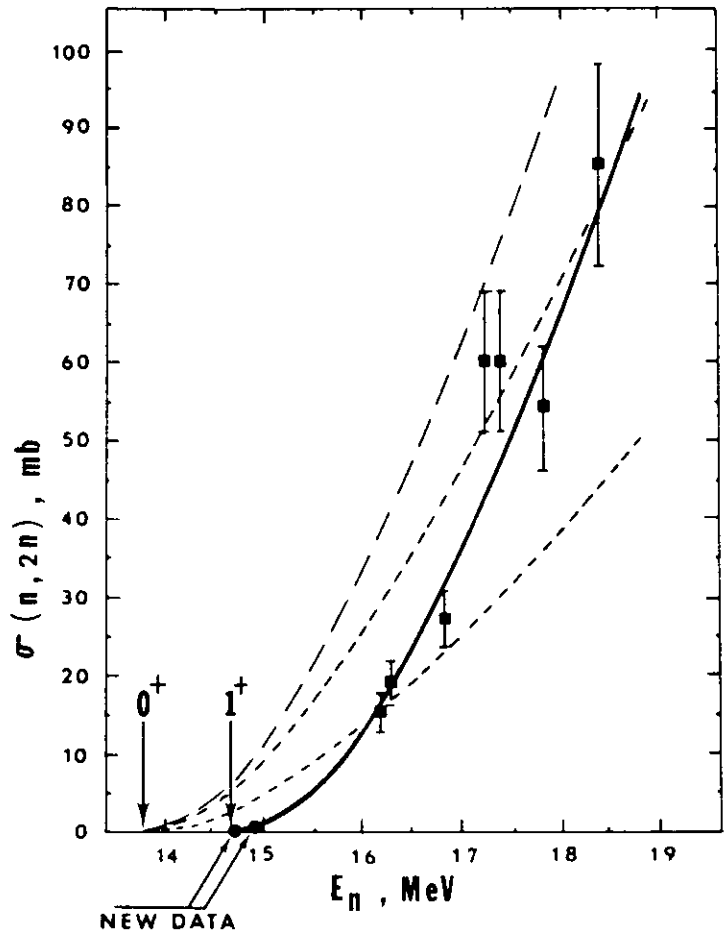


FIGURE 5. Comparison of Theoretical (n,2n) Cross Sections with the Data of Reference 1 (Shown as Squares) and the Recent Data Taken at PPPL Near Threshold (Shown as Filled Circles).

the data does not completely rule out a small component of the near threshold cross section being associated with the direct production of the $0^+$ isomeric state. In order to determine whether or not there is any appreciable cross section related to the direct production of the $0^+$ state, a new set of experiments was preformed at the Princeton Plasma Physics Laboratory in March 1983, using their small D-T neutron generator. The neutron energies used in this experiment were in the range of 14.6 to 14.9 MeV which nicely brackets the threshold neutron energy, En(lab) = 14.636 MeV, for the production of the $1^+$ state. The very low cross section (less than 1 mb) measured in this region confirms the lack of any (n,2n) cross section associated with the direct production of the $0^+$ state effectively raises the Q-value for this reaction channel by 730 keV.

The experimentally determined cross section curves are plotted in Fig. 6 for the direct production of the $3^+$ state at 416.9 keV and the $1^+$ state at 1057.8 keV. These curves are compared to the neutron energy spectra associated with ion plasma temperatures of 1 keV, 16 keV, and 25 keV. The $3^+$ cross section samples the central part of these distributions while the $1^+$ is sensitive to the high energy tails of the distributions. Figure 7 shows the same normalized ratio, $\sigma(n,2n)/\sigma(n,p)$ for the $5^+$ ground state (through the direct production of the $3^+$ state) as was shown in Fig. 3. The slope of this curve is much steeper than in Fig. 3 which suggests increased sensitive to the ion temperature. A similar curve can not be generated for the $0^+$ as fed through the $1^+$ because the threshold for the $1^+$ state is above the energy distribution for the low ion temperatures. The long dashed curve in Fig. 7 is

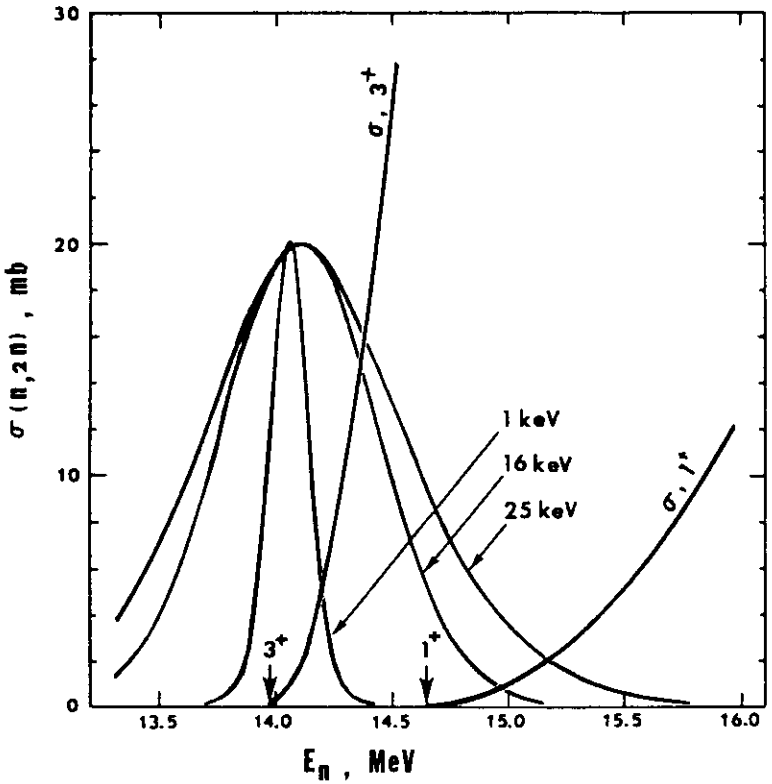


FIGURE 6. Comparison of the Experimentally Determined Cross Sections for the Direction Production of the $3^+$ State at 416.9 keV and the $1^+$ State at 1057.8 keV with the Neutron Energy Spectra Associated with Ion Plasma Temperatures of 1 keV, 16 keV, and 25 keV, for D-T Plasmas.

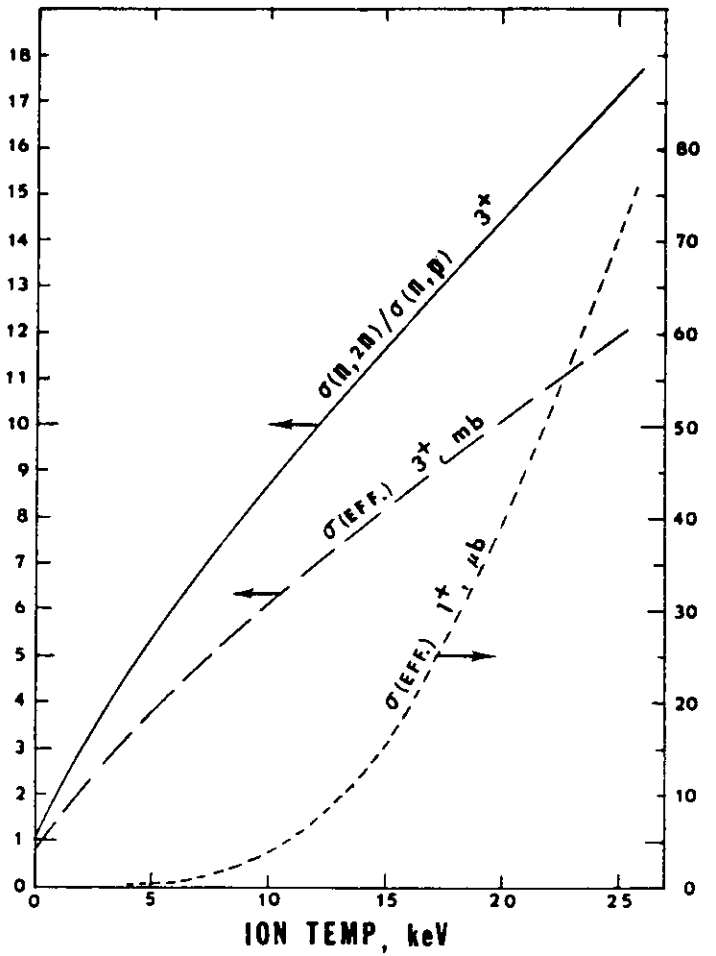


FIGURE 7. Normalized Ratio of the (n,2n) Cross Section to the (n,p) Cross Section for the $3^+$ State at 416.9 keV (Solid Line) and the Effective (n,2n) Cross Section for the Direct Formation of the $3^+$ State (Long Dashed Line) and the Effective Cross Section for the Direct Formation of the $1^+$ State (Short Dashed Line) as a Function of the Plasma Ion Temperature.

the effective cross section for the production of the $3^+$ state. This effective cross section is defined as the number of radioactive nuclei produced divided by the neutron flux through the sample (n/cm) times the number of atoms in the sample. The short dashed curve is the effective cross section for the production of the $1^+$ state. The values of this curve are given in $\mu$b by the scale on the right. These cross sections may seem small but it should be remembered that measurements at PPPL were of this same magnitude. The measured effective cross section of 50 $\mu$b $\pm$ 10 $\mu$b was made with a small sample (2 gm) and a relatively low total flux of $1.5 \times 10^9$ neutrons/cm$^2$ per shot. A typical TFTR shot is expected to produce $10^{12}$ neutrons/cm$^2$ at the monitoring location so it should be possible to make measurements at the 1-3 $\mu$b level. This corresponds to ion temperatures as low as 6 keV.

## 6.0 References


1. G. S. Mani, G. J. McCallum, and A. T. G. Fergurson, Nucl. Phys. 19, p. 535 (1960).

2. R. K. Smither and L. R. Greenwood, "Measurement of the $^{27}Al(n,2n)^{26}Al$ Cross Section", Dosimetry and Damage Analysis, DOE/ER-0046/9, p. 55-68 (May 1982).


## 7.0 Future Work

Additional experiments are planned at both PPPL and LLL to improve our knowledge of these (n,2n) cross sections in Al near threshold.

## 8.0 Publications

None.

## HELIUM PRODUCTION CROSS SECTIONS FOR 14.8-MeV NEUTRONS

D. W. Kneff, B. M. Oliver, R. P. Skowronski, and H. Farrar IV (Rockwell International, Energy Systems Group)

### 1.0 Objective

The objectives of this work are to measure helium generation rates of materials for Magnetic Fusion Reactor applications in the ~14.8-MeV T(d,n) neutron environment, and to develop helium accumulation neutron dosimeters for this test environment.

### 2.0 Summary

Total helium production cross sections have been determined at $E_n$ = 14.8 MeV for C (graphite), Y, Ag, and Ta irradiated in RTNS-II, and for $^{6}Li$, $^{7}Li$, $^{10}B$, and $^{11}B$ irradiated in RTNS-I. The RTNS-I measurements duplicate previous RTNS-II analyses of boron and lithium. The new boron results are in excellent agreement with the RTNS-II results, but the lithium cross sections show large scatter (~10-20%) relative to our RTNS-II measurements. This large scatter is due in part to the uncertainties associated with the subtraction of the large helium contribution from the fluorine in the irradiated LiF samples.

### 3.0 Program

Title: Helium Generation in Fusion Reactor Materials
Principal Investigators: D. W. Kneff and H. Farrar IV
Affiliation: Rockwell International, Energy Systems Group

### 4.0 Relevant DAFS Program Plan Task/Subtask

Subtask II.A.2.2 Flux-Spectral Definition in RTNS-II
Subtask II.A.4.2 T(d,n) Helium Gas Production Data

## 5.0 Accomplishments and Status

Total helium production cross section measurements have been completed for C (graphite), Y, Ag, and Ta samples irradiated in the ~14.8-MeV T(d,n) neutron spectrum of the Rotating Target Neutron Source-II (RTNS-II), and for $^{6}LiF$, $^{7}LiF$, $^{10}B$, and $^{11}B$ samples irradiated at RTNS-I. These measurements were part of a program supported by the Office of Basic Energy Sciences of the U.S. Department of Energy. The irradiations were joint Rockwell International-Argonne National Laboratory (ANL)-Lawrence Livermore National Laboratory (LLNL) experiments. The helium analyses were performed using high-sensitivity gas mass spectrometry. The neutron fluence at each sample location was determined by detailed neutron fluence mapping of the irradiation volume for each experiment.[1,2]

The RTNS-II measurement results are presented in Table 1. The Y, Ag, and Ta samples were irradiated as pure element chunks, while carbon was irradiated as graphite pieces encapsulated in miniature platinum capsules. These results represent 14 independent helium analyses, for samples located at different positions within the 2-cm-diameter irradiation capsule. Silver was included primarily to extend helium generation cross section systematics as a function of atomic number. The graphite cross section result (893 ± 60 mb) is in excellent agreement with previous RTNS-II measurements (900 ± 70 mb),[3] which used carbon in the form of diamond.

TABLE 1

EXPERIMENTAL HELIUM GENERATION CROSS SECTIONS FOR ~14.8-MeV NEUTRONS

| Material | Cross Section (mb) | Material | Cross Section (mb) |
|---|---|---|---|
| C (graphite) | 893 ± 60 | Ag | 7.6 ± 0.6 |
| Y | 9.3 ± 0.7 | Ta | 1.10 ± 0.09 |

Several titanium wire segments which were also irradiated in the RTNS-II experiment, adjacent to a number of platinum capsules, were analyzed during this reporting period to provide additional data on fluence gradients. The individual titanium cross section determinations exhibited small scatter ($1\sigma < \pm 3\%$) and the averaged cross section result (38 ± 3 mb) agreed very well with our previously reported cross section results from two RTNS-I irradiations (38 ± 3 mb, 37 ± 3 mb).[3]

The Li, LiF, and B results from RTNS-I are summarized in Table 2, along with our previously reported RTNS-II measurements.[4] The lithium isotopes were irradiated as unencapsulated $^{6}LiF$ and $^{7}LiF$ crystals, and the lithium cross sections were obtained by unfolding the fluorine cross section from the LiF results. The fluorine value used was 501 ± 36 mb, based on our previous measurements for $PbF_2$, irradiated in RTNS-II.[4] The boron isotopes were irradiated as unencapsulated $^{10}B$ and $^{11}B$ crystals. Table 2 also includes current helium production cross section evaluations[5-7] for comparison with the measurements.

Examination of the boron results in Table 2 shows excellent agreement between our RTNS-I and RTNS-II measurements. In the case of $^{10}B$, the ENDF/B-V (n,total helium) evaluation is about 12% low relative to our cross section results. For $^{11}B$, no direct comparisons can be made with the ENDF/B-V evaluation, because the evaluation includes only the $(n,\alpha)$ reaction channel. Some additional measurements were also performed during the reporting period with $^{10}B$ samples irradiated at RTNS-II, at large distances from the high-flux irradiation region (including the back cell wall). These measurements confirmed that $^{10}B$ self-shielding, combined with the post-irradiation etching of the samples' surfaces, removed the contribution of thermalized room-return neutrons to helium production in all of the RTNS-irradiated $^{10}B$ samples.

The RTNS-I $^{6}Li$ and $^{7}Li$ measurements were of particular interest because our RTNS-II results for $^{6}Li$ differ significantly from recent cross section

TABLE 2

BORON AND LITHIUM TOTAL HELIUM GENERATION CROSS SECTIONS FOR ~14.8-MeV NEUTRONS

| Material | Cross Section (mb)[a] | | |
|---|---|---|---|
| | RTNS-I | RTNS-II[b] | Evaluation |
| $^{10}B$ | 699 ± 66 | 691 ± 49 | 610[d] |
| $^{11}B$ | 306 ± 29 | 306 ± 22 | 31[e] (n,α) only |
| $^{6}LiF$ | 541 ± 51 | 569 ± 41 | -- |
| $^{6}Li$ (c) | 583 ± 98 | 639 ± 75 | 462[d], 521[f] |
| $^{7}LiF$ | 422 ± 40 | 441 ± 32 | -- |
| $^{7}Li$ (c) | 343 ± 76 | 381 ± 58 | 356[g], 336[h] |

[a] For LiF, the cross section values are the average cross sections per atom of material. The cross section per molecule of LiF is the reported cross section times 2.

[b] Reference 4.

[c] Derived from LiF, assuming $\sigma(F)$ = 501 ± 36 mb.

[d] (n,total helium), from ENDF/B-V.

[e] (n,α), from ENDF/B-V.

[f] (n,nd)α + (n,2np)α + (n,t)α, from ENDL (Reference 6).

[g] (n,nt)α + (n,2nd)α, from ENDF/B-V.

[h] (n,nt)α from P. G. Young (Reference 7) plus (n,2nd)α from ENDF/B-V.

evaluations (Table 2). The $^{6}Li$ results also differ from the results of a separate, short RTNS-I test irradiation conducted by E. Goldberg (LLNL), in which Rockwell also participated. The latter test irradiation, for which the results are not fully analyzed, gave a cross section of 523 mb (±~10%) for $^{6}Li$(n,total helium),[8] which agrees with the LLNL ENDL evaluation.[6] A concurrent Rockwell add-on experiment gave a $^{7}Li$(n,total helium) cross section of 397 ± 75 mb, in general agreement with our RTNS-II

results. For this RTNS-I test irradiation, the Monte Carlo code TART was used in the calculation of neutron fluences at the carefully measured $^{6}$LiF and $^{7}$LiF sample locations. The samples were encapsulated in vanadium, for which a relatively large (~10-15%) helium background correction was required. The helium generation concentrations were measured at Rockwell.

Comparison of the Rockwell RTNS-I and RTNS-II results in Table 2 shows that the $^{6}$LiF and $^{7}$LiF cross sections are consistent within their relatively large uncertainties (~±9%). They are also generally consistent with values derived from the LLNL RTNS-I experiment (505 mb for $^{6}$LiF and 449 mb for $^{7}$LiF). However, subtraction of the fluorine cross section (with its own uncertainties) significantly increased the data scatter, and increased the lithium cross section uncertainties. In particular, the Rockwell RTNS-I $^{6}$Li results overlap both the RTNS-II measurements and the significantly lower ENDL cross section evaluation. A new experiment is needed, designed specifically to reduce the measurement uncertainties. An RTNS experiment with this objective is in the planning stages, possibly using encapsulated $^{6}$Li and $^{7}$Li metal samples instead of lithium compounds.

## 6.0 References


1. D. W. Kneff, B. M. Oliver, M. M. Nakata, and H. Farrar IV, "RTNS-II Fluence Mapping and Helium Generation Cross Sections," in Damage Analysis and Fundamental Studies, Quarterly Progress Report January-March 1982, DOE/ER-0046/9, U.S. Department of Energy, 16 (1982).

2. D. W. Kneff, B. M. Oliver, M. M. Nakata, and H. Farrar IV, "Helium Generation Cross Sections for Fast Neutrons," in Proc. Symp. on Neutron Cross-Sections from 10 to 50 MeV, M. R. Bhat and S. Pearlstein, eds., BNL-NCS-51245, Brookhaven National Laboratory, N.Y., p. 289 (1980).

3. D. W. Kneff, B. M. Oliver, M. M. Nakata, and H. Farrar IV, "Experimental Helium Generation Cross Sections for Fast Neutrons," J. Nucl. Mater., 103 & 104, 1451 (1981).

4. D. W. Kneff, B. M. Oliver, M. M. Nakata, and H. Farrar IV, "Helium Production Cross Sections for 14.8-MeV Neutrons," in Damage Analysis and Fundamental Studies, Quarterly Progress Report April-June 1982, DOE/ER-0046/10, U.S. Department of Energy, 19 (1982).

5. Evaluated Nuclear Data File (ENDF/B-V).

6. R. J. Howerton, et al., Evaluated Nuclear Data Library (ENDL), Lawrence Livermore National Laboratory.

7. P. G. Young, "Evaluation of n + $^{7}$Li Reactions Using Variance-Covariance Techniques," Trans. Am. Nucl. Soc., 39, 272 (1981).

8. E. Goldberg (private communication).

## 7.0 Future Work

The helium analysis of RTNS-II-irradiated materials will continue. Primary near-term emphasis will be on Be, N, O, and Mn.

## 8.0 Publications

None.

## The Effects of Collision Cascade Properties on the Diffusion of Point Defects in Irradiated Materials

Philip Chou and Nasr M. Ghoniem (University of California at Los Angeles)

### 1.0 Objective

The objective of this work is to investigate the effects of cascade size, PKA energy and cascade properties on the stochastic diffusion of point defects.

### 2.0 Summary

New solutions to the point defect continuity equations are developed in this work. The random production of cascades in structural materials leads to stochastic fluctuations in point defect concentrations in any localized area in the irradiated solid. Previous treatments havew assumed a point source of vacancies or interstitials after cascade production. In the present analysis, we model vacancies and interstitials as concentric spheres. The sizes of the spheres are found by separate Monte Carlo calculations. Our calculations indicate that the relative fluctuation in point defect concentrations decreasesas a function of cascade size or PKA energy. Cascades in a fusion reactor spectrum are so large that fluctuations in vacancy concentrations are small, and their behavior may be adequately approximated by rate theory. However, the relative fluctuation in the interstitial concentration is very significant. In some processes, rate theory applied to interstitials may not be adequate.

### 3.0 Program

Title: Helium Effects on the Swelling of Steels
Principal Investigator: N.M. Ghoniem
Affiliation: University of California at Los Angeles

### 4.0 Relevant DAFS Program Plan Task/Subtask

Subtask Group C: Damage Microstructure Evolution and Mechanical Behavior
Problem b.5: Effect of damage rate and primary recoil spectrum.

### 5.0 Accomplishments and Status

#### 5.1. Introduction

During the last two decades, rate theory has been applied to the interaction of point defects with microstructural features. In this approach, both vacancies and interstitials are assumed to be produced uniformly in time and homogeneously in space. Based on this concept for point defect generation, rate equations have been developed for the description of diffusion, recombination and interaction of point defects with dislocations, grain boundaries, cavities, and precipitates.

Under neutron or ion irradiations, point defects are produced in ensembles resulting from a sequence of collisions in cascades. As such, primary knock-on atoms (PKA's) generate a series of displacements that are closely situated. The generation of cascades is random in space and time. Therefore, a microstructural feature will see and interact with a fluctuating concentration of point defects. Rate theory fails to account for the fluctuations in point defect concentration, since the theory is formulated for the average behavior of defects. For non-linear phenomena, such as irradiation creep and defect nucleation, it is expected that rate theory gives inaccurate results. Mansur, Coghlan and Brailsford[1] formulated a cascade-diffusion theory for the description of point defect concentration in irradiated solids. They represented defect cascades as points ($\delta$ functions) in space. They also applied the theory to void growth[1] and irradiation creep.[2] Gurol and Wolfer[3] also used the same approach in a Fokker-Planck formulation of the climb-glide creep model to analyze defect concentration fluctuation effects on irradiation creep. By essentially using the point model for the cascade, Marwick[4] allowed the cascades to diffuse initially to a radius of 30 angstroms before starting long range diffusion of the cascades. He was able to analytically describe the root mean square (RMS) value of the fluctuations in point defect concentration at different temperatures. However, the radius selected in his treatment is much smaller than the size of high energy cascade and/or the inter-sink distance for absorption (mean free path), that it can still be regarded as a point model. In the present analysis, we will relax the assumption of point cascades ($\delta$ functions) and address the effects of cascade properties; such as size, PKA energy and number of defects, upon the fluctuations in point defect concentrations.

## 5.2. Theory

Diffusion of point defect in irradiated materials is governed by the space-time continuity equatons. These equations have the form:

$$\frac{\partial C_v}{\partial t} = P(\bar{r}_c, t_c)_v - \alpha C_v C_i - D_v S_v C_v + \nabla D_v \nabla C_v \qquad (1)$$

and

$$\frac{\partial C_i}{\partial t} = P(\bar{r}_c, t_c)_i - \alpha C_v C_i - D_i S_i C_i + \nabla D_i \nabla C_i \qquad (2)$$

where subscripts v and i stand for vacancy and interstitial, respectively. C is the point defect concentration, S is the total effective sink strength, $\alpha$ is the point defect mutual recombination coefficient, and D is the point defect diffusion coefficient. It has the form

$$D = D_o e^{-E_m/kT} \qquad (2)$$

where $D_o$ is the diffusion coefficient constant, $E_m$ is the defect migra-

tion energy, k is Boltzmann's constant, and T is the absolute temperature. The production rate of point defects by irradiation in equations (1) and (2) is represented by a time-space function $P(\bar{r}_c, t_c)$ where $\bar{r}_c$ is the vector position of defect generation, and $t_c$ is the time of defect generation.

Production of point defects is random, both in space and time. However, for ion and neutron irradiation, this "randomness" is not complete, since ensembles of defects are produced in close spatial proximity. Moreover, the time interval for the generation of such ensembles of defects is extremely short, on the order of $10^{-11}$ seconds. This is typically 5-6 orders of magnitude shorter than the diffusion time of the fastest moving species (self interstitials). During this time interval, a major fraction of the point defects generated in the ensembles is lost due to defect quenching within the cascade (instantaneous recombination). The effect can be separated from the mutual recombination terms in equations (1) and (2) because of the time scale involved. Therefore, it is possible to separate point defect generation from their subsequent diffusion and interaction; that is if one is only interested in the behavior of the contents of one cascade. Needless to say that it is quite formidable to solve equations (1) and (2) for an arbitrary random source of point defects $P(\bar{r}_c, t_c)$.

In order to obtain an analytic solution, simplifications in equations (1) and (2) are needed. In this regard, the nonlinear point defect mutual recombination term $\alpha C_i C_v$ is neglected in both equations. Furthermore, it is assumed that point defect diffusion coefficient is space independent.

If the point defect source $P(\bar{r}_c, t_c)$ is taken to be a unit delta function $\delta(\bar{r}-\bar{r}_c)\delta(t'-t_c)$, the Green's function $G(|\bar{r}-r_c|, t'-t_c)$ will be the solution for equations (1) and (2) for $t' > t_c$. It has the form

$$G(|\bar{r}-\bar{r}_c|, t'-t_c) = \frac{e^{-DS(t'-t_c)}\, e^{-\frac{(\bar{r}-\bar{r}_c)^2}{4D(t'-t_c)}}}{[4\pi D(t'-t_c)]^{3/2}} \qquad (4)$$

where t' is the real time and $\bar{r}$ is the vector position of the point of observation.

Earlier attempts to describe point defect diffusion resulting from randomly produced cascades have treated cascades as points in space and time. In the work of Mansur, Coghlan and Brailsford[1] the point defect concentration contributed by a cascade containing $\nu$ defects (a cascade strength of $\nu$ defects) for either interstitials or vacancies is given by

$$C(x,t) = \frac{\nu e^{-DSt}\, e^{-x^2/4Dt}}{(4\pi Dt)^{3/2}} \tag{5}$$

where the notations $x = |\bar{r}-\bar{r}_s|$ and $t = t'-t_c$ are used. Physically speaking, t is the time elapsed after the generation of the cascade and x is the distance between the point of observation and the point of cascade generation. Marwick[4] allowed the point cascades to diffuse for a time $t_o$ to an "effective" radius $r_o$, such that

$$t_o = \frac{r_o^2}{4D} \tag{6}$$

The cascade, therefore, has an initial Gaussian distribution of defects and the point defect concentration distribution is given by

$$C(x,t) = \frac{\nu e^{-DSt}\, e^{-x^2/4D(t+t_o)}}{[4\pi D(t+t_o)]^{3/2}} \tag{7}$$

it is shown[3,4] that the relative RMS (RMS/average concentration) value is quite large for both vacancies and interstitials. For vacancies under various irradiation conditions within typical temperature ranges, this value is 2-20, while for interstitials, it is around $10^4$ - $2\times10^5$. It has also been shown[2,3] that non-linear irradiation phenomena are very sensitive to this parameter. It is important therefore to assess the dependence of this value on cascade properties, such as cascade size, cascade strength (defect content) and PKA energy.

In order to take account of the cascade size effect in this analysis, we consider a cascade produced at time $t_c$ and position $\bar{r}_c$ with an initial point point defect distribution $P(\bar{r}_c,t_c)_{v,i}$ where v and i stand for vacancy cascade and interstitial cascade, respectively. The solution to equations (1) and (2) with defect source $P(\bar{r}_c,t_c)_{v,i}$ by using the green's function for $t' > t$ is given as

$$C_{v,i}(x,t) = \int_{\bar{v}_c} G(x,t)P(\bar{r}_c,t_c)_{v,c}\, d^3r_c \tag{8}$$

Again, the notations $x = |\bar{r}-\bar{r}_c|$ and $t = t'-t_c$ are used. The above integragration is performed over the cascade volume $\bar{v}_c$.

From previous experimental observations, it has been concluded that depleted zones are mainly composed of vacancies, while the near outer cascade regions contain self interstitials. Therefore, in our approach,

vacancies and interstitials are assumed to separate into two distinct regions within the cascade volume, after initial instantaneous recombination. For further simplicity, we represent vacancies as a uniform distribution inside a sphere of radius $r_s$. The interstitial cascade is then represented as a uniform distribution inside a spherical shell of inner radius $r_s$ and shell thickness dr. The solutions of equations (1) and (2) are then obtained directly by applying equation (8) to equation (4) with the appropriate form of $P(\bar{r}_c, t_c)$. For the vacancy cascade, the vacancy concentration $C_v(x,t)$ is given by:

$$C_v(x,t) = \frac{3\nu e^{-DSt}}{8\pi r_s^3} \left\{ \operatorname{erf}\left(\frac{x+r_s}{4Dt}\right) - \operatorname{erf}\left(\frac{x-r_s}{4Dt}\right) - \frac{4Dt}{x(\pi)^{1/2}} \left[ e^{\frac{(x-r_s)^2}{4Dt}} - e^{-\frac{(x+r_s)^2}{4Dt}} \right] \right\} \tag{9}$$

where erf stands for error function, and the concentration contributed by an interstitial cascade is as follows

$$C_i(x,t) = \frac{3\nu e^{-DSt}}{8\pi dr\,(r_s^2 + r_s dr + dr^2)} \left\{ \operatorname{erf}\left(\frac{x+r_s+dr}{4Dt}\right) - \operatorname{erf}\left(\frac{x-r_s-dr}{4Dt}\right) \right.$$

$$+ \operatorname{erf}\left(\frac{x+r_s}{4Dt}\right) - \operatorname{erf}\left(\frac{x-r_s}{4Dt}\right) - \frac{4Dt}{x(\pi)^{1/2}} e^{-\left[\frac{(x-r_s-dr)^2}{4Dt}\right]}$$

$$\left. -e^{-\frac{(x+r_s+dr)^2}{4Dt}} + e^{-\frac{(x-r_s)^2}{4Dt}} - e^{-\frac{(x+r_s)}{4Dt}} \right] \Bigg\} \tag{10}$$

The relationship between the PKA energy, cascade size and cascade strength (defect content) are obtained from a new Monte Carlo code developed by Chou and Ghoniem[5], TRIPOS, for the TRansport of Ions in POlyatomic Solids. The code uses the Monte Carlo method to simulate ion transport in amorphous polyatomic media, made of multilayers. It is worth mentioning that a quenching survival efficiency (fraction) is needed to correlate the cascade defect contents resulting from TRIPOS calculations to the actual cascade defect contents which are left to diffuse and interact with microstructural features.

## 5.3. MONTE CARLO ANALYSIS

In order to reduce computing time, Mansur, Coghlan and Brailsford[1]

found that it is sufficiently accurate to consider the cascades generated within a distance of seven absorption mean free paths to the point of interest. Therefore, we will neglect all cascades generated beyond seven mean free paths. An absorption mean free path $\ell$ is given as

$$\ell = (S)^{-1/2} \tag{11}$$

In the following, we use the Monte Carlo method for the superposition of solutions represented by equations (8) and (9). The position of generation for any defect cascade which will contribute to the defect concentration is given as follows

$$x = 7\ell\ (\xi)^{1/3} \tag{12}$$

where $\xi$ stands for a generated random number between 0 and 1.0. To decide on the time of generation, a Poisson's distribution is used. The distribution has the form

$$P(N,R) = \frac{e^{-R} R^N}{N!} \tag{13}$$

where R is the average number of cascades generated in a unit time within a sphere of seven absorption mean free path radius. N is the actual number of cascades generated within a given unit time. Let us define a cumulative distribution function $P_c(n)$ as

$$P_c(n) = \sum_{N=0}^{n} P(N,R) \tag{14}$$

First of all, a random number $\xi_1$ has to be called. Then it is compared to $P_c(n)$. If $P_c(n) < \xi_1 < P_c(n+1)$, it is assumed that n cascades are generated in the time interval of interest. Then a series of n random numbers can be called to place the cascades randomly within the time interval.

## 5.4. RESULTS

In this analysis, the following parameters are used to represent nickel for the sake of comparison with reference (1): $D_o^v = 0.014\ cm^2/s$, $E_m^v = 1.4$ eV, $S_v = 10^{11}\ cm/cm^3$, $D_o^i = 0.008\ cm^2/s$, $E_m^i = 0.15$ eV and $S_i = 1.1 \times 10^{11}$, where subscripts and superscripts v and i stand for vacancy and interstitial, respectively. The defect generation rate is $10^{-6}$ dpa/s and the temperature is 500°C. Figure (1) shows the cascade concentration distribution for vacancies as a function of both time and distance away from the point of generation for the case of a point source (function) with one vacancy. Figure (2) shows similar results for vacancy cascade, when the cascade initial defect contents are homogeneously distributed over a sphere of 100 angstroms radius. A comparison of figures (1) and (2) shows that the vacancy concentration is insensitive to the geometrical shape of the

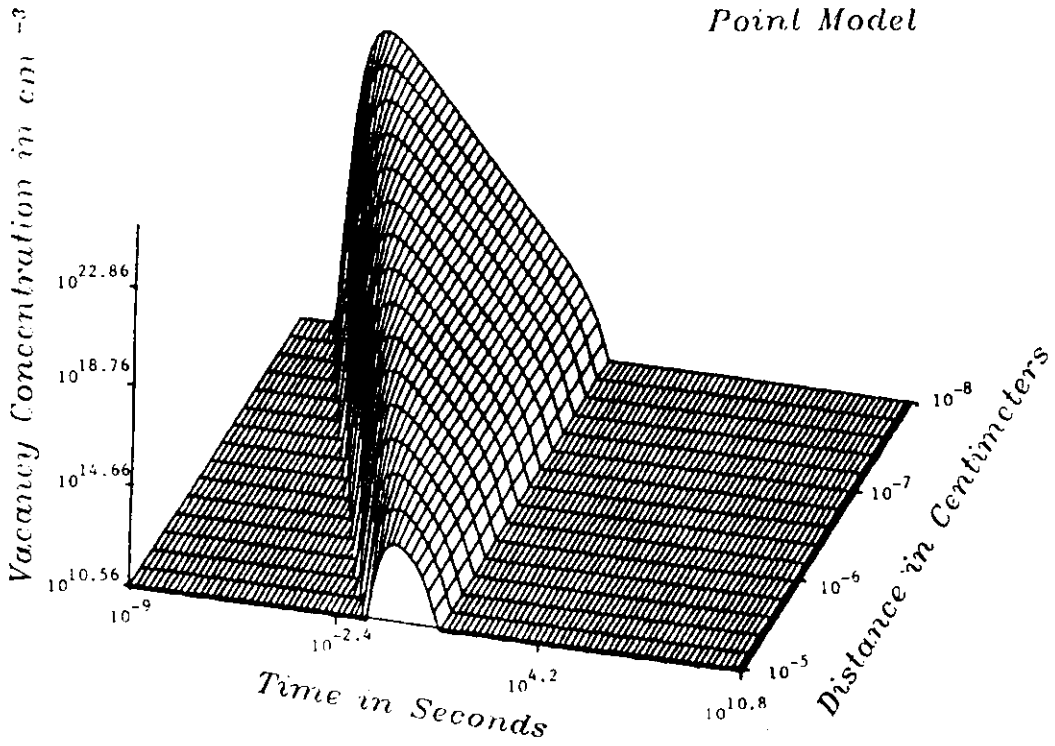


FIGURE 1. Vacancy Concentration as Functions of Time and Distance for Point Cascade with Unit Strength.

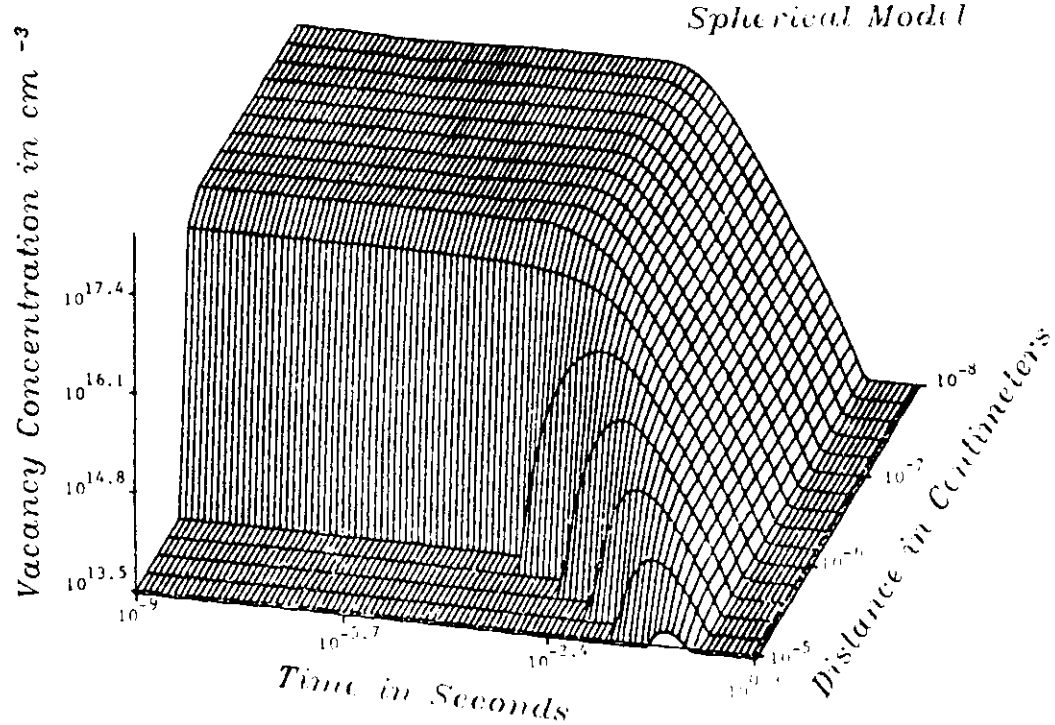


FIGURE 2. Vacancy Concentration as Functions of Time and Distance for Spherical Cascade with Unit Strength and a Radius of 100 Angstroms.

cascade at large distances away from the center of the cascade and after long times. However, if the cascade is produced within a short distance of the observation point, the geometrical shape of the cascade is expected to have a significant impact on the vacancy concentration. In the following analysis, we consider cascades containing 100 defects without including the relationship between cascade size and cascade strength (contents).

Figure (3) shows a typical plot of point density for cascade generation in space and time using our Monte Carlo scheme. The cascade arrival rate is 7.7 cascades/second. Figures (4) and (5) show the fluctuation of the vacancy concentration as a function of time due to point cascades and spherical cascades with a radius of 1000 angstroms, respectively. It is generally observed that larger cascades result in less fluctuations in vacancy concentration as compared to to point cascades. Figure (6) shows a comparison between the rate theory prediction for the average vacancy concentration and the Monte Carlo simulations of both point cascades and spherical cascades with a radius of 1000 angstroms as a function of the number of sampled cascades. It is clear that a statistical sampling on the order of a few thousand cascades is needed for vacancy cascades before agreement between rate theory and cascade-diffusion theory is achieved. Interstitial cascades have a much shorter mean lifetime, that a smaller sample size of interstitial cascades is needed before rate theory and cascade diffusion theory reach agreement. Figure (7) shows the relative RMS value as a function of vacancy cascade radius. It is shown that for cascade radius less than 100 angstroms, the point cascade approximation is sufficiently good. For large sizes, however, the relative RMS value can be small such that the rate theory is expected to be a good approximation for vacancies. Figure (8) shows the relative RMS value as a function of the interstitial inner radius. The behavior for interstitial cascades is comparable to that of vacancy cascades with the exception that the magnitude of the relative RMS value is four orders of magnitude higher than that for vacancy cascades.

In the preceeding analysis, a cascade strength of 100 defects is used. In reality, however, larger size cascades generally contain more point defects. Under a constant irradiation dose rate, the arrival rate of larger size cascades will be smaller. It will increase the fluctuations in defect concentrations due to the lower frequency of occurance. Therefore, the validity of the previous conclusions is not general, and additional efforts are needed to investigate the relationships among PKA energy, cascade size and cascade strength. In order to complete the task, we have performed PKA transport analysis by running the TRIPOS code. Figure (9 shows the average number of defects generated before quenching (instantaneous recombination) as a function of PKA energy by using the TRIPOS code. Figure (10) shows cascade quenching survival coefficient (fraction) as a function of PKA energy which is determined by Heinisch.[6] The cascade strength is obtained by multiplying the number of freshly produced defects in each cascade by the quenching survival coefficient. Figure (11) is a plot of the average cascade size (diameter) as a function of the PKA

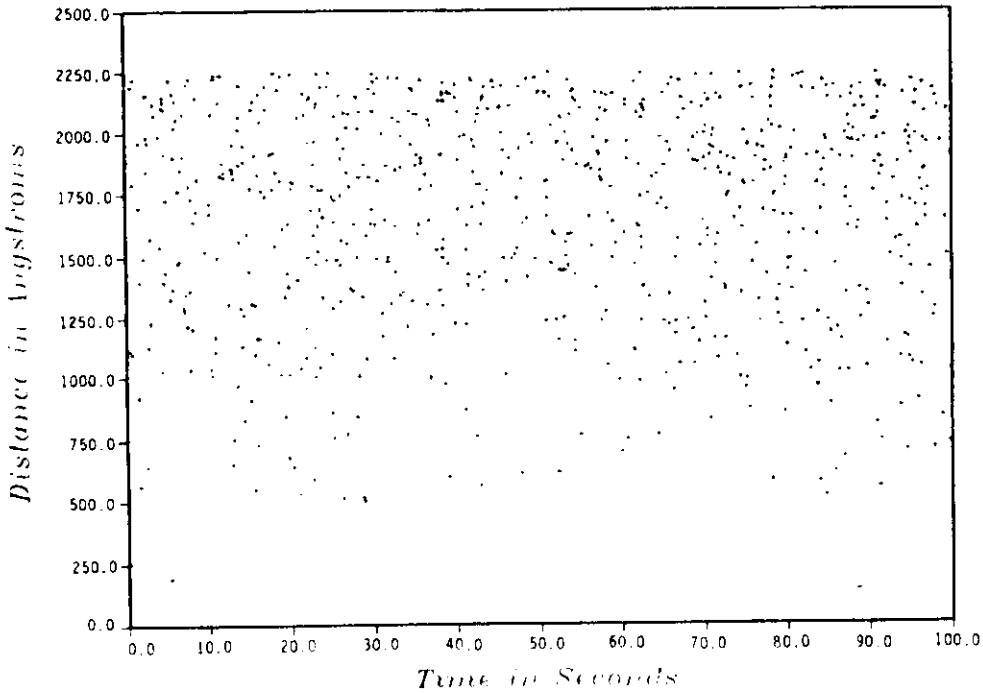


FIGURE 3. Points of Cascade Arrival in Time and Space for a Sampling Time of 100 seconds. The average cascade arrival rate is 7.7 cascades/sec.

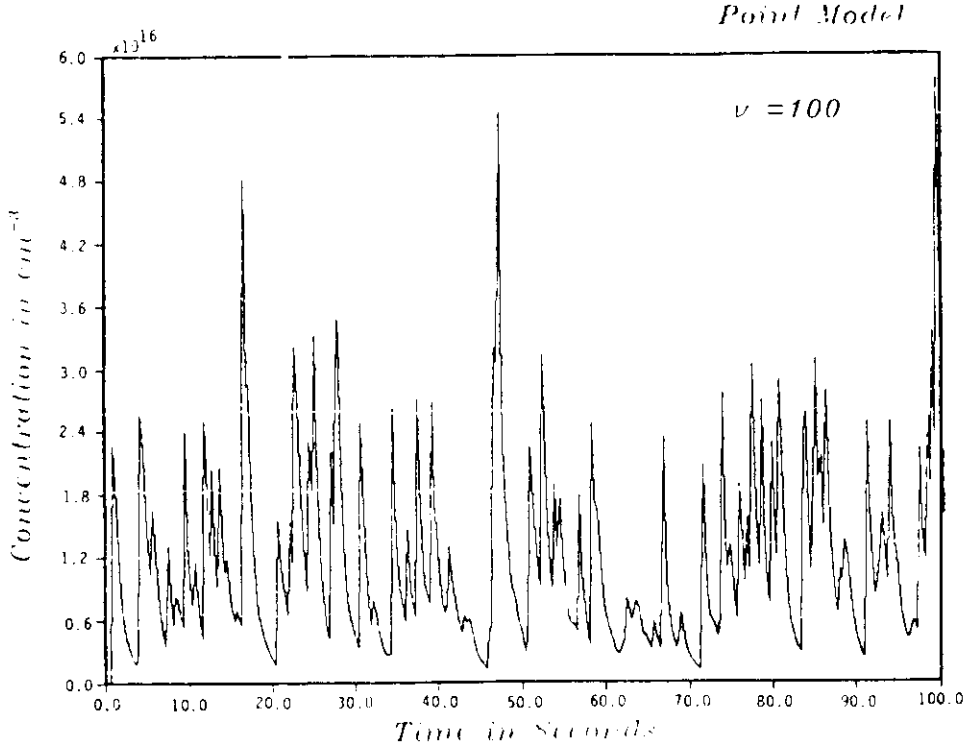


FIGURE 4. Vacancy Concentration as a Function of Time for Point Cascade Model.

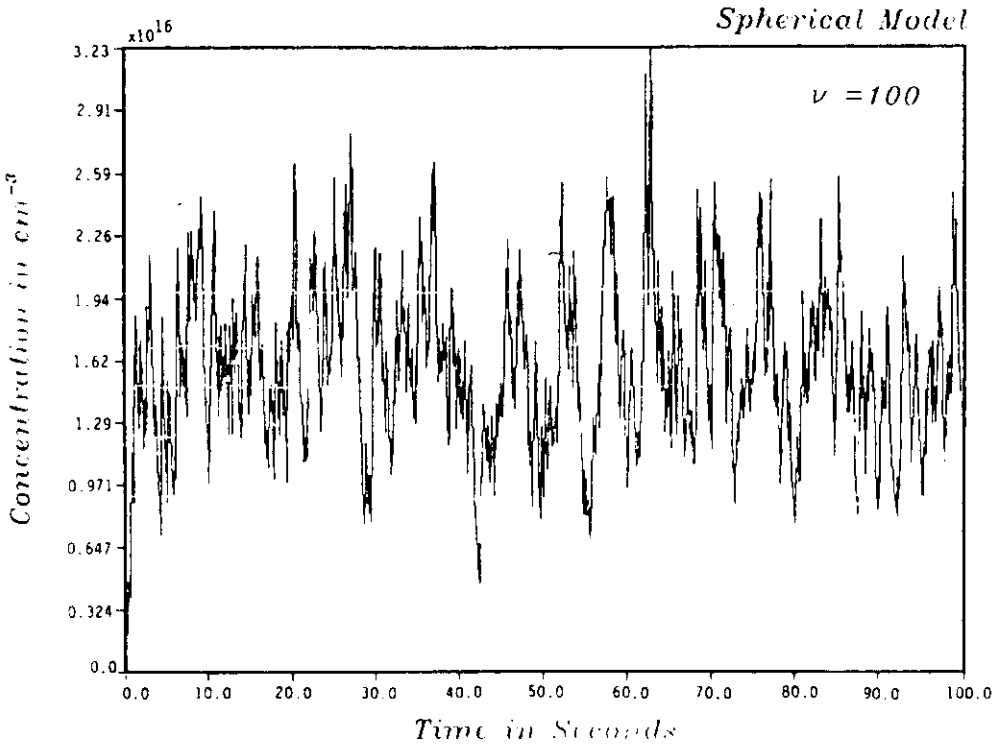


FIGURE 5. Vacancy Concentration as a Function of Time for Spherical Cascades with Radii of 1000 Angstroms.

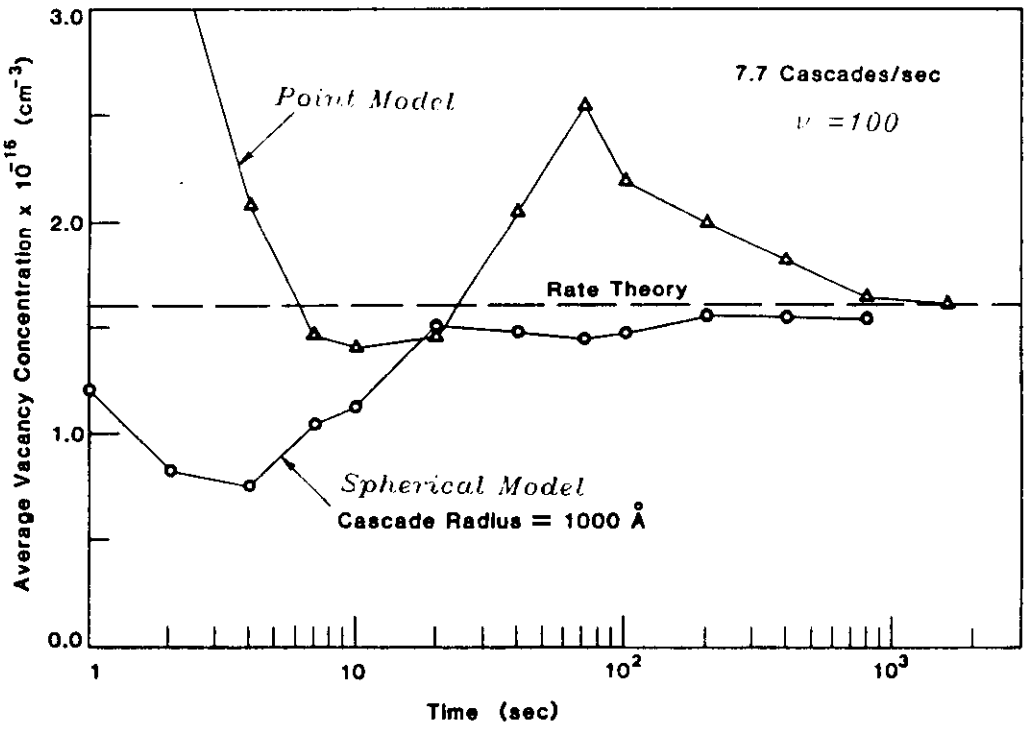


FIGURE 6. Vacancy Concentration as a Function of Time Sampled.

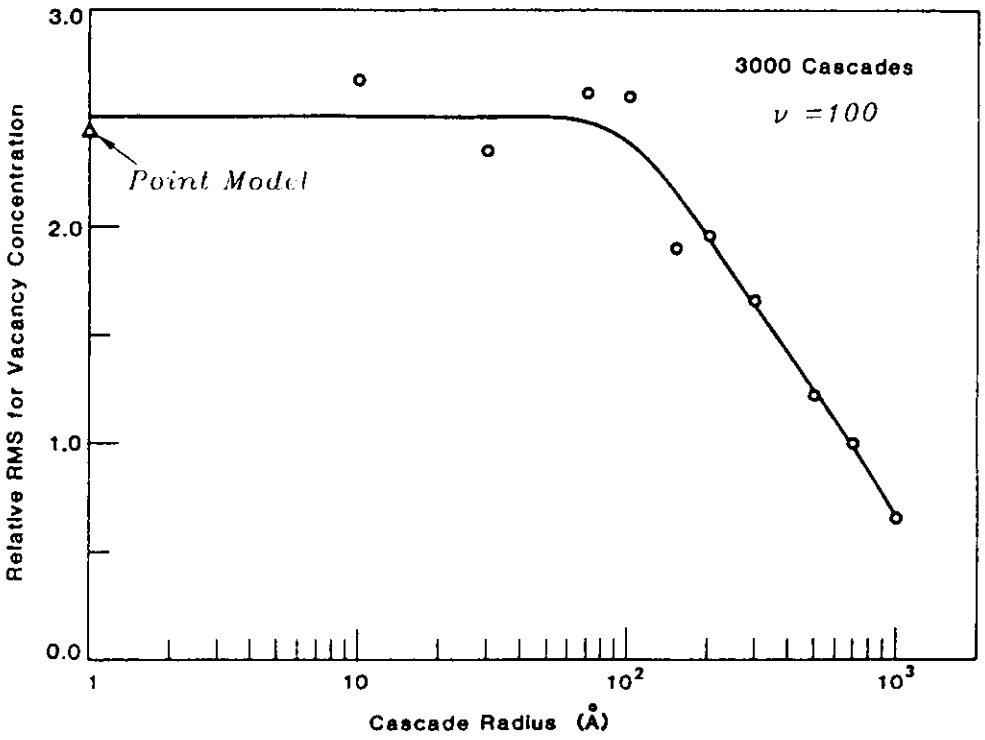


FIGURE 7. Relative RMS Value for Vacancy Concentration as a Function of Cascade Radius.

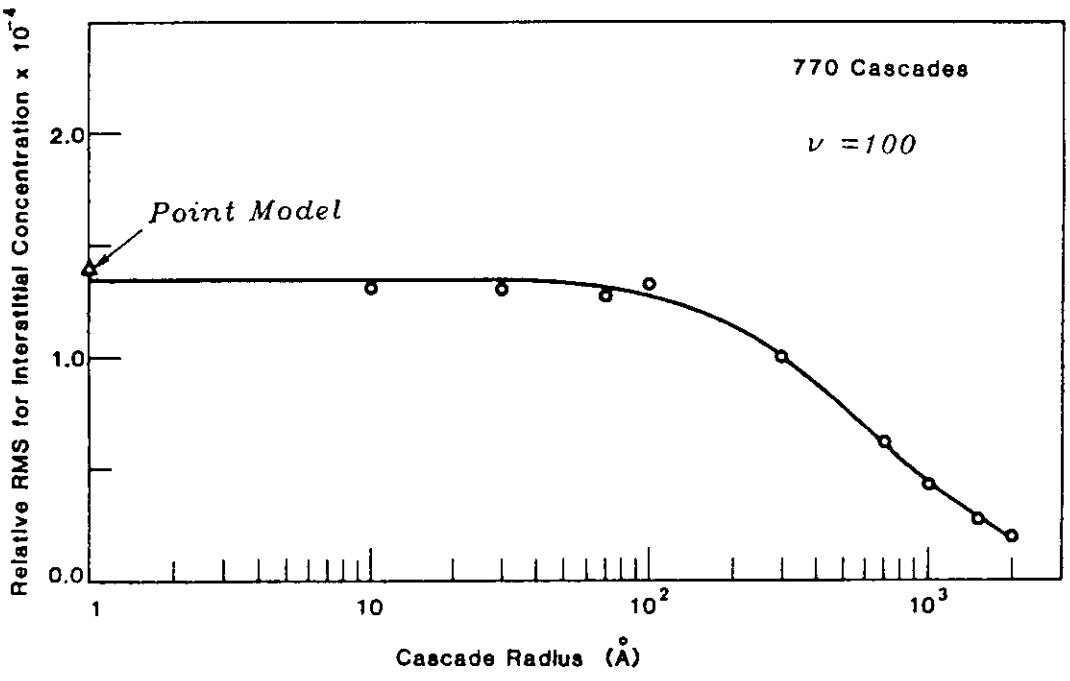


FIGURE 8. Relative RMS Value for Interstitial Concentration as a Function of Cascade Radius.

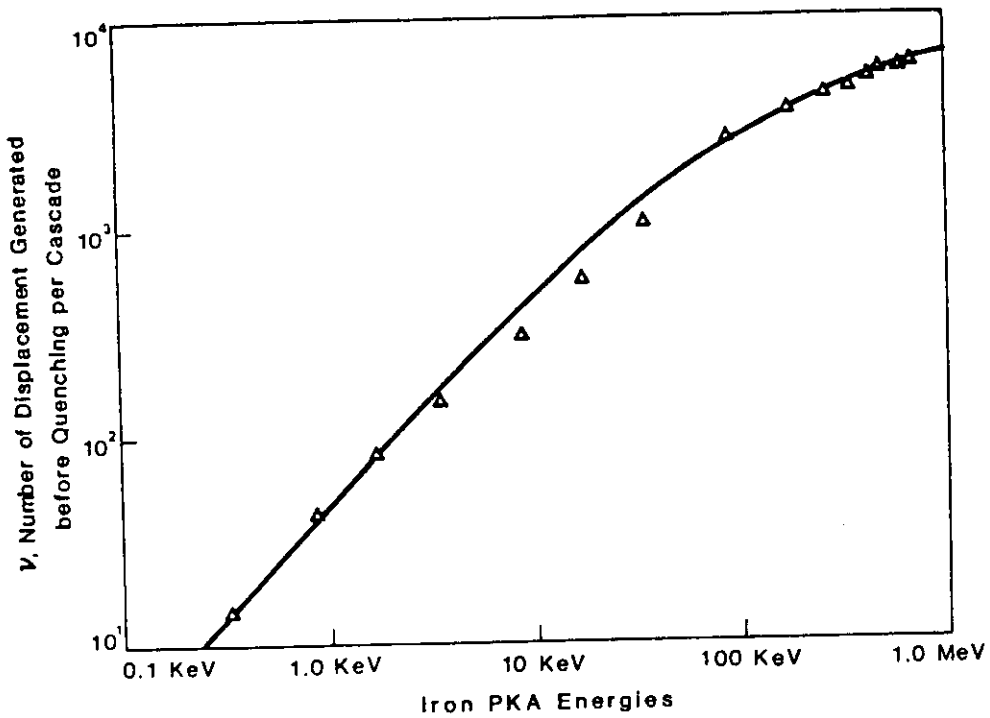


FIGURE 9. Average Number of Defects Generated in Each Cascade as a Function of Iron PKA Energy Before Cascade Quenching.

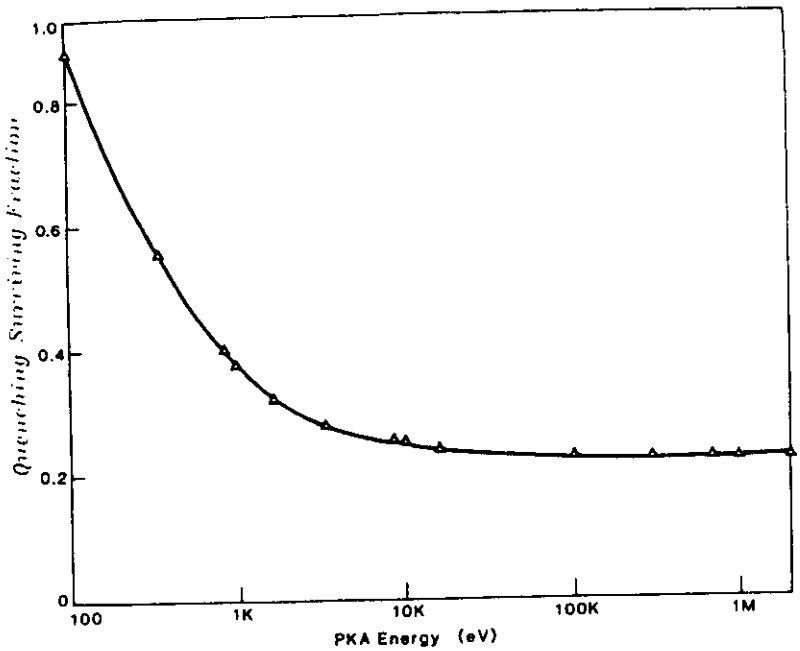


FIGURE 10. Cascade Quenching Surviving Fraction as a Function of PKA Energy for Iron.

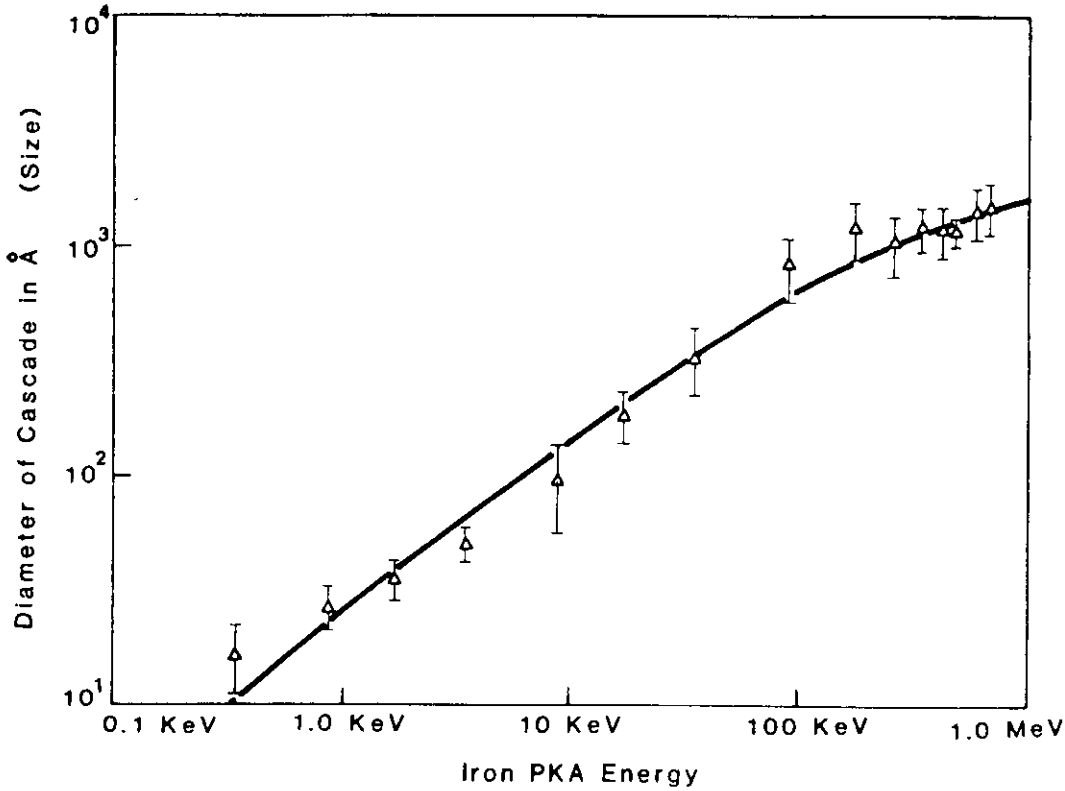


FIGURE 11. Cascade Size (Diameter) as a Function of PKA Energy for Iron.

energy. The relationship between the cascade strength and cascade radius is shown in figure (12). This figure is obtained by combining the results in figures (9), (10), and (11). Figures (13) and (14) show the vacancy relative RMS value for both point cascades and spherical cascades as functions of cascade radius and cascade strength, respectively. It shows in both figures that for larger cascade radius and higher cascade strength, the point cascade model predicts a larger magnitude of fluctuations in vacancy concentration. On the other hand, the spherical cascade model predicts that the fluctuations increase first, then level off, and eventually decrease as a function of the cascade size and cascade strength. Also, the point cascade model always predicts a higher relative RMS value as compared to the spherical cascade model, the effect is especially significant for larger cascade size and higher cascade strength. This can be explained by the fact that a larger cascade size inherently causes less fluctuation due to the assumption that defects are homogeneously distributed within the cascade volume for the spherical cascade model. This effect dominates the increase in fluctuations due to the lower arrival frequency of large size cascades. Figures (15) and (16) show the interstitial relative RMS value for both point cascades and spherical cascades as a function of the cascade radius and the cascade strength, respectively. Interstitial cascades show the same behavior as vacancy cascades and again the relative RMS value for interstitial cascades is about four orders of magnitude higher than that of vacancy cascades.

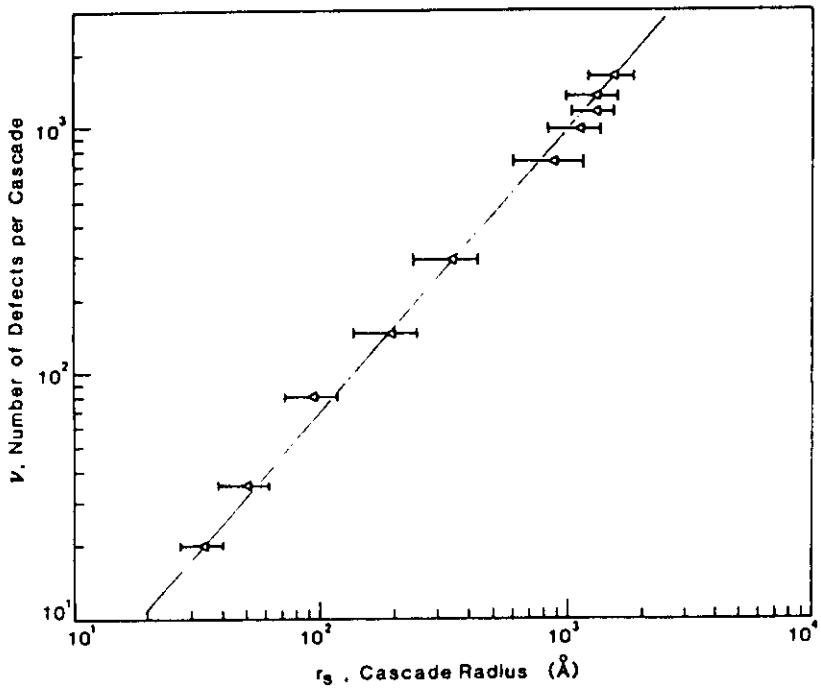


FIGURE 12. Cascade Strength (Surviving Defects per Cascade After Quenching) as a Function of Cascade Radius.

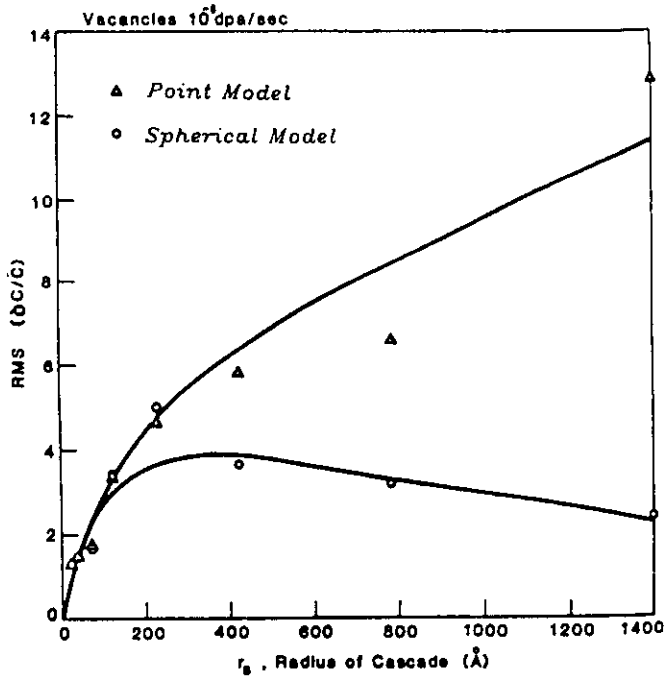


FIGURE 13. Relative RMS Value for Vacancy Concentration as a Function of Cascade Radius.

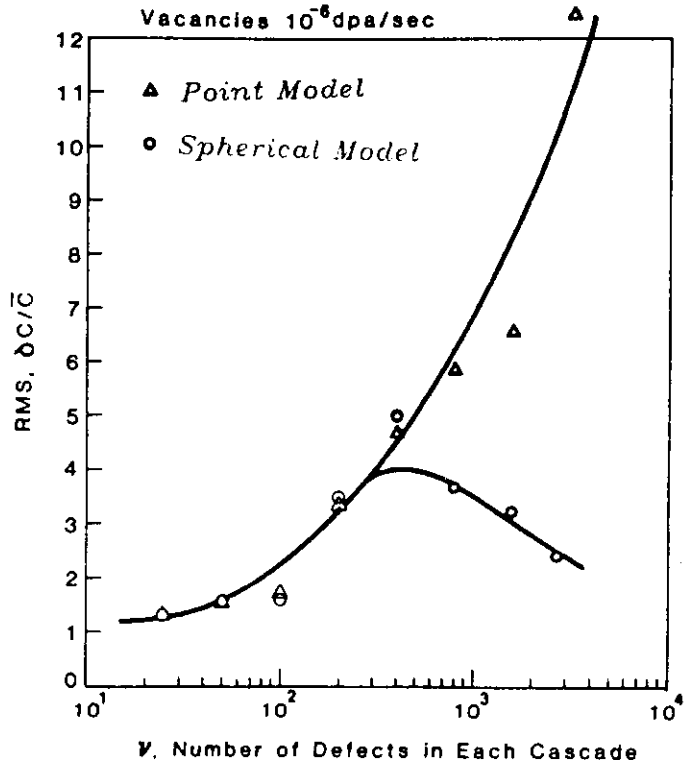


FIGURE 14. Relative RMS Value for Vacancy Concentration as a Function of Cascade Strength.

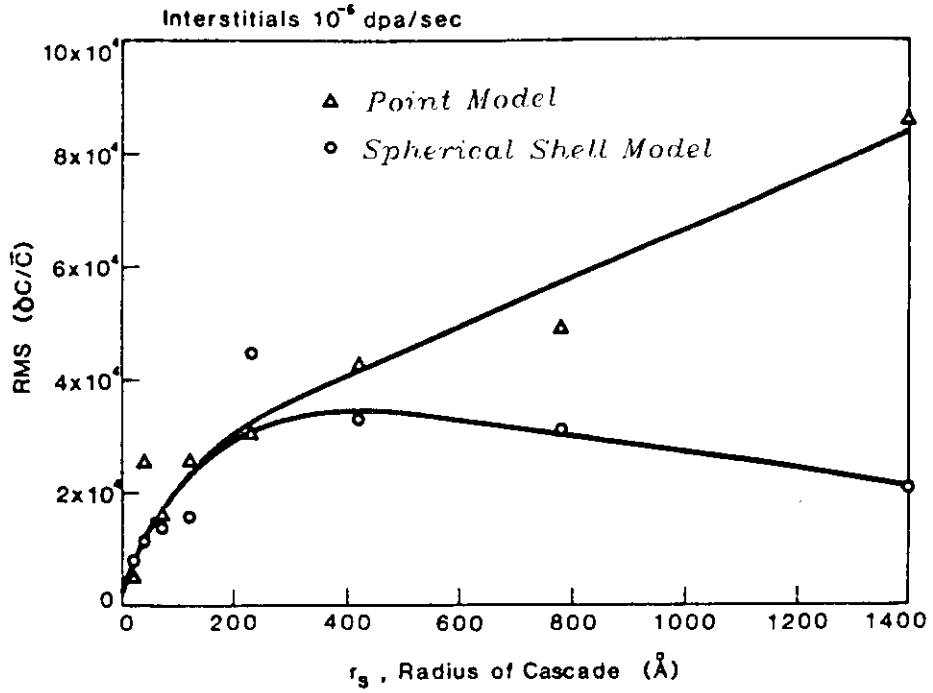


FIGURE 15. Relative RMS Value for Interstitial Concentration as a Function of Cascade Inner Radius.

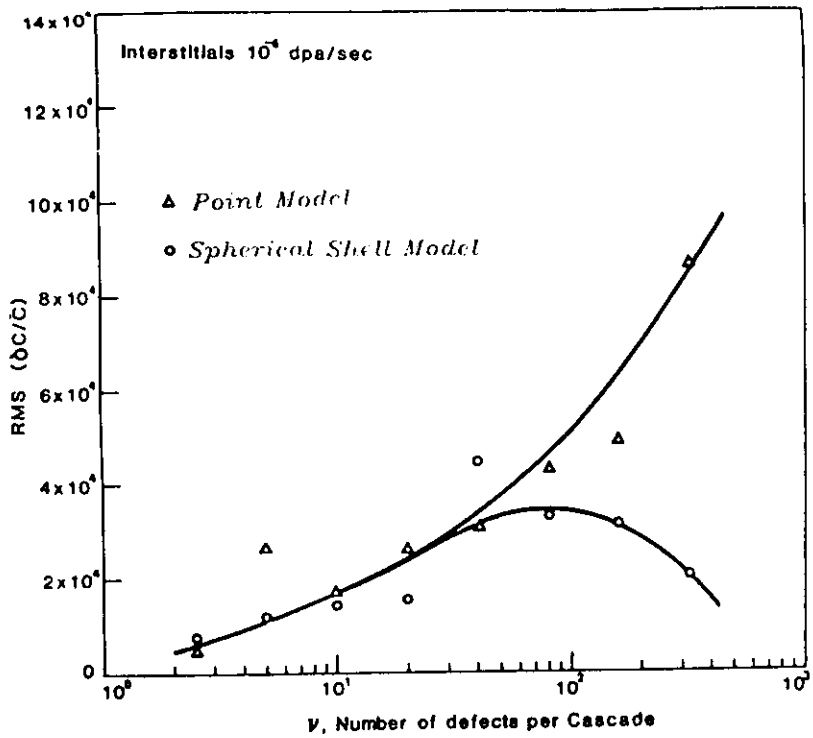


FIGURE 16. Relative RMS Value for Interstitial Concentration as a Function of Cascade Strength.

## 5.5. CONCLUSIONS

From the results shown, the fluctuations in point defect concentrations can be reduced if the cascade size effect is taken into account. For small size cascades with a radius less than 100 angstroms, the point cascade model is a good approximation. For large size cascades, the spherical cascade model predicts a lower magnitude of fluctuations in point defect concentration as compared to the point cascade model. The effect is much more significant for cascades with cascade sizes relevant to anticipated fusion neutron spectra. In reality, however, cascades generally have shape irregularities with strong directionality, especially for high PKA energies. Also, point defects are distributed inhomogeneously within the cascade volume. Therefore, it is unclear how the assumption of a homogeneous defect distribution within the spherical cascade volume can affect the magnitude of fluctuations in point defect concentrations. As mentioned earlier, non-linear phenomena, such as irradiation creep and defect nucleation are very sensitive to the magnitude of fluctuations in instantaneous local point defect concentrations. Therefore, efforts should be made to assess the effects of irregularity in the cascade shape and inhomogeneity in the defect distribution within the cascade volume on the fluctuations in point defect concentrations before non-linear phenomena can be correctly addressed.

REFERENCES


1. L.K. Mansur, W.A. Coghlan, and A.D. Brailford, J. Nucl. Mater. 85&86, 591 (1979).

2. L.K. Mansur, W.A. Coghlan, T.C. Reiley, and W.G. Wolfer, J. Nucl. Mater. 103&104, 1257 (1981).

3. H. Gurol and W.G. Wolfer, "Investigation of Cascade-Induced Point Defect Fluctuations", to be published in J. Nucl. Mater. (1983).

4. A.D. Marwick, "Fluctuations in Defect Concentration due to Inhomogeneous Production of Point Defects by Collision Cascades", IBM Report RC9276 (#40768), IBM (1982).

5. S.P. Chou and N.M. Ghoniem, "Precipitate Dissolutions due to High Energy Cascades", to be published in J. Nucl. Mater. (1983).

6. H.L. Heinisch, private communication, 1983.

# C H A P T E R  3

## REDUCED ACTIVATION MATERIALS

## ACTIVATION OF COMPONENTS OF A FUSION ALLOY

F. M. Mann (Hanford Engineering Development Laboratory)

### 1.0 Objective

The objective of this work is to determine the activation of the constituents of potential fusion alloys so as to guide metallurgists in selecting low activation materials.

### 2.0 Summary

The activation of 27 elements at the STARFIRE first wall position for a two (2) year irradiation period and for various cooling times was calculated. Comparing the results to present NRC regulations indicates that N, Ni, Cu, Nb, and Mo additions to steels might face restrictions.

### 3.0 Program

Title: Irradiation Effects Analysis (AKJ)
Principal Investigator: D. G. Doran
Affiliation: Hanford Engineering Development Laboratory

### 4.0 Relevant DAFS Program Plan Task/Subtask

No relevant task.

### 5.0 Accomplishments and Status

In order to tailor the composition of an alloy so that the alloy produces a low level of radioactivity, the activation of each of the elements comprising the alloy must be known. In a previous quarterly contribution[1], the activation of the major constituents of 316 SS, HT-9, and V-15% Cr-5% Ti

in a fusion environment was discussed. This contribution extends the list of elements and compares the results to the NRC regulation covering the land disposal of nuclear waste (10 CFR 61).

The REAC Activation and Transmutation Code System[2] was used to calculate the activation of 27 elements (Li, Be, B, C, N, O, Mg, Al, Si, P, S, Ti V, Cr, Mn, Fe, Co, Ni, Cu, Zr, Nb, Mo, Sn, Hf, Ta, W, and Pb) for a two year irradiation at the STARFIRE[3] first wall and for various cooling times [$t_c$ = 1.0 x $10^y$ and 3.0 x $10^y$ days, where y = -2(1)6]. As part of this effort, the REAC cross section library was expanded to include over 1500 reactions (see Table 1).

Table 2 presents the decay rate for each of the 27 elements after 10 days, 3 x $10^4$ days (~80 years), and 3 x $10^5$ days (~800 years) along with the major reactions producing the activity. Table 3 presents dose rates at 1 meter for 10 days, 100 days, and 3 x $10^3$ days (~8 years). Table 4 shows the density and isotopic abundances used in the calculation.

The Nuclear Regulatory Commission has recently (1/83) enacted a regulation covering the land disposal of nuclear waste (10 CFR 61). This regulation which is based upon fission reactor experience covers the disposal of a limited number of radionuclides. Table 5 displays the activation products after 3 x $10^3$ days (~8 years), a time not atypical of that between irradiation and disposal, as well as the NRC limits for Class A (least restrictive case) and for Class C (most restrictive case) waste. The ratio of the calculated activation to the NRC limit shown in Table 5 provides the maximum initial concentration of the element based on each particular activation product. Table 6 summarizes the data from Table 5, giving the resulting maximum initial concentration of each element. Numbers greater than 1. in either Table 5 or 6 imply that, for normal densities, even pure materials would not be limited at 10 MW-y/$m^2$.

TABLE 1

CONTENTS OF HEDL ACTIVATION LIBRARY (February 1983)

| ISOTOPE | N,N* | N,2N | N,3N | N,NA | N,NP | N,ND | N,NT | N,NH | N,4N | N,G | N,P | N,D | N,T | N,H | N,A | N,2P |
|---|---|---|---|---|---|---|---|---|---|---|---|---|---|---|---|---|
| LI 6 | X | X | X | X | X | A | * | X | X | E | TE | X | TE | X | X | X |
| LI 7 | X | TE | X | TE | * | X | X | X | X | E | X | E | X | X | X | X |
| BE 9 | X | TA | T | T | T | T | T | T | X | E | TE | E | E | X | TE | T |
| BE 10 | X | * | * | * | * | * | * | * | * | * | * | * | * | * | * | * |
| B 10 | X | T | T | T | T | X | * | * | X | E | TE | TE | T | T | TE | T |
| B 11 | X | TE | T | T | T | T | T | T | * | E | TE | * | E | * | TE | T |
| C 12 | X | T | T | X | T | * | * | * | * | E | TE | TE | T | T | TE | T |
| C 13 | X | T | T | T | T | T | T | T | * | * | T | * | * | * | T | T |
| C 14 | X | * | * | * | * | * | * | * | * | * | * | * | * | * | * | * |
| N 14 | X | TE | T | T | T | T | * | * | * | E | TE | TE | TE | T | TE | T |
| N 15 | X | TE | T | TE | TE | T | T | T | * | E | TE | E | E | * | TE | T |
| O 16 | X | TA | T | TA | TA | T | T | T | * | E | TE | TE | T | T | TE | T |
| O 17 | X | TE | T | TE | TE | T | T | T | * | E | TE | E | * | * | TE | T |
| O 19 | X | T | T | T | T | T | T | T | * | * | T | * | * | * | T | T |
| F 19 | X | TE | T | * | * | * | T | T | * | E | TE | * | * | T | T | T |
| NE 20 | X | T | T | * | * | T | T | * | * | * | T | * | T | * | * | T |
| NE 21 | X | * | T | * | T | * | T | * | * | * | T | T | * | T | * | T |
| NE 22 | X | * | * | * | T | T | * | T | * | * | T | * | * | * | T | T |
| NA 22 | * | * | * | * | * | * | * | * | * | * | * | * | * | * | * | * |
| NA 23 | X | TE | T | * | * | * | * | T | * | E,* | TE | * | * | T | TE | T |
| MG 24 | X | TA | T | T | TA | T | T | T | * | A | TE | T | T | T | TA | T |
| MG 25 | X | TA | T | T | T | T | T | T | * | A | TA | T | T | T | TA | T |
| MG 26 | X | TA | TA | T | T | T | T | T | * | A | TA | * | * | * | TA | T |
| AL 26 | * | * | * | * | * | * | * | * | * | * | * | * | * | * | * | * |
| AL 27 | X | TE,* | T | T | T | T | T | T | * | E | TE | TE | TE | T | TE | T |
| SI 28 | X | T | T | T | T | T,* | T | T | * | A | TA | T | T,* | T | TA | T |
| SI 29 | X | TA | T | TA | TA | T | T,* | T | * | A | TA | T | T | T | TA | T |
| SI 30 | X | TA | TA | TA | TA | T | T | T | * | A | TA | * | * | * | TA | T |
| P 31 | X | TE | T | T | TE | T | T | T | * | E | TE | T | T | T | TE | T |
| S 32 | X | TA | T | T | TA | T | T | T | * | A | TE | T | TA | T | TA | T |
| S 33 | X | TA | T | TA | TA | T | T | T | * | A | TA | TA | T | T | TA | T |
| S 34 | X | TA | T | TA | TA | T | T | T | * | A | TA | A | * | * | TA | T |
| S 36 | X | TA | TA | TA | TA | T | T | T | * | A | T | T | T | T | T | T |
| AR 36 | X | TA | T | * | * | T | T | * | * | A | TA | * | T | * | * | T |
| AR 38 | X | TA | * | * | * | T | * | T | * | A | TA | * | T | * | TA | T |
| AR 39 | X | * | * | * | * | * | * | * | * | * | * | * | * | * | * | * |
| AR 40 | X | TA | * | * | T | T | * | T | * | A | TA | T | T | T | TA | T |
| K 39 | X | TA,TA | * | * | * | T | * | T | * | A | TA | * | T | * | TA | T,Y |
| K 40 | X | * | *,* | * | * | * | * | * | * | * | * | * | * | * | * | * |
| K 41 | X | TA | * | * | * | TA | * | T,Y | *,Y | A | TE | * | T | T,Y | TA | T |
| CA 40 | X | TA | T | * | * | T,* | * | T | * | A | TA | * | *,* | * | TA | T |
| CA 41 | X | * | * | * | * | * | *,* | * | * | * | * | * | * | * | * | * |
| CA 42 | X | TA | * | * | * | T | * | T | * | * | TA | * | T | * | TA | T |
| CA 43 | X | * | T | TA | T | * | T | * | * | * | TA | TA | * | T | * | T |
| CA 44 | X | * | * | * | T | T | * | T | * | A | TA | TA | T | T | TA | T |
| CA 46 | X | TA | * | T | T | T | T | T | * | A | TA | T | T | T | TA | T |
| CA 48 | X | TA | * | T | T | T | T | T | * | A | TA | T | T | T | T | * |
| SC 45 | * | TA,TA | * | * | * | * | * | T | *,* | A,A | * | * | * | T | T | T |
| TI 46 | X | TA | T | TA | TA | T,* | T | T | * | A | TE,Y | T | TH,* | T | TA | T |
| TI 47 | X | TA | T | TA | TE | T | T,* | T | * | A | TE | TA,Y | T | T | TA | T |
| TI 48 | X | TA | T | TA | TE | TH | TH | T | * | A | TE | T | TH,Y | T | TE | T |
| TI 49 | X | TA | T | TA | TA | T | T | T | * | A | TA | T | T | T | TA | T |
| TI 50 | X | TA | TA | TA | TA | T | T | T | * | A | TA | T | T | T | TE | T |
| V 50 | X | TA | T | TA,Y | TA | T | T | T | * | A | TA | T | T | T | TA | T |
| V 51 | X | TE | T | TE | TE | T | T | T | * | E | TE | TE | TE | T | TE | T |
| CR 50 | X | TE | T | TE | TA | T | T | T | * | A | TA | T | T | T | TE | T |
| CR 52 | X | TE | T | TE | TE | T | T | T | * | * | TA | T | T | T | TE | T |
| CR 53 | X | TE | T | TE | TA | T | T | T | * | * | TA | T | T | T | TE | T |
| CR 54 | X | TE | TE | T | TA | T | T | T | * | A | TA | T | T | T | TE | T |
| MN 53 | X | *,* | *: | * | * | * | * | * | * | * | * | * | * | * | * | * |
| MN 55 | X | TE | TE | TE | TE | T | T | T | *,* | E | TE | TE | * | TE | TE | T |
| FE 54 | X | L,Y | L,* | L | L | TH,* | TH | T | X | E | L | L | TH,* | T | L | T |
| FE 55 | X | * | *,Y | * | * | * | *,* | * | *,* | * | * | * | * | * | * | * |
| FE 56 | X | L | L | L | L | TH | TH | T | L,Y | * | L | T | TH | T | L | T |
| FE 57 | X | T | TA | T | TA | T | T | T | * | * | TA | T | T | T | T | T |
| FE 58 | X | T | T | T | TA | T | T | T | * | E | TA | T | T | T | TA | T |
| CO 59 | X | TA,TA | T | TA | TA | T | T | T | * | EA,EA | TE | TE | TE | TE | TE | T |
| CO 60 | * | * | * | * | * | * | * | * | * | * | * | * | * | * | * | * |
| NI 58 | X | TE | T | T | TA | TH | TH | T | * | E | TA,TA | T | TH | T | TE | T |
| NI 59 | X | T | T | T | T,* | T | T | T | * | E | TE | T,* | T | T | TE | T |
| NI 60 | X | TE | T | T | T | T,* | T | T | * | * | TA,TA | T | T,* | T | T | T |
| NI 61 | X | T | T | T | TA,TA | T | T,* | T | * | * | TA | T | T | T | T | T |
| NI 62 | X | T | T | T | TA | T | T,* | T | * | E | TA,TA | T | T | T | TE | T |
| NI 63 | * | * | * | * | * | * | * | * | * | * | * | * | * | * | * | * |
| NI 64 | X | TA | T | TA | TA | T | T,* | T | * | A | TA | T | T | T | TA | * |

TABLE 1 (Cont'd)

| ISOTOPE | N,N* | N,2N | N,3N | N,NA | N,NP | N,ND | N,NT | N,NH | N,4N | N,G | N,P | N,D | N,T | N,H | N,A | N,2P |
|---|---|---|---|---|---|---|---|---|---|---|---|---|---|---|---|---|
| CU 63 | X | TA | T | TA | TA | T | T | T | * | A | TE | T | T | T | TE,* | T |
| CU 65 | X | TE | TA | TA | TA | T | T | T | * | A | TA | T | T | T | TA,TA | T |
| ZN 64 | X | T | T | * | * | T | T | * | * | * | T | * | T | * | * | T |
| ZN 66 | X | T | * | * | * | T | * | T | * | * | T | * | T | * | T | T |
| ZN 67 | X | * | T | T | T | * | T | * | * | * | T | T | * | T | * | T |
| ZN 68 | X | * | * | * | T | T | * | T | * | *,* | T,* | T | T | T | T | T |
| ZN 70 | X | T,* | * | T | T | T,* | T | T | * | *,* | T,* | T | T,* | * | T | * |
| ZR 90 | X | TE,* | T | T | TA,Y | T,* | T,* | T | *,* | * | TE,* | TA,Y | T,* | T | TE,* | T |
| ZR 91 | X | TE,Y | TA,* | T,* | TA,* | T,Y | T | T | * | A | TE,* | TA,* | T,Y | T | TE | T |
| ZR 92 | X | TE | TA,Y | T | TA,* | T,* | T,Y | T | *,* | A | TE | TA,* | T,* | T | TE | T |
| ZR 93 | X | * | * | * | * | *,* | *,Y | * | *,* | * | *,Y | * | *,* | * | * | * |
| ZR 94 | X | TE | TA | TA | T,Y | T | T,* | T | * | A | TE | T,Y | T | T | TE | T |
| ZR 96 | X | TE | T | T | T | T | T,Y | T | * | * | T,* | T | T | T | TE | T |
| NB 91 | *,* | *,Y | *,* | *,* | *,Y | *,* | * | *,Y | *,* | *,* | * | *,Y | *,* | *,Y | *,Y | *,* |
| NB 92 | *,* | *,* | *,Y | *,Y | * | *,Y | *,* | *,Y | *,* | *,* | *,* | * | *,Y | *,* | *,Y | *,Y |
| NB 93 | A | TA,TA | TA,TA | TA,TA | T,* | T | T,Y | T,* | *,Y | A,* | TE | T,* | T | T,Y | TE,* | T |
| NB 93* | * | *,* | *,* | *,* | *,* | * | *,Y | *,* | *,Y | *,* | * | *,* | * | *,Y | *,* | * |
| NB 94 | * | *,* | *,* | *,* | * | *,* | * | *,Y | *,* | *,* | * | *,* | *,* | * | *,Y | *,Y |
| MO 92 | X | TA,* | T | T | T,TA | T,Y | T,* | T,* | * | A,* | TA,TA | TA,TA | T,Y | T,Y | TA,* | T |
| MO 93 | * | * | *,* | *,* | *,* | *,* | *,Y | *,Y | * | *,* | *,* | * | *,Y | * | *,* | * |
| MO 94 | X | TA,TA | TA | T,Y | TA,* | T,* | T,* | T | *,* | A | TA,* | TA,* | T,TA | T | TA | T |
| MO 95 | X | TA | TA,* | TA | T,* | T,* | T,* | T | * | A | TA,* | T,* | T,* | T | TA | T |
| MO 96 | X | TA | TA | TA | T,* | T,* | T,* | T | * | A | TA,* | T,* | T,* | T | TA | T |
| MO 97 | X | TA | TA | T | T,* | T,* | T,* | T | * | A | TA,Y | T,* | T,* | T | TA | T |
| MO 98 | X | TA | TA | T | T,Y | T,* | T,* | T | * | A | TA,* | T,* | T,* | T | TA | T |
| MO100 | X | TA | T | T | T,* | T,* | T,* | T | * | A | TA,* | T,* | T,* | T | TA | T |
| TC 99 | * | * | *,* | *,* | * | * | * | * | *,* | * | * | * | * | *,Y | * | *,* |
| SN112 | X | T | T | T | T,* | T,* | T,* | T | *,* | *,* | T,* | T,* | T,* | T | T | T,* |
| SN114 | X | T,* | T | T | T,* | T,* | T,* | T,* | * | * | T,* | T,* | T,* | T | T,* | T,* |
| SN115 | X | T | T,* | T,* | T,* | T,* | T,* | T | * | * | T,* | T,* | T,* | T,* | T | T |
| SN116 | X | T | T | T | T,* | T,* | T,* | T,* | *,* | *,* | T,* | T,* | T,* | T | T,* | T,* |
| SN117 | * | T | T | T | T,* | T,* | T,* | T | * | * | T,* | T,* | T,* | T,* | T | T |
| SN118 | X | T,* | T | T | T,* | T,* | T,* | T,* | * | *,* | T,* | T,* | T,* | T | T,* | T,* |
| SN119 | * | T | T,* | T | T,* | T,* | T,* | T | * | * | T,* | T,* | T,* | T,* | T | T |
| SN120 | X | T,* | T | T | T,* | T,* | T,* | T,* | *,* | *,* | T,* | T,* | T,* | T | T,* | T,* |
| SN122 | X | T,* | T | T | T,* | T,* | T,* | T,* | *,* | *,* | T,* | T,* | T,* | T | T,* | *,* |
| SN124 | X | T,* | T | T | T,* | T,* | T,* | *,* | *,* | *,* | T,* | T,* | T,* | * | *,* | * |
| HF174 | X | TE | T | T | T | T,* | T,* | T | * | * | TE,* | T | T,* | T | T | T |
| HF176 | X | TE | T | T | T | T,* | T | T | * | *,* | TE,* | T | T,* | T | T | T,Y |
| HF177 | * | TE | T | T | T,* | T | T,* | T | * | *,* | TE,* | T,* | T | T,Y | T | T,Y |
| HF178 | * | TE,* | T | T | T,* | T,* | T | T,Y | * | *,* | TE,* | T,* | T,* | T,Y | T,Y | T,Y |
| HF178* | * | *,* | * | * | *,* | *,* | * | *,Y | * | *,* | *,* | *,* | *,* | *,Y | *,Y | *,Y |
| HF179 | * | TE,* | TA,* | T,Y | T,* | T,* | T,* | T,Y | * | A,* | TE | T,* | T,* | T,Y | T,Y | T |
| HF180 | * | TE,* | TA,* | T,Y | T | T,* | T,* | T,Y | *,* | A | TE | T | T,* | T | T,Y | * |
| TA180 | * | * | *,* | *,* | *,* | *,* | *,* | *,* | * | * | *,* | *,* | *,* | *,* | *,* | * |
| TA181 | X | TA,TA | TE | TA,* | T,* | T,* | T | *,* | A,A | TE | T,* | T,* | T | T,* | T | T |
| W 180 | X | TA,* | TA | T | T | T,* | T | T,* | * | A | TA,* | T | T,* | T,* | T,TA | T,* |
| W 182 | X | TE | TA | T,* | T | T,* | T | T,* | *,* | A,* | TE,* | T | T,* | T,* | TA,TA | T |
| W 183 | * | TA | TE | T,TA | TE,* | T | T,* | T | * | A | TE | T,* | T | T | TA,* | T,* |
| W 184 | X | TA,* | TA | T,* | TE | T,* | T | T | * | A,* | TE | T | T,* | T,* | TE | T |
| W 186 | X | TE,* | TA | T,* | TE | T | T | T | *,* | A | TE | T | T | T | TE | * |
| AU197 | X | TA,TA | *,Y | *,* | * | *,* | * | T,* | * | E,* | TA,* | * | *,* | T,* | TE,* | T,* |
| HG196 | X | *,* | * | * | *,Y | * | *,Y | *,* | *,* | *,* | *,* | *,Y | * | * | *,* | *,* |
| HG198 | X | T,* | * | * | T,* | T,* | T,Y | T,* | *,* | *,* | T,* | *,Y | T,* | T | T,* | T,* |
| HG199 | * | * | T,* | *,* | T,* | T,* | T,* | T | * | * | T | T,* | T,Y | T,* | * | * |
| HG200 | X | *,* | * | * | T | T,* | *,* | T,* | *,* | * | T,* | T | T,* | * | T,* | T,Y |
| HG201 | X | * | *,* | T,* | T,* | T | T,* | T | * | * | T | T,* | T | T,Y | * | T |
| HG202 | X | * | * | * | T | T,* | T | T,Y | *,* | H | T | T | T,* | T | T,Y | T |
| HG204 | X | T | * | T | T | T | T,* | T | * | H | T | T | T | T | T | * |
| PB204 | * | TA,Y | TA,* | T | T | T | T | T | *,Y | A | TA | T | TA | T | T | T |
| PB205 | X | *,* | *,Y | * | * | * | * | * | *,* | * | * | * | * | * | * | * |
| PB206 | X | TA | TA,* | T | T | T | T | T | *,Y | A,* | TA,* | T | TA | T | TA | T |
| PB207 | * | TA | TA | TA | T,* | T | T | T | *,* | A | TA,Y | T,* | T | T | TA | T |
| PB208 | X | TA,* | TA | T | T,Y | T,Y | T | T | * | A | T | T,Y | T,Y | T | T | * |

E=ENDF/B-V A=ACTL-78 L=LANL H=HEDL T=THRESH X=NOT ALLOWED Y=IT DECAY ONLY, T .LT. 1 M *=NONE

OTHER REACTIONS:
LI-6(N,2NA):E
LI-7(N,2NA):E
B-10(N,ND2A):E (N,2NP):E (N,TA):E
C-12(N,N2A):E
N-14(N,2A):E
FE-54(N,2NP):L (N,2NA):L (N,3NA):L
FE-56(N,2NP):L (N,2NA):L (N,3NA):L

TABLE 2

DECAY RATE ($Ci/m^3$) AFTER 2-YEAR IRRADIATION AT STARFIRE FIRST WALL (7.2 MW-yr/$m^2$)

| Element | Decay Rate | Decay = 10 days Major Reaction[A] | | Decay = $3 \times 10^4$ days (82 years) Value | Major Reaction[A] | | Decay = $3 \times 10^5$ days (820 years) Value | Major Reaction[A] | |
|---|---|---|---|---|---|---|---|---|---|
| Li | 2.4(8)[B] | $^{6}Li(n,\alpha)^{3}H$ | (94%) | 2.4(6)[B] | $^{6}Li(n,\alpha)^{3}H$ | (94%) | * | - - - - - - - - | |
| Be | 1.8(6) | $^{9}Be(n,x)^{3}H$ | (100%) | 1.8(4) | $^{9}Be(n,x)^{3}H$ | (100%) | 1.1 | $^{9}Be(n,\gamma)^{10}Be$ | (100%) |
| B | 2.1(7) | $^{10}B(n,x)^{3}H$ | (50%) | 2.1(5) | $^{10}B(n,x)^{3}H$ | (50%) | 160. | $^{11}B(n,np)^{10}Be$ | (95%) |
| | | $^{11}B(n,x)^{3}H$ | (50%) | | $^{11}B(n,x)^{3}H$ | (50%) | | | |
| C | 1.22 | $^{13}C(n,\gamma)^{14}C$ | (79%) | 1.22 | $^{13}C(n,\gamma)^{14}C$ | (79%) | 1.13 | $^{13}C(n,\gamma)^{14}C$ | (76%) |
| | | $^{13}C(n,\alpha)^{10}Be$ | (21%) | | $^{13}C(n,\alpha)^{10}Be$ | (21%) | | $^{13}C(n,\alpha)^{10}Be$ | (24%) |
| N | 9.0(5) | $^{14}N(n,x)^{3}H$ | (97%) | 2.6(4) | $^{14}N(n,p)^{14}C$ | (67%) | 2.6(4)[B] | $^{14}N(n,p)^{14}C$ | (100%) |
| | | | | | $^{14}N(n,x)^{3}H$ | (33%) | | | |
| O | 19. | $^{17}O(n,\alpha)^{14}C$ | (83%) | 18. | $^{17}O(n,\alpha)^{14}C$ | (83%) | 18. | $^{17}O(n,\alpha)^{14}C$ | (83%) |
| | | $^{18}O(n,n\alpha)^{14}C$ | (17%) | | $^{18}O(n,n\alpha)^{14}C$ | (17%) | | $^{18}O(n,n\alpha)^{14}C$ | (17%) |
| Mg | 5.9(5) | $^{25}Mg(n,\alpha)^{22}Na$ | (65%) | 1.4(5) | $^{25}Mg(n,x)^{3}H$ | (61%) | 1.3(3) | $^{25}Mg(n,x)^{3}H$ | (100%) |
| | | $^{25}Mg(n,x)^{3}H$ | (22%) | | $^{25}Mg(n,\alpha)^{22}Na$ | (31%) | | | |
| | | $^{24}Mg(n,\tau)^{22}Na$ | (12%) | | | | | | |
| Al | 8.1(3) | $^{27}Al(n,x)^{3}H$ | (89%) | 110. | $^{27}Al(n,x)^{3}H$ | (64%) | 41. | $^{27}Al(n,2n)^{26}Al$ | (100%) |
| | | $^{27}Al(n,\alpha)^{24}Na$ | (11%) | | $^{27}Al(n,2n)^{26}Al$ | (36%) | | | |
| Si | 2.6(5) | $^{29}Si(n,x)^{3}H$ | (100%) | 2.6(3) | $^{29}Si(n,x)^{3}H$ | (100%) | * | - - - - - - - - | |
| P | 1.2(7) | $^{31}P(n,x)^{3}H$ | (50%) | 6.0(4) | $^{31}P(n,x)^{3}H$ | (100%) | * | - - - - - - - - | |
| | | $^{31}P(n,x)^{32}P$ | (50%) | | | | | | |
| S | 6.0(7) | $^{32}S(n,p)^{32}P$ | (99%) | 1.1(4) | $^{32}S(n,x)^{3}H$ | (100%) | 25. | $^{33}S(n,2p)^{32}Si$ | (100%) |
| Ti | 2.0(7) | $^{46}Ti(n,p)^{46}Sc$ | (47%) | 930. | $^{47}Ti(n,x)^{3}H$ | (65%) | * | - - - - - - - - | |
| | | $^{48}Ti(n,\alpha)^{45}Ca$ | (29%) | | $^{49}Ti(n,x)^{3}H$ | (33%) | | | |
| V | 1.2(6) | $^{50}V(n,2n)^{49}V$ | (59%) | 470. | $^{51}V(n,x)^{3}H$ | (84%) | * | - - - - - - - - | |
| | | $^{51}V(n,\alpha)^{47}Sc$ | (19%) | | $^{50}V(n,x)^{3}H$ | (16%) | | | |
| | | $^{51}V(N,\alpha)^{48}Sc$ | (17%) | | | | | | |
| Cr | 1.6(8) | $^{52}Cr(n,2n)^{51}Cr$ | (76%) | 4.1(3) | $^{52}Cr(n,x)3_{H}$ | (57%) | * | - - - - - - - - | |
| | | $^{50}Cr(n,\gamma)^{51}Cr$ | (20%) | | $^{53}Cr(n,x)^{3}H$ | (32%) | | | |
| Mn | 3.4(8) | $^{55}Mn(n,2n)^{54}Nm$ | (100%) | * | - - - - - - | | * | - - - - - - - - | |
| Fe | 1.3(8) | $^{56}Fe(n,2n)^{55}Mn$ | (81%) | 400. | $^{57}Fe(n,x)^{3}H$ | (86%) | 11. | $^{54}Fe(n,d)^{54}Mn$ | (100%) |
| | | $^{54}Fe(n,p)^{54}Mn$ | (11%) | | | | | | |
| Co | 2.5(9) | $^{59}Co(n,\gamma)^{60}Co$ | (80%) | 4.0(4) | $^{59}Co(n,\gamma)^{60}Co$ | (100%) | * | - - - - - - - - | |
| | | $^{59}Co(n,2n)^{58}Co$ | (19%) | | | | | | |
| Ni | 5.7(8) | $^{58}Ni(n,d)^{57}Co$ | (48%) | 3.3(5) | $^{62}Ni(n,\gamma)^{63}Ni$ | (85%) | 7.0(3) | $^{58}Ni(n,\gamma)^{59}Ni$ | (63%) |
| | | $^{58}Ni(n,p)^{58}Co$ | (44%) | | $^{64}Ni(n,2n)^{63}Ni$ | (15%) | | $^{62}Ni(n,\gamma)^{63}Ni$ | (19%) |
| | | | | | | | | $^{60}Ni(n,2n)^{59}Ni$ | (14%) |

# TABLE 2 (Cont'd)

| Element | Decay Rate | Decay = 10 days Major Reaction[A] | | Decay = $3 \times 10^4$ days (82 years) Value | Major Reaction[A] | | Decay = $3 \times 10^5$ days (820 years) Value | Major Reaction[A] | |
|---|---|---|---|---|---|---|---|---|---|
| Cu | 7.0(6) | $^{63}Cu(n,\alpha)^{60}Co$ | (66%) | 2.5(5) | $^{63}Cu(n,p)^{63}Ni$ | (80%) | 1.1(3) | $^{63}Cu(n,p)^{63}Ni$ | (86%) |
| | | $^{63}Cu(n,x)^{3}H$ | (22%) | | | | | | |
| Zr | 3.0(7) | $^{90}Zr(n,2n)^{89}Zr$ | (44%) | 1.3(3) | $^{91}Zr(n,x)^{3}H$ | (30%) | 75. | $^{94}Zr(n,2n)^{93}Zr$ | (92%) |
| | | $^{96}Zr(n,2n)^{95}Zr$ | (41%) | | $^{94}Zr(n,n\alpha)^{90}Sr$ | (27%) | | | |
| | | | | | $^{92}Zr(n,x)^{3}H$ | (14%) | | | |
| | | | | | $^{90}Zr(n,x)^{3}H$ | (10%) | | | |
| Nb | 1.0(6) | $^{93}Nb(n,x)^{3}H$ | (65%) | 5.7(4) | $^{93}Nb(n,\gamma)^{94}Nb$ | (87%) | 4.9(4) | $^{93}Nb(n,\gamma)^{94}Nb$ | (100%) |
| | | $^{93}Nb(n,\alpha)^{90}Y$ | (29%) | | $^{93}Nb(n,x)^{3}H$ | (13K%) | | | |
| Mo | 3.3(7) | $^{98}Mo(n,\gamma)^{99}Mo$ | (32%) | 4.4(4) | $^{92}Mo(n,\gamma)^{93}Mo$ | (62%) | 3.8(4) | $^{92}Mo(n,\gamma)^{93}Mo$ | (63%) |
| | | $^{100}Mo(n,2n)^{99}Mo$ | (15%) | | $^{94}Mo(n,2n)^{93}Mo$ | (36%) | | $^{94}Mo(n,2n)^{93}Mo$ | (36%) |
| Sn | 2.8(7) | $^{124}Sn(n,2n)^{123}Sn$ | (92%) | 110. | $^{117}Sn(n,x)^{3}H$ | (27%) | * | - - - - - - - - | |
| | | | | | $^{119}Sn(n,x)^{3}H$ | (23%) | | | |
| | | | | | $^{120}Sn(n,x)^{3}H$ | (15%) | | | |
| | | | | | $^{118}Sn(n,x)^{3}H$ | (15%) | | | |
| | | | | | $^{116}Sn(n,x)^{3}H$ | (14%) | | | |
| Hf | 1.1(9) | $^{180}Hf(n,\gamma)^{181}Hf$ | (100%) | 69. | $^{177}Hf(n,x)^{3}H$ | (36%) | * | - - - - - - - - | |
| | | | | | $^{178}Hf(n,x)^{3}H$ | (21%) | | | |
| | | | | | $^{179}Hf(n,x)^{3}H$ | (20%) | | | |
| | | | | | $^{180}Hf(n,x)^{3}H$ | (19%) | | | |
| Ta | 2.3(10) | $^{181}Ta(n,\gamma)^{182}Ta$ | (100%) | 120. | $^{181}Ta(n,x)^{3}H$ | (100%) | * | - - - - - - - - | |
| W | 6.6(8) | $^{182}W(n,2n)^{181}W$ | (40%) | 48. | $^{183}W(n,x)^{3}H$ | (31%) | .002 | $^{186}W(n,n\alpha)^{182}Hf$ | (100%) |
| | | $^{184}W(n,\gamma)^{185}W$ | (29%) | | $^{184}W(n,x)^{3}H$ | (27%) | | | |
| | | $^{186}W(n,2n)^{185}W$ | (24%) | | $^{182}W(n,x)^{3}H$ | (23%) | | | |
| | | | | | $^{186}W(n,x)^{3}H$ | (18%) | | | |
| Pb | 3.0(4) | $^{206}Pb(n,\alpha)^{203}Hg$ | (82%) | 20. | $^{206}Pb(n,2n)^{205}Pb$ | (58%) | 12. | $^{206}Pb(n,2n)^{205}Pb$ | (100%) |
| | | $^{204}Pb(n,p)^{204}Tl$ | (11%) | | $^{208}Pb(n,x)^{3}H$ | (19%) | | | |
| | | | | | $^{206}Pb(n,x)^{3}H$ | (15%) | | | |

A Only reactions providing over 10% of the decay rate are given.

B X(Y) Read as $X \times 10^{Y}$.

* Less than $10^{-3}$ Curies/$m^3$.

TABLE 3

DOSE RATE 1 METER (rem/h-$m^3$) AFTER 2-YEAR IRRADIATION AT STARFIRE FIRST WALL (7.2 MW-yr/$m^2$)

| | | Decay = 10 days | | | Decay = 100 days | | | Decay = $3 \times 10^3$ days (8.2 years) | |
|---|---|---|---|---|---|---|---|---|---|
| Element | Dose Rate | Major Reaction[A] | | Value | Major Reaction[A] | | Value | Major Reaction[A] | |
| Mg | 6.1(5)[B] | $^{25}Mg(n,\alpha)^{22}Na$ | (82%) | 5.7(5)[B] | $^{25}Mg(n,\alpha)^{22}Na$ | (82%) | 6.9(4)[B] | $^{25}Mg(n,\alpha)^{22}Na$ | (82%) |
| | | $^{24}Mg(n,\gamma)^{22}Na$ | (15%) | | $^{24}Mg(n,\gamma)^{22}Na$ | (15%) | | $^{24}Mg(n,\gamma)^{22}Na$ | (15%) |
| Al | 1.8(3) | $^{27}Al(n,\alpha)^{24}Na$ | (97%) | 60. | $^{27}Al(n,2n)^{26}Al$ | (100%) | 60. | $^{27}Al(n,2n)^{26}Al$ | (100%) |
| Si | 38. | $^{29}Si(n,2p)^{28}Mg$ | (100%) | * | - - - - - - | | * | - - - - - - - - | |
| Ti | 1.4(7) | $^{46}Ti(n,p)^{46}Sc$ | (79%) | 6.1(6) | $^{46}Ti(n,p)^{46}Sc$ | (85%) | * | - - - - - - - - | |
| | | $^{47}Ti(n,d)^{46}Sc$ | (13%) | | $^{47}Ti(n,d)^{46}Sc$ | (14%) | | | |
| V | 4.2(5) | $^{51}V(n,\alpha)^{48}Sc$ | (95%) | * | - - - - - - | | * | - - - - - - - - | |
| Cr | 4.0(6) | $^{52}Cr(n,2n)^{51}Cr$ | (70%) | 3.7(5) | $^{52}Cr(n,2n)^{51}Cr$ | (80%) | * | - - - - - - - - | |
| | | $^{50}Cr(n,\gamma)^{51}Cr$ | (18%) | | $^{50}Cr(n,\gamma)^{51}Cr$ | (20%) | | | |
| | | $^{50}Cr(n,t)^{48}V$ | (11%) | | | | | | |
| Mn | 1.7(8) | $^{55}Mn(n,2n)^{54}Mn$ | (100%) | 1.4(8) | $^{55}Mn(n,2n)^{54}Mn$ | (100%) | 2.3(5) | $^{55}Mn(n,2n)^{54}Mn$ | (100%) |
| Fe | 7.1(6) | $^{54}Fe(n,p)^{54}Mn$ | (95%) | 5.6(6) | $^{54}Fe(n,p)^{54}Mn$ | (99%) | 8.9(3) | $^{54}Fe(n,p)^{54}Mn$ | (100%) |
| Co | 3.0(9) | $^{59}Co(n,\gamma)^{60}Co$ | (90%) | 2.7(9) | $^{59}Co(n,\gamma)^{60}Co$ | (95%) | 9.1(8) | $^{59}Co(n,\gamma)^{60}Co$ | (100%) |
| Ni | 1.9(8) | $^{58}Ni(n,p)^{58}Co$ | (81%) | 9.0(7) | $^{58}Ni(n,p)^{58}Co$ | (69%) | 2.7(6) | $^{60}Ni(n,p)^{60}Co$ | (985) |
| | | $^{58}Ni(n,d)^{57}Co$ | (13%) | | $^{58}Ni(n,d)^{57}Co$ | (22%) | | | |
| Cu | 6.3(6) | $^{63}Cu(n,\alpha)^{60}Co$ | (100%) | 6.1(6) | $^{63}Cu(n,\alpha)^{60}Co$ | (100%) | 2.1(6) | $^{63}Cu(n,\alpha)^{60}Co$ | (100%) |
| Zr | 2.6(7) | $^{90}Zr(n,2n)^{89}Zr$ | (63%) | 3.6(6) | $^{96}Zr(n,2n)^{95}Zr$ | (83%) | 5.2(4) | $^{94}Zr(n,2n)^{93}Zr$ | (92%) |
| | | $^{96}Zr(n,2n)^{95}Zr$ | (30%) | | $^{94}Zr(n,\gamma)^{95}Zr$ | (17%) | | | |
| Nb | 6.5(4) | $^{93}Nb(n,\gamma)^{94}Nb$ | (75%) | 6.5(4) | $^{93}Nb(n,\gamma)^{94}Nb$ | (75%) | 6.0(4) | $^{93}Nb(n,\gamma)^{94}Nb$ | (82%) |
| | | $^{93}Nb(n,p)^{93}Zr$ | (25%) | | $^{93}Nb(n,p)^{93}Zr$ | (25%) | | $^{93}Nb(n,p)^{93}Zr$ | (18%) |
| Mo | 9.9(6) | $^{92}Mo(n,n)^{88}Zr$ | (24%) | 2.4(6) | $^{92}Mo(n,n)^{88}Zr$ | (77%) | 6.4(4) | $^{92}Mo(n,\gamma)^{93}Mo$ | (61%) |
| | | $^{98}Mo(n,\gamma)^{99}Mo$ | (21%) | | | | | | |
| | | $^{92}Mo(n,p)^{92}Nb^{m}$ | (18%) | | | | | | |
| | | $^{100}Mo(n,2n)^{99}Mo$ | (10%) | | | | | | |
| Sn | 7.2(5) | $^{114}Sn(n,2n)^{113}Sn$ | (85%) | 4.2(5) | $^{114}Sn(n,2n)^{113}Sn$ | (85%) | .02 | $^{124}Sn(n,2n)^{123}Sn$ | (54%) |
| | | $^{124}Sn(n,2n)^{123}Sn$ | (14%) | | $^{124}Sn(n,2n)^{123}Sn$ | (15%) | | $^{114}Sn(n,2n)^{113}Sn$ | (46%) |
| Hf | 1.3(9) | $^{180}Hf(n,\gamma)^{181}Hf$ | (100%) | 2.8(8) | $^{180}Hf(n,\gamma)^{181}Hf$ | (100%) | * | - - - - - - - - | |
| Ta | 1.8(10) | $^{181}Ta(n,\gamma)^{182}Ta$ | (100%) | 1.0(10) | $^{181}Ta(n,\gamma)^{182}Ta$ | (100%) | 260. | $^{181}Ta(n,\gamma)^{182}Ta$ | (100%) |
| W | 5.5(6) | $^{186}W(n,\gamma)^{187}W$ | (36%) | 2.6(6) | $^{184}W(n,\gamma)^{185}W$ | (34%) | 1.1(5) | $^{184}W(n,\gamma)^{185}W$ | (54%) |
| | | $^{182}W(n,2n)^{181}W$ | (19%) | | $^{186}W(n,2n)^{185}W$ | (29%) | | $^{186}W(n,2n)^{185}W$ | (46%) |
| | | $^{184}W(n,\gamma)^{185}W$ | (18%) | | $^{182}W(n,2n)^{181}W$ | (24%) | | | |
| | | $^{186}W(n,2n)^{185}W$ | (15%) | | | | | | |
| Pb | 4.1(3) | $^{206}Pb(n,\alpha)^{203}Hg$ | (98%) | 1.1(3) | $^{206}Pb(n,\alpha)^{203}Hg$ | (100%) | 0.48 | $^{204}Pb(n,p)^{204}Tl$ | (76%) |
| | | | | | | | | $^{206}Pb(n,t)^{204}Tl$ | (76%) |

Li, Be, B, C, N, O, P, S have dose rates less thab $10^{-3}$ Rem/h-$m^3$.

* Dose rate less than $10^{-3}$ rem/h-$m^3$.

A Only reactions providing over 10% of the dose rate are given.

B X(Y) read as X x $10^{Y}$.

TABLE 4

ISOTOPIC ABUNDANCES

| Element | Density (g/m) | Isotopic Abundances Mass (% abundances) |
|---|---|---|
| Li | 0.54 | 6(7.5), 7(92.5) |
| Be | 1.85 | 9(100.) |
| B | 2.34 | 10(20.), 11(80.) |
| C | 2.26 | 12(99.89), 13(0.11) |
| N | 0.81* | 14(99.63), 15(0.37) |
| O | 1.14* | 16(99.758), 17(0.038), 18(0.204) |
| Mg | 1.74 | 24(78.909), 25(10.00), 26(11.01) |
| Al | 2.70 | 27(100.0) |
| Si | 2.33 | 28(92.33), 29(4.67), 30(3.10) |
| P | 1.82 | 31(100.0) |
| S | 2.07 | 32(95.02), 33(0.75), 34(4.21), 36(0.017) |
| Ti | 4.51 | 46(8.25), 47(7.45), 48(73.7), 49(5.4), 50(5.2) |
| V | 6.1 | 50(0.25), 51(99.75) |
| Cr | 7.19 | 50(4.35), 52(83.79), 53(9.50), 53(2.36) |
| Mn | 7.43 | 55(100.0) |
| Fe | 7.86 | 54(5.8), 56(91.8), 57(2.1), 58(0.3) |
| Co | 8.9 | 59(100.0) |
| Ni | 8.9 | 58(68.3), 60(26.1), 61(1.1), 62(3.6), 64)0.9) |
| Cu | 8.96 | 63(69.2), 65(30.8) |
| Zr | 6.49 | 90(51.5), 91(11.2), 92(17.1), 94(17.4), 96(2.8) |
| Nb | 8.4 | 93(100) |
| Mo | 10.2 | 92(14.8), 94(9.3), 95(15.9), 96(16.7), 97(9.6), 98(24.1), 100(9.6) |
| Sn | 7.30 | 112(1.01), 114(0.67), 115(0.38), 116(14.7), 117(7.7), 118(24.3), 119(8.6), 120(32.4), 122(4.6), 124(5.6) |
| Hf | 13.1 | 174(0.16), 176(5.2), 177(18.6), 178(27.1), 179(13.7), 180(35.2) |
| Ta | 16.6 | 180(0.012), 181(99.988) |
| W | 19.3 | 180(0.13), 182(26.3), 183(14.3), 184(30.67), 186(28.6) |
| Pb | 11.4 | 204(1.42), 206(24.1), 207(22.1), 208(52.4) |

*Density of liquid.

TABLE 5

ACTIVATION PRODUCTS FROM FUSION FIRST WALL PER 10 MW-yr/$m^2$ AFTER x 3 $10^3$ DAYS (8.2 yr)

| Element | Activation Product | | 10 CFR 61 Limit ($c/m^3$) | | Ratio | |
|---|---|---|---|---|---|---|
| | Isotope | Decay Rate ($c/m^3$) | Class A | Class C | Class A | Class C |
| Li | $^{3}H$ | 2.1(8)@ | 40 | * | 1.9(-7)@ | * |
| Be | $^{3}H$ | 1.7(6) | 40 | * | 2.4(-5) | * |
| B | $^{3}H$ | 1.8(7) | 40 | * | 2.2(-6) | * |
| | $^{10}Be$ | 220. | -- | -- | -- | -- |
| C | $^{14}C$ | .13 | 8 | 80 | 62. | 615. |
| | $^{10}Be$ | .036 | -- | -- | -- | -- |
| N | $^{3}H$ | 7.4(5) | 40 | * | 5.4(-5) | * |
| | $^{14}C$ | 2.5(4) | 8 | 80 | 3.3(-4) | .0033 |
| O | $^{14}C$ | 26. | 8 | 80 | 31. | 3.1 |
| Mg | $^{3}H$ | 1.2(5) | 40 | * | 3.3(-4) | * |
| | $^{22}Na$ | 7.3(4) | 700 | * | .0096 | * |
| Al | $^{3}H$ | 6.3(3) | 40 | * | .0063 | * |
| | $^{26}Al$ | 56. | -- | -- | -- | -- |
| Si | $^{3}H$ | 2.3(5) | 40 | * | 1.7(-4) | * |
| P | $^{3}H$ | 5.3 | 40 | * | 7.5 | * |
| S | $^{3}H$ | 4.5(4) | 40 | * | 8.9(-4) | * |
| | $^{32}Si$ | 15. | -- | -- | -- | -- |
| | $^{32}P$ | 15. | -- | -- | -- | -- |
| Ti | $^{3}H$ | 8.2(4) | 40 | * | 4.9(-4) | * |
| | $^{45}Ca$ | 27. | 700 | * | 26. | * |
| V | $^{3}H$ | 4.2(4) | 40 | * | 9.5(-4) | * |
| | $^{49}V$ | 1.9(3) | 700 | * | .37 | * |
| Cr | $^{49}V$ | 1.1(6) | 700 | * | 6.4(-4) | * |
| | $^{3}H$ | 4.9(5) | 40 | * | 8.2(-5) | * |
| Mn | -- | -- | | | | |
| Hf | $^{3}H$ | 6.1(3)@ | 40 | * | 0.0066 | * |
| Ta | $^{179}Ta$ | 2.8(5) | 700 | * | 0.0025 | * |
| | $^{3}H$ | 1.1(4) | 40 | * | 0.0036 | * |
| | $^{182}Ta$ | 470. | 700 | * | 1.5 | * |
| W | $^{185}W$ | 3.1(7) | 700 | * | 2.3(-5)@ | * |
| | $^{3}H$ | 4.2(3) | 40 | * | 0.0095 | * |
| | $^{179}Ta$ | 88. | 700 | * | 8.0 | * |
| Pb | $^{204}Tl$ | 1.3(3) | 700 | * | .54 | * |
| | $^{3}H$ | 730. | 40 | * | .055 | * |
| | $^{205}Pb$ | 16. | -- | -- | -- | -- |

+Calculations based on 2 FPY years using STARFIRE first wall spectrum.
*Limited by practical considerations such as the effects of external radiation and internal heat generation on transportation, handling, and disposal.
--Not explicitly included in 10 CFR 61 (1/83).
@X(Y) should be read as X x $10^{Y}$.

TABLE 6

ESTIMATED MAXIMUM FRACTIONAL WEIGHT CONCENTRATIONS
PER 10 MW-y/$m^2$ (10 CFR 61) (All Tritium Expelled)

| Element | Class A Disposal | Class C Disposal |
|---|---|---|
| C | 62. | 615. |
| N | .00033(330 ppm) | .0033 |
| O | .31 | 3.1 |
| Mg | .0096 | * |
| Ti | 26 | * |
| V | .37 | * |
| Cr | .00064(640 ppm) | * |
| Fe | 6400. | * |
| Co | 7.5(-7)[A](.75 ppm) | * |
| Ni | 4.(-5)(40 ppm) | 0.0091 |
| Cu | 6.(-6)(6 ppm) | 0.0012 |
| Zr | 1.2(-5)(12 ppm) | 2.1 |
| Nb | 2.9(-7)(.29 ppm) | 2.9(-6)[A](2.9 ppm) |
| Mo | 4.7(-5)(47 ppm) | 4.7(-4)(470 ppm) |
| Sn | .0040 | * |
| Ta | .0025 | * |
| W | 2.3(-5)(23 ppm) | * |
| Pb | .54 | * |

No limits on Li, Be, B, Al, Si, P, S, Mn, Hf.

Those elements under lined may be affected by new regulations.

*Limited by practical considerations such as the effects of external radiation and internal heat generation on transport, handling, and disposal.

A X (Y) should be read as X x $10^Y$.

Serious limits are placed on the initial concentrations of N (3300 ppm), Ni (9100 ppm), Cu (1200 ppm), Nb (2.9 ppm), and Mo (470 ppm) if the material is to be disposed of under 10 CFR 61. Other limitations may arise as new activation products are added to 10 CFR 61 and from internal heat generation or external radiation concerns (e.g., Mn, Hf, and Ta produce a high dose rate even after 1000 days of cooling). In almost all the materials studied, large amounts of tritium are produced. How the tritium diffuses could greatly affect waste options.

## 6.0 References


1. F. M. Mann, "Activation of Components of a Fusion Alloy," Damage Analysis and Fundamental Studies, Quarterly Progress Report, October-December 1982, DOE/ER-0046/12.

2. F. M. Mann, Transmutation of Alloys in MFE Facilities as Calculated by REAC (A Computer Code System for Activation and Transmutation), HEDL-TME 81-37, August, 1982.

3. C. C. Baker et al., STARFIRE, A Commercial Tokamak Fusion Power Plant Study, Argonne National Laboratory Report, ANL/FPP-80-1, 1980.


## 7.0 Future Work

As 10 CFR 61 is based on a limited number of radioisotopes, future work will include a comparison between the present results and limits obtained in a manner similar to that of the NRC (Battelle Northwest Laboratories is presently doing this study). Additional work will also include different reactor positions and types and different power histories. Libraries will also be examined to ensure completeness.

# C H A P T E R  4

## FUNDAMENTAL MECHANICAL BEHAVIOR

# GRAIN BOUNDARY CHEMISTRY, HYDROGEN EMBRITTLEMENT AND STRESS CORROSION BEHAVIOR OF HT9

R. H. Jones (Pacific Northwest Laboratory)
M. T. Thomas (Pacific Northwest Laboratory)

## 1.0 Objective

The purpose of this evaluation was to evaluate the effect of grain boundary impurity segregation on the hydrogen embrittlement and stress corrosion of HT-9. This information will be used to identify test conditions for sub-critical crack growth testing and critical flaw size analysis. The purpose of this research was to identify potential environmental-material interaction processes.

## 2.0 Summary

The grain boundary phosphorus and sulfur concentrations of HT-9 were found to depend on heat treatment in a manner consistent with other ferritic steels. After a tempering treatment of 2.5 hrs at 760°C the grain boundary phosphorus and sulfur concentrations were 0.015 and 0.03 monolayers, respectively while after a heat treatment of 240 hrs at 540°C their grain boundary concentrations were 0.04 and 0.01 monolayers, respectively. Straining electrode tests at cathodic and anodic test potentials revealed that HT-9 is sensitive to hydrogen embrittlement but not stress corrosion at 25°C in an acidic electrolyte. The reduction of area was 13% at cathodic test potentials and 60% in air and at anodic test potentials. This decrease in reduction of area was accompanied by an increase in quasi-cleavage and intergranular fracture.

## 3.0 Program

Title: Mechanical Properties
Principal Investigator: R. H. Jones
Affiliation: Pacific Northwest Laboratory

## 4.0 Relevant DAFS Program Plan Task/Sub-Task

Subtask II.C.8 Effects of Helium and Displacements on Fracture
Subtask II.C.9 Effects of Hydrogen on Fracture
Subtask II.C.12 Effects of Cycling on Flow and Fracture

## 5.0 Accomplishments and Status

### 5.1 Background

Ferritic stainless steels are being considered for structural applications in fusion reactors where hydrogen embrittlement and stress corrosion may occur. Since the integrity of the plasma chamber and structural components is an important factor in fusion reactor design, potential material degradation processes are of great concern. Segregation of impurity elements such as phosphorus and sulfur have been shown to have an effect on the hydrogen embrittlement and intergranular corrosion of ferritic steels[1-3] and it is known that phosphorus and sulfur segregation can occur during heat treatment, fabrication and service above 450°C. Therefore, the effects of impurity segregation on the hydrogen embrittlement and stress corrosion of ferritic stainless steels are being determined as a part of their evaluation for fusion reactor structural applications.

### 5.2 Experimental Procedure

#### 5.2.1 Material

Samples for straining electrode tests were taken from a piece of 13 mm thick plate of the Fusion AOD heat (No. 9607) of HT-9 received from General Atomics. Samples were removed such that their tensile axis was in the transverse direction. The chemical composition of this material as reported by General Atomics is given in Table 1. From this table it can be seen that this heat of HT-9 has 325 at. ppm phosphorus and 123 at. ppm sulfur which are both

TABLE 1

CHEMICAL COMPOSITION OF FUSION AOD PROCESSED HT9 (HEAT NO. 9607)
(wt fraction)

| C | Si | Mn | P | S | Cr | Mo | Ni | V | W | Fe |
|---|---|---|---|---|---|---|---|---|---|---|
| 0.20 | 0.24 | 0.57 | 0.018 | 0.007 | 11.64 | 1.01 | 0.52 | 0.30 | 0.57 | Bal. |

sufficient quantities to produce grain boundary segregation. Grain boundary chemistry analysis and straining electrode tests were performed on material given the following heat treatments:

1) 1040°C for 30 min, air-cooled + 760°C for 2-1/2 hr, air-cooled
2) Same as 1 + 240 hr at 500°C.

### 5.2.2 Grain Boundary Chemical Analysis

Grain boundary chemical analysis was performed using PHI model 595 and 545 Auger Electron Spectrometers (AES). The Model 595 spectrometer has a spatial resolution of less than 0.1 μm which allows segregation to be measured on very small segments of grain boundary or other microstructural features. Notched cylindrical specimens were fractured in the AES chamber in a vacuum of $1 \times 10^{-7}$ Pa ($8 \times 10^{-10}$ Torr) or better to minimize contamination.

Samples analyzed with the PHI Model 595 were fractured at -197°C while samples analyzed with the PHI Model 545 were hydrogen charged and fractured at 25°C. Hydrogen charging was done in a 1 N $H_2SO_4$ + 200 mg/ℓ $As_2O_3$ solution at a cathodic potential of -1.0 V (SCE) at 20°C for 16 h. Hydrogen charging facilitated intergranular fracture as shown in Figure 1 and allowed grain boundary chemical analysis to be obtained with the lower resolution (3-5 μm) PHI Model 545 AES. The results obtained with the two instruments were very comparable.

Typically Auger Spectra were taken with an exciting electron beam accelerating voltage of 5 kV, modulation voltage of 4 Vpp, incident electron current of

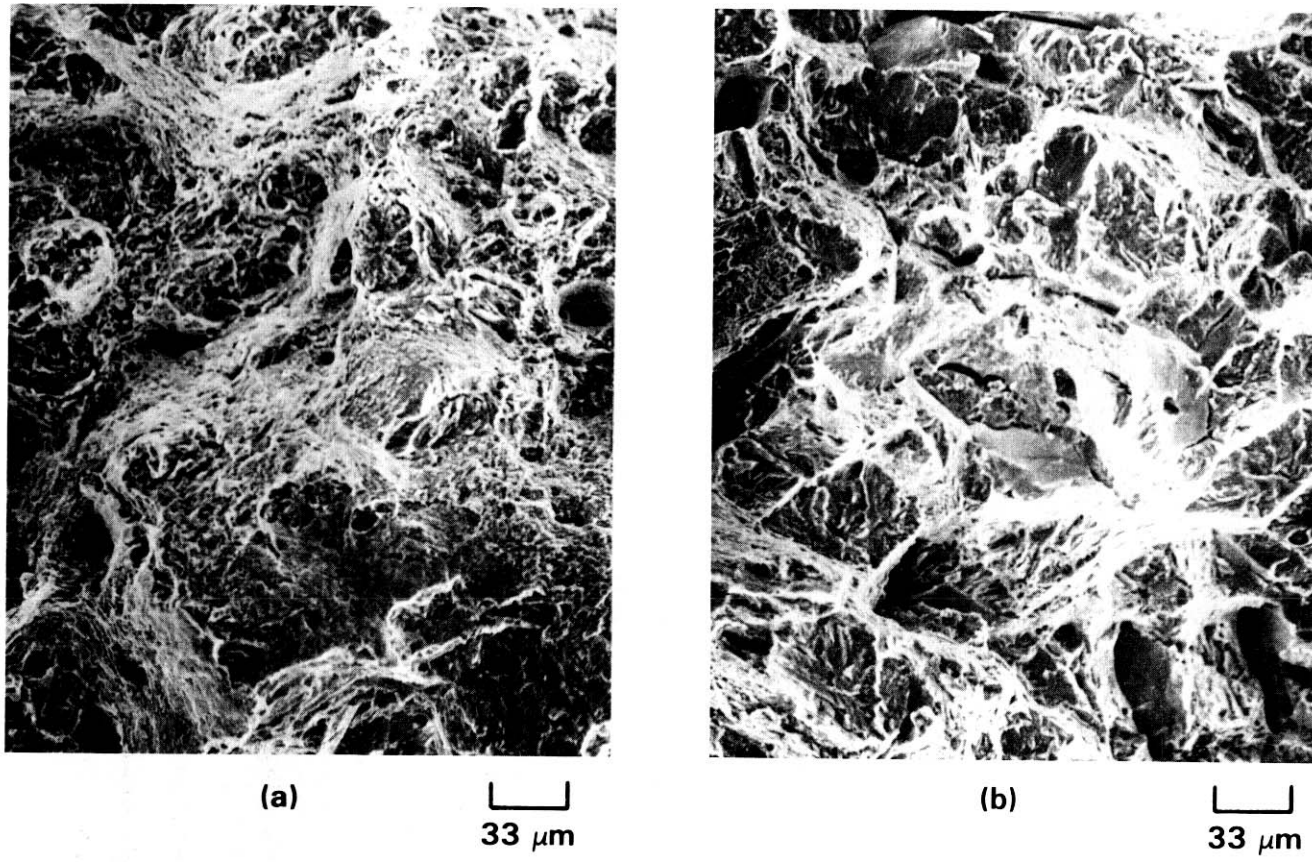


FIGURE 1. Scanning Electron Micrographs of HT9 Heat Treated at 760°C Plus 540°C and Fractured in the Auger Electron Spectrometer: a) -197°C and b) Hydrogen-Charged and Fractured at 20°C.

about 1 μA and a time constant of 0.03 sec. On occasion, a 10-kV electron beam energy was used to improve the spatial resolution for scanning Auger micrographs. All analysis with the 545 system was done with a focused beam, <3 μm, to obtain compositions from single intergranular surfaces. The beam diameters of both AES systems are smaller than the grain size of HT-9. Measurements were made on fracture surfaces judged to be intergranular by examining the secondary electron image available on the scanning Auger system. Many of these fracture surfaces were also examined by conventional SEM to confirm the fracture mode. The reported compositions are the average of at least fifteen analyses.

Grain boundary surface coverages for segregated elements were estimated from the Auger peak signal amplitude using an approximation developed by Hondros and Seah.[4] For grain boundary coverages of 1/2 of a monolayer or less, the coverage $C_X$ of element X on an iron substrate is approximated by

$$C_X = \lambda_X \frac{S_{Fe}}{S_X} \frac{I_X}{I_{Fe}} \qquad (1)$$

where

$I_{Fe}$ = observed peak to peak Auger signal for the 703-eV iron peak,

$I_X$ = observed peak to peak Auger signal for the segregated element X,

$S_x$ & $S_{Fe}$ = relative sensitivities for pure bulk materials,

$\lambda_X$ = electron escape depths, in monolayers.

The elemental sensitivities were obtained from the Handbook of Auger Electron Spectroscopy[5] and the escape depths calculated by

$$\lambda_X = 0.18 \sqrt{E_X}$$

where

$E_X$ is the energy of the Auger electron in eV and the constant which has units of monolayers per $eV^{1/2}$, was obtained by averaging compiled electron escape depth data.(4,6)

This calculation procedure does not give absolute surface coverages, but provides a useful and reproducible indication of the amount of material on the surface and allows meaningful comparisons between specimens. The difficulty in determining absolute concentrations is due to the uncertainty in a number of factors, the more important ones being the sensitivity, electron escape depths, electron backscattering corrections and unknown surface atomic densities. For many materials, the absolute surface concentrations have an accuracy of about $\pm$35%. Relative concentration differences for a given material can be determined to about $\pm$5%. However, for some adsorbate-matrix couples which have been studied by various techniques, it is possible to have a greater confidence in this surface concentration calculation. In particular, the S-Fe system has been studied with low energy electron diffraction (LEED) and saturated sulfur surface coverage on some iron planes has been shown to be 1/2 of a monolayer.[7,8] We have used the above calculational method to estimate oxygen and sulfur coverage on iron foils and obtained results in good agreement (to within 15%) with the LED studies.

After completing Auger analysis on the fracture surfaces, some specimens were argon ion sputter profiled to determine the thickness of the segregants. In all cases, the profile showed that the elements segregated to the grain boundary were within the first monolayer. One would expect the signal from a monolayer or submonolayer thick deposit to decrease exponentially with sputtering time,[7] which is the behavior observed in these specimens. Molybdenum and phosphorus have overlapping Auger electron transitions, therefore it was necessary to correct the phosphorus signals for the small molybdenum signal. This was done by using spectra of pure molybdenum and subtracting the weighted fraction of molybdenum from the phosphorus signal. The molybdenum concentration was determined from a non-overlapping signal at higher energies. Also, 1% of a monolayer was subtracted from the phosphorus concentration since iron has a small low energy signal which overlaps with the phosphorus signal.

### 5.2.3 Microstructural Analysis

Both optical and transmission electron microscopy were used to characterize the microstructure of HT-9. Standard metallographic techniques were used to prepare samples for examination with a Zeiss ultraplot metallograph. Photographs of the microstructure in the transverse and longitudinal directions are shown in Figure 2. It can be seen that the prior austenite grain size is about 100 m while a large stringer inclusion (unidentified) is also shown in Figure 2a. Also, the sub-grain structure is apparent in Figure 2b.

Samples for transmission electron microscopy were prepared from 0.5 mm thick slices which were transverse to the rolling direction. The slices were mechanically polished to 0.05 mm and electrochemically thinned in a 3 vol% perchloric acid-methyl alcohol solution. The solution temperature was -20°C and the polishing voltage was 12 V DC. Electropolished samples were polished to perforation in a twin jet apparatus (Metal-Thin$^{TM}$) with a 2 vol% perchloric-ethyl alcohol solution at a temperature of -30°C. A polishing current of 190 mA was used. The foils were examined in a 120 kV Philips EM400T TEM/STEM microscope with a Kevex thin window detector and Tracor Northern 2000 analyzer for energy dispersive x-ray analysis. The microstructure was that of a carbide stabilized sub-grain structure as shown in Figure 3a. The prior austenite grain boundaries were decorated with a significant density of carbides. Further analysis is being conducted to determine the carbide chemistries following heat treatment at 760°C and 540°C.

### 5.2.4 Dynamic Fracture

The dynamic fracture properties of HT-9 were measured over the temperature range -70°C to +70°C using full sized Charpy type samples tested according to ASTM E-23. An instrumented Tinius Olsen Model 74 LB was used to test the samples. An ETI 300 microprocessor controlled data acquisition system was used to record the load-time data. Dynamic load-deflection and energy-deflection curves were recorded and the yield and maximum loads, yield stress and energy to crack initiation and total fracture were determined.

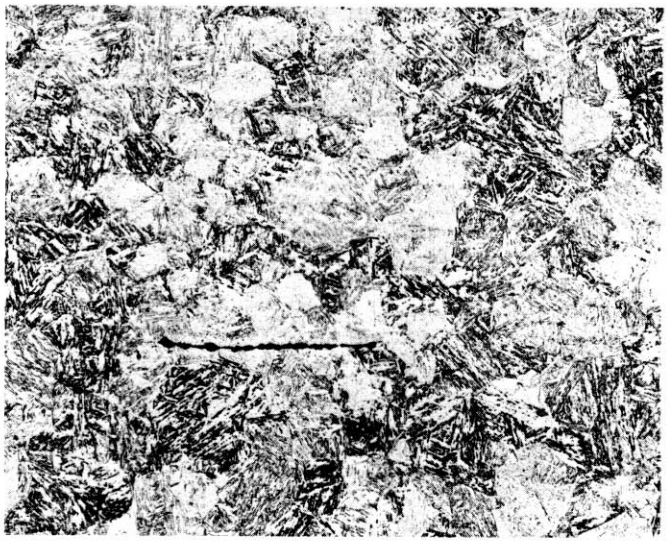

(a) 100 μm

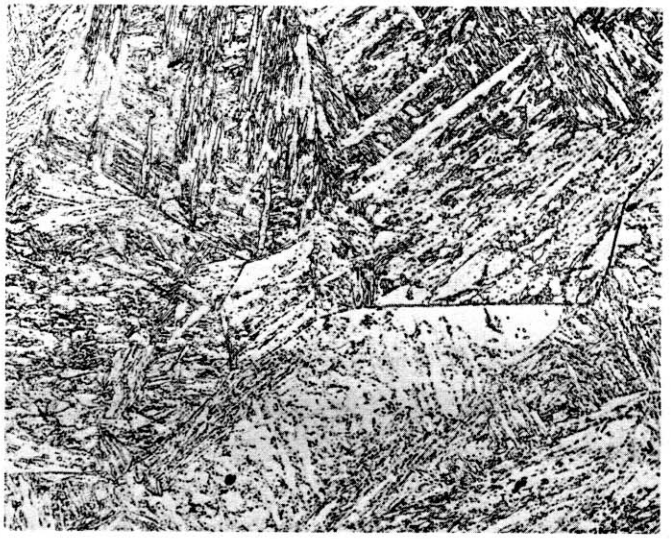

(b) 20 μm

FIGURE 2. Optical Micrograph of HT9 Heat Treated at 760°C: a) Transverse Section and b) Longitudinal Section.


FIGURE 3a. Transmission Electron Micrograph of HT9 Heat Treated at 760°C Showing Subgrain Structure and Carbide Distribution.


FIGURE 3b. Transmission Electron Micrograph Showing Carbide Density Along Prior Austenite Grain Boundary.

### 5.2.5 Straining Electrode Test

Tensile specimens were uniaxially strained in an inverted load frame immersed in a 1N $H_2SO_4$ (pH = 0.3) solution. The loading frame was chemically isolated from the solution by a thick unichrome coating while the grips and pull rods were isolated with teflon sleeves. A cylindrical platinum mesh counter electrode surrounded the specimen while the specimen potential was measured and controlled with a Princeton Applied Research Model 173 potentiostat. All tests were conducted potentiostatically. The reference saturated calomel electrode was isolated from the specimen solution by a Luggin probe-liquid salt bridge. The tip of the probe penetrated the cylindrical platinum electrode and was positioned within 2-3 mm of the specimen surface. The salt bridge and reference solutions were also 1N $H_2SO_4$. All solutions were made by adding reagent grade sulfuric acid to distilled water. The specimens were cleaned in solution by applying a 0.05 V anodic potential for 5 min prior to applying the load and test potential. A strain rate of $7 \times 10^{-5}$ $s^{-1}$ was used for the tests at cathodic potentials and $1 \times 10^{-6}$ $s^{-1}$ at anodic potentials. The current densities ranged from about 100 $mA/cm^2$ at -1.0 V to 0.5 $mA/cm^2$ at +1.0 V. The corrosion potential was -0.45 V (SCE).

The fracture mode of the dynamic fracture and straining electrode samples were examined by scanning electron microscopy (SEM). The amount of intergranular fracture was determined from the SEM micrographs using a line intercept method. Corrections for the projected area of the fracture face were not made.

## 5.3 Experimental Results

### 5.3.1 Grain Boundary Chemistry

The results of the grain boundary chemistry analysis are given in Table 2 where it can be seen that a grain boundary phosphorus concentration of 0.015 monolayers resulted with heat treatment number 1 and 0.04 monolayers with heat treatment number 2. Also, sulfur segregation decreased from

TABLE 2

GRAIN BOUNDARY CHEMISTRY OF HT9

| Treatment | Chemical Composition, Monolayers | | | | | |
|---|---|---|---|---|---|---|
| | P | S | Mo | Cr | C | O |
| Number 1<br>760°C/2.5 h | 0.015 | 0.03 | 0.02 | 0.53 | 0.14 | 0.16 |
| Number 2<br>760°C/2.5 h<br>540°C/240 h | 0.04 | 0.01 | 0.03 | 0.73 | 0.14 | 0.10 |
| HT-9 ESR Processed[10]<br>1040°CC/30 min<br>750°C/1 h | 0.012 | 0.004 | 0.013 | 0.24 | 0.08 | --- |
| HT-9[11]<br>1000°C/1 h<br>650°C/1 h | ND[a] | 0.001 | 0.004 | 0.17 | 0.04 | --- |
| HT-9[11]<br>1000°C/1 h<br>650°C/1 h<br>550°C/100 h | ND | 0.003 | ND | 0.09 | 0.02 | |

(a) Not detected.

0.03 monolayers with heat treatment number 1 to 0.01 monolayers with heat treatment number 2. The displacement of phosphorus by sulfur from the grain boundaries of iron at 500°C has been observed by Jones et al.[9] and was thought to result from a competitive segregation process. Therefore the decreased sulfur segregation in HT-9 with heat treatment number 2 may be the result of competitive segregation and not merely scatter in the data. The grain boundary chemistry results show an increase in the molybdenum and chromium concentration at the grain boundaries, but these increases may have resulted from increased grain boundary carbide precipitation and not from segregation. The large chromium concentration at the grain boundary is

probably associated with chromium rich carbides as verified by Energy Dispersive x-ray Analysis of thin foils.

The increase in the grain boundary phosphorus concentration is also shown by the histogram given in Figure 4. After heat treatment number 1 a maximum phosphorus concentration of 0.05 monolayers was observed while after heat treatment number 2, a maximum concentration of 0.12 monolayers was observed. The minimum phosphorus concentration observed was similar for both heat treatments. The distribution of phosphorus on the fracture surface of HT-9 is shown in Figure 5 for a sample given heat treatment number 1 and analyzed with the PHI Model 595. The association between the flat intergranular features in Figure 5a and the high phosphorus concentrations in Figure 5b is clearly shown. The limited number of intergranular faces in Figure 1 resulted from fracturing HT-9 at -197°C while fracturing hydrogen charged samples at 25°C produced a large number of intergranular faces for analysis. The distribution of phosphorus in a direction perpendicular to the intergranular surface was examined by Ar ion sputter profiling. The phosphorus concentration was found to decrease rapidly with sputtering in a manner consistent with the phosphorus being located within the first monolayer.

Comparison between the present data and that reported by Hyzak and Garrison[10] and Lechtenberg[11] is given in Table 2. This comparison shows that after heat treatment number 1 the present data and that reported by Hyzak and Garrison[10] are very comparable with the exception for sulfur and chromium. The greater amount of sulfur in the present results may reflect the difference in the AOD and ESR processed HT-9 bulk chemistries. The AOD and ESR processed material have bulk sulfur concentrations of 123 appm and 53 appm, respectively. The bulk phosphorus concentration did not change significantly with further processing as the AOD and ESR processed material have bulk concentrations of 325 appm and 290 appm, respectively. The larger chromium concentration at the grain boundary in the present results probably reflects the longer tempering time (2.5 h versus 1.0 h) at 760°C.

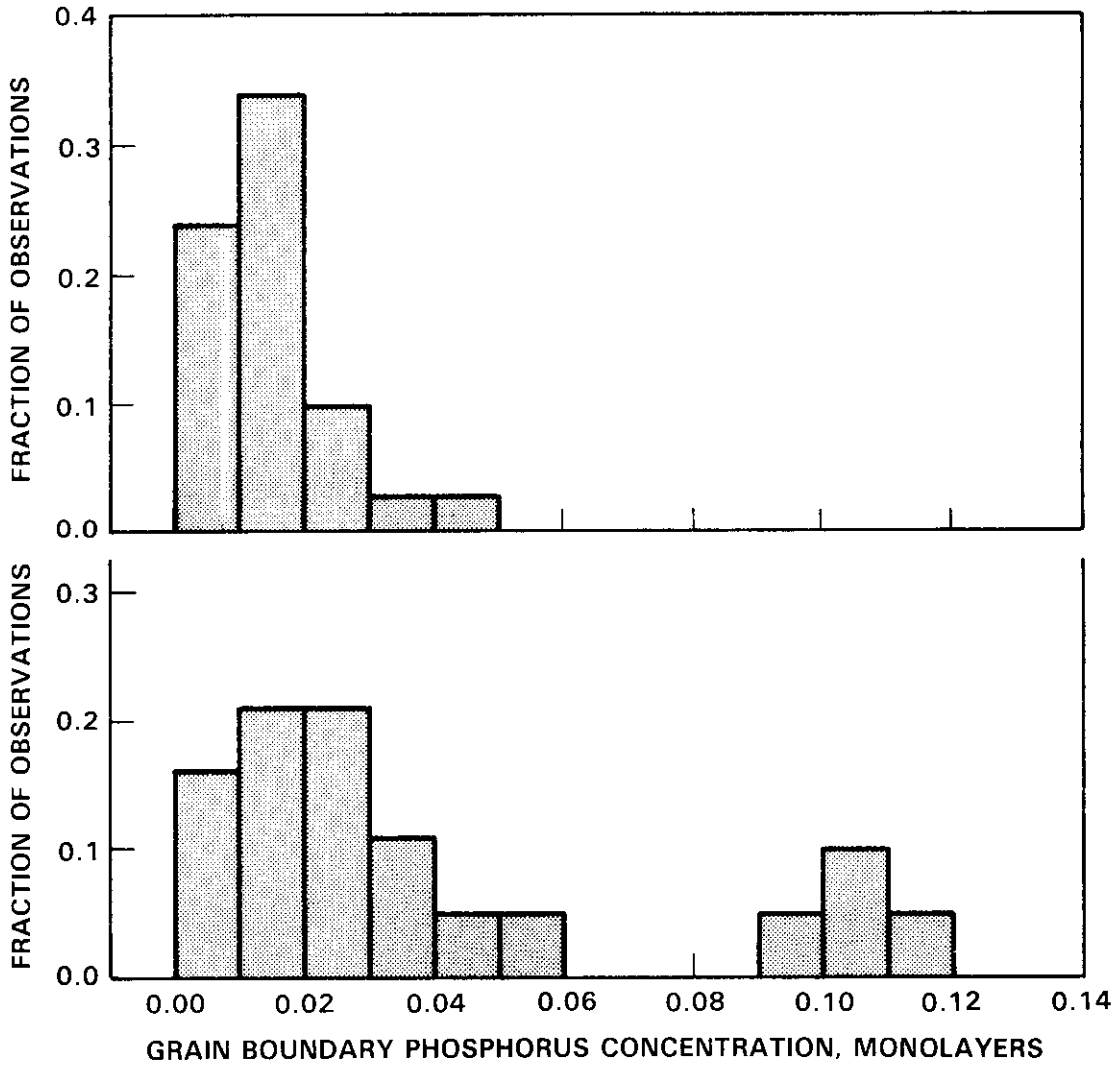


FIGURE 4. Grain Boundary Phosphorus Histograms for HT9 Heat Treated at: a) 760°C/2.5 h and b) 760°C/2.5 h + 540°C/240 h.

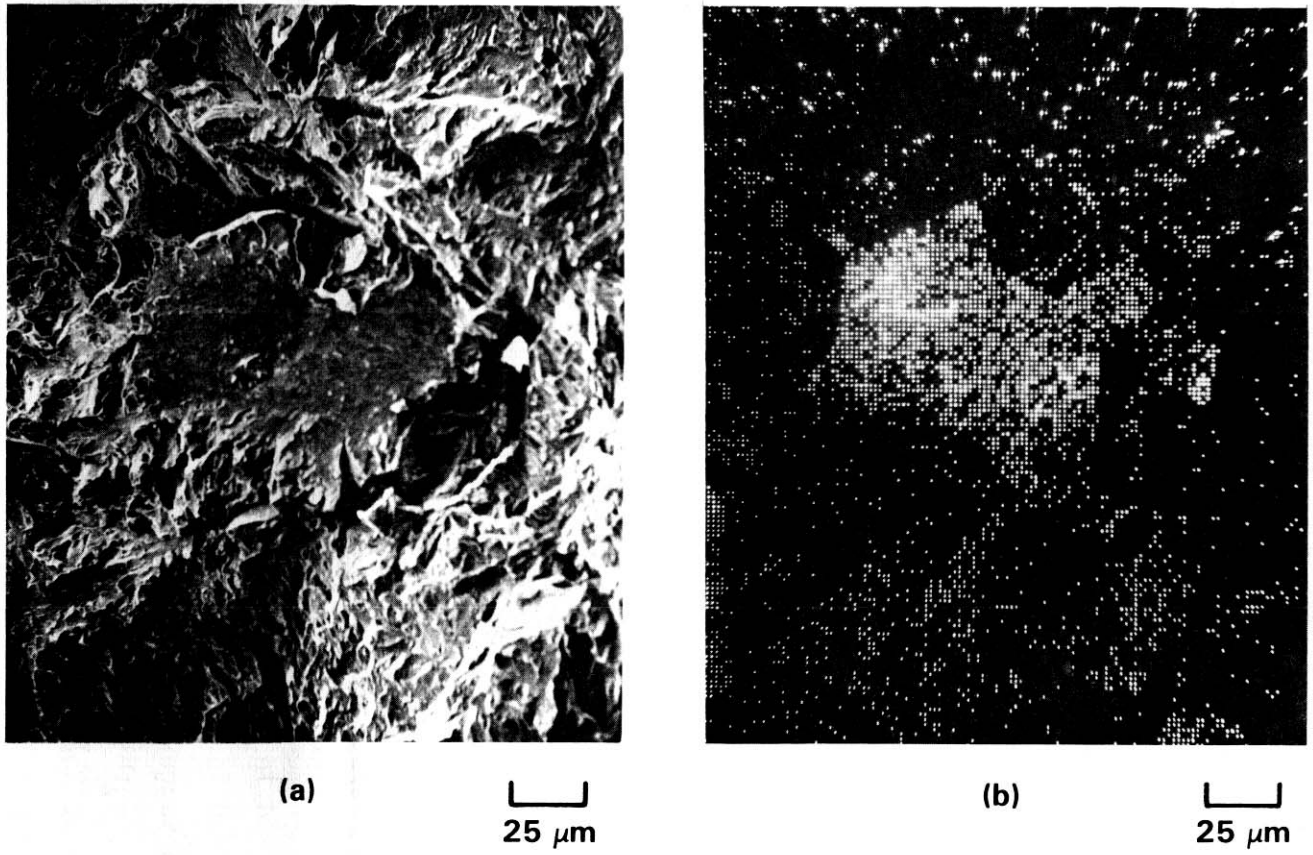


FIGURE 5. Comparison Between Fracture Surface and Phosphorus Distribution for HT9 Heat Treated at 760°C Plus 540°C and Fractured in the Model 595 AES: a) Secondary Electron Image and b) Phosphorus Elemental Map.

The fracture surface chemical compositions reported by Lechtenberg[11] show much lower concentrations for all the elements than the present results or those reported by Hyzak and Garrison.[10] These values are more consistent with those reported by Hyzak and Garrison[10] for ductile fracture regions. The fracture and analysis method used by Lechtenberg[11] would also indicate that these results were from transgranular and not intergranular surfaces because fracture of HT-9 at low temperature without hydrogen precharging produces very little intergranular fracture which therefore requires a high resolution (~0.1 μm) AES to obtain compositional data from intergranular surfaces.

### 5.3.2 Dynamic Fracture Properties

The dynamic fracture properties of HT-9 heat treated at 760°C and 760°C + 540°C are given in Table 3 and Figure 6 for temperatures of -69°C to +70°C. A lower shelf energy of 15 J and an upper shelf energy of 75-80 J were observed for both heat treatments while a 10°C increase in the transition temperature was observed for HT-9 heat treated at 540°C relative to material heat treated at 760°C. This small shift in the ductile to brittle transition temperature reflects a decrease in the total fracture energy at 5°C from 65 J to 50 J. The fracture energy at initiation, Table 3, does not show the same difference as the total energy, therefore, the shift is due primarily to a change in the energy needed to propagate a crack. The yield load and dynamic yield strength showed a small increase with decreasing temperature for both heat treatments although the spread in the data was greater for material heat treated at 540°C. This spread in the data was generally towards higher dynamic yield strengths. This suggested increase in yield strength is substantiated by the tensile yield strengths obtained from the straining electrode tests at slower strain rates and at 25°C where an increase from 525 MPa to 610 MPa resulted after heat treatment at 540°C.

The fracture mode of samples tested at 5°C reveals the reason for the shift in the DBTT where more ductile rupture was present in material heat treated at 760°C than material heat treated at 540°C, Figure 7a,b. The dynamic fracture

TABLE 3

DYNAMIC FRACTURE PROPERTIES OF HT9

| Heat Treatment | Test Temp., °C | $P_y$ kN | $P_{max}$ kN | $\sigma_y$ MPa | $E_I$ J | $E_T$ J |
|---|---|---|---|---|---|---|
| Number 1 760°C/2.5 h | 70 | 15.3 | 19.5 | 786 | 28.2 | 80.7 |
| | 53 | 15.1 | 19.6 | 778 | 33.6 | 81.1 |
| | | 14.2 | 18.9 | 733 | 27.5 | 79.2 |
| | 21 | 15.5 | 20.0 | 802 | 29.8 | 81.0 |
| | | 14.8 | 19.3 | 766 | 28.3 | 76.9 |
| | 5 | 16.6 | 20.9 | 854 | 30.6 | 69.0 |
| | | 16.0 | 20.7 | 827 | 35.5 | 61.2 |
| | -19 | 17.6 | 20.9 | 907 | 29.7 | 40.4 |
| | | 16.6 | 18.8 | 859 | 17.5 | 26.6 |
| | -39 | 16.6 | 20.8 | 859 | 23.2 | 27.4 |
| | | 16.5 | 19.0 | 852 | 15.3 | 19.9 |
| | -69 | 17.4 | 20.9 | 896 | 14.0 | 19.1 |
| | | 17.8 | 20.0 | 919 | 9.5 | 13.6 |
| Number 2 760°C/2.5 h + 540°C/240 h | 70 | 15.4 | 19.3 | 793 | 27.9 | 77.0 |
| | 53 | 15.2 | 19.5 | 786 | 28.5 | 77.6 |
| | | 15.4 | 18.9 | 795 | 28.1 | 73.4 |
| | 21 | 15.8 | 20.0 | 814 | 20.9 | 70.0 |
| | | 14.7 | 19.1 | 759 | 28.3 | 66.4 |
| | 5 | 16.0 | 19.6 | 826 | 28.9 | 50.3 |
| | | 17.1 | 19.4 | 884 | 28.1 | 50.2 |
| | -19 | 15.9 | 19.3 | 819 | 17.1 | 28.6 |
| | | -- | -- | -- | -- | 25.1 |
| | -41 | 20.3 | 20.4 | 1049 | 20.3 | 25.2 |
| | | 16.0 | 18.4 | 827 | 9.8 | 13.7 |
| | -69 | 18.9 | 20.7 | 977 | 12.5 | 17.5 |
| | | 17.6 | 19.6 | 907 | 11.1 | 14.2 |

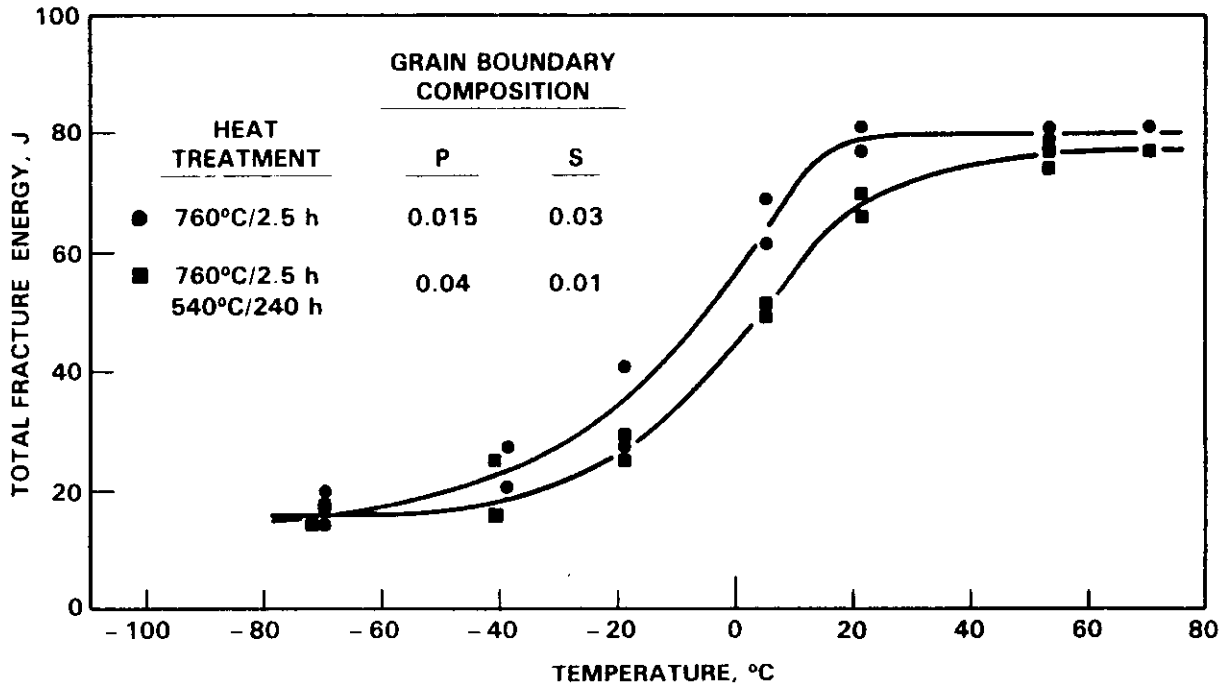


FIGURE 6. Charpy V Notch Results for HT9.

mode at 5°C was a mixture of ductile rupture and quasi-cleavage with only a few intergranular features. Therefore, it is concluded that the yield strength increase from the 540°C heat treatment caused the small shift in DBTT and that grain boundary chemistry did not have a significant effect. Even at -69°C, intergranular fracture did not contribute to the lower shelf fracture energy. There was a noticeable decrease in the amount of ductile rupture at -69°C; however, intergranular fracture comprised only a few percent of the total fracture surface for both heat treatments, Figure 7c,d.

The fracture energy versus temperature curve for HT-9 heat treated at 760°C, Figure 6, is similar to the $k_Q$ versus temperature curve of Lechtenberg[11]; however, he reported a shift of 80°C in the transition temperature with aging 100 h at 550°C. A shift of 10°C was observed in the present material. The fracture modes were similar in both cases and it is concluded that the difference in the DBTT shift resulted from a different response of the yield strength of HT-9 to aging.

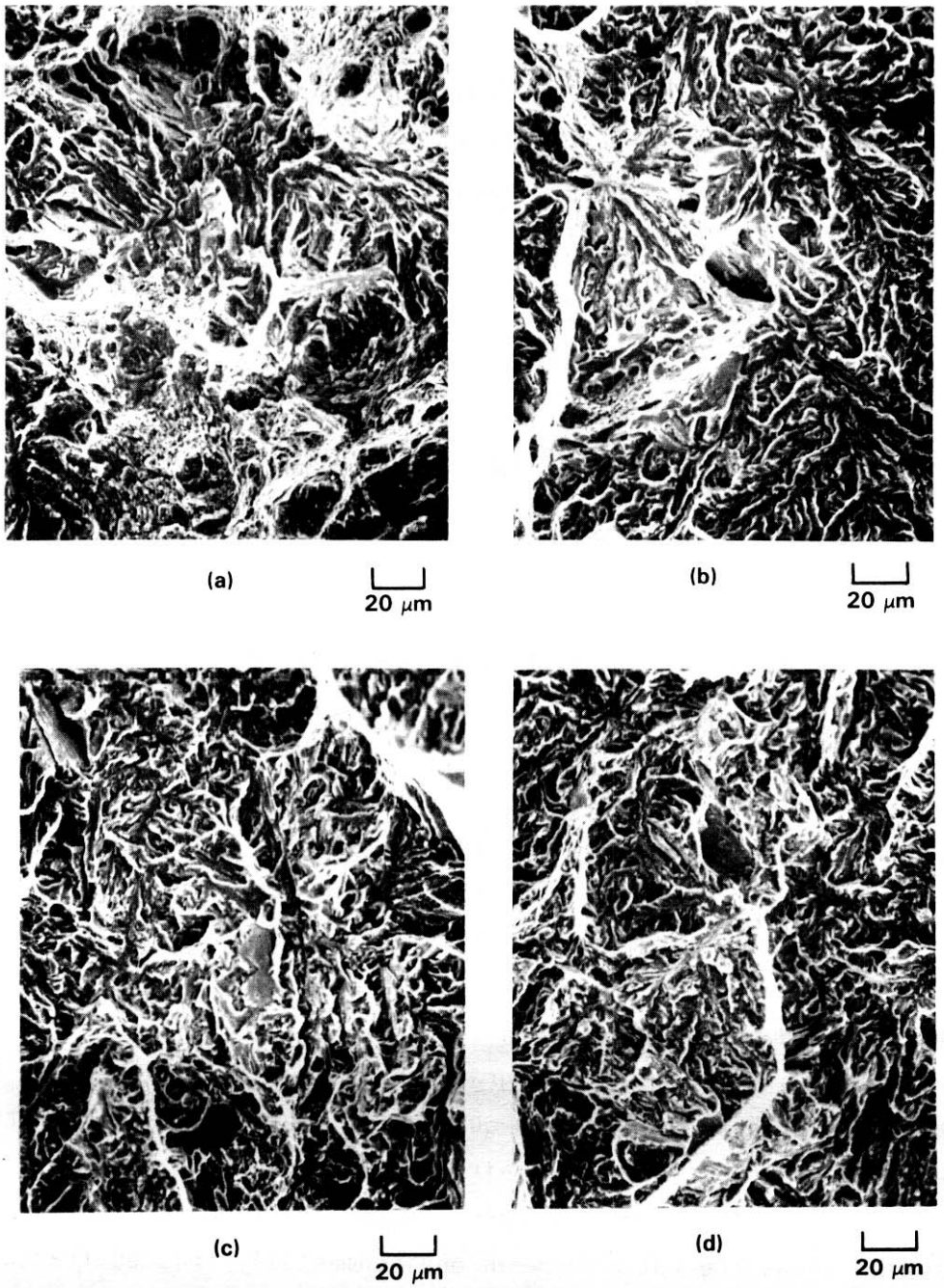


FIGURE 7. Scanning Electron Micrographs of Charpy Impact Samples of HT9: a) Heat Treated at 760°C, Tested at 5°C, b) Heat Treated at 760°C Plus 540°C, Tested at 5°C, c) Heat Treated at 760°C, Tested at -69°C, and d) Heat Treated at 760°C Plus 540°C, Tested at -69°C.

### 5.3.3 Environmental Effects on Tensile Behavior

HT-9 was found to be sensitive to external, cathodic hydrogen but no evidence of stress corrosion susceptibility was observed at 25°C. The test results were independent of heat treatment and clearly demonstrated that HT-9 is susceptible to intergranular fracture in the presence of hydrogen but that grain boundary segregation of small quantities of sulfur and phosphorus do not promote IGSCC at 25°C.

#### 5.3.3.1 Effects of Hydrogen

The polarization behavior of HT-9 in 1N $H_2SO_4$ determined at a scan rate of 1 mV/s is given in Figure 8 along with the reduction of area of HT-9 following straining electrode tests at cathodic and anodic potentials. The polarization curve shows that HT-9 passivates in 1N $H_2SO_4$ at anodic potentials of +0.2 to +1.0 V (SCE) with active corrosion at potentials of -0.45 to -0.1 V (SCE).

The results of the straining electrode tests, Figure 8, show that the reduction of area of HT-9 decreases from 57% in air to 13% at -0.6 V and -1.0 V (SCE). The ductility of HT-9 in cathodic straining electrode tests is very similar to the ductility of material pre-charged at cathodic potentials which can be seen by comparing the reduction of area results in Figure 8 with the results given by Hyzak and Garrison[12] in their Figure 1. This decrease in the reduction of area is accompanied by an increase in the depth of environmentally induced cracks which were a mixture of intergranular and quasi-cleavage type fracture and in the ratio of intergranular to quasi-cleavage type fracture within the environmentally induced cracks. In air, the fracture mode was ductile, micro-void coalesence type fracture. Examples of the fracture surfaces are given in Figure 9 which shows the ratio between environmentally induced fracture to the final ductile shear fracture and Figure 10 which shows the fracture appearance within the environmentally induced cracks at $E_c$, -0.6 V and -1.0 V and the fracture mode in air. The extent of intergranular fracture within the environmentally induced cracks increased from 15% at -0.45 V (SCE) to 55% at -1.0 V (SCE) for material heat treated at 760°C but reached only 35% at -1.0 V

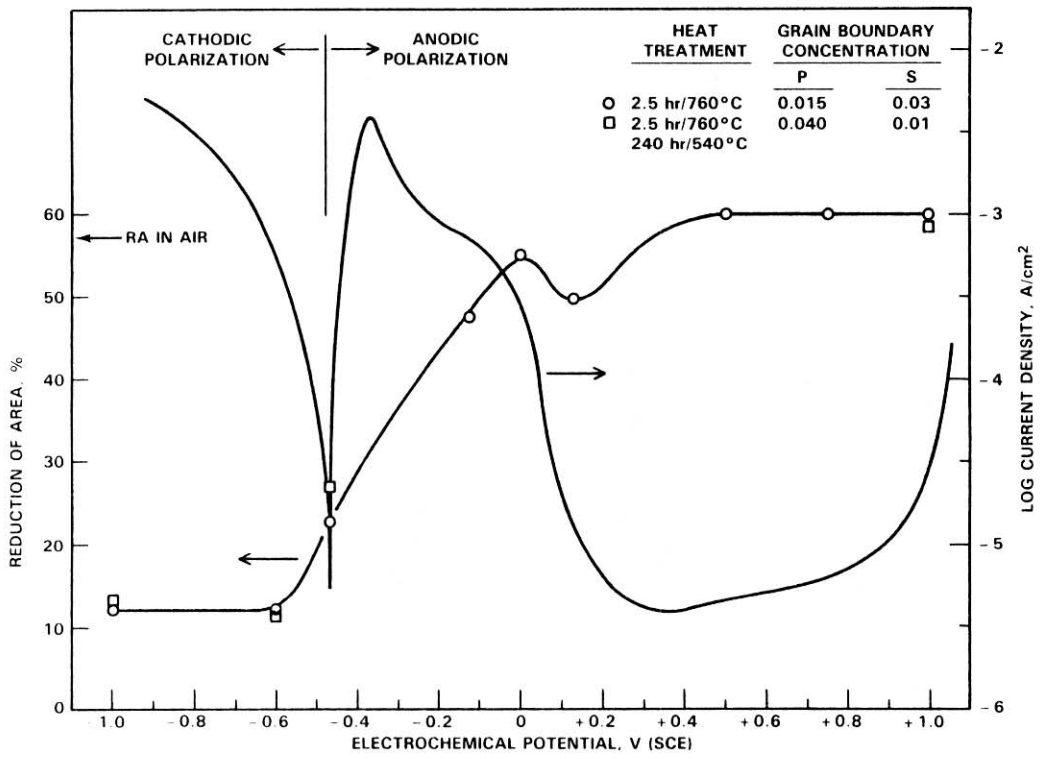


FIGURE 8. Tensile Ductility and Polarization Behavior of HT9 in 1 N $H_2SO_4$ at 25°C.

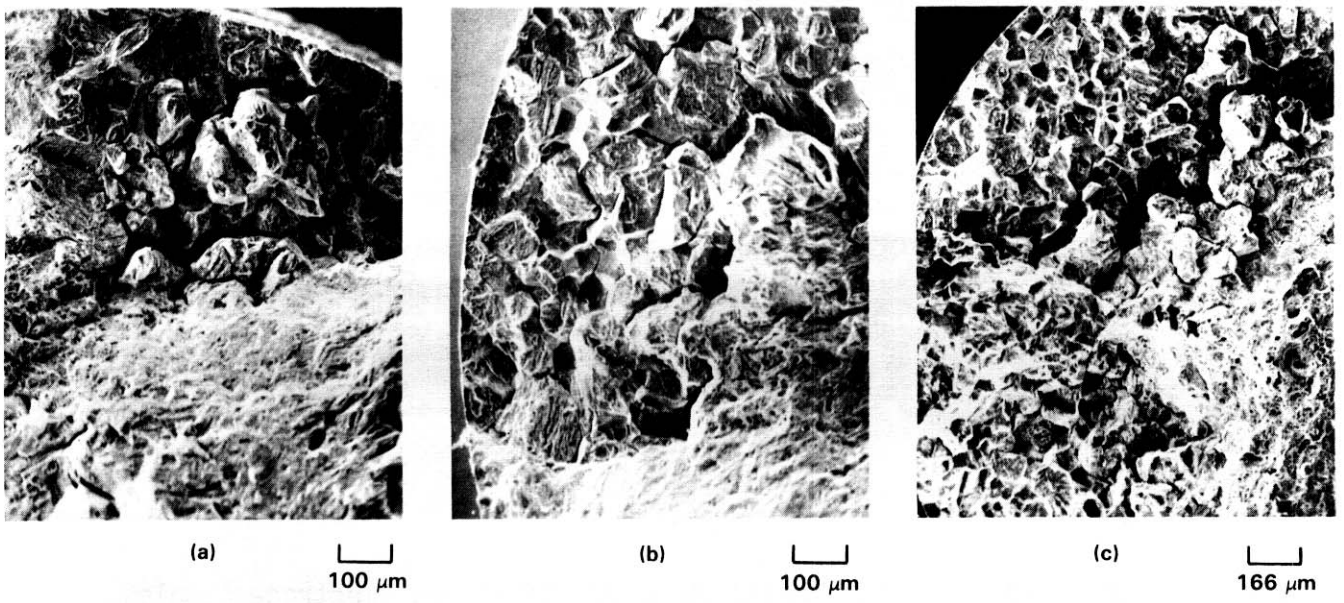


FIGURE 9. Scanning Electron Micrographs of HT9 Straining Electrode Samples Heat Treated at 760°C and Tested in 1 N $H_2SO_4$ at 25°C: a) Open Circuit Potential, -0.45 V (SCE), b) -0.6 V (SCE), and c) -1.0 V (SCE)

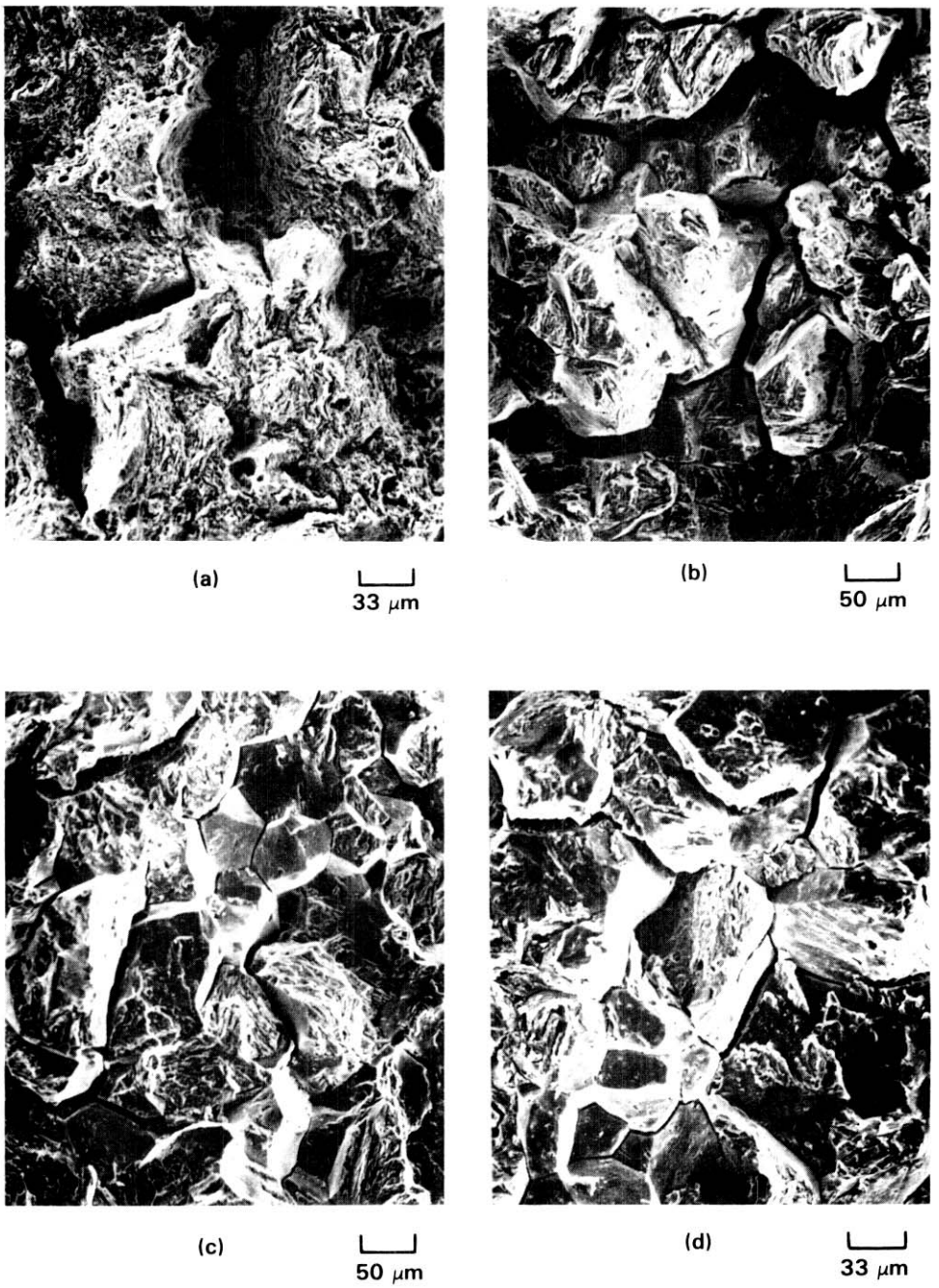


FIGURE 10. Scanning Electron Micrograph of HT9 Straining Electrode Samples Heat Treated at 760°C and Tested: a) in Air in 1 N $H_2SO_4$ at 25°C, b) Open Circuit Potential, -0.45 V (SCE), c) -0.6 V (SCE), and d) -1.0 V (SCE).

in material heat treated at 540°C, Figure 11. This result indicates that grain boundary sulfur segregation causes more intergranular fracture in the presence of hydrogen than does phosphorus. A similar effect was demonstrated in iron tested at cathodic potentials by Jones et al.[9] where they found that phosphorus had a negligible effect on the intergranular fracture of low strength iron at cathodic test potentials while sulfur had a significant effect. In the case of low strength iron the reduction of area was insensitive to the fracture mode while the total strain to failure was less for 100% intergranular fracture than for 50% and 0% intergranular fracture. In the present case, both the reduction of area and strain to failure are insensitive to amount of intergranular fracture, Figure 12, in the hydrogen induced cracks. Since the depth of the mixed mode, environmentally induced cracks increased with increasing cathodic potentials, the ductility of HT-9 decreased because of an increased hydrogen induced crack growth rate. The hydrogen induced crack growth rate is insensitive to the relative amount of intergranular and quasi-cleavage type fractures and appears to be primarily dependent on the amount of hydrogen which increases with increasing cathodic potentials. The hydrogen induced crack growth rate is also insensitive to the small yield strength increase from 525 MPa to 610 MPa which resulted from the 540°C heat treatment even though this yield strength change had a small effect on the dynamic fracture properties.

The apparent insensitivity of the hydrogen induced crack growth rate and hence the ductility of HT-9 to the relative amount of intergranular and transgranular fracture may be explained by one of the following mechanisms: 1) the crack growth rates are dominated by the amount of available hydrogen or hydrogen uptake rate, 2) the hydrogen induced intergranular and transgranular crack growth rates are equal and therefore the crack growth rate is insensitive to the proportion of each mode or 3) the transgranular fracture mode is very slow such that a decrease from 65% to 45% transgranular fracture was insufficient to cause a significant change in the crack growth rate. The answer to this question will have to wait for the results of sub-critical crack growth rate tests which are in progress.

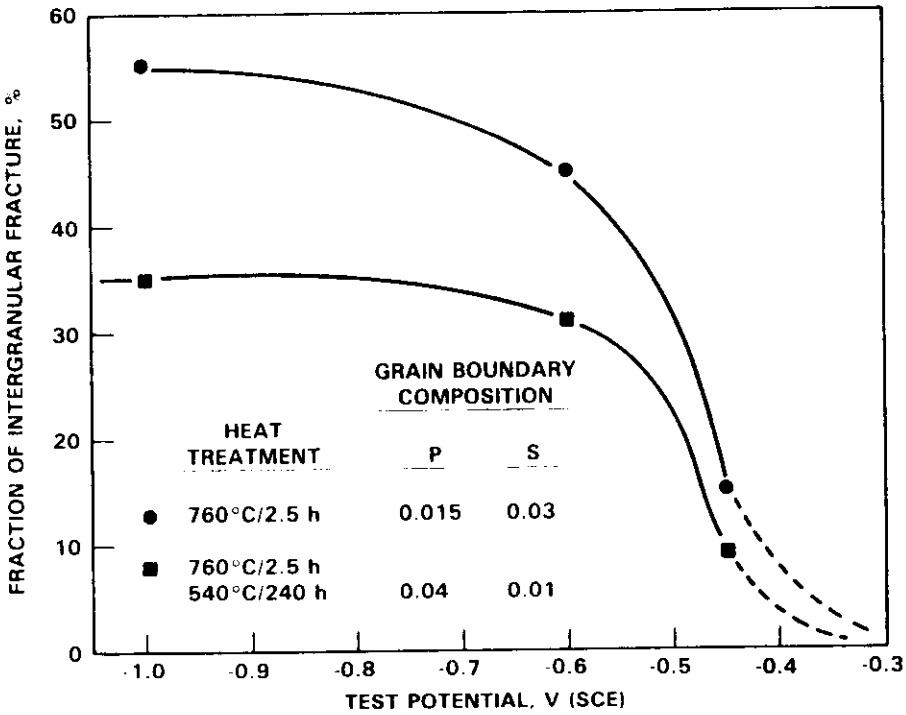


FIGURE 11. Fracture Mode Versus Test Potential for HT9.

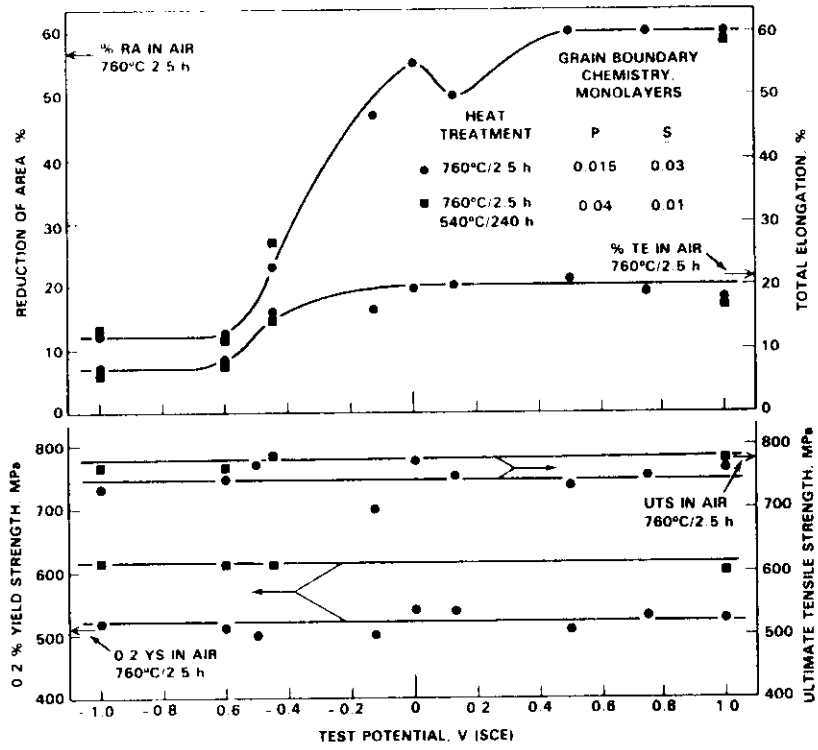


FIGURE 12. Straining Electrode Results for HT9 Tested at 25°C in 1 N $H_2SO_4$.

5.3.3.2 Stress Corrosion Behavior

The slow strain rate ($10^{-6}$ $s^{-1}$) tensile properties of HT-9 did not show any indication of a susceptibility to stress corrosion cracking in the passive (+0.3 to 0.9 V) or transpassive (>+0.9 V) corrosion regimes, Figures 8 and 12. The reduction of area and total elongation of HT-9 were equal to the values obtained in air. In the active to passive transition corrosion regime (-0.35 to +0.3 V) the reduction of area was slightly below the values obtained in air which may suggest a slight susceptibility to stress corrosion. The reversible hydrogen potential is -0.2 V (SCE) for pH = 0.3; therefore, the decreased ductility at -0.125 to +0.125 V (SCE) is not related to hydrogen effects. The greatest susceptibility to stress corrosion cracking generally occurs in the active to passive transition and transpassive corrosion regimes. There was no indication of intergranular fracture in tests conducted at anodic potentials, Figure 13, therefore the lower ductility probably reflects a susceptibility to transgranular stress corrosion. The mechanism of this stress corrosion reaction of HT-9 in the active to passive transition has not been identified.

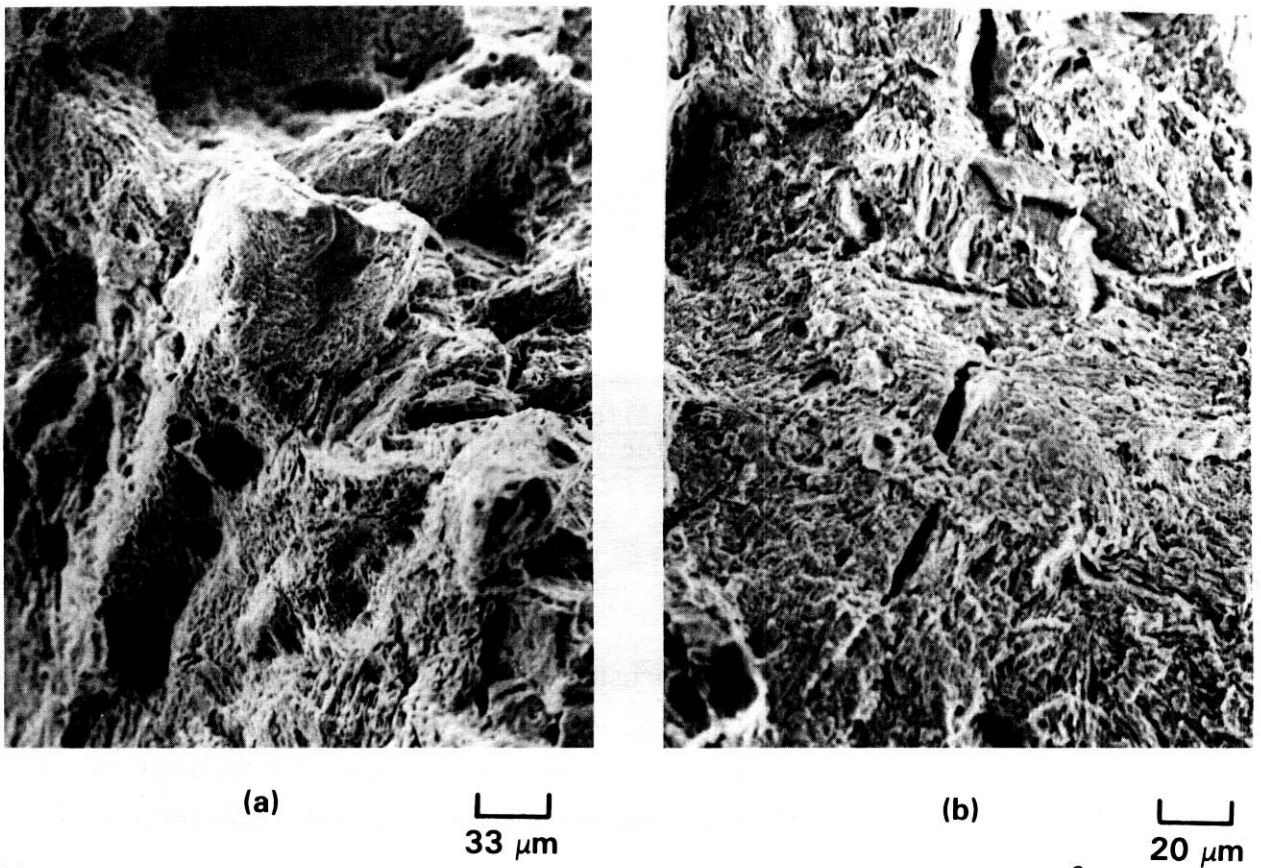


FIGURE 13. Scanning Electron Micrographs of HT9 Heat Treated at 760°C and Tested in 1 N $H_2SO_4$ at 25°C: a) -0.125 V (SCE) and b) +0.125 V (SCE)

## 6.0 References


1. R. H. Jones, S. M. Bruemmer, M. T. Thomas and D. R. Baer, Met. Trans. A, 12A, 1621 (1981).

2. J. Kameda and C. J. McMahon, Jr., Met Trans. A, 12A, 31 (1981).

3. C. L. Briant, Scripta Met., 15, 1013 (1981).

4. E. D. Hondros and M. P. Seah, International Metals Reviews, 222, 262 (1977).

5. L. E. Davis, N. C. MacDonald, P. W. Palmberg, G. F. Riach and R. E. Weber, Handbook of Auger Electron Spectroscopy, Physical Electronics Industries, Eden Prairie (1976).

6. M. P. Seah and W. A. Dench, Surface and Interface Analyses, 1, 2 (1979).

7. H. J. Grabke, E. M. Petersen and S. R. Srinivasan, Surf. Sci., 1,2 (1977).

8. M. T. Thomas, D. R. Baer, R. H. Jones and S. M. Bruemmer, J. Vac. Sci. and Tech., 17,25 (1980).

9. R. H. Jones, S. M. Bruemmer, M. T. Thomas and D. R. Baer, Scripta Met., 16, 615 (1982).

10. J. M. Hyzak and W. M. Garrison, Alloy Development for Irradiation Performance Semi-Annual Progress Report for period ending March 31, 1982, DOE/ER-0045/8, 401 (1982).

11. T. A. Lechtenberg, Alloy Development for Irradiation Performance Semi-Annual Progress Report for Period Ending Sept. 30, 1981, DOE/ER-0045/7, 168 (1981).

12. J. M. Hyzak and W. M. Garrison, Alloy Development for Irradiation Performance Semi-Annual Report for Period Ending March 31, 1982, DOE/ER-0045/8, 461 (1982).


## 7.0 Future Work

Sub-critical crack growth rates and thresholds for HT-9 will be measured at cathodic potentials. Material heat treated at 760°C for 2.5 h and 760°C/2.5 h plus 540°C for 240 h will be evaluated. This information will be used to indicate the effect of grain boundary impurity-environmental interactions on critical flaw sizes in fusion reactors. These results must be verified with irradiated material tested in reactor environments before they can be applied to reactor design.

# RADIATION-INDUCED SEGREGATION OF PHOSPHORUS IN FUSION REACTOR MATERIALS

J. L. Brimhall, D. R. Baer, R. H. Jones, Pacific Northwest Laboratory

## 1.0 Objective

The purpose of this study is to determine the critical material and irradiation parameters which control the radiation induced segregation of impurity elements in fusion reactor materials.

## 2.0 Summary

The radiation induced surface segregation of phosphorus in stainless steel decreased continually with dose levels beyond 0.8 dpa. This decrease in the surface segregation of phosphorus at high dose levels has been attributed to removal of the phosphorus layer by ion sputtering. Phosphorus cannot be replenished since essentially all of phosphorus within the irradiation zone has been segregated to the surface. Sputter removal may explain the previously reported absence of phosphorus segregation in ferritic alloys irradiated at high doses (>1 dpa). Irradiation of ferritic alloys to low doses has shown measureable surface segregation of phosphorus. The magnitude of the segregation in ferritics is still much less than in stainless steel. This sputtering phenomenon places an inherent limitation to the heavy ion irradiation technique for the study of surface segregation of impurity elements. Alternate methods for examining this phenomena are being examined.

## 3.0 Program

Title: Mechanical Properties
Principal Investigator: R. H. Jones
Affiliation: Pacific Northwest Laboratory

## 4.0 Relevant DAFS Program Plan Task/Sub-Task

Subtask II.C.14 Models of Flow and Fracture under Irradiation
Subtask II.C.1 Effect of Material Parameters on Microstructure

## 5.0 Accomplishments and Status

### 5.1 Introduction

Radiation induced segregation of alloying elements to interfacial sinks is a well established phenomenon. Various physical and mechanical properties can be altered by radiation induced segregation of certain elements. Segregation of such impurity elements as phosphorus to the grain boundaries may have a marked effect on such properties as fracture toughness, hydrogen embrittlement, stress corrosion or corrosion fatigue. The radiation induced segregation of impurity elements has not been widely studied, however, and is the main subject of the current research reported here.

The radiation induced segregation of phosphorus and other impurity elements in a variety of candidate fusion reactor alloys has been previously reported (1,2,3). This research has utilized heavy ion irradiation to induce segregation near the free surface of the alloys. In the present work, the dose dependence of the phosphorus segregation in austenitic stainless steel and ferritic alloys has been extended to both lower and higher dose levels. In addition, a high phosphorus containing iron alloy has also been studied in order to optimize phosphorus segregation conditions.

## 5.2 Experimental Details

The surface segregation of phosphorus was analyzed in austenitic 316 SS, ferritic HT-9, Fe+0.03 at. %P, Fe+0.1 at. %P and Ni+0.03 at. %P. The 316SS and HT-9 were obtained from the fusion materials stockpile and the heat treatments reported previously.[1] The iron-phosphorus and and nickel phosphorus alloys were annealed at 1325K for 30 min. and furnace cooled. The specimens were mechanically polished and given a final electropolish after the heat treatments to remove any degree of thermal segregation. All the alloys were irradiated with 5 MeV $Ni^{++}$ ions to dose levels ranging from 0.01 to 12 dpa and at temperatures of 775 and 875K. The near surface composition after irradiation was analyzed by Auger Electron Spectroscopy (AES). The concentration profiles of up to six elements were obtained by sputter profiling using $Ar^{+}$ ions in the AES chamber. A sputter removal rate of 0.05nm/min was used for the near surface region and the rate was increased at greater depths from the surface. Full range AES scans were periodically taken to check the entire compositional spectrum. The data is presented as the peak height ratio (PHR) of the particular element to the bulk iron signal. The iron signal was changing rapidly in the region of maximum phosphorus concentration, so the iron signal in the bulk region was considered more appropriate for normalizing the data.

## 5.3 Results and Discussion

Radiation induced segregation of phosphorus to the surface is very strong in 316SS. The PHR for phosphorus as a function of distance from the bombarded surface is shown in figure 1 for several doses. The phosphorus concentration decreases rapidly from the surface indicating that the phosphorus is largely confined to the surface region. In contrast to this, the PHR for nickel shows a more gradual decrease in the concentration of nickel, Figure 1.

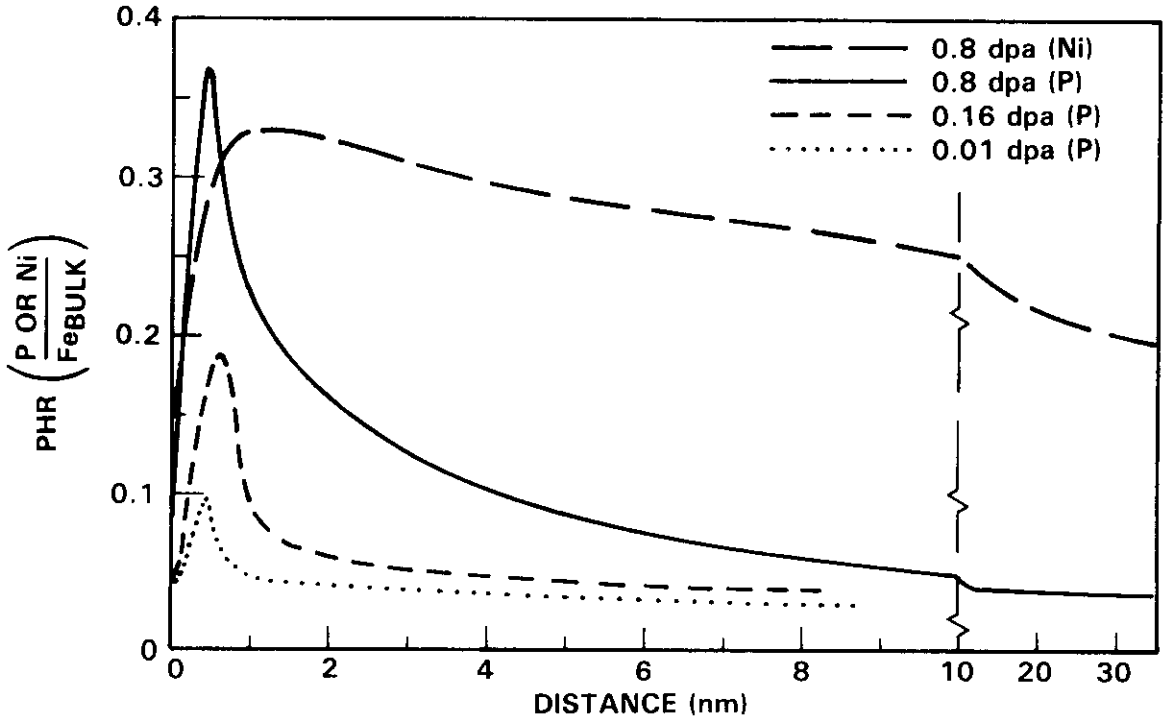


FIGURE 1. Concentration (PHR) of Phosphorus and Nickel as a Function of Distance from Surface in 316 Stainless Steel Irradiated at 875 K to Several Dose Levels.

A plot of the dose dependence of the maximum phosphorus segregation in stainless steel shows a decrease in segregation beyond ∿0.8dpa with virtually no segregation observed at a dose of 12 dpa, Figure 2. A comparable plot for the maximum PHR for nickel shows a continual increase in segregation to high dose levels, Figure 2. The max PHR for nickel shows a linear fit when plotted against $(\text{dose})^{\frac{1}{2}}$. A $t^{\frac{1}{2}}$ dependence for radiation induced surface segregation has been reported in other work.[4] The strong nickel segregation at the high dose levels indicates that the specimen were highly irradiated and there were no experimental abnormalities which could account for the low phosphorus segregation.

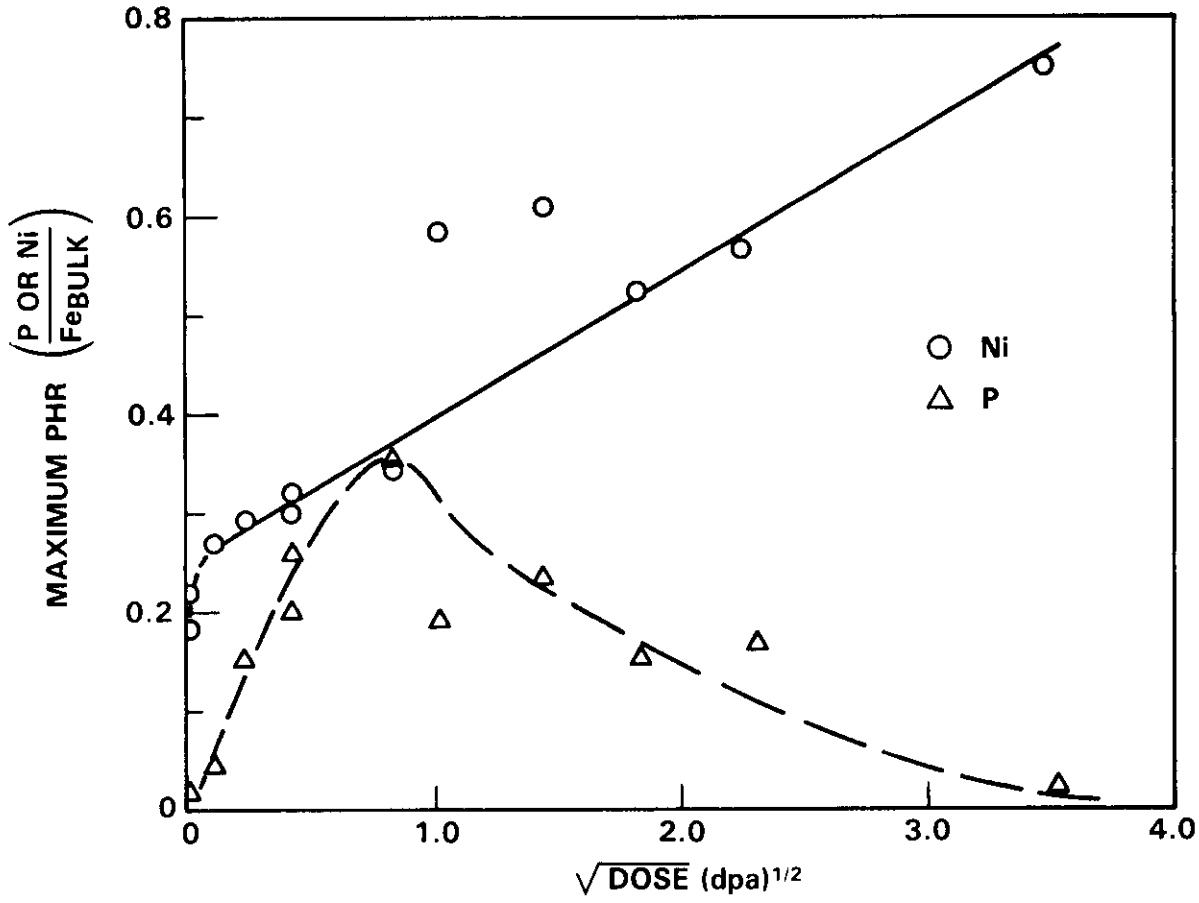


FIGURE 2. Dose Dependence of the Maximum Observed PHR for Phosphorus and Nickel in 316 Stainless Steel, Ion Irradiated at 875 K.

A similar dose dependence was observed in the Fe+0.03 at.%P and Ni+0.03 at.%P alloys as shown in Figure 3. Although there is not much data, the greatest segregation (PHR) was observed at the lowest dose. The high dose level showed practically no phosphorus segregation. In the Ni+0.0.03%P, the magnitude of the segregation was about 1/3 that observed in the 316 SS.

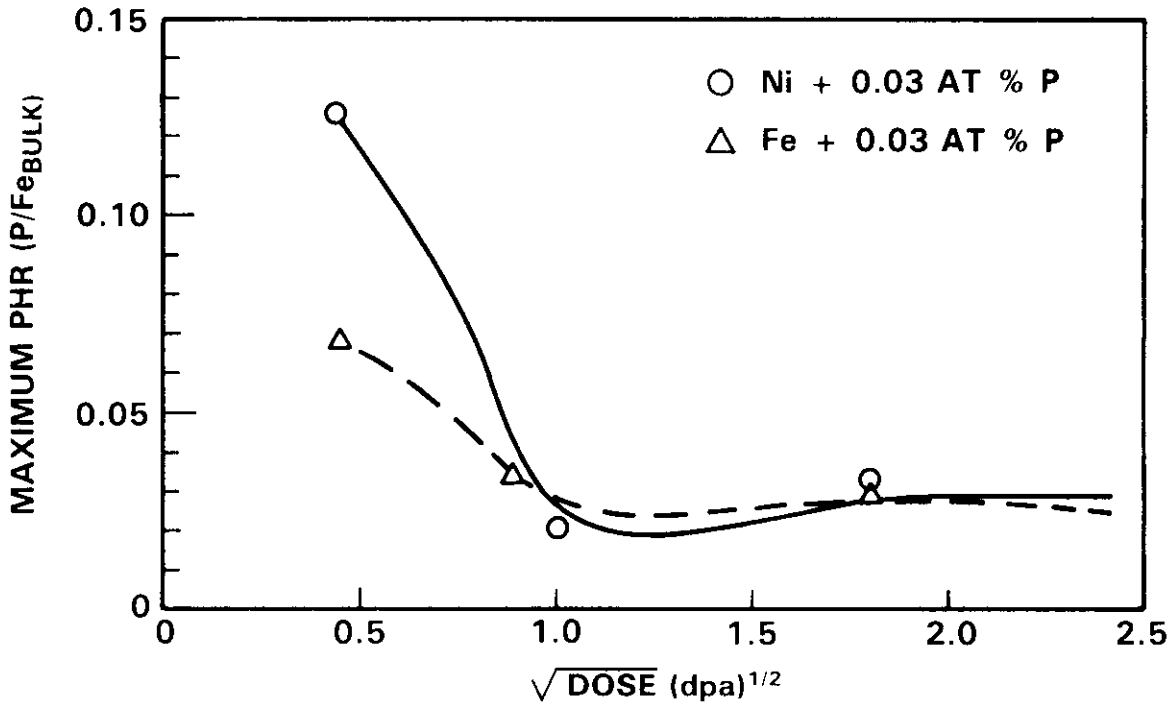


FIGURE 3. Dose Dependence of the Maximum Observed PHR for Phosphorus in Iron-Phosphorus and Nickel-Phosphorus Alloy, Ion Irradiated at 875 K.

The observed maximum in the dose dependence of phosphorus segregation strongly suggests the removal of phosphorus by ion sputtering. The phosphorus is segregated in a very narrow region near the surface and the sputtering from the heavy ions can eventually erode this phosphorus containing region. The sputtering yield, S, from heavy ions has not been well studied. An extrapolation of data from argon ion sputtering of copper suggests that S could be as high as one. Assuming S=1, a fluence of $6 \times 10^{15}$ ions $cm^2$ (1 dpa) would remove 3.3 atom layers or $\sim$1 nm. Since the peak in the phosphorus concentration is less than 1 nm from the surface, a significant fraction of the phosphorus would be removed after this dpa level.

A mechanism of this type implies that the phosphorus cannot be replenished once it is sputtered away. A conservative estimate of the phosphorus segregated to the surface would be the equivalent of one full

monolayer. For 316SS with ∿600ppm phosphorus, all the phosphorus from a layer 0.5μm deep would be required to produce this monolayer. This is nearly the entire radiation zone. Phosphorus would have to diffuse in from beyond the radiation zone to replenish the lost phosphorus removed by sputtering. This is a very slow process compared to the radiation induced processes so there is effectively no replenishment. Sputtering then places an inherent experimental limitation for this irradiation technique, at least with impurity elements like phosphorus. The segregation of nickel, which is also being sputtered, is little affected. The concentration profile of nickel is not sharp and there is a high bulk concentration of nickel to draw from.

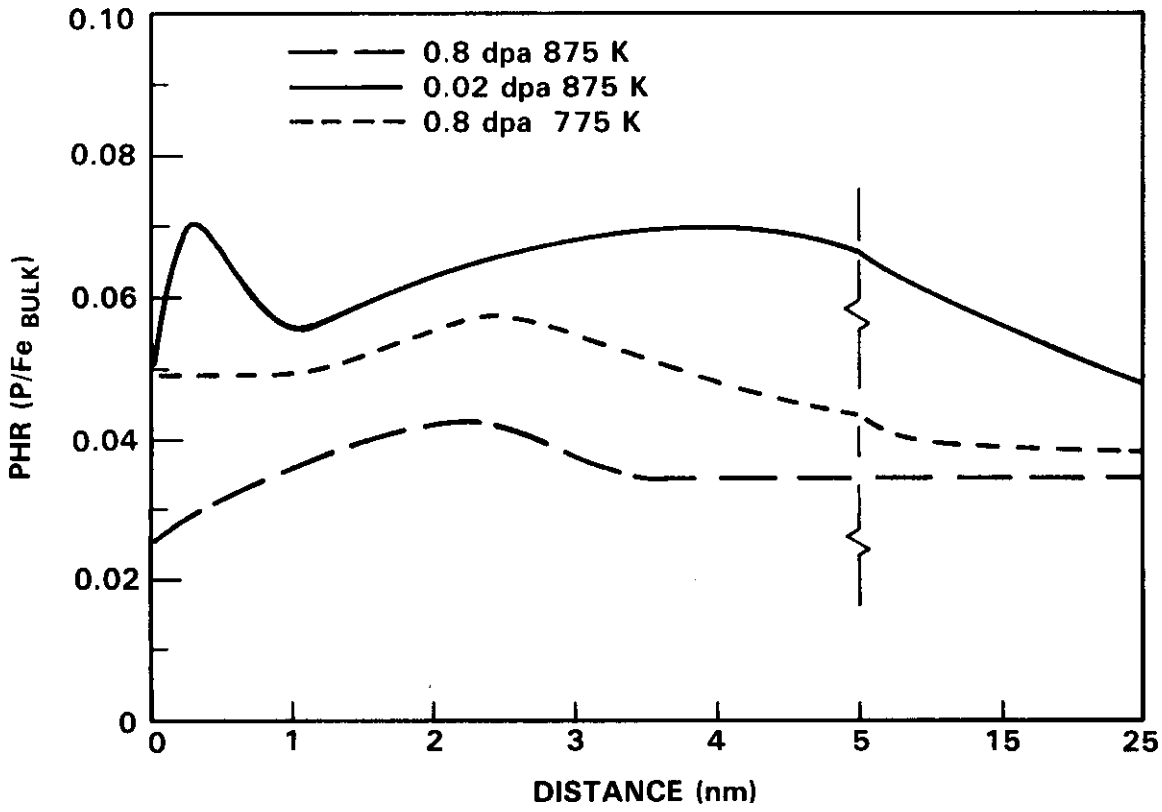


FIGURE 4. Concentration (PHR) of Phosphorus as a Function of Distance from the Surface in HT9, Ion Irradiated under Several Dose and Temperature Conditions.

The sputter phenomenon can also explain the lack of phosphorus segregation in ferritic alloys, which had been previously reported.[2,3] These alloys had been irradiated to doses of ∿3 dpa. Ion irradiation of HT-9 and the iron phosphorus alloys to low dose levels shows small, but measurable surface segregation of phosphorus. Several phosphorus concentration profiles (PHRs) for HT-9 and Fe+0.1 at.%P irradiated at several low doses are shown in Figures 4 and 5. The Fe+0.1 at.%P alloy shows somewhat more pronounced phosphorus segregation than HT-9. Both, however, show much less phosphorus segregation than in 316 SS. The curves in Figures 4 and 5 also show an apparent double peak in the phosphorus concentration. A high concentration of sulfur was always noted in the region between the double peaks. The effect of sulfur was most pronounced in the Fe+0.1 at.%P alloy, but was present in all the ferritic alloys. No such sulfur effect was observed in 316 SS. The exclusion of phosphorus by sulfur is a well known phenomenon in thermal segregation studies.

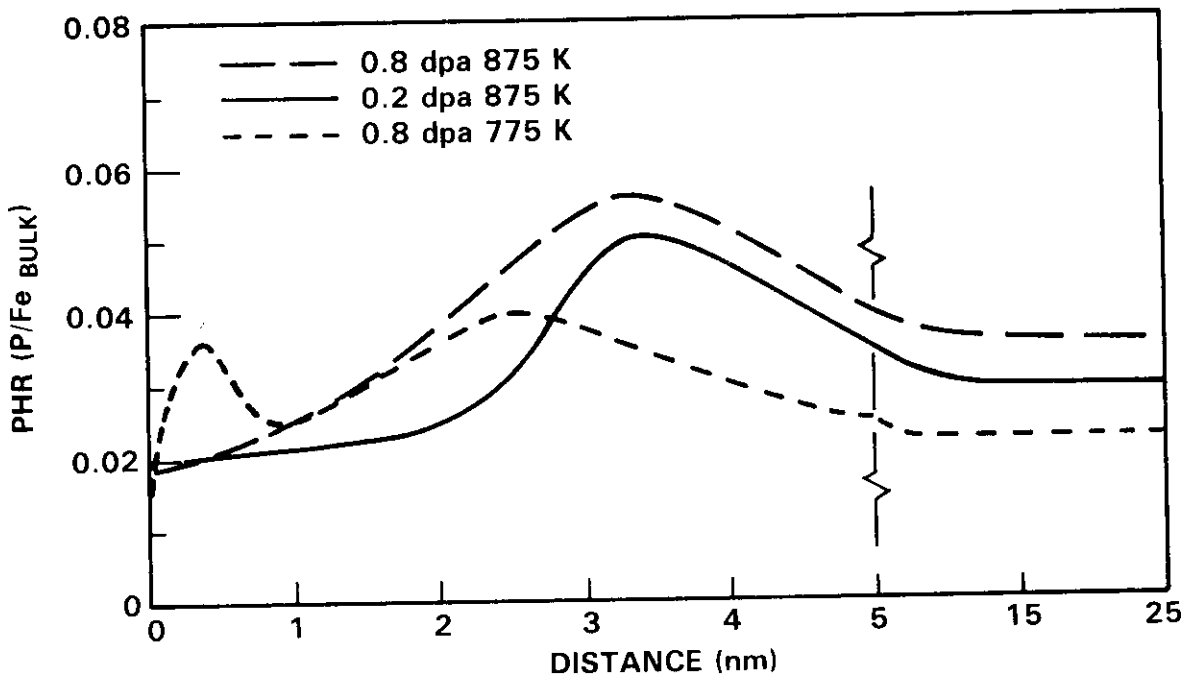


FIGURE 5. Concentration (PHR) of Phosphorus as a Function of Distance from the Surface in Fe+0.1 at.%P, Ion Irradiated Under Several Dose and Temperature Conditions.

The AES data for phosphorus in all of the ferritic alloys was not much above background levels. Even the Fe+0.1 at.%P alloy which had considerably more phosphorus than the 316 SS showed much less segregation than in the stainless steel. It was, therefore, not possible to establish any definitive trends as to dose or temperature dependence or effect of bulk phosphorus concentration on the radiation induced segregation behavior in the ferritic alloys.

## 5.4 References


1. J. L. Brimhall and R. H. Jones, "Radiation Induced Segregation of Impurities to Grain Boundaries", DAFS Quarterly Report DOE/ER-0046/5 (1981). 114.

2. J. L. Brimhall, D. R. Baer and R. H. Jones, "Radiation Induced Segregation in Candidate Fusion Reactor Alloys", J.Nucl. Mat., 103 & 104 (1981) 1379.

3. J. L. Brimhall, D. R. Baer and R. H. Jones, "Effect of Radiation on Phosphorus Segregation", to be published in J. Nucl. Mat.

4. L. E. Rehn, "Surface Modification and Radiation Induced Segregation" in Metastable Materials Formation by Ion Implantation. North Holland, New York 1982, p. 17.


## 6.0 Future Work

Binary and ternary alloys will be irradiated to evaluate compositional effects such as that due to minor alloying elements. Specially prepared tensile specimens of 316SS with a gage thickness of ~130μm will be irradiated with high energy deuterons. These specimens will be treated so as to induce intergranular fracture upon deformation in the AES chamber. The extent of phosphorus segregation to the grain boundary region will be determined by AES analysis of the fractured surfaces.

# C H A P T E R  5

## CORRELATION METHODOLOGY

## THE DEVELOPMENT OF MODEL-BASED SWELLING EQUATIONS FOR FUSION DESIGN APPLICATIONS

R. E. Stoller and G. R. Odette (University of California, Santa Barbara)*

### 1.0 Objective

The objective of this work is to develop a model-based design equation for the swelling of 20% cold worked AISI 316 Stainless Steel.

### 2.0 Summary

The predictions of a rate theory swelling model, calibrated to fission reactor data, have been used to develop preliminary design equations for the swelling of 20% cold worked AISI 316 Stainless Steel in a fusion reactor first wall. These equations complement two empirical equations which have been developed elsewhere, based on data from either mixed or fast spectrum irradiation environments. These equations describe the fluence and temperature dependence of the predicted swelling in a simple analytic form. The new equations are compared with the earlier data-based equations.

### 3.0 Program

Title: Damage Analysis and Fundamental Studies for Fusion Reactor Materials Development

Principle Investigators: G. R. Odette and G. E. Lucas

Affiliation: University of California, Santa Barbara

### 4.0 Relevant DAFS Program Plan Task/Subtask

Subtask C Correlation Methodology; Effects of Helium on Microstructure

---

*Support for one of the authors (Stoller) is provided by the DOE Magnetic Fusion Energy Technology Fellowship Program, administered by the Oak Ridge Associated Universities, Oak Ridge, Tennessee.

## 5.0 Accomplishments and Status

### 5.1 Introduction

The design of near term fusion test facilities and first generation reactors required extensive use of the radiation effects data obtained from fission reactor irradiations. Since the fusion neutron environment will be quite different from that found in fission reactors[1], purely empirical design equations will be subject to considerable uncertainty. One potentially important factor is that the helium generation rate for 316 stainless steel will be ∿ 30 times greater in a fusion reactor spectrum than in a typical fast reactor spectrum (e.g., the Experimental Breeder Reactor-II, EBR-II) (∿ 10 appm He/dpa vs. ∿ 0.3 appm he/dpa)[1]. The influence of the high helium level has not yet been determined[2-5]. However, a comparison of very limited data from both the High Flux Isotope Reactor (HFIR), which produces a high He/dpa ratio[1,6], and EBR-II for one heat of cold-worked stainless steel suggests that helium may have a significant influence on some aspects of microstructural evolution[2,3]. Charged particle data also demonstrates a strong effect of helium in some circumstances[2]. Nevertheless, widely divergent conclusions concerning the influence of helium on microstructural evolution have been reached by various workers[3,4].

As a result of these differing analyses, two design equations for the swelling of 20% cold worked 316 Stainless Steel have been proposed[7,8]. One of these equations emphasizes the results of HFIR irradiation experiments[7] while the other is primarily based on the extensive breeder program data base for this material[8]. Depending upon the fluence and temperature of interest, the two equations can predict widely varying swellings.

As a complement to these data-based equations, the predictions of a rate theory model of cavity swelling have been used to develop three additional swelling equations, based on systematic modifications of models calibrated to the fission reactor swelling behavior.

## 5.2 Theoretical Model

### 5.2.1 Model Description

The details of the model have been described previously[9,10]. The important elements of the model are as follows:

1. Calculation of point defect concentrations using standard conservation equations and observed or hypothesized temperature dependent sink densities (dislocations, cavities, subgrains, and transient vacancy clusters). Interstitial bias is assigned only to the dislocations.
2. Helium is partitioned to the various extended defects based on their relative sink strength. Dislocations act as helium trapping sites/collectors for bubbles. For temperatures greater than 400°C, precipitates act as helium collectors for precipitate associated bubbles and voids.
3. Void nucleation results from the growth of small helium stabilized bubbles to a critical size. The critical size is reduced for precipitate associated bubbles[9,10].
4. Bias driven void growth.

### 5.2.2 Model Predictions

The model was primarily calibrated using a set of swelling data from the so-called first core steels[11]. These data were chosen because they represent a fairly well characterized set of experiments on similar heats over a broad temperature and fluence range. A secondary calibration requirement was that the model predict a bifurcation of bias driven void to bubble and/or dislocation dominated to cavity sink dominated cavity growth mechanism in roughly the range of the dpa and microstructure observed in the HFIR irradiations. The calibration of the model has also been previously described elsewhere in more detail[9,10].

The results of the model calibration are shown in Figure 1. The trend band for the first core data is shown as a grey-hatched region; reasonable agreement has been obtained in the temperature and fluence range of interest.

### 5.2.3 Extrapolation of Model to Fusion Conditions

The most systematically observed trend in the data which deals with helium effects is the tendency toward increased cavity densities at higher helium levels[2,5]. Hence, in this work we have focused on this effect. The correlation between cavity density ($N_c$) and helium generation can be given approximately as:

$$N_c(G^i_{He}) \approx N_c(G^f_{He})\left[\frac{G^f_{He}}{G^f_{He}}\right]^p \qquad (1)$$

where $G^f_{He}$ is the ratio of transmutant helium produced to displacement damage (He/dpa) in a fast breeder reactor. The exponent p is typically observed to be in the range of 0 to 1 and is often taken at a nominal value of .5. In an earlier report[10], we discussed in some detail the influence of p and the He/dpa ratio on the model's predictions for fusion.

Figure 2; a,b,c compare the fluence dependence of the model's swelling predictions for fusion with the breeder values at three temperatures and three values of p. Reference to these figures indicates that below 650°C the predicted swelling for fusion is significantly greater than for breeder conditions independent of the value of p chosen. In developing the design equations we have chosen values of p = 0.2, 0.5, and 0.8, yielding low, intermediate and high cavity densities, respectively. This attempts to set crude mechanistic limits on the predictions.

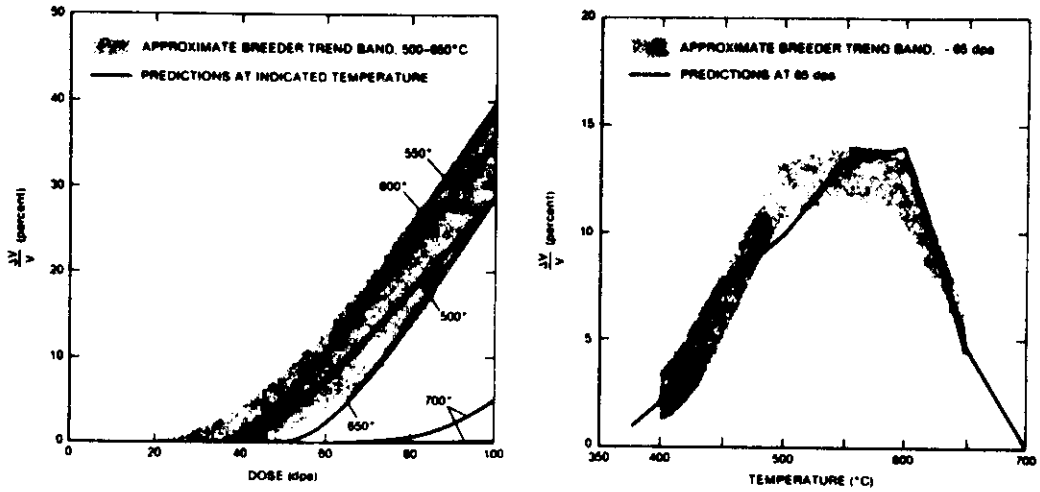


FIGURE 1. Results of Model Calibration. Predicted and observed fluence and temperature dependence of swelling for fast reactor conditions.

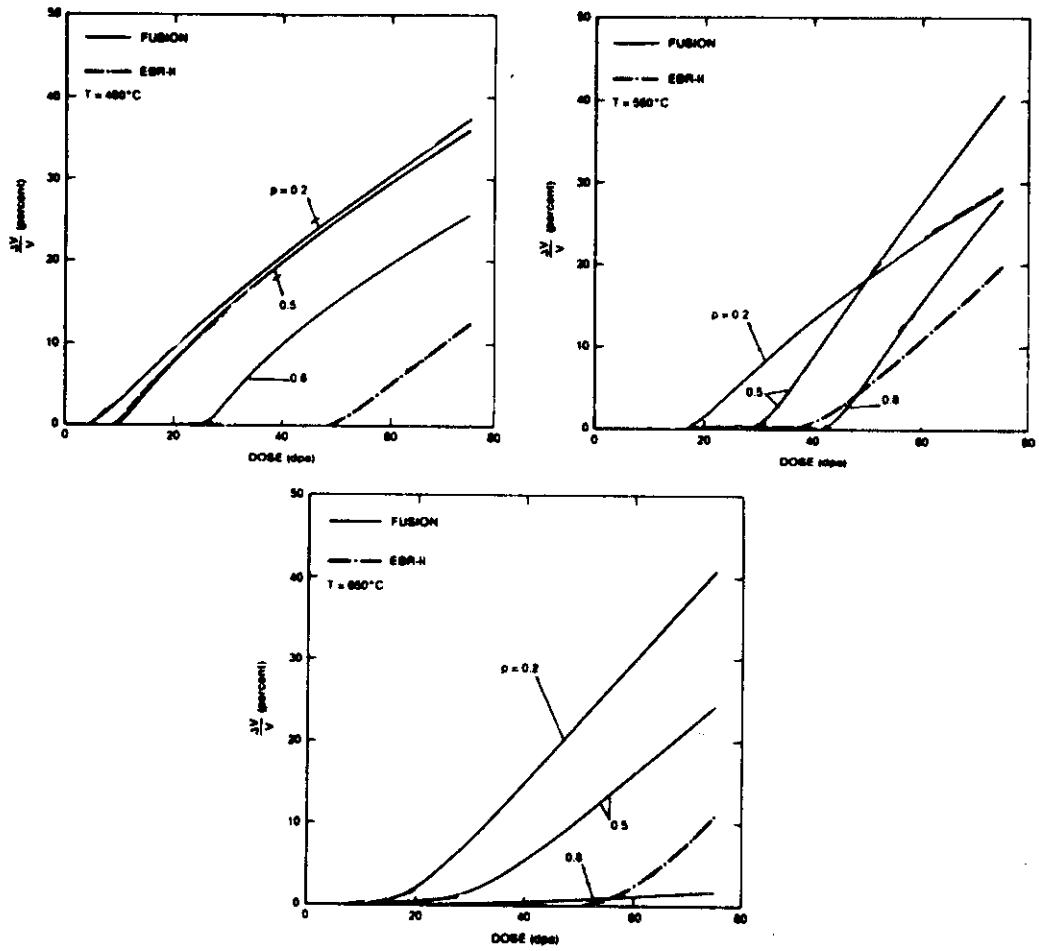


FIGURE 2. Predicted Fluence Dependence of Swelling for Fusion at Indicated Temperatures and Values of the Cavity Scaling Exponent p. Swelling under fast reactor conditions is also plotted for comparison.

## 5.3 Development of Design Equations

For temperatures up to 600°C and doses to 100 dpa, we have fit the predicted swelling values, S, using a function of the following form:

$$S(T,d) = A(T)(d-\tau(T)) - B(T)(d-\tau(T))^a \quad \text{for } d > \tau \qquad (2)$$

where T is the irradiation temperature (°C), d is the dose (dpa) and A, B, and $\tau$ are temperature dependent fit parameters. The parameter A is approximately equal to the predicted maximum swelling rate and $\tau$ corresponds to the 1% swelling dose. A value of the exponent a = 1.25 is required to yield the proper curvature in the swelling curves.

Best fit values of A, B, and $\tau$ were computed using a nonlinear least squares regression program for each of the three values of p. Individual fits for A, B, and $\tau$ as a function of temperature were then obtained in each case. These functions are given below in Equations 3-5.

For the p = 0.2 case:

$$A(T) = 1.285 \exp\left[-\frac{(T-500)^2}{8100}\right] + 0.80 \exp\left[-\frac{(T-615)^2}{500}\right] + 0.09 \exp\left[-\frac{(T-380)^2}{2000}\right] \qquad (3a)$$

$$B(T) = 0.225 \exp\left[-\frac{(T-500)^2}{5300}\right] \qquad (3b)$$

$$\tau(T) = 5.88 + \exp\left[-\frac{(T-250^{\,2}}{7250}\right] + \text{amax1}\left[0.0, 19.0 \tanh\left[\frac{(T-500)}{45}\right]\right]^* \qquad (3c)$$

For the p = 0.5 case:

$$A(T) = 1.08 \exp\left[-\frac{(T-450)^2}{6500}\right] + 1.12 \exp\left[-\frac{(T-555)^2}{3550}\right]$$

$$+ 0.04 \exp\left[-\frac{(T-400)^2}{500}\right] \quad (4a)$$

$$B(T) = 0.235 \exp\left[-\frac{(T-485)^2}{7400}\right] + 0.035 \exp\left[-\frac{(T-400)^2}{900}\right]$$

$$+ 0.04 \exp\left[-\frac{(T-540)^2}{1000}\right] \quad (4b)$$

$$\tau(T) = 8.5 + 16.5 \exp\left[-\frac{(T-300)^2}{8700}\right] + 24.5 \exp\left[-\frac{(T-558)^2}{2100}\right] \quad (4c)$$

For the p = 0.8 case:

$$A(T) = 1.07 \exp\left[-\frac{(T-426)^2}{5050}\right] + 1.30 \exp\left[-\frac{(T-550)^2}{1250}\right]$$

$$+ 1.40 \exp\left[-\frac{(T-550)^2}{1450}\right] \quad (5a)$$

$$B(T) = 0.20 \exp\left[-\frac{(T-430)^2}{5200}\right] + 0.22 \exp\left[-\frac{(T-505)^2}{1900}\right]$$

$$+ 0.20 \exp\left[-\frac{(T-555)^2}{1200}\right]$$

$$+ \text{amax1}\,[0.0,\ 3.1 \times 10^{-3}(550-T)]^* \quad (5b)$$

---

*The amax1 functions tuncates the indicated terms if they are less than zero.

$$\tau(T) = 53.0 \exp\left[-\frac{(T-342)^2}{4800}\right] + 42.5 \exp\left[-\frac{(T-500)^2}{4500}\right]; \; T < 500°C$$

$$= 42.8 + 7.0 \times 10^{-4} (T-500)^2; \; T \geq 500°C \qquad (5c)$$

The model-based design equation is compared with the two data based equations in Figure 3. In the case of the HFIR-based equation, a 50°C temperature shift has been applied in plotting the results since this equation was developed prior to the discovery that the actual irradiation temperatures in the HFIR were systematically higher then had been earlier reported[12,13]. The curve shown for the breeder-based equation does not include the helium bubble contribution which the authors recommend including[8]; this term would yield a small amount of swelling at low temperature (< 0.5% at 100 dpa and 300°C).

With the exception of the HFIR-based results at low temperatures, the model's predictions at the fusion He/dpa ratio tend to exceed the values predicted by the empirical equations. Earlier reports[2,9] have discussed the results of dual ion irradiation experiments as well theoretical work which suggests that cavity swelling may not be a monotonic function of the He/dpa ratio; indeed, the results shown in Reference 9 predict peak swelling near the fusion He/dpa ratio nearly independent of the assumption one makes regarding cavity density scaling (value of p). The major predicted effect of higher helium levels is to reduce the incubation time (or increase the low exposure swelling) and to extend the high swelling regime down to lower temperatures. Notably, the total swelling is predicted to be relatively insensitive to temperature from about 400 to 600°C at high exposures.

## 5.4 Conclusion

It is important to recognize the limitations of these correlations. In particular, a number of assumptions used in the theoretical extrapolation have not been empirically verified; clearly, any fine structure in the model

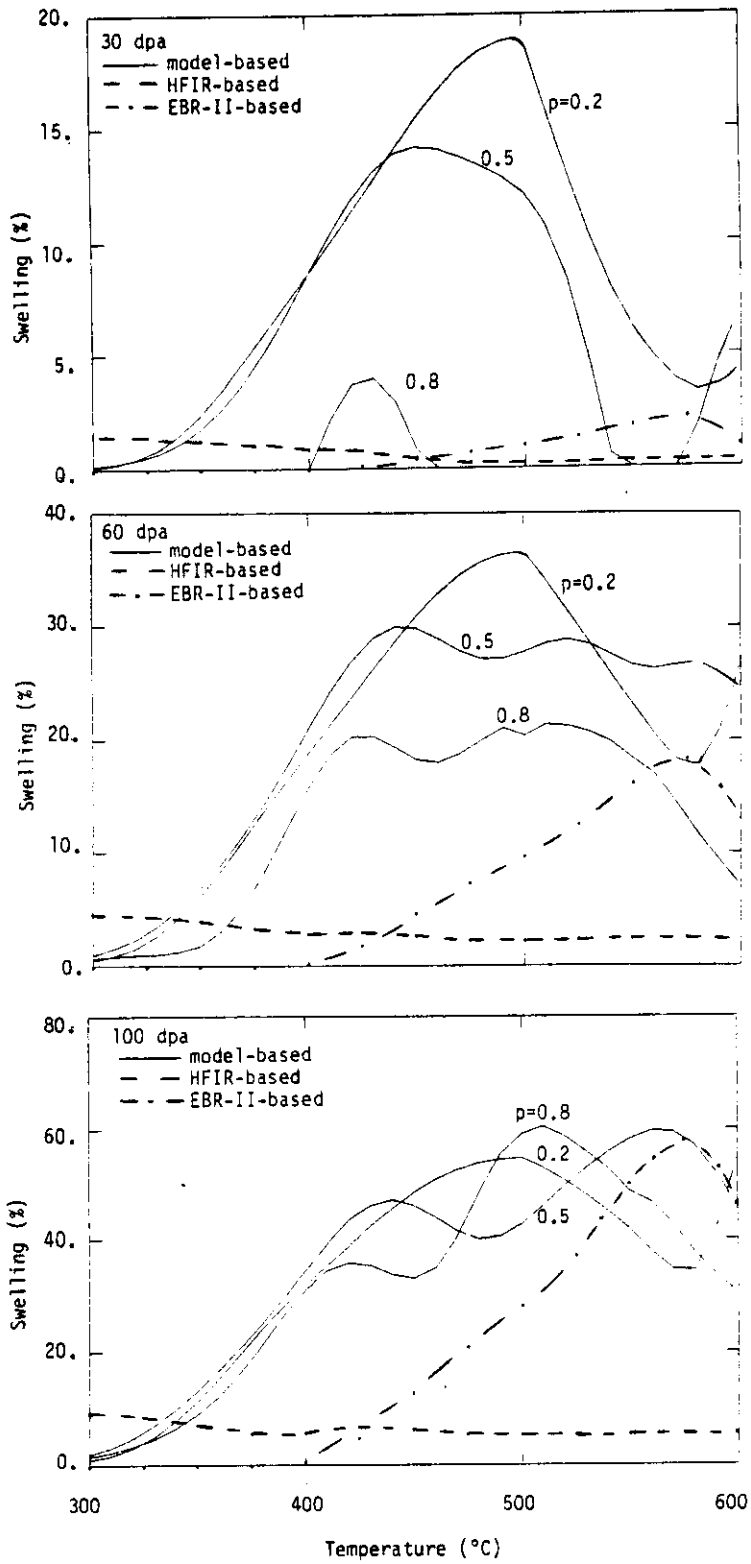


FIGURE 3. Comparison of Predicted Swelling for Fusion Using Three Different Design Equations.

predictions (absolute swelling levels, variations of swelling over small temperature ranges, etc) cannot be considered to be reliable. Nevertheless, we believe that the broad trends predicted (e.g., reduced incubation times) may be significant since they are based on well established mechanisms and thermodynamic/kinetic principles.

The swelling equations which have been developed are most appropriate for use in fusion reactor design studies which require simple analytical expressions for property changes as a function of temperature and irradiation dose. If used to complement empirical design equations based on fission reactor data, these results should aid in an evaluation of the relative importance of swelling in potential fusion reactor designs. Taken together, they provide reasonable the best available bounds on the swelling behavior of 20% cold worked 316 stainless steel in a fusion reactor.

## 6.0 References


1. Kulcinski, G. L., Doran, D. G., and Abdow, M. A., ASTM STP-570, 1974, pp. 329-350.

2. Odette, G. R., Maziasz, P. J., and Spitznagel, J. A., J. Nuc. Mat., Vol. 103-104, 1981, pp. 1289-1303.

3. Maziasz, P. J., and Grossbeck, M. L., ibid, pp. 987-992.

4. Brager, H. R., and Garner, F. A., ibid, pp. 993-998.

5. Fanell, K., Radiation Effects, Vol. 53, 1980, pp. 175-194.

6. Simons, R. L., ASTM STP-683, 1978, pp. 365-379.

7. Maziasz, P. J., and Grossbeck, M. L., Alloy Development for Irradiation Performance, Quarterly Progress Report, DOE/ER-0045/7, 3/82.

8. Garner, F. A., Maziasz, P. J., and Wolfer, W. G., Damage Analysis and Fundamental Studies (DAFS), Quarterly Progress Report, DOE/ER-0046/6, 8/81.

9. Stoller, R. E., and Odette, G. R., ASTM STP-782, 1982, pp. 275-294.

10. Stoller, R. E., and Odette, G. R., DAFS Quarterly Progress Report.

11. Bates, J. F., and Korenko, M. K., Nucl. Tech., Vol. 48, 1980, pp. 303-314.

12. Yang, W. J. S., and Garner, F. A., ASTM STP-782, 1982, pp. 196-206.

13. Maziasz, P. J., and Grossbeck, M. L., ADIP Quarterly Progress Report, DOE/ER-0045/6, 12181.

## 7. Future Work

These equations will be updated as improved models are developed and additional data for calibrating such models becomes available.

## BIAS IN FERRITIC AND AUSTENITIC ALLOYS

J.J. Sniegowski and W.G. Wolfer (University of Wisconsin)

### 1.0 Objective

Explore the causes and nature of the swelling resistance of ferritic alloys in comparison to austenitic alloys.

### 2.0 Summary

The swelling behavior of austenitic and ferritic alloys is briefly reviewed and the hypothesis is advanced that a fundamental difference exists between these two alloy classes which originates from the difference in the net bias. Since the net bias depends most critically on the relaxation volumes of interstitials and vacancies, experimental and theoretical values are discussed and reviewed. It is shown that the interstitial relaxation volume for fcc metals is almost twice as large as its value for bcc metals, whereas the reverse is true for the vacancy relaxation volume.

In order to obtain the net bias, the bias factors of voids and dislocations for both interstitial and vacancy capture are required. Equations are given for these bias factors and the net bias is computed. If the relaxation volumes for interstitials and vacancies are 1.8 $\Omega$ and -0.1 $\Omega$ in austenitic steels, and 1.1 $\Omega$ and -0.5 $\Omega$ in ferritic steels, respectively, it is found that the net bias is smaller by about a factor of four in ferritic steels as compared to austenitic steels. We show that with the obtained value of the net bias in austenitic steels, an upper swelling rate of about 1.4%/dpa is expected. This compares favorably with the empirical value of about 1%/dpa.

### 3.0 Program

Title: Effect of Radiation and High Heat Flux on the Performance of First Wall Components

Principal Investigator: W.G. Wolfer
Affiliation: University of Wisconsin-Madison

## 4.0 Relevant DAFS Program Task/Subtask

Task II.C.2 Effects of Helium on Microstructure
Subtask C Correlation Methodology

## 5.0 Status and Accomplishments

### 5.1 Introduction

The experimental evidence on swelling in ferritic and austenitic alloys as shown in Fig. 1 suggests that there is a fundamental difference between the two classes of alloys with regard to their propensity for void formation under irradiation. Whereas the latter class exhibits, after an initial stable period of low swelling, a steady state swelling rate on the order of 1%/dpa, the former class has either a much longer stable period, a much lower rate for steady-state swelling, or both. Unfortunately, the experimental data accumulated so far for ferritic alloys allow only one unambiguous conclusion to be drawn: namely that the initial stable period is long in comparison to most austenitic alloys. Although there still exists the possibility that ferritic alloys may eventually swell at a similar rate we like to present theoretical arguments which indicate that the basic driving force for both void nucleation and growth is substantially different in the two alloy classes. The difference originates at a fundamental level in connection with the relaxation volumes of self-interstitials and vacancies. Whereas in face-centered cubic metals the relaxation volume of an interstitial is large and that of a vacancy small, the body-centered cubic metals have smaller interstitial relaxation volumes but larger vacancy relaxation volumes. This results in a large net bias for the fcc metals but a small one for bcc metals. Accordingly, we suggest that this is one of the fundamental causes for the greater swelling

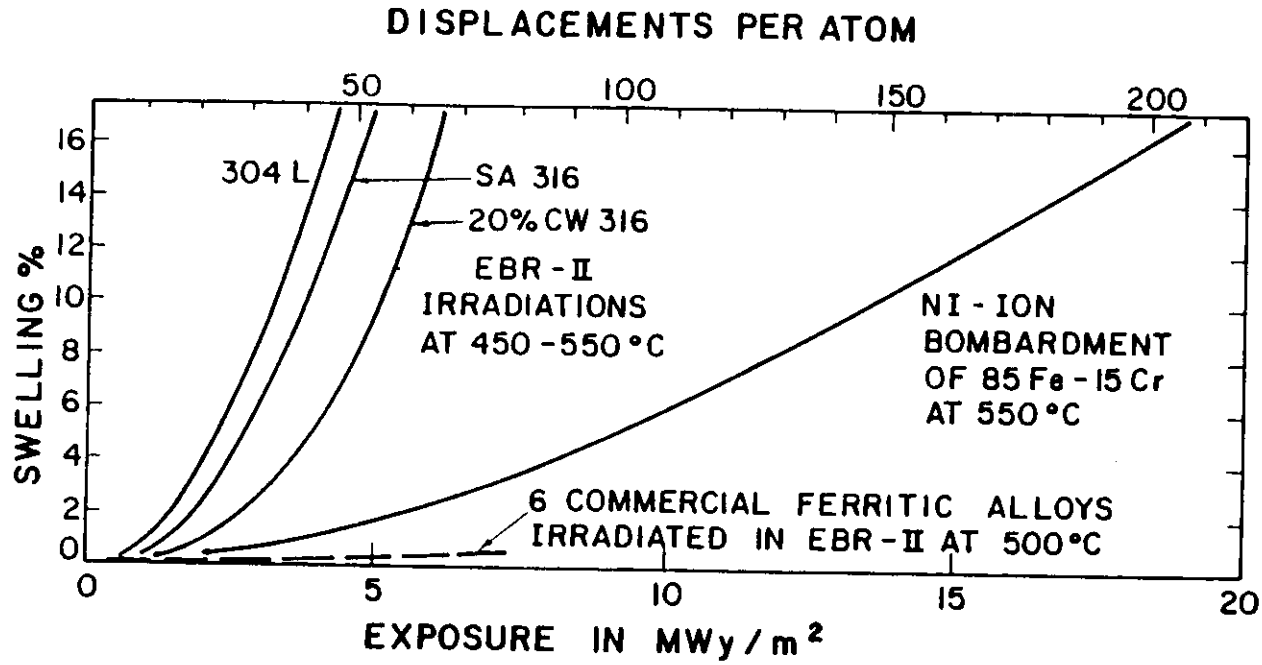


FIGURE 1. Comparison of Swelling for Austenitic and Ferritic Alloys Based on the Following Sources; 304 L -- swelling in annealed fuel capsules, Garner & Porter[1]; SA 316 and 20% CW 316 -- DO-heat irradiated in EBR-II and HFIR, Maziazs & Grossbeck[2], Brager & Garner[3]; 85 Fe-15 Cr -- Johnston, Lauritzen, Rosolowski & Turkalo[4]; ferritic alloys -- Powell, Peterson, Zimmerschied & Bates[5].

resistance of bcc metals and alloys in general, and of ferritic alloys in particular.

We realize of course that there are other fundamental differences between the two crystal structures and their associated microstructures, and that these differences can further accentuate the dissimilarity in the swelling behavior. For example, martensitic and heat-treated steels contain very high densities of dislocations and boundaries in comparison to austenitic steels. As a result, point defect losses to these sinks are high in martensitic and many ferritic alloys. Furthermore, the friction stress for dislocation glide is also higher in bcc metals as compared to fcc metals, and this may result in a denser dislocation network produced during irradiation.

Other causes for the dissimilarity in swelling may arise from the precipitate structure. Due to the much lower solubility for interstitial elements in the ferrite phase and as a result of tempering and heat treatment, a high density of finely dispersed precipitate particles is often present in ferritic and tempered martensitic alloys. These precipitates may provide a high density of recombination sites. With all these factors compounded, the substantial difference in the swelling behavior of austenitic and ferritic alloys should not be unexpected.

Many of the microstructural differences mentioned above may not be stable under irradiation at elevated temperatures. For example, the high dislocation density in martensitic steels may eventually recover. The small carbide precipitates may be dissolved by high-energy collision cascades, and a coarser precipitate structure may form after prolonged irradiation. At temperatures around 400°C and higher, tempering of martensite eventually results in the formation of equi-axed ferrite grains. Therefore, at these elevated temperatures, the high sink density provided by the initial martensite boundaries may eventually be lost.

Therefore, the ultimate swelling resistance of all ferritic and martensitic alloys may in the final analysis depend only on the net bias. We consider its value of the utmost importance.

For its evaluation in the following sections, the relaxation volumes of the self-interstitial and the vacancy are required. The experimental and theoretical results obtained for these volumes are reviewed in Section 5.2. Since the net bias depends on differences in bias factors for dislocations and voids, these factors and their determination will be reviewed in Section 5.3. Finally, numerical results for the net bias are presented in Section 5.4 as a function of the point defect relaxation volumes.

## 5.2 Relaxation Volumes of Point Defects

The formation of point defects is accompanied by volume changes of the crystal lattice. These volume changes determine, at least to first order, the strength of the interaction with stress fields. By way of introducing the following notation, the definitions for different volumes associated with point defects are recapitulated.

A vacancy can be thought of as having been created by removing an atom from a regular lattice site and by depositing it on an external surface, a grain boundary, or into the core of an edge dislocation. The volume change connected with this process is referred to as the vacancy formation volume

$$\Delta V_v^f = v_v^f + \Omega \ , \tag{1}$$

where $\Omega$ is the atomic volume and $v_v^f$ is the relaxation volume of the vacancy in its stable configuration. When the vacancy diffuses, the lowest possible activation energy for migration is realized in the saddle-point configuration for which the volume change is denoted by

$$\Delta V_v^s = v_v^s + \Omega = \Delta V_v^f + \Delta V_v^m \tag{2}$$

where $\Delta V_v^m$ is the activation volume for vacancy migration and $\Delta V_v^s$ is also referred to as the activation volume for self-diffusion. The latter can be determined experimentally by measuring the pressure dependence of the self-diffusion coefficient.

Formation and relaxation volumes for the self-interstitial are defined in an analogous manner. However, there occurs a change in sign when removing an atom from an external surface, a grain boundary, or from an edge dislocation core and inserting it interstitially into the lattice. Accordingly,

$$\Delta V_I^f = v_I^f - \Omega \tag{3}$$

and $$\Delta V_I^s = v_I^s - \Omega = \Delta V_I^f + \Delta V_I^m \ . \qquad (4)$$

The first-order interaction energy of a point defect with the hydrostatic stress field $\sigma_H(\vec{r})$ produced by a remote source is now given by $(-\sigma_H v)$ at all points in a solid except at locations which represent sinks or sources for point defects. At these points, the first-order interaction energy may be given by $(-\sigma_H \Delta V^f)$, depending on the sink type, its orientation with the applied stress, etc. For evaluating the equilibrium concentration of point defects and its dependence on stress, the interaction energy $(-\sigma_H \Delta V^f)$ is in general the relevant quantity. For bias calculations, however, the interaction energy $(-\sigma_H v^s)$ and the relaxation volume $v^s$ in the saddle-point are the appropriate quantities.

### 5.2.1 Relaxation Volumes for Self-Interstitials

Relaxation volumes for self-interstitials in their stable configuration, i.e. $v_I^f$, can be determined from diffuse x-ray scattering and lattice parameter measurements on single crystals irradiated at liquid helium temperatures. A recent review of the results obtained by these techniques is given by Ehrhart,[6] and his results are listed in Tables 1 and 2.

It is generally believed that the relaxation volume of the self-interstitial in the saddle-point is very close to its value in the stable configuration. Experimental support for this conclusion is provided by the field-ion microscopy work of Seidman et al.[7] According to these results, $\Delta V_I^m/\Omega < 0.03$ for Pt and $\Delta V_I^m/\Omega < 0.02$ for W.

The large values for the relaxation volume, $v_I^f$, in cubic metals can be rationalized in terms of the most efficient hard-sphere packing of the atoms which comprise the dumbbell interstitial and its next nearest neighbors. Based on this idea and Zener's approach to compute volume changes due to internal stresses, Wolfer[8] has developed a model for the relaxation volume of self-interstitials in cubic metals. Results of this model together with

TABLE 1

RELAXATION VOLUMES FOR SELF-INTERSTITIALS IN FCC METALS

| Metal | $(v_I^f/\Omega)_{th}$ | $(v_I^f/\Omega)_{exp}$ |
|---|---|---|
| Ag | 1.81 | --- |
| Al | 1.86 | 1.9 ± 0.3 |
| Au | 1.69 | --- |
| Ca | (1.49) | --- |
| Cu | 1.75 | 1.55 ± 0.2 |
| Ir | (2.26) | --- |
| Ni | 1.85 | 1.8 ± 0.3 |
| Pb | 1.63 | --- |
| Pd | 1.4 | --- |
| Pt | 1.9 | 1.8 ± 0.3 |
| Rh | (2.13) | --- |
| Sr | (1.41) | --- |
| Th | 1.75 | --- |
| Yb | (1.46) | --- |
| $Ni_3Fe$ | --- | 1.45 ± 0.3 |
| NiCu | --- | 1.6 ± 0.3 |

Values in parenthesis are based on estimates for the pressure derivative of the shear modulus.
Experimental values as given by Ehrhart.[6]

TABLE 2

RELAXATION VOLUMES FOR SELF-INTERSTITIALS IN BCC METALS

| Metals | $(v_I^f/\Omega)_{th}$ | $(v_I^f/\Omega)_{exp}$ |
|---|---|---|
| Cr | (0.88) | --- |
| Cs | (0.80) | --- |
| α-Fe | 0.91 | 1.1 ± 0.2 |
| K | 0.76 | --- |
| Li | 0.70 | --- |
| Mo | 0.85 | 1.1 ± 0.2 |
| Na | 0.76 | --- |
| Nb | 0.76 | --- |
| Rb | 0.75 | --- |
| Ta | 0.78 | --- |
| V | (0.77) | --- |
| W | 0.92 | --- |

Values in parenthesis are based on estimates for the pressure derivative of the shear modulus.
Experimental values as given by Ehrhart.[6]

the experimentally obtained values are listed in Tables 1 and 2 for fcc and bcc metals, respectively.

It is seen from Table 1 that the theoretical results are in good agreement with the experimentally measured values in the case of fcc metals, and that the interstitial relaxation volume is around 1.8 $\Omega$.

For bcc metals, the results in Table 2 show that the relaxation volume is smaller by almost a factor of two. The theoretical values are close to the lower bound of the experimental range for the two metals where a comparison can be made, namely $\alpha$-Fe and Mo.

### 5.2.2 Relaxation Volumes for Vacancies

Although the activation volume $\Delta V_v^s$ for self-diffusion can be simply determined by measuring self-diffusion as a function of pressure, there are only a few measurements available as compiled recently by Peterson[9] for pure metals. Experimentally determined values for the vacancy formation volume, $\Delta V_v^f$, are equally few in number, and they have recently been reviewed by Ehrhart.[6] Table 3 provides a list of these values together with two additional parameters for fcc binary alloys of iron and nickel. The range of values for the Fe-Ni alloys are due to Goldstein et al.,[10] whereas the value for the ordered alloy $Ni_3Fe$ is due to Ehrhart.[6] It is reassuring to see that the formation and the activation volumes for the alloys are quite similar to the values in the pure metals of the same structure. Furthermore, the formation and the activation volumes are comparable in magnitude, implying that in fcc metals and alloys, $|\Delta V_v^m/\Omega|$ is on the order of 0.1.

Unfortunately, no clear trend seems to emerge yet for the bcc metals except that the alkali metals exhibit low values for activation volume $\Delta V_v^s/\Omega$. Let us therefore consider a theoretical approach to evaluate $\Delta V_v^s/\Omega$.

TABLE 3

MEASURED VOLUMES ASSOCIATED WITH VACANCIES IN FCC AND BCC METALS

| Metal | $\Delta V_v^s/\Omega$ | $\Delta V_v^f/\Omega$ |
|---|---|---|
| Ag | 0.9 | 0.95 |
| Al | 0.71, 1.3 | --- |
| Au | 0.72 | 0.85 |
| Cu | 0.9 | 0.75 |
| Ni | --- | 0.8 |
| Pb | 0.73 | --- |
| Pt | --- | 0.8 |
| Fe-Ni | 0.86 to 0.96 | --- |
| $Ni_3Fe$ | --- | 0.85 |
| α-Fe | --- | ~ 0.75 |
| K | 0.57 | --- |
| Li | 0.28 | --- |
| Mo | --- | ~ 0.75 |
| Na | 0.32 to 0.59 | --- |

Sherby et al.[11] have proposed semi-empirical correlations for both the activation energy and volume for self-diffusion. According to their analysis, self-diffusion energies can be related to the melting temperature $T_M$ as

$$Q = kT_M(\kappa + \psi) \tag{5}$$

where k is the Boltzmann constant, $\kappa$ is a crystal structure factor ($\kappa$ = 14 for bcc, $\kappa$ = 17 for fcc) and $\psi$ is the valence of the element. For the activation volume, the relationship

$$\Delta V_v^s = k(\kappa + \psi)\Delta V_M/\Delta S_M \tag{6}$$

is obtained based on the assumption that the activated state of the saddle-point configuration forms a liquid-like cluster. Here $\Delta V_M$ and $\Delta S_M$ are the volume and the entropy change upon melting, respectively. Evaluating the activation volume with Eq. (6), Sherby et al.[11] conclude that $\Delta V_v^s/\Omega$ is about

0.8 for fcc crystals (except noble gases), 0.6 for hcp crystals, and 0.4 for bcc crystals.

We can combine Eqs. (5) and (6), obtain

$$\Delta V_v^S = (Q/T_M)(\Delta V_M/\Delta S_M) \tag{7}$$

and then use only experimental values to determine $\Delta V^S$. The activation energies, Q, were obtained from a recent compilation by Peterson,[9] and all other parameters are from the compilation by Turkdogan.[12] Melt volume changes for $\gamma$-Fe were obtained by extrapolating the temperature dependence of the molar volume[13] for $\gamma$-Fe up to the melting point. For the bcc metals Cr, Mo, Nb, and W no melt volume changes are available, and an average value of 4% was assumed in this case. Several metals exhibit different activation energies for self-diffusion for low and for high temperatures.[9] Therefore, Eq. (7) is evaluated for both values. The various parameters used and the results are shown in Table 4 separated into groups of fcc and bcc metals.

With the exceptions of Ag and Li, the computed values for $\Delta V_v^S/\Omega$ are in fair agreement with the measured values. The computed value of the activation volume for $\delta$-Fe is less than the value of 0.95 estimated by Ehrhart for $\Delta V_v^f$ from the experimental result for $\alpha$-Fe. The computed value of 0.55 for $\Delta V_v^S$ in Mo is also smaller than the measured range for $\Delta V_v^f$. Although this comparison is questionable because of the uncertain nature of Eq. (7), the following trends are suggested:

$\Delta V_v^S$ for bcc crystals is indeed somewhat less than the corresponding value in fcc crystals, although the difference is not always as large as Sherby et al.[11] claimed. The alkali metals do have low values of $\Delta V_v^S$ but they may not be representative of other bcc metals. Based on the only two cases available, the computed values for $\Delta V_v^S$ are smaller than the values for $\Delta V_v^f$ as estimated from experimental results[6] for the bcc metals $\alpha$-Fe and Mo. It then appears possible that for bcc metals $\Delta V_v^S < \Delta V_v^f$, and a large negative relaxation volume

TABLE 4

COMPUTED ACTIVATION VOLUMES FOR SELF-DIFFUSION IN FCC AND BCC METALS

| Metal | $T_M$ (°K) | $\Delta S_M$ (cal/mol) | $\Delta V_M/\Omega$ (%) | Q (kcal/mol) | $\Delta V_V^S/\Omega$ |
|---|---|---|---|---|---|
| Ag | 1234 | 2.19 | 3.405 | 40.6 | 0.51 |
| | | | | 50.5 | 0.64 |
| Al | 933 | 2.76 | 6.99 | 29.5 | 0.80 |
| | | | | 36.3 | 0.99 |
| Au | 1336 | 2.25 | 5.48 | 40.6 | 0.74 |
| | | | | 54.6 | 1.00 |
| Cu | 1356 | 2.3 | 3.94 | 47.7 | 0.60 |
| | | | | 59.7 | 0.75 |
| γ-Fe | (1809) | 1.82 | 4.737 | 67.86 | 0.98 |
| Ni | 1726 | 2.42 | 6.33 | 66.4 | 1.01 |
| | | | | 85.3 | 1.29 |
| Pb | 601 | 1.91 | 3.80 | 26.1 | 0.86 |
| Pt | 2042 | 2.3 | 6.61 | 68.2 | 0.96 |
| Cr | 2130 | 1.9 | (4.0) | 73.7 | (0.73) |
| δ-Fe | 1809 | 1.82 | 3.92 | 56.9 | 0.68 |
| K | 336 | 1.66 | 2.54 | 9.75 | 0.44 |
| Li | 381 | 1.58 | 2.78 | 12.0 | 0.56 |
| | | | | 15.9 | 0.74 |
| Mo | 2903 | 2.3 | (4.0) | 92.2 | (0.55) |
| Na | 370 | 1.67 | 3.25 | 8.41 | 0.44 |
| | | | | 10.60 | 0.56 |
| Nb | 2750 | 2.34 | (4.0) | 96.0 | (0.59) |
| W | 3673 | 2.3 | (4.0) | 153.0 | (0.72) |

as suggested by Sherby et al.[11] may be associated with the saddle-point configuration of the vacancy as a result of the more open bcc lattice structure.

## 5.3 Sink Bias Factors

Void nucleation as well as growth depends critically on the net bias. As shown by Si-Ahmed and Wolfer[14] this net bias for a void containing x vacancies can be defined as

$$B(x) = \frac{\langle Z_I \rangle}{\langle Z_v \rangle} - \frac{A_o(x) Z_I^o(x)}{A_o(x-1) Z_v^o(x-1)} \tag{8}$$

where $A_o(x)$ is the surface area of the void, and $Z_I^o(x)$ and $Z_v^o(x)$ are the void bias factors for interstitials and vacancies, respectively. The sink-averaged bias factors $\langle Z_I \rangle$ and $\langle Z_v \rangle$ can be assumed to be equal to the dislocation bias factors $Z_I^d$ and $Z_v^d$ if dislocations represent the predominant sink. For the early stage of nucleation this is certainly the case. For large vacancy clusters with $x > 10$ the difference between $A_o(x-1)$ and $A_o(x)$ and between $Z_v^o(x-1)$ and $Z_v^o(x)$ may be neglected, and we can define the net bias as

$$B(x) \cong \frac{Z_I^d}{Z_v^d} - \frac{Z_I^o(x)}{Z_v^o(x)} \tag{9}$$

which then agrees with the definition of the net bias for void growth.

### 5.3.1 Void Bias Factors

If U(r) represents the interaction energy of the point defect with the void, then the void bias factors can be computed from the following expression[14]

$$Z^o(a) = \{\int_0^1 d\left(\frac{a}{r}\right) \exp[U(r)/kT]\}^{-1} \tag{10}$$

for a void of radius a, where $a = (3\Omega x/4\pi)^{1/3}$. For voids without an associated segregation shell, the interaction energy is given by

$$U(r) = -\frac{r}{a^3}\left[\left(\frac{r}{a} - 1\right)^3 + \alpha_o\left(\frac{r}{a} - 1\right)^6\right]^{-1} + \frac{3\alpha^G}{8\mu^2}\frac{a^6}{r^6}\left(p - \frac{2\gamma}{a}\right)^2 . \tag{11}$$

Here, the first term represents the image interaction[15] with the void

surface, and it depends on the parameters

$$\Gamma = \mu v^2 \frac{(1 + \nu)^2}{36\,\pi(1 - \nu)}, \qquad \alpha_o = (7 - 5\nu)/30 \tag{12}$$

where $\mu$ is the shear modulus, $\gamma$ is the Poisson's ratio, and v is the relaxation volume of the point defect. The second term constitutes the modulus interaction,[16] and it depends on the shear polarizability $\alpha^G$ of the point defect and on the effective pressure $(p - 2\gamma/a)$ on the void surface. Here, p is the gas pressure in the void and $\gamma$ is the surface tension.

For very small voids with radii a approaching atomic dimensions, it can be shown that the far-field image interaction becomes equal to a modulus interaction of a vacancy with the stress field of a point defect. The vacancy is modeled in this context as an inhomogeneous inclusion whose bulk and shear moduli are zero. The shear polarizability of such a vacancy or void is given by

$$\alpha^G_{void} = -\mu \frac{4\pi}{3} a^3 \frac{15(1 - \nu)}{7 - 5\nu} \tag{13}$$

and its relaxation volume by

$$\delta V = \frac{4\pi}{3} a^3 \frac{9(1 - \nu)}{4\mu(1 + \nu)} \left(p - \frac{2\gamma}{a}\right). \tag{14}$$

Based on this interpretation, we may include the second term in Eq. (11) into the first term and write

$$U(r) \cong -\frac{\Gamma}{a^2} \left[\left(\frac{r}{a} - 1\right)^3 + \lambda'\left(\frac{r}{a} - 1\right)^6\right]^{-1} \tag{15}$$

where

$$\lambda = \alpha_o - \frac{\Gamma\, 8\, \mu^2}{a^3\, 3\alpha^G (p - 2\gamma/a)^2}. \tag{16}$$

The interaction energy U(r) varies strongly with the distance r from the void center. With increasing r, the variation is in fact proportional to $(a/r)^6$. Therefore, the factor exp[U/kT] in the integral of Eq. (10) is practically one

for large distances r. For short distances, however, U(r) assumes large negative values, and the integrand becomes zero. As a result we may use the following approximation

$$\int_0^1 d\left(\frac{a}{r}\right) \exp[U(r)/kT] \cong \int_0^{a/r_c} d\left(\frac{a}{r}\right) = \frac{a}{r_c} \tag{17}$$

where $r_c$ is defined as that distance for which

$$\exp[U(r_c)/kT] = \frac{1}{f} \tag{18}$$

where 1/f may be selected to be a number between the two extreme values 0 and 1 for the exponential. Equation (18) can be solved for $r_c/a$ which then according to Eq. (10) is equal to the void bias,

$$Z^o(a) \cong \frac{r_c}{a} = 1 + \left[\frac{\sqrt{1 + \eta} - 1}{2\lambda}\right]^{1/3} , \tag{19}$$

where

$$\eta = 4\lambda\Gamma/[a^3 kT \ln f] . \tag{20}$$

The void bias obtained with Eq. (19) compares very favorably with earlier results for which the integration in Eq. (10) was carried out numerically. Furthermore, the results of Eq. (19) are insensitive to the choice of the parameter f as long as (1/f) is not too close to either 0 or 1. Table 5 demonstrates this insensitivity to the choice of f for the void bias factor ratio of a "void" with radius equal to the Burger's vector. The reason for this insensitivity is that exp(U/kT) exhibits a very sharp transition from values close to one to very small values at $r \cong r_c$.

### 5.3.2 Dislocation Bias Factors

The interaction energy of point defects with edge dislocations has been treated extensively by Wolfer and Ashkin.[15] The dominant long-range size interaction is given by

TABLE 5

SENSITIVITY OF THE VOID BIAS* TO THE PARAMETER f

| f | 1.1 | 1.2 | 1.5 | 2.0 | 4 | 10 |
|---|---|---|---|---|---|---|
| $Z_I^o(b)/Z_v^o(b)$ | 1.734 | 1.743 | 1.742 | 1.730 | 1.697 | 1.660 |

*For 500°C, $v_I = 1.4\ \Omega$, $v_v = -0.2\ \Omega$, $\alpha_I^G = \alpha_v^G = 0$

$$U_1^d(r,\phi) = -B_o \cos\phi/r \tag{21}$$

where

$$B_o = v\,\frac{\mu b}{3\pi}\,\frac{1+\nu}{1-\nu} \tag{22}$$

and $\phi$ is the angle of the radius vector $\vec{r}$ with the normal vector of the glide plane. At short distances, the modulus interaction becomes dominant, and it is given by

$$U_2^d(r,\phi) = (A_o + A_2 \cos 2\phi)/r^2 \tag{23}$$

where

$$A_o = [\alpha^K(1-2\nu)^2 + \tfrac{4}{3}\,\alpha^G(1-\nu+\nu^2)]/4\pi(1-\nu)]^2 \tag{24}$$

and

$$A_2 = [(\alpha^K - \tfrac{2}{3}\,\alpha^G)(1-2\nu)^2 + 4\alpha^G\nu(1-\nu)]/[4\pi(1-\nu)]^2\ . \tag{25}$$

The bulk polarizabilites, $\alpha^K$, of point defects are small in comparison to the shear polarizabilities, and they have been neglected in the present study.

Using a Poisson's ratio of $\nu = 0.3$ one finds that

$$A_o = 0.0136\ \alpha^G$$
$$A_2 = 0.0094\ \alpha^G\ .$$

Therefore, $A_o$ is the dominant term, and the term $A_2 \cos 2\phi$ merely represents an angular modulation of the dominant attractive part of the modulus interaction. On average, we may therefore use the approximation

$$U_2^d(r,\phi) \cong A_0/r^2 \ . \tag{26}$$

To evaluate the dislocation bias factor, the crystal around an edge dislocation can be divided into three regions. In the core region $r < c$, the modulus interaction $U_2^d$ is so strong that its radial variation over a distance b exceeds the migration energy $E^m$ of the point defect; i.e.

$$b \frac{dU_2^d}{dr} > E^m \ . \tag{27}$$

The condition for equality then defines the capture radius c at which no further thermal activation is required for the point defect to migrate into the dislocation core region.

Next to the core region, there exists a region $c < r < d$, in which $U_2^d$ is still dominant. In the outermost region, the size interaction $U_1$ becomes dominant and $U_2^d$ can be neglected. However, since both interactions have an angular dependence, the radial distance d depends in fact on the angle.

In the present study, we have therefore selected the minimum distance d, which occurs in the direction where $U_1^d$ exhibits a maximum, i.e. for $\phi = \pm\pi/2$, depending on the sign of the relaxation volume v. Accordingly,

$$d = b^2|A_0 - A_2|/|B_0| \ . \tag{28}$$

By solving a steady-state diffusion equation in the two outer regions and matching the solutions approximately at $r = d$, the following equation is obtained for the dislocation bias factor:

$$Z^d = \ln (R/c)/(Q_1 - Q_2) \tag{29}$$

where 2R is the average distance between dislocation and

$$Q_1 = \frac{K_0(r_0/R)}{I_0(r_0/R)} - \frac{K_0(r_0/d)}{I_0(r_0/d)} \tag{30}$$

and $$Q_2 = \frac{1}{2} \exp(r_2^2/d^2)\ I_o^{-2}(r_o/d)[E_1(r_2^2/d^2) - E_1(r_2^2/c^2)] \ . \qquad (31)$$

Here $$r_o = |B_o/2kT| \ , \qquad (32)$$

$$r_2^2 = |A_o/kT| \ , \qquad (33)$$

$I_o(x)$ and $K_o(x)$ are the modified Bessel functions of zero-th order and $E_1(x)$ is the exponential integral.

## 5.4 Results

The bias factor formulae derived in the previous section have been numerically evaluated to obtain the net bias parameter of Eq. (9) for various void radii. The materials parameters used were those for nickel, and the point defect parameters were

$$\alpha_I^G = -2.4 \times 10^{-17} \text{ J} \ , \qquad \alpha_v^G = -2.4 \times 10^{-18} \text{ J}$$

$$v_I/\Omega = 0.7 \text{ to } 2.2 \ , \qquad v_v/\Omega = -0.5 \text{ to } -0.1 \ .$$

In order to simulate austenitic alloys, it was assumed that the shear polarizabilities are the same as those for nickel, whereas the relaxation volumes were assumed to be $v_I/\Omega = 1.8$ and $v_v/\Omega = -0.1$ in accordance with the results of Tables 1 and 3.

For ferritic alloys, it was assumed that $v_I/\Omega = 1.1$ and $v_v/\Omega = -0.5$. The difference in shear moduli, atomic volumes, and in Burger's vectors between austenitic and ferritic alloys was neglected in the present study, and the same surface energy of $\gamma = 1$ J/m$^2$ was selected for both materials. The net bias differences displayed in Fig. 2 is therefore entirely due to the differences in the relaxation volumes.

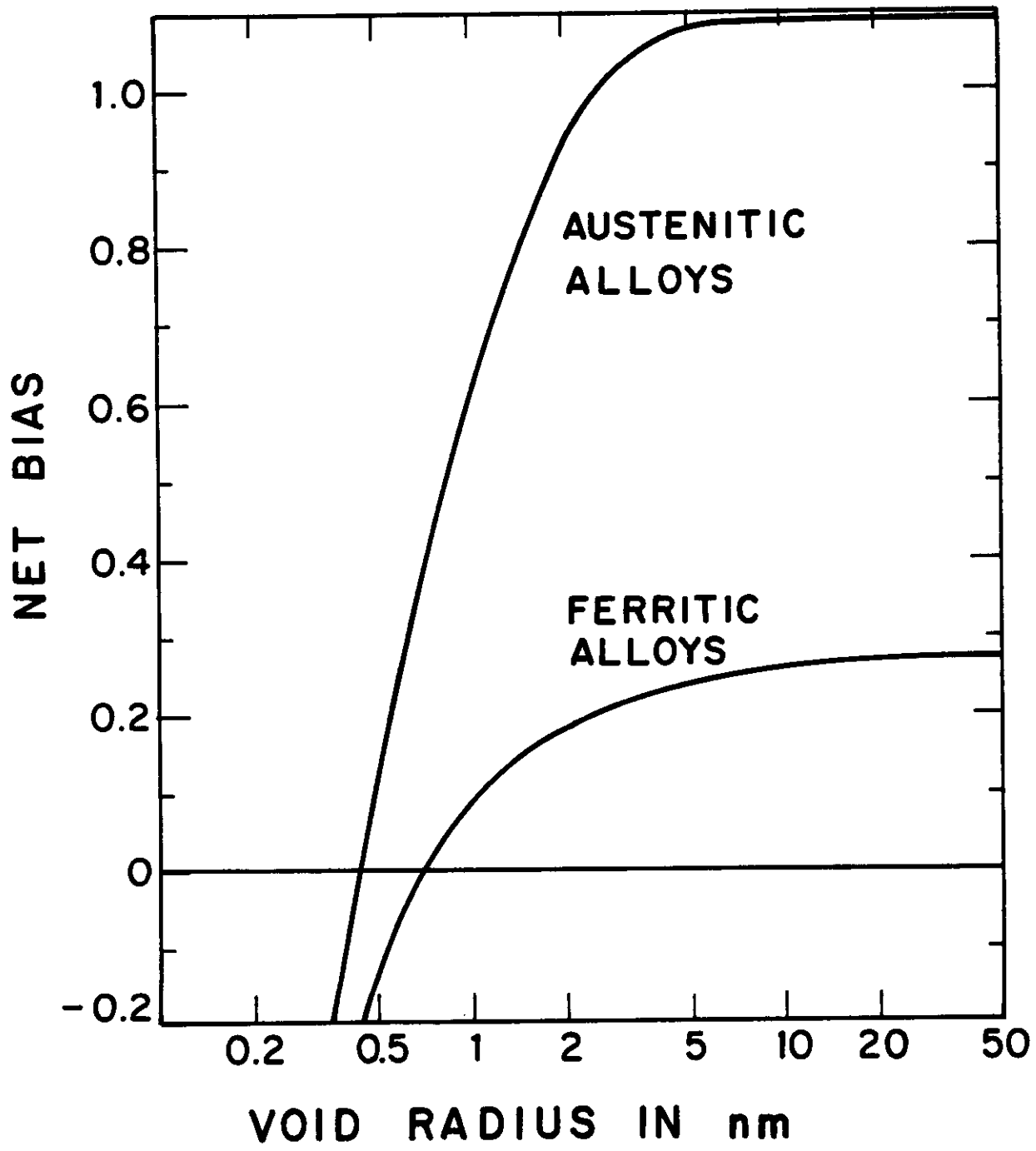


FIGURE 2. Net Bias for Voids in Austenitic and Ferritic Alloys.

The results in Fig. 2 demonstrate the following important findings. The net bias of small voids is negative, indicating a preferential absorption for interstitials even in the presence of dislocations. Therefore, for voids to nucleate, either segregation and/or internal gas pressure is required. For larger void sizes with diameters visible in the electron microscope, the net bias is positive and voids continue to grow. If a positive net bias of 0.2 is required for nucleation to occur, then ferritic alloys are seen to exhibit a much greater resistance than austenitic alloys for void nucleation.

For void diameters greater than 20 μm, the net bias reaches a constant value. This value is substantially larger in austenitic alloys as compared to ferritic alloys.

It may appear that a net bias of the order of one, as displayed in Fig. 2 for the austenitic alloys, is too large in comparison to previously reported values in the literature. Therefore, the corresponding steady-state swelling rate may appear to be excessive. However, as shown below, this is not the case.

In a previous contribution, Wolfer and Garner[16] have shown that the steady state swelling rate can be expressed as

$$\frac{d}{dt}\frac{\Delta V}{V} \cong \frac{S_o S_d}{(S_o + S_d)^2} B \cdot F \qquad (34)$$

where $S_o$ and $S_d$ are the sink strength of voids and dislocations respectively, and F is a function weakly dependent on temperature and total sink strength, but strongly dependent on the rate of point defect production, P, which can be written as

$$P = \beta \dot{D} \qquad (35)$$

where $\dot{D}$ is the displacement rate and $\beta$ is the fraction of point defects which survive in-cascade recombination and clustering. $\beta$ is of the order of 0.1.

We may now express the swelling rate in units of (%/dpa) and write Eq. (34) as

$$\frac{d(\Delta V/V\%)}{d(dpa)} = \frac{S_o S_d}{(S_o + S_d)^2} 100\ \beta B(F/P) \ . \tag{36}$$

As previously shown,[16] $F/P \leq 1/2$. Furthermore, the factor

$$\frac{S_o S_d}{(S_o + S_d)^2} \leq \frac{1}{4} \tag{37}$$

where the equal sign holds when the void sink strength equals the dislocation sink strength.

Using these upper bounds and the value $\beta = 0.1$ we find that

$$\frac{d(\Delta V/V\%)}{d(dpa)} \leq 1.25\ B\ (\%/dpa) \ . \tag{38}$$

Based on the net bias results of Fig. 2, we expect therefore that the swelling rate in austenitic alloys is less or equal to about 1.4 (%/dpa). This value is remarkably close to the empirical value of 1 (%/dpa) found for the steady-state swelling rate in type 304 and 316 stainless steels. Our present assessment of the steady-state swelling rate in ferritic steels indicates that it should be lower by a factor of four compared to the austenitic steels.

This assessment is based on a relaxation volume of $-0.5\ \Omega$ for the vacancy and $1.1\ \Omega$ for the interstitial. The latter value has an uncertainty of $\pm 0.2\ \Omega$, and it can therefore be considered as fairly reliable. The most uncertain parameter remains the vacancy relaxation volume for the saddle-point configuration in $\alpha$-Fe. If we had assumed that its value is the same for both the austenitic and the ferritic phase, namely equal to $-0.1\ \Omega$, then the steady-state swelling rate for the ferritic alloys would be expected to be between 55% and 70% of the swelling rate of austenitic alloys.

On the other hand, if we assume that the vacancy relaxation volume for vacancies is as low as -0.5 $\Omega$ and that the interstitial relaxation volume is equal to 0.9 $\Omega$, the computed value for $\alpha$-Fe according to Table 2, then the steady-state swelling rate for ferritic alloys is predicted to be only 10% of the one for austenitic alloys.

## 6.0 References


1. F.A. Garner and D.L. Porter, "Factors Influencing the Swelling of 300 Series Stainless Steels," DAFS Quarterly Progress Report DOE/ER-0046/9, May 1982, p. 170.

2. P.J. Maziasz and M.L. Grossbeck, J. Nucl. Matls., 103 & 104, 987 (1981).

3. H.R. Brager and F.A. Garner, J. Nucl. Matls., 103 & 104, 993 (1981).

4. W.G. Johnston, T. Lauritzen, J.H. Rosolowski, and A.M. Turkalo, "Void Swelling in Ferritic Alloys Bombarded with Nickel Ions," in Effects of Radiation on Materials, Proc. 11th Internat. Symp., Eds. H.R. Brager and J.S. Perrin, ASTM-STP-782, 809 (1982).

5. R.W. Powell, D.T. Peterson, M.Z. Zimmerschied, and J.F. Bates, J. Nucl. Matls., 103 & 104, 969 (1981).

6. P. Ehrhart, Conf. on Dimensional Stability and Mechanical Behaviour of Irradiated Metals and Alloys, BNES, London, 1983, paper P17.

7. D.N. Seidman, J. Phys. F: Met. Phys., 3, 393 (1973).

8. W.G. Wolfer, J. Phys. F: Met. Phys., 12, 425 (1982).

9. N.L. Peterson, J. Nucl. Matls., 69 & 70, 3 (1978).

10. J.I. Goldstein, R.E. Hanneman, R.E. Ogilvie, Trans. AIME, 223, 812 (1965).

11. O.D. Sherby, J.L. Robbins, and A. Goldberg, J. Appl. Phys., 41, 3961 (1970).

12. E.T. Turkdogan, Physical Chemistry of High Temperature Technology, Academic Press, New York, 1980, Table 1.2 and Table 3.5.

13. W. Hume-Rothery, The Structures of Alloys of Iron, Pergamon Press, Oxford, 1980, p. 22.

14. A. Si-Ahmed and W.G. Wolfer, "Effect of Radiation-Induced Segregation on Void Nucleation," in Effects of Radiation on Materials, Proc. 11th Internat. Symp., Eds. H.R. Brager and J.S. Perrin, ASTM-STP-782, 1008 (1982).

15. W.G. Wolfer and M. Ashkin, J. Appl. Phys., 47, 791 (1976).

16. W.G. Wolfer and F.A. Garner, "Temperature Dependence of the Swelling Rate in Austenitic Stainless Steels," DAFS Quarterly Progress Report DOE/ER-0046/12, Feb. 1983, p. 141.

## 7.0 Future Work

The bias factor evaluation will be refined to include differences in basic lattice properties, such as elastic moduli, Burger's vectors, and atomic volumes. Because of the large impact of the vacancy relaxation volume $v_f^s$ in bcc iron, a theoretical approach will be developed to more accurately compute this parameter.

## EFFECT OF BUBBLE RADIUS ON THE EQUATION OF STATE FOR GASES

M.F. Wehner and W.G. Wolfer (University of Wisconsin-Madison)

### 1.0 Objective

Curvature corrections are derived for the equation of state of gaseous helium. These corrections become important for small helium bubbles when the radius of the gas atom approaches a considerable fraction of the radius of curvature of the cavity wall.

### 2.0 Summary

The gas pressure derived from a thermodynamic equation of state is only equal to the gas-kinetic pressure exerted on a surface whose radius of curvature is very large compared with the radius of the gas molecules or atoms. For very small gas bubbles, curvature corrections are required. They are derived from a particle distribution function near a curved surface and from the pair distribution function. Using an approach developed by Shinomoto these functions are evaluated by an iterative procedure for a hard-sphere gas. It is found that the gas-kinetic pressure in small bubbles can be significantly larger than the pressure obtained from the thermodynamic equation of state. Graphical results are presented for this enhancement which depends both on the bubble radius and on the gas density.

### 3.0 Program

Title: Effects of Radiation and High Heat Flux on the Performance of First Wall Components

Principal Investigator: W.G. Wolfer

Affiliation: University of Wisconsin-Madison

## 4.0 Relevant DAFS Program Plan Task (Subtasks)

Task II.C.2 Effects of Helium on Microstructure
Subtask C Correlation Methodology

## 5.0 Accomplishment and Status

### 5.1 Introduction

The formation of helium bubbles in solids evolves through various stages, from the atomistic stage which is more aptly described in terms of helium-vacancy clusters, to the macroscopic stage of gas-filled cavities. For the latter case, the helium can be treated as a gas whose pressure is given by the macroscopic equation of state contained within a well-defined volume. In the atomistic stage, however, no precise volume can be defined and no meaningful pressure can be assigned to only a few helium atoms. Instead, it is necessary to describe this stage with molecular dynamics and realistic interatomic potentials. It is generally believed, that a macroscopic description for helium bubbles becomes adequate when the cluster contains hundreds of vacancies and a similarly large number of helium atoms. Clearly, this leaves a rather wide gap between atomistic clusters and macroscopic bubbles, providing apparently no valid description for the most important size class, namely the critical sizes for void and bubble nucleation. These critical sizes comprise clusters with ten to a hundred vacancies and a similar number of helium atoms.

In order to bridge this gap, it is most desirable to extend the range of the macroscopic description of bubbles to smaller sizes. If a significant extension can be made, it is perhaps possible to extrapolate it to atomistic clusters. A specific example of such an extrapolation will be given presently.

Several macroscopic concepts need to be carefully examined before extending them to atomistic cluster sizes: the surface tension of cavities and vacancy

clusters; the gas-kinetic pressure exerted by the gas atoms on the cavity wall; and the effective location of the cavity wall when the cavity radius becomes comparable to the range of the interatomic forces.

The concept of surface tension for small vacancy clusters has been examined recently by Si-Ahmed and Wolfer.[1] The energy of a vacancy cluster containing x vacancies is written as

$$E(x) = (4\pi)^{1/2}(3\Omega x)^{2/3}\gamma(x) \tag{1}$$

where $\Omega$ is the volume per atom and $\gamma(x)$ the surface energy assumed to depend on the cluster size. This expression (1) was then compared to results from computer simulations of vacancy clusters with $x > 10$ performed by Mruzik and Russell,[2] and it was found that $\gamma(x)$ exhibits a small decrease from its value for a flat surface as x decreased. In order to extrapolate this result to even smaller clusters, the computer simulation results of Doyama and Cotterill[3,4] were used. These results provide energies for mono-, di-, tri-, and tetravacancies in copper. Interpolation between these results and those by Mruzik and Russell[2] gave the approximate, but simple result that

$$\gamma(x) = \gamma_\infty\left(1 - \frac{8}{x + 0.2}\right) \tag{2}$$

This equation is approximate to the extent that the precise values of the energies of small vacancy clusters do not fall on a smooth, monotonic curve. The minor deviation from Eq. (2) reflect the simple fact that the number of broken bonds in forming small vacancy clusters also increases with x in a non-monotomic fashion. Nevertheless, Eq. (2) is not only adequate for void nucleation studies but also quite important. For example, if the approximation $\gamma(x) = \gamma_\infty$ were used for small clusters, the computed void nucleation rates would decrease by several orders of magnitude. This clearly indicates that macroscopic concepts applied to small defect clusters require careful examination.

In the present paper we derive an equation for the gas-kinetic pressure exerted on curved surfaces. The method, described in Section 5.2, is based on Shinomoto's approach[5] to obtain the pair distribution function for a hard-sphere gas. Numerical results are then presented in Section 5.3

## 5.2 Shinomoto's Theory for a Hard-Sphere Gas

Consider a gas of average atom density n consisting of hard-sphere particles of radius a. Let g(r) denote the radial distribution function defined in the usual manner[6] that $2\pi n g(r) r^2\, dr$ is the number of particles to be found between the radii r and r + dr from the center of any test particle. Instead of the radial distance r we may also use the distance x = r - a from the surface of the test particle to the centers of surrounding atoms, and we may write instead

$$g(r) = g_a(x) \tag{1}$$

If the test particle has now a different radius, say R, than all the other particles in the gas, we denote this radial distribution function by $g_R(x)$.

Shinomoto makes now the usual assumption[7] that the radial distribution function can be represented in the form

$$g_R(x) = \exp[-\phi(x)/kT] \tag{2}$$

where the effective pair potential is given by

$$\phi(x) = -\int_{\infty}^{x} F(x')\, dx' \tag{3}$$

and F(x) is the force exerted on a generic particle located at a distance x from the test particle's surface. This force is the net action of the collisions of this generic particle at distance x with all remaining particles surrounding it. These remaining particles are indicated by dashed circles in

Figs. 1 and 2 when the "test particle" has a convex and a concave surface, respectively. The test particle's surface is to represent in the following the curved surface of the cavity or wall.

The density of the remaining particles is now given by $ng_a(a)g_R(\tilde{x}_R)$ where $\tilde{x}_R$ is the particle's distance to the surface of the test particle. These particles exert on the generic particle (indicated by the solid small circle in Figs. 1 and 2) the following net force in the direction perpendicular to the test particle's surface:

$$F(x) = 2\pi(2a)^2 nkTg_a(a) \int_{\theta_o(x)}^{\pi} g_R[\tilde{x}(x,\cos\theta)]\cos\theta \sin\theta \, d\theta \qquad (4)$$

If the generic particle is at a distance $x < 3a$ from the test particle's surface, the impingement angle $\theta$ is limited to the range $\theta_o < \theta < \pi$, where $\theta_o$ can be obtained from the triangle (TGP) in Figs. 1 and 2 by simple trigonometric considerations. The result is

$$\cos\theta_o(x) = \begin{cases} ((x \pm R)^2 + 4a^2 - (a \pm R)^2)/(4a(x \pm R)) & \text{for } a < x < 3a \\ 1 & \text{for } x > 3a \end{cases} \qquad (5)$$

A similar trigonometric analysis gives the distance $\tilde{x}_R$ of the generic particle from the test surface:

$$\tilde{x}_R(x,\cos\theta) = [(x \pm R)^2 + 4a^2 - 4a(x \pm R)\cos\theta]^{1/2} \mp R \qquad (6)$$

The upper (lower) signs in Eqs. (5) and (6) apply to the convex (concave) test surface.

We may abbreviate the formulae somewhat by introducing the hard-sphere packing fraction

$$y = \frac{4\pi}{3} a^3 n \qquad (7)$$

and the new integration variable

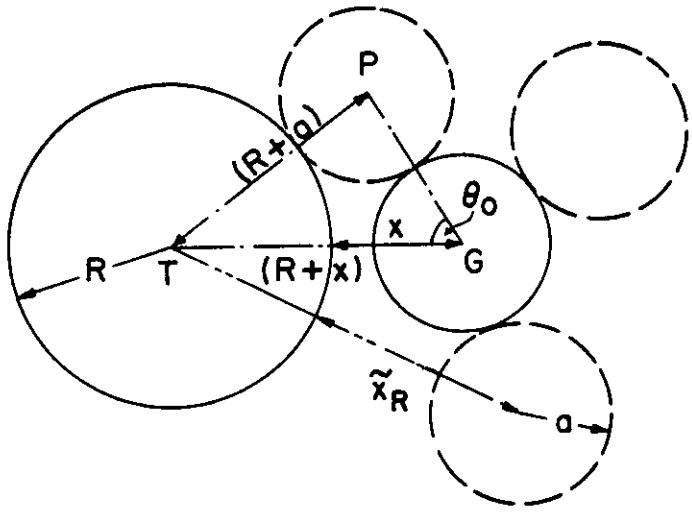


FIGURE 1. Test Particle with a Convex Surface Surrounded by Gas Atoms.

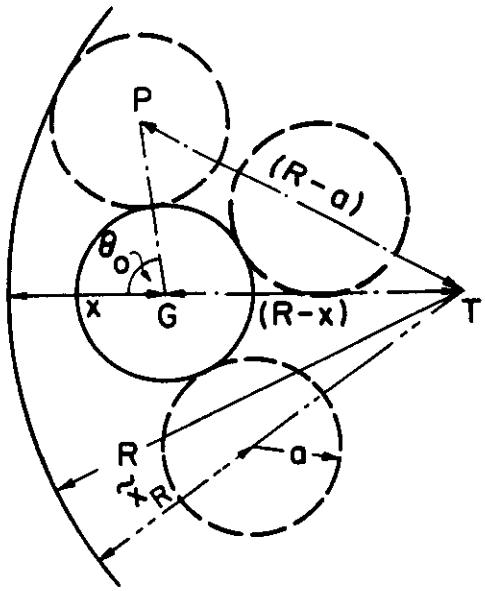


FIGURE 2. Test Particle with a Concave Surface and Adjacent Gas Atoms.

$$u = \cos\theta \tag{8}$$

Inserting then Eq. (4) into Eq. (3) and subsequently into Eq. (2) we obtain an integral equation for the radial distribution function of the form

$$\ln g_R(x) = y g_a(a) \frac{6}{a} \int_{\infty}^{x} dx' \int_{-1}^{\cos\theta_o(x')} g_R[\tilde{x}_R(x',u)]u\, du \tag{9}$$

If we set $R = +a$, we obtain also an integral equation for the pair distribution function $g_a(x)$ given by

$$\ln g_a(x) = y g_a(a) \frac{6}{a} \int_{\infty}^{x} dx' \int_{-1}^{u_a(x')} g_a[\tilde{x}_a(x',u)]u\, du \tag{10}$$

where

$$u_a(x) = \begin{cases} (x + a)/4 & \text{for } a \leq x \leq 3a \\ 1 & \text{for } x \geq 3a \end{cases} \tag{11}$$

and

$$\tilde{x}_a(x,u) = [(x + a)^2 + 4a^2 - 4au(x + a)]^{1/2} - a \tag{12}$$

Equations (9) and (10) must either be solved numerically or by iteration. The latter method was chosen for the present paper, and it is described in the following section. Once $g_R(x)$ has been determined, the gas-kinetic pressure exerted on the curved test surface is given by[8]

$$p = nkTg_R(a) \tag{13}$$

For a flat test surface, $R \to \infty$, Eq. (13) should reproduce the known results for the equation of state for a hard-sphere gas, namely[9]

$$z = p/nkT = (1 + y + y^2 - y^3)/(1 - y)^3 \tag{14}$$

As Shinomoto has shown,[5] this is indeed the case. Although his equation of

state is not of the same mathematical form as Eq. (14), it gives practically identical results for hard-sphere packing fractions $y \lesssim 0.47$.

Our evaluation of Eq. (13) for curved surfaces with finite radius R extends then the results of Shinomoto.

## 5.3 Evaluation of the Hard-Sphere Equation of State

In evaluating Eqs. (9) and (10), we follow the iteration procedure used by Shinomoto for the flat test surface.

In the zero-order approximation, we assume that $g_a(a) \cong 1$ and $g_R(\tilde{x}) \cong 1$. This is a reasonable assumption for a dilute gas, i.e. for small packing fraction y. Equation (14) gives then

$$F_0(x) = \begin{cases} -\frac{3}{a}\, ykT[1 - \cos^2 \theta_0(x)] & \text{for } a < x < 3a \\ 1 & \text{for } x > 3a \end{cases} \tag{15}$$

which results in the effective pair potential

$$\phi_0(x) = \int_{\infty}^{x} F_0(x')\, dx' = \begin{cases} -ykT\psi_0(x) & \text{for } a < x < 3a \\ 0 & \text{for } x > 3a \end{cases} \tag{16}$$

where

$$\frac{1}{3}\,\psi_0(x) = \frac{1}{a}\int_{x}^{3a} [1 - \cos^2 \theta_0(x')]\, dx' = (3 - \xi) - \frac{1}{16}\left\{\frac{1}{3}\,[(3 + \rho)^3 - (\xi + \rho)^3]\right. \tag{17}$$

$$\left. - 2[(1 + \rho)^2 - 4](3 - \xi) - [(1 + \rho)^2 - 4]^2[(3 + \rho)^{-1} - (\xi + \rho)^{-1}]\right\}$$

and

$$\xi = x/a\ ,\ \rho = \pm R/a \tag{18}$$

The radial distribution function in zero-order approximation is then given by

$$g_R^o(x) = \begin{cases} 0 & \text{for } x < a \\ \exp[y\psi_o(x)] & \text{for } a < x < 3a \\ 1 & \text{for } x > 3a \end{cases} \tag{19}$$

The pair distribution function $g_a(x)$ at contact, i.e. for $x = a$, is obtained from Eq. (19) by setting $R = +a$ or $\rho = +1$; accordingly

$$g_a^o(a) = \exp\left(\frac{5}{2} y\right) \tag{20}$$

In the next, i.e. first-order approximation, we use now Eqs. (19) and (20) in Eq. (4) and compute an improved force function

$$F_1(x) = \frac{3y}{2a} kT \exp\left(\frac{5}{2} y\right) \int_{\theta_o}^{\pi} g_R^o[\tilde{x}(x,\cos\theta)]\cos\theta \sin\theta \, d\theta \tag{21}$$

$$= \frac{6}{a} ykT \exp\left(\frac{5}{2} y\right) \int_{\tilde{x}_o}^{\tilde{x}_1} g_R^o(\tilde{x}) f(x,\tilde{x}) \, d\tilde{x}$$

where

$$f(x,\tilde{x}) = \frac{(x \pm R)^2 - (\tilde{x} \pm R)^2 + 4a^2}{8a^2(x \pm R)}$$

and $\tilde{x}_o = x - 2a$ , $\tilde{x}_1 = x + 2a$ for $3a < x < 5a$

and $\tilde{x}_o = a$ , $\tilde{x}_1 = x + 2a$ for $a < x < 3a$ .

In order to evaluate the integral in Eq. (21) we make the low-density approximation

$$g_R^o(x) = \exp[y\psi_o(x)] \cong 1 + y\psi_o(x) \qquad \text{for } a < x < 3a$$

The integral can now be evaluated in closed form for the inner region, i.e. for $a < x < 3a$, and for the outer region $3a < x < 5a$. For $x > 5a$, $F_1(x) = 0$.

The effective pair potential in first-order requires then an additional integration, namely

$$\phi_1(x) = \int_x^{5a} F_1(x')\, ds' \tag{22}$$

Although all these integrations are elementary, the number of terms involved becomes very large. Therefore, in order to avoid errors, the integrations have been done in closed form with an algebraic manipulation routine REDUCE2 supplied by the MFE computing center. The result for $\phi_1(a)$ is given by

$$\phi_1(a)/(nykT) = M(a,y,R)/N(a,y,R) \tag{23}$$

where

$$\begin{aligned} M(a,y,R) = {} & 478953\, a^9y - 459270\, a^9 + 358668\, a^8Ry - 3061800\, a^8R \\ & - 959364\, a^7R^2y - 6327720\, a^7R^2 - 1864296\, a^6R^3y - 6667920\, a^6R^3 \\ & - 1491210\, a^5R^4y - 4207140\, a^5R^4 - 683424\, a^4R^5y - 1693440\, a^4R^5 \\ & - 193284\, a^3R^6y - 441000\, a^3R^6 - 33528\, a^2R^7y - 72240\, a^2R^7 \\ & - 3287\, aR^8y - 6790\, aR^8 - 140\, R^9y - 280\, R^9 \end{aligned} \tag{24}$$

and

$$\begin{aligned} N(a,y,R)/70 = {} & 6561\, a^9 + 24057\, a^8R + 37908\, a^7R^2 + 34020\, a^6R^3 \\ & + 19278\, a^5R^4 + 7182\, a^4R^5 + 1764\, a^3R^6 + 276\, a^2R^7 \\ & + 25\, aR^8 + R^9 \end{aligned} \tag{25}$$

The equation of state in the first-order approximation is then given by

$$p/nkT = \exp[-\phi_1(a)/kT] \tag{26}$$

For a convex surface with a positive radius of curvature, the compressibility

factor (p/nkT) is shown in Fig. 3 as a function of the hard-sphere packing fraction and for different radii of curvature. Note, that the compressibility factor and hence the pressure decreases with decreasing radius of curvature for a given packing fraction. As a result, the gas-kinetic pressure on a protrusion in a flat wall is actually less than the pressure on the flat portions.

For the case of small cavities the situation reverses. The curvature is now concave and characterized by negative values of R in the present convention. As the results show in Fig. 4, the compressibility factor and hence the pressure increases as the radius of curvature becomes smaller in absolute terms. Hence, for the same packing fraction, a gas exerts a greater gas-kinetic pressure on a small cavity than on a larger one. This can be simply explained by the observations that gas atoms impinging on a concave surface will on average impart a greater momentum component perpendicular to this surface than when the surface is flat, or worse yet, convex in curvature. This observation also makes it plausible that a curvature effect will only become significant when the curvature radius approaches the atomic radius of the gas particles.

In order to show the relative effect of curvature, we evaluate the ratio of the gas pressure on a curved surface to the pressure on a flat surface. Figure 5 gives this ratio for convex curvature, and Fig. 6 the results for concave curvature or cavities. Figure 6 shows that for a cavity radius equal to four atomic radii, the gas-kinetic pressure can be up to twice the value computed with the conventional equation of state.

## 5.4 Discussion

The evaluation of the effect of curvature on the gas-kinetic pressure is carried out in the present paper for hard-sphere atoms impinging on a hard wall. In reality, both the interaction among the gas atoms and between gas atoms and wall atoms is via interatomic potentials whose repulsive cores are

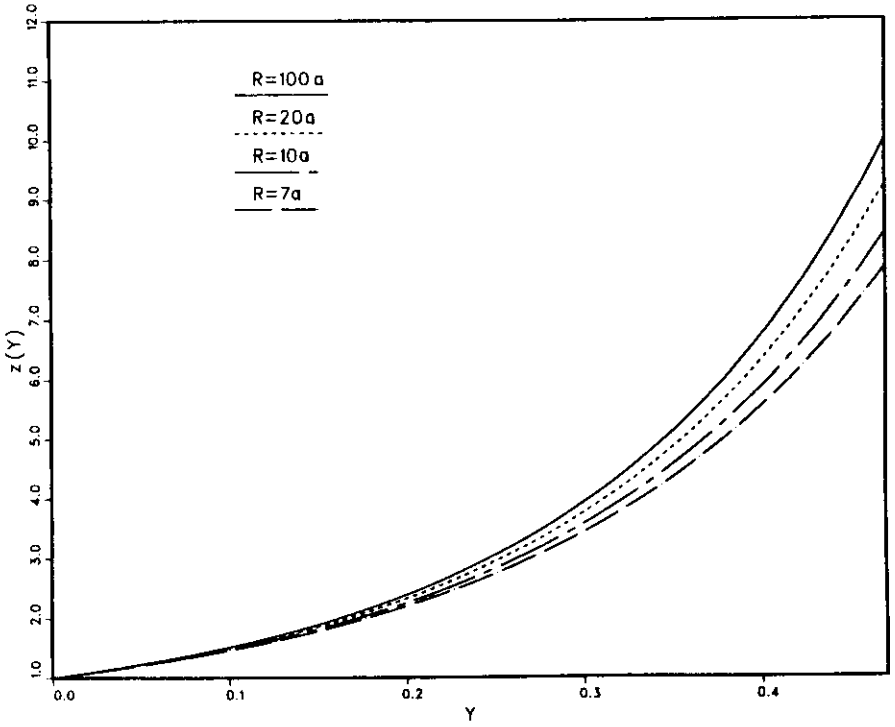


FIGURE 3. Compressibility Factor Versus Hard-Sphere Packing Fraction for a Gas Impinging on a Convex Surface with Radii of Curvature in Units of Gas Atom Radius.

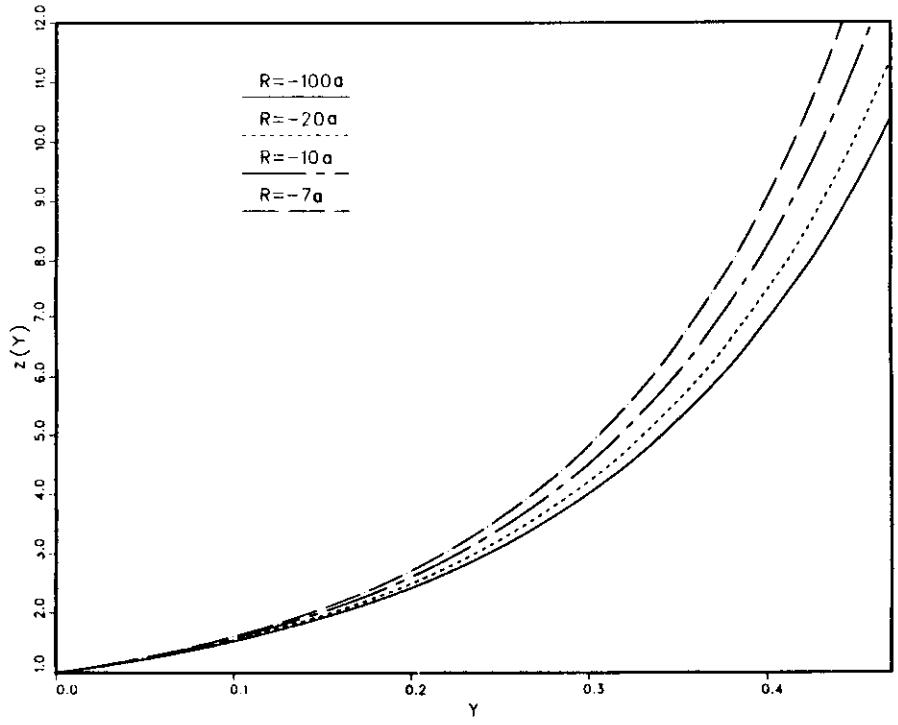


FIGURE 4. Compressibility Factor Versus Hard-Sphere Packing Fraction for a Gas Impinging on a Concave Surface with Radii of Curvature in Units of Gas Atom Radius.

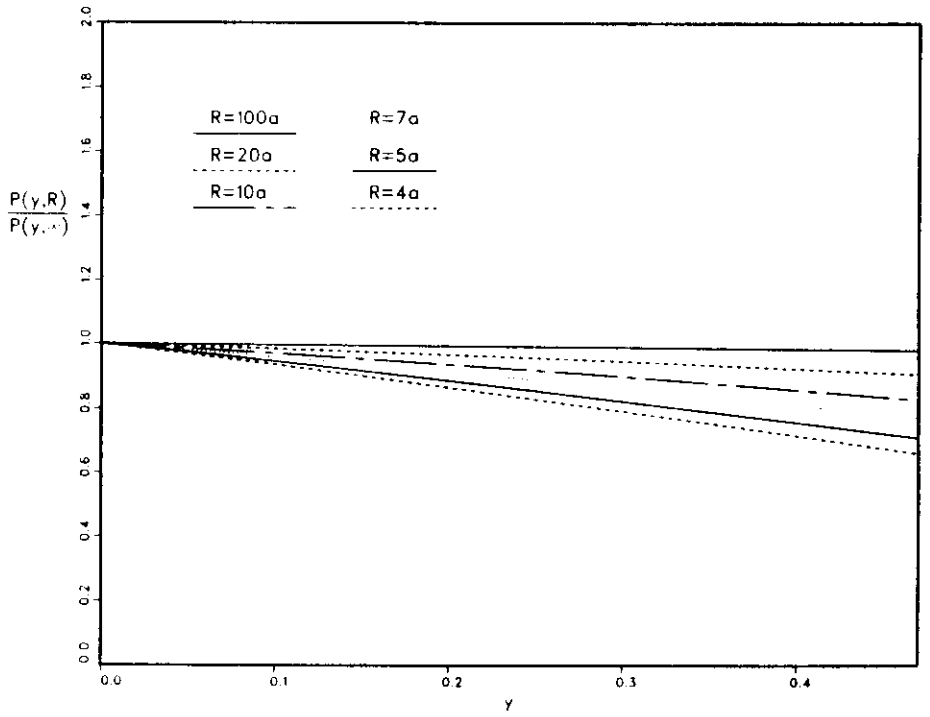


FIGURE 5. Ratio of Pressures on a Convex and a Flat Surface.

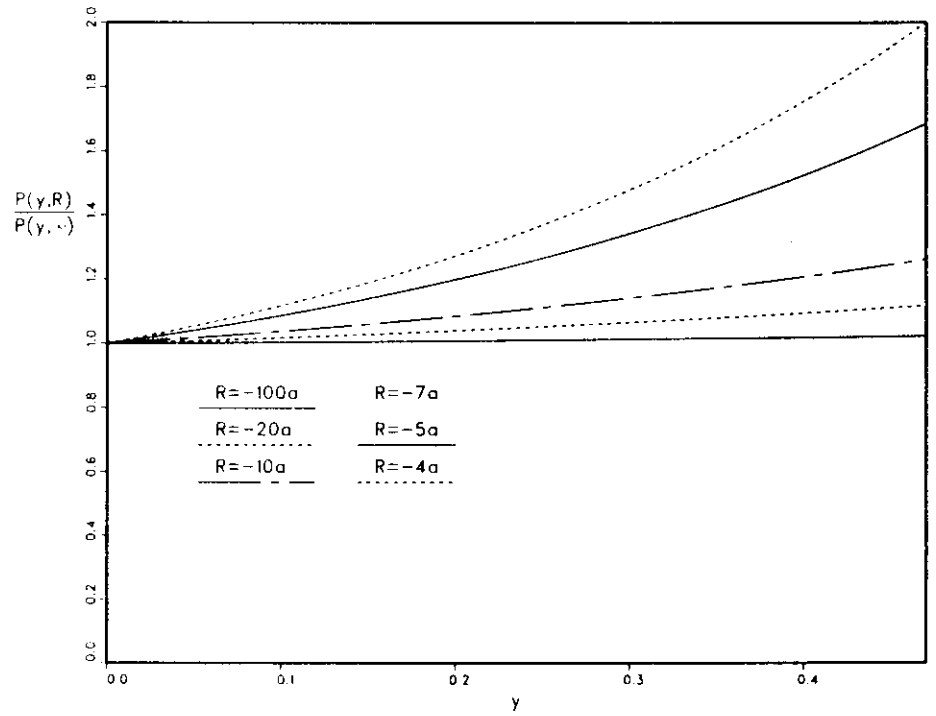


FIGURE 6. Ratio of Pressures on a Concave or Cavity Surface and a Flat Surface.

"soft." With regard to the collisional interaction among gas atoms, it has been shown[10] that an effective diameter $d(T,n) = 2a$ can be assigned to the helium atoms which is a function of temperature and of the gas density n. When this diameter is used in the hard-sphere equation of state, the results obtained are in excellent agreement with the experimentally determined equation of state. Since there is in principle no difference between the effective interatomic distance of two colliding particles of the same kind and the effective interatomic distance of two different kinds of particles colliding, one moving and the other at rest, the same concept of effective diameter should also apply to the atoms forming the cavity wall. As a result, the effective location of the cavity wall, or the effective cavity radius, will be a function of the gas temperature and density. However, employing these effective radii R and a, the curvature effect on the gas-kinetic pressure should still be given by the results obtained in the previous sections. Therefore, we conclude that the curvature effect is largely independent of the precise shape of the interatomic potentials, and it is well approximated by effective hard-sphere potentials with appropriately chosen effective radii. For helium, this effective radius is $d(T,n)/2$ as given by Glasgow and Wolfer.[10] For the atoms of the cavity wall, similar expressions will have to be derived in future investigations.

In most theoretical treatments, the equation of state for real gases and liquids is derived from the Helmholtz free energy, A. In turn, this quantity is obtained from statistical mechanics utilizing given interatomic potentials. The pressure is then found by evaluating the derivative $-\partial A/\partial V$, where V is the volume of the system. This is referred to as the thermodynamic pressure.

Borstnik et al.[8] have, on the other hand, derived the gas-kinetic pressure on a flat rigid wall for a gas whose atoms interact via a Lennard-Jones potential. They obtained the gas atom density as a function of the distance to the wall by solving the BGYB equation. If $n(a)$ is then the density of gas atoms in contact with the wall and $\overline{n}$ the average density far from the wall, they define the gas-kinetic pressure as $p = n(a)kT$. This definition agrees

with ours used in the present investigation. However, it remains to be shown that this definition leads to the same pressure as the thermodynamic pressure, at least in the case of a flat wall. To this end, Borstnik et al. show that if the gas-kinetic pressure is to be identical with the thermodynamic pressure, then

$$[n(a) - \bar{n}]/\bar{n} = B_2(T)\bar{n}$$

for low average gas densities. Here, $B_2(T)$ is the second virial coefficient whose temperature dependence is well known both from experimental measurements as well as from statistical mechanics calculations. Indeed, Borstnik et al. find that the relative density change at a flat wall, i.e. $[n(a) - \bar{n}]/\bar{n}$ has precisely the same temperature dependence as the second virial coefficient. Therefore, they conclude that the correct relationship between the gas-pressure on a surface and the gas density is indeed given by $p = n(a)kT$, where $n(a)$ is the density of gas atoms in instantaneous contact with the wall. This represents also our central relationship for obtaining the gas pressure on curved surfaces.

## 6.0 References


1. A. Si-Ahmed and W.G. Wolfer, "Effect of Radiation-Induced Segregation on Void Nucleation," Effects of Radiation on Materials, H.R. Brager and J.S. Perrin (Eds.), ASTM-STP-782 (1982), p. 1008.

2. M.R. Mruzik and K.C. Russell, Surface Science, 67, 205 (1977).

3. M. Doyama and R.M.J. Cotterill, Lattice Defects and Their Interactions, R.R. Hasiguti (Ed.), Gordon and Breach, New York (1967), p. 81.

4. R.M.J. Cotterill and M. Doyama, ibid, p. 1.

5. S. Shinomoto, Phys. Letters, 89A, 19 (1982).

6. J.O. Hirschfelder, C.F. Curtiss, and R.B. Bird, Molecular Theory of Gases and Liquids, Wiley, New York (1954), p. 84.

7. P.A. Egelstaff, An Introduction to the Liquid State, Academic Press, New York (1967), p. 15.

8. B. Borstnik, D. Janezic, and A. Azman, Mol. Physics, 42, 721 (1981).

9. N.F. Carnahan and K.E. Starling, J. Chem. Phys., 33, 1439 (1960).

10. B.B. Glasgow and W.G. Wolfer, "Extension and Comparison of Various Equations of State for Gaseous and Solid Helium," DAFS Quarterly Progress Report, DOE/ER-0046/12 (May 1983).

## 7.0 Future Work

The effective location of a cavity wall or the effective cavity radius will be derived in future investigations. This will allow us to extend the macroscopically based description for gas bubbles to near-atomic dimensions.

## CONTRIBUTION OF VACANCIES TO THE EQUATION OF STATE OF SOLID HELIUM

W.G. Wolfer (University of Wisconsin)

### 1.0 Objective

To assess the possible contribution of vacancies formed in solid helium to its equation of state.

### 2.0 Summary

As a result of the light mass of helium atoms, their thermal vibrational amplitudes are relatively large in the solid state. Therefore, vacancies form readily, and their equilibrium concentration is high. Their contribution to the free energy and to the equation of state for solid helium is evaluated. It is found, that vacancies make only a minor contribution to the equation of state at high temperatures of interest to radiation damage and blistering applications.

### 3.0 Program

Title: Effect of Radiation and High Heat Flux on the Performance of First Wall Components

Principle Investigator: W.G. Wolfer

Affiliation: University of Wisconsin-Madison

### 4.0 Relevant DAFS Program Task/Subtask

Task II.C.2 Effects of Helium on Microstructure

Subtask C Correlation Methodology

### 5.0 Accomplishment and Status

In a previous contribution, Glasgow and Wolfer[1] have developed an equation

of state (EOS) for solid helium and thereby extended their earlier[2] results for the gas law of helium at very high pressures believed to exist in small helium bubbles. This extension of the EOS to solid densities was found necessary in order to cover the range of densities and temperatures at which helium exists in small vacancy clusters.

The earlier developed EOS for solid helium relied upon extensive quantum-mechanical calculations reported in the literature for the ground-state pressure of solid helium at 0 K, and on a Mie-Grüneisen EOS for the pressure contributed by thermal lattice vibrations. However, the effect of vacancies on the solid EOS for helium was neglected.

In the present paper, this possible contribution of vacancies is investigated and evaluated both as a function of temperature and density. As in other solid crystals, the concentration of vacancies in solid helium is given by

$$n_v = \exp[-G_v^{He}/kT] \tag{1}$$

where $n_v$ is given in atomic fractions. However, in contrast to most solids, the Gibbs free energy for vacancy formation, $G_v^{He}$, in solid helium depends strongly on the pressure or the density.

Figure 1 shows the values of $(G_v^{He}/k)$ as reported in the literature and compiled in Ref. 2 as a function of the packing fraction

$$y_o = \frac{\pi}{6} \sigma^3 N/V \tag{2}$$

where $\sigma$ = 0.2637 nm, and N is the number of helium atoms in the volume V. It is seen, that the vacancy formation energy at densities below $y_o \cong 0.24$ is only about $4 \times 10^{-4}$ eV, but it rapidly increases for higher densities prevalent in solid helium at high temperatures.

In order to be able to extrapolate the results shown in Fig. 1 to these higher

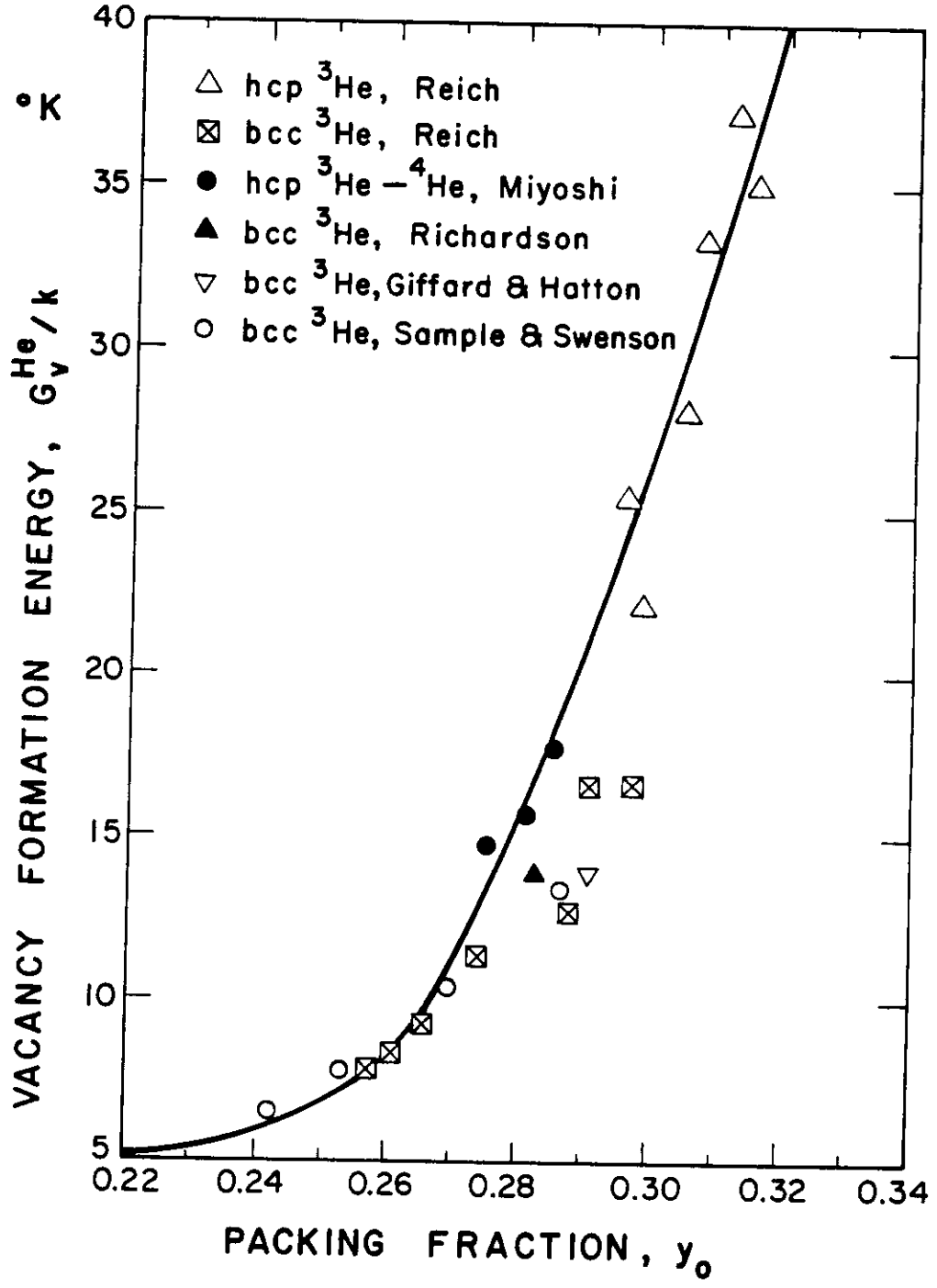


FIGURE 1. Gibbs Free Energy for Vacancy Formation in Solid Helium as a Function of Density.

densities, the data were fitted to the following expression

$$G_v^{He}/k = 5 + 8.75 \ln\{[1 + \exp(80\ x)]/[1 + \exp(-21.6)]\} \tag{3}$$

where

$$x = y_o - 0.27. \tag{4}$$

The solid line represents Eq. (3) and shows it to be a satisfactory correlation. Note that $G_v^{He}$ increases linearly with $y_o$ for high densities according to Eq. (3).

The presence of vacancies in the solid helium phase adds a contribution $A_v$ to the Helmholtz free energy

$$A = A_s + A_v \tag{5}$$

where $A_s$ is the contribution given earlier,[1] and

$$A_v = N_v G_v^{He} - kT \ln[W(N_v)] \ . \tag{6}$$

Here, $N_v = n_v N$ and

$$\ln W(N_v) \cong N(1 + n_v) \ln (1 + n_v) - N n_v \ln n_v \ . \tag{7}$$

Using the thermodynamic definition of the pressure $p = -(\partial A/\partial V)$ we find the following results for the compressibility factor of solid helium:

$$z = pV/NkT = z_s + z_v \tag{8}$$

where $z_s$ was given previously,[1] and

$$z_v = (y_o/kT)(\partial G_v^{He}/\partial y_o) n_v[1 + \ln (1 + n_v)] \tag{9}$$

is the contribution due to vacancies.

TABLE 1

CONTRIBUTION OF VACANCIES TO THE COMPRESSIBILITY FACTOR OF SOLID HELIUM

| Density (moles/cm$^3$) | $y_o$ | $z_v$ | | |
|---|---|---|---|---|
| | | 200 | 600 | 1000 K |
| 0.05 | 0.29 | 1.2628 | 0.4608 | 0.2815 |
| 0.10 | 0.58 | 0.8566 | 0.7131 | 0.5171 |
| 0.15 | 0.87 | 0.4024 | 0.6996 | 0.5988 |
| 0.20 | 1.16 | 0.1818 | 0.6172 | 0.6186 |
| 0.25 | 1.45 | 0.0800 | 0.5169 | 0.6017 |
| 0.30 | 1.74 | 0.0344 | 0.4205 | 0.5642 |
| 0.35 | 2.03 | 0.0145 | 0.3361 | 0.5167 |
| 0.40 | 2.33 | 0.0060 | 0.2656 | 0.4656 |
| 0.45 | 2.62 | 0.0024 | 0.2082 | 0.4147 |
| 0.50 | 2.91 | 0.0010 | 0.1621 | 0.3663 |

The numerical evaluation of Eq. (9) gives the results shown in Table 1. Over the same density range, $z_s$ varies from 10 to about 100 at T = 200 K, and from 10 to about 40 at T = 1000 K. Hence, with the exception of low temperatures and densities, the contribution of vacancies to the solid EOS can be neglected. Even for T = 200 K and a density of about 0.10 moles/cm$^3$, which is close to the estimated density where the gas-solid phase transition occurs,[1] the contribution of vacancies to the compressibility factor z is only about 6%. As the density or the temperature increases this contribution diminishes.

In summary, vacancies in solid helium make a small contribution on the order of a few percent to the pressure. Considering the large uncertainties still associated with the theoretical evaluation of $z_s$, and the complete lack of data, an inclusion of the vacancy contribution into the solid EOS of helium is not warranted at the present time.

## 6.0 References

1. B.B. Glasgow and W.G. Wolfer, "Extension and Comparison of Various Equations of State for Gaseous and Solid Helium," DAFS Quarterly Progress Report, DOE/ER-0046/12 (May 1982).

2. H.R. Glyde, "Solid Helium," Chapter 7 in Rare Gas Solids, Vol. 1, Eds. M.L. Klein and J.A. Venables, Acad. Press, London, 1976.

## 7.0 Future Work

A more refined model will be developed for the solid EOS of helium and for the phase transition from gas to solid.

# GRAIN BOUNDARY HELIUM DEPOSITION IN NICKEL-BEARING ALLOYS IRRADIATED IN MIXED SPECTRUM REACTORS

B. Esmailzadeh and A. Kumar (University of Missouri-Rolla)

## 1.0 Objective

The object of this effort is to determine the effect of nickel segregation on changes in helium deposition rate at the grain boundary in nickel-bearing alloys under irradiation in mixed spectrum reactors (e.g. HFIR) as a result of the sequential $^{58}Ni(n,\gamma)^{59}Ni,(n,\alpha)^{56}Fe$ nuclear reactions.

## 2.0 Summary

A general derivation was performed to determine the helium deposition rate at the grain boundary in nickel-bearing alloys under irradiation in mixed spectrum nuclear reactors. The segregation of nickel causes the deposition rate at the boundary to increase in grains of sizes larger than twice the range of alpha particles created by the sequential $^{58}Ni(n,\gamma)^{59}Ni(n,\alpha)^{56}Fe$ nuclear reactions. The grain boundaries of smaller grains are subjected to a lowering of the deposition rate as a result of the nickel segregation.

## 3.0 Program

Title: Radiation Effects in Materials

Principal Investigator: A. Kumar, research sponsored by University of Missouri, Department of Nuclear Engineering

Affiliation: University of Missouri-Rolla

4.0 Relevant DAFS Program Plan Task/Subtask

Subtask II C.2. Effect of Helium on Microstructure

## 5.0 Accomplishments and Status

### 5.1 Introduction

The helium embrittlement of fcc metals is a major life-limiting factor when these alloys are used as structural materials and exposed to high neutron fluences. The sources of helium in mixed spectrum reactors such as HFIR are mainly two, namely boron ($^{10}B$) and nickel ($^{58}Ni$) in nickel-bearing materials. While boron, present as an impurity, burns out quite rapidly at very low fluences due to its large absorption cross-section for thermal neutrons the supply of nickel is essentially inexhaustible during the service life of the structural material. Nickel produces helium by the sequential absorption of two thermal neutrons i.e. $^{58}Ni(n,\gamma)^{59}Ni(n,\alpha)^{56}Fe$[1]. In addition, nickel segregates at grain boundaries[2] when nickel-bearing materials interact with the fast neutron component of the mixed spectrum reactors. This suggests the possibility that nickel segregation combined with the two-step transmutation reaction may be a major cause of helium being found preferentially on the grain boundaries.

A general derivation was performed to determine the changes in helium deposition rate at the grain boundary as a result of nickel segregation. Calculations were performed for both Nimonic PE-16 alloy and stainless steel, using various grain sizes and nickel concentration profiles.

## 5.2 Determination of Helium Deposition Rate at Grain Boundaries

### 5.2.1 Nickel Concentration Profile in the Grain

Fig.1 shows the model of a grain along with the nickel concentration profile. The grain is modeled to be an infinite slab with a thickness t. The initial uniform concentration is $C_o$. All concentrations are expressed in atomic per cent. After segregation has occurred, the concentration at the grain boundary is assumed to be 75%, characteristic of the $Ni_3Si$ precipitate. The concentration is assumed to drop linearly away from the grain boundary up to a distance $x_1$. The concentration is uniform ($=C_3$) for the distance ($x_2-x_1$) and then rises linearly to the 75% level at the grain boundary. In Fig.1, the range of alpha particles, R, is smaller than t. In Fig.2, R is larger than t but smaller than 2t. The value of $C_3$ is determined by conservation of nickel atoms after segregation, with distance $x_1$, as an independent variable. In Fig.1,

$C = C_2 = 75\%,\ x = 0$ and $x = t$ (1)

$C = C_1 x + C_2,\ x \leq x_1$ (2)

$C = C_3,\ x_1 < x < x_2$

$C = C_3 - C_1 (x - x_2),\ x_2 < x < t$

For fig. 2, $t < R < 2t$

$C = C_1 x + C_2,\ x \leq x_1$

$C = C_3,\ x_1 < x \leq x_2$

$C = C_3 - C_1 (x - x_2),\ x_2 < x \leq x_3,\ x_3 = t$

$C = C_1 (x - x_3) + C_2,\ x_3 \leq x \leq x_4$

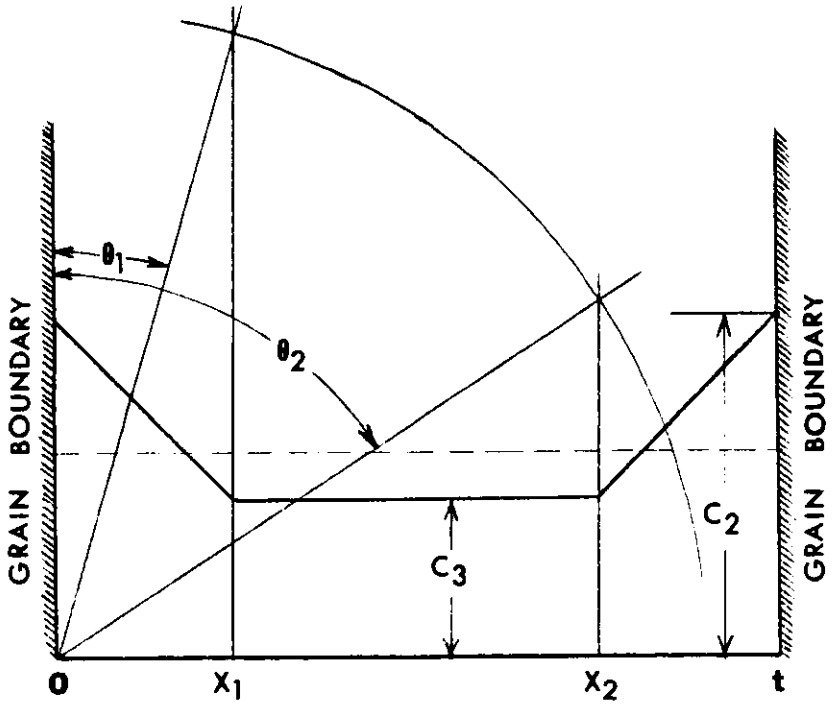


FIGURE 1. Concentration Profile in Grain of Thickness Greater than the Range of Alpha Particles.

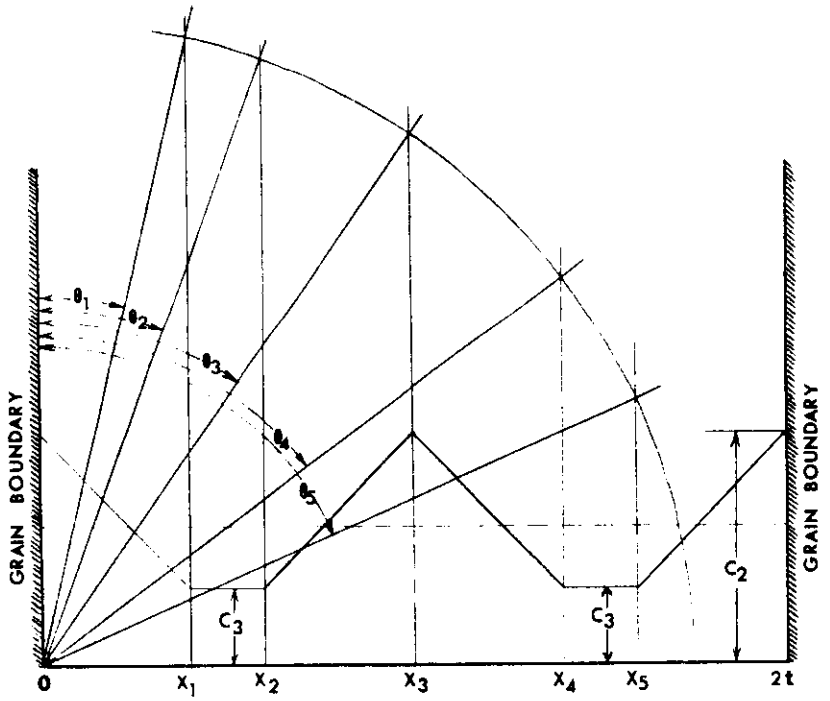


FIGURE 2. Concentration Profile in Grain Thickness Less than the Range of Alpha Particles.

TABLE 1

CONCENTRATION PARAMETERS FOR NIMONIC PE-16

| t(μm) | 5 μm | | 10 μm | | 15 μm | | 18 μm | | 20 μm | | 50 μm | |
|---|---|---|---|---|---|---|---|---|---|---|---|---|
| $x_1$ (μm) | $C_1$ | $C_3$ | $C_1$ | $C_3$ | $C_1$ | $C_3$ | $C_1$ | $C_3$ | $C_1$ | $C_3$ | $C_1$ | $C_3$ |
| 0.5 | -66.7 | 41.7 | -63.2 | 43.4 | | | | | | | | |
| 1.0 | -37.5 | 37.5 | -33.3 | 41.7 | -32.1 | 42.9 | -31.8 | 43.2 | -31.6 | 43.3 | -30.6 | 44.4 |
| 1.5 | -28.6 | 32.1 | -23.5 | 39.7 | | | | | | | | |
| 2.0 | -25.0 | 25.0 | -18.8 | 37.5 | -17.03 | 40.4 | -16.9 | 41.3 | -16.7 | 41.7 | -15.6 | 43.8 |
| 2.5 | -24.0 | 15.0 | -16.0 | 35.0 | | | | | | | | |
| 3.0 | | | -14.3 | 32.1 | -12.5 | 37.5 | -12.0 | 39.0 | -11.8 | 39.7 | -10.6 | 43.1 |
| 3.5 | | | -13.2 | 28.9 | | | | | | | | |
| 4.0 | | | -12.5 | 25.0 | -10.2 | 34.1 | - 9.6 | 36.4 | - 9.4 | 37.5 | - 8.2 | 42.4 |
| 4.5 | | | -12.1 | 20.5 | | | | | | | | |
| 5.0 | | | -12.0 | 15.0 | - 9.0 | 30.0 | - 8.3 | 33.5 | - 8.0 | 35.0 | - 6.7 | 41.7 |
| 6.0 | | | | | - 8.3 | 25.0 | - 7.5 | 30.0 | - 7.1 | 32.1 | - 5.7 | 40.9 |

TABLE 2

CONCENTRATION PARAMETERS FOR STAINLESS STEEL

| $t(\mu m)$ | $10\mu m$ | | $18\mu m$ | | $20\mu m$ | | $50\mu m$ | |
|---|---|---|---|---|---|---|---|---|
| $x_1(\mu m)$ | $C_1$ | $C_3$ | $C_1$ | $C_3$ | $C_1$ | $C_3$ | $C_1$ | $C_3$ |
| 0.2 | -321.5 | 10.7 | | | | | | |
| 0.5 | -132.6 | 8.7 | -129.6 | 10.2 | -129.2 | 10.4 | | |
| 0.7 | - 96.8 | 7.3 | | | | | | |
| 1.0 | | | - 66.7 | 8.3 | - 66.3 | 8.7 | -64.3 | 10.7 |
| 1.25 | | | - 54.2 | 7.3 | | | | |
| 1.4 | | | | | - 48.4 | 7.3 | | |

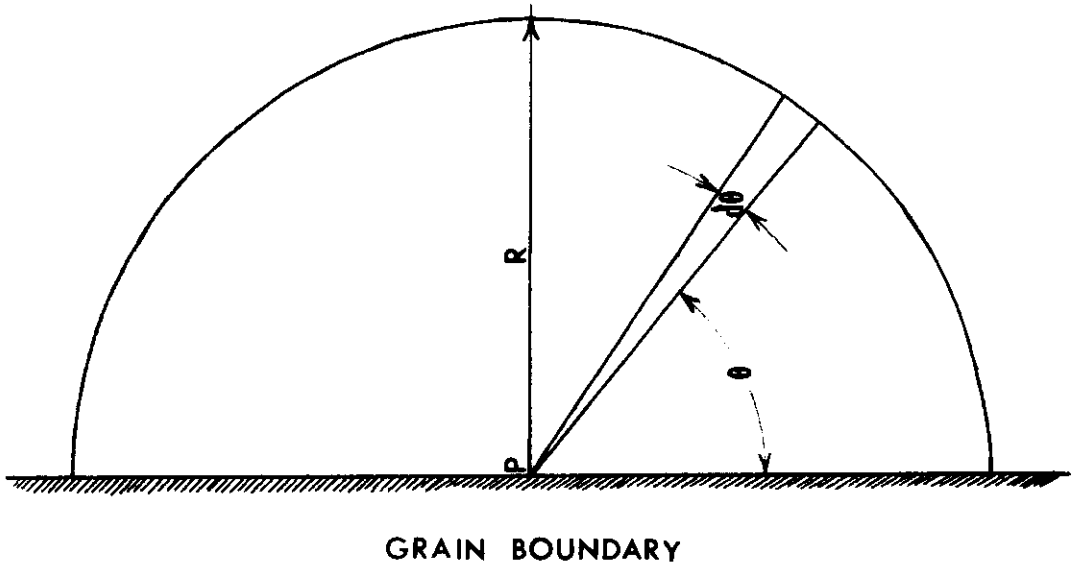


FIGURE 3. Source Surface That Deposits Helium at Grain Boundary.

$C=C_3$, $x_4 \leq x \leq x_5$

$C=C_3-C_1(x-x_5)$, $x_5 \leq x \leq 2t$

The parameters $C_n$, n=1,2,...are given in Tables 1 and 2.

## 5.2.2. Helium Deposition Rate at the Grain Boundary

Fig.3 shows one-half of the source surface that may deposit alpha particles at the point P. Following an analysis given in an earlier report[3] it can be shown that the volumetric deposition rate at the grain boundary in Fig.1 will be

$$\dot{D}_{He} = \int_0^{\theta_1} (C_1 x + C_2) \cos\theta \, d\theta + \int_{\theta_1}^{\theta_2} C_3 \cos\theta \, d\theta + \int_{\theta_2}^{\pi/2} [C_3 - C_1(x-x_2)] \cos\theta \, d\theta$$

where, $\theta_1 = \sin^{-1}(x_1/R)$

$\theta_2 = \sin^{-1}(x_2/R)$

and $x = R\sin\theta$. $\dot{D}_{He}$ is in units of deposition rate per unit source strength.

In Fig.2, $t<R<2t$

$$\dot{D}_{He} = \int_0^{\theta_1} (C_1 x + C_2) \cos\theta \, d\theta + \int_{\theta_1}^{\theta_2} C_3 \cos\theta \, d\theta + \int_{\theta_2}^{\theta_3} [C_3 - C_1(x-x_2)] \cos\theta \, d\theta$$

$$+ \int_{\theta_3}^{\theta_4} [C_2 + C_1(x-x_3)] \cos\theta \, d\theta + \int_{\theta_4}^{\theta_5} C_3 \cos\theta \, d\theta + \int_{\theta_5}^{\pi/2} [C_3 - C_1(x-x_5)] \cos\theta \, d\theta$$

where $\theta_n = \sin^{-1}(x_n/R)$, n=1,2,3,4,5.

and $x = R\sin\theta$

## 5.3 Results and Discussion

Fig.4 shows the ratio of helium deposition rates at the grain boundary after and before nickel segregation occurs in the alloy Nimonic PE-16. Before segregation, this alloy has a uniform concentration of 45% Ni. The distance $x_1$ in Fig.1 may increase with irradiation. Fig.4 shows that the grain boundary is subjected to an increased amount of helium deposition if the grain thickness is larger than 18,μm ie., more than twice the range (R) of alpha particles. For a given thickness of the grain the increase in deposition of helium at the grain boundary rises with increased values of $x_1$. Also, for fixed values of $x_1$ helium deposition at the boundary is larger for thicker grains. For grain sizes smaller than twice the range of alpha particles the helium deposition rate at the grain boundary goes down as a result of the segregation. For PE-16 the change in the helium deposition rate does not exceed 5% for $x_1$=1μm compared to the case in which no segregation occurs. Fig.5 shows the $\dot{D}_{He}/\dot{D}_{He}$ ($x_1$=0) ratio for stainless steel. The nickel concentration is assumed to be 12% everywhere before segregation occurs. The helium deposition ratios are considerably higher (or lower for t <2R) than those of PE-16 as shown in Fig.4. However, even for stainless steel, the helium deposition grain boundaries does not exceed 20% for $x_1$<1μm compared to the case in which no segregation takes place. $x_1$<1μm is a more realistic assumption[2,4].

## 5.4 Conclusion

The nickel segregation that occurs at grain boundaries during neutron-

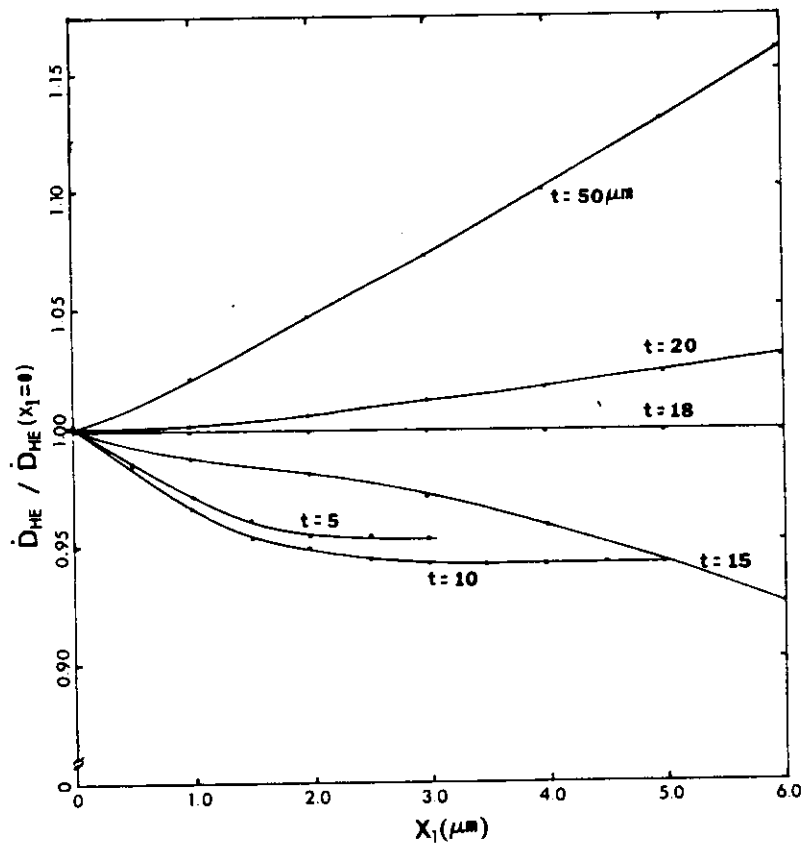


FIGURE 4. Fractional Change in Helium Deposition at Grain Boundary in Nimonic PE-16.

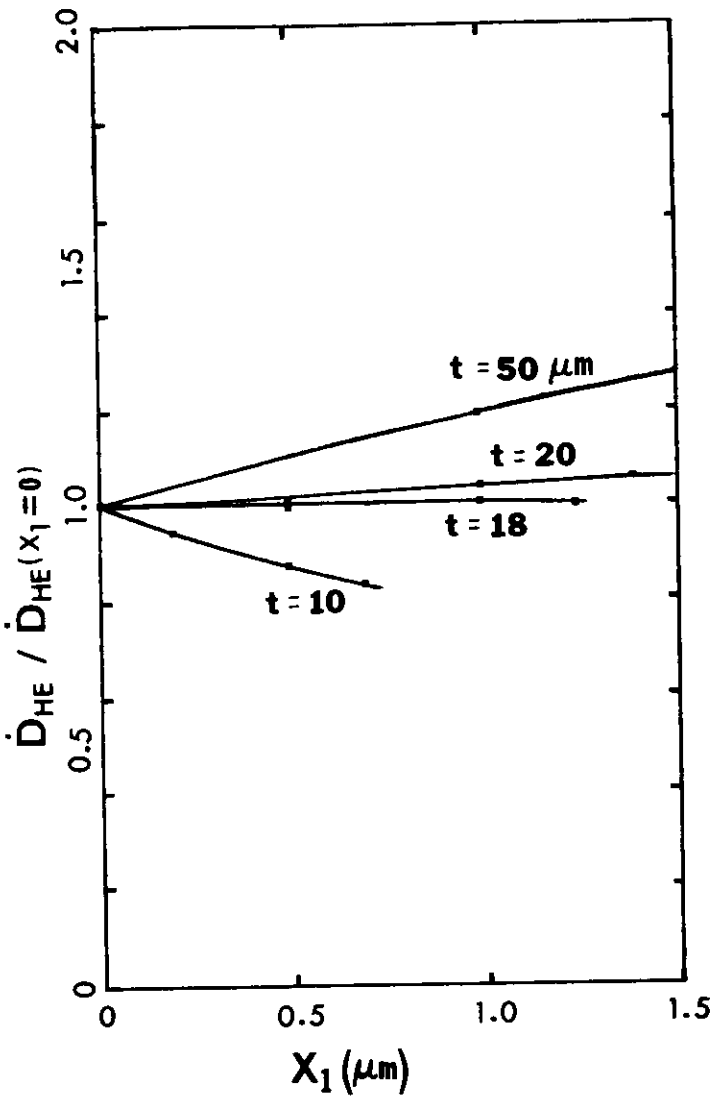


FIGURE 5. Fractional Change in Helium Deposition At Grain Boundary in Stainless Steel.

irradiation leads to increase in the amount of helium deposited at grain boundaries. The amount depends on the nickel content of the alloy,the degree and extent of the segregation and the grain size. For the most realistic cases the calculated increase is insufficient in itself to account for the observation that helium occurs preferentially at grain boundaries. Some method of helium transport must be involved.

## 6.0 References


1. L.R. Greenwood," A New Calculation of Thermal Neutron Damage and Helium Production in Nickel," To appear in J.Nucl.Mat. 1983.
2. H.R. Brager and F.A. Garner," The Radiation-Induced Evolution of AISI-316 (DO-HEAT) in HFIR and EBR II," DAFS Quarterly Proress Report, DOE/ER - 0046/7, 1981. p127.
3. A. Kumar and F.A. Garner," Transmutation - Induced Deposition Profiles in Halos Surrounding Spherical Precipitates," DAFS Quarterly Progress Report, DOE/ER - 0046/12, 1983.
4. H.Q. Lam, A. Kumar, and H.Wiedersich," Kinetics of Radiation-Induced Segregation in Ternary Alloys," ASTM STP 782, H.R. Brager and J.S. Perrin,eds., 1982. 985-1007.

A Computerized "Reference Manual" for Literature on Helium Effects

Nasr M. Ghoniem (University of California at Los Angeles) and Philip Masiasz (Oak Ridge National Laboratory)

## 1.0 Objective

The objective of this work is to report on a new "reference manual" for available literature on helium effects on solids under irradiation.

## 2.0 Summary

Helium gas is quite insoluble in most solids. However, once it is introduced, even in the smallest quantities, it is found in some cases to influence the properties in a dramatic way. The interest in helium effects on materials dates back to the late 60's for applications where helium was either generated or implanted by irradiation. Fast Breeder Reactor technology has pushed the understanding of helium effects a long way in the 70's. During the late 70's and early 80's, we have been witnessing a great surge of research on helium effects for applications in Fusion Reactor Technology. In this computerized reference manual, we have compiled all available articles on helium interaction with solids. The open literature articles are grouped in approximate categories that combine them in a coherent way. The subject categories are: blistering, microstructure, transport and migration, bubble mobility, cavity nucleation, cavity growth and swelling, creep rupture, precipitation, similarities with noble gases, mechanical properties, helium production, and finally helium equation of state.

## 3.0 Program

Title: Helium Effects on the Swelling of Steels
Principal Investigator: N.M. Ghoniem
Affiliation: University of California at Los Angeles

## 4.0 Relevant DAFS Program Plan Task/Subtask

This computerized data base is deemed to be relevant to all tasks within the DAFS program.

## 5.0 Accomplishments and Status

### 5.1 Introduction

A great deal of effort has been invested in research on the effects of helium on the properties of solids. In particular, the emphasis has been directed toward the understanding of mechanicm influencing crucial design properties such as helium blistering, swelling, high temperature embrittlement, and mechanical properties.

This report is intended to help organize the research output in the area of helium effects, and guide the research community into directions where more active investigators are needed. During the exercise it has become obvious to us that there is indeed a common thread between seemingly unrelated research efforts. In order to understand helium effects on swelling, as an example, one has to start from understanding its migration mechanisms, clustering and interaction with various defects (such as in blistering or nucleation), influence on the microstructure, and finally on the behavior of gas-filled cavities.

Much has been discussed about the importance of the level of helium on retaining damage in structural materials. This is obviously justifiable since the swelling and mechanical properties of fusion reactor structural materials may depend on the presence of helium. It is interesting to observe, however, the escalation in the number of publications on helium for this particular reason. Our comprehensive and detailed understanding of the effects of helium on materials and its interaction with radiation-induced damage has emerged only during the past two decades. A computerized report has been written on helium effects, with the hope that it will be useful to researchers, managers and students who are interested in the effects of helium on performance of materials in an irradiation environment.

The contents of this report are kept and maintained on the UCLA IBM-3033 Computer. Any future updates can easily be included. The chapters deal with references on specific areas. Some articles may deal with more than one subject. However, they were approximately classified according to the major emphasis. In each chapter the references are listed alphabetically, and chronically for the same author. The report is now published as a UCLA document, and is available upon request.

## 5.2. Historical Perspective

It is particularly instructive to view work and ideas on helium mirgration, clustering, and effects on properties today in light of their development in fission reactor work prior to about 1970. This section relies heavily on reviews by R. Blackburn (Met. Rev. 2 (1966)159), D.J. Reed (Rad. Effects 47 (1980)237) as well as books by D.S. Billington and J.H. Crawford, Jr. (Radiation Damge in Solids, Princeton University Press, 1961) and M.W. Thompson (Defects and Radiation Damage in Metals, Cambridge University Press, 1969). This section will also deal with highlights rather than being comprehensive. Several broad and interrelated areas of study are found to be: (a) observed microstructure and properties due to the effects of helium, (b) bulk diffusion and release during annealing, and (c) atomistic interactions with the lattice and point defects. Although initially regarded as curiosities for permeation studies without chemical reactivity, inert gases were studied seriously as they began to impact nuclear reactor technology. Some examples are helium embrittlement of various structural and cladding materials and fuel swelling and fusion gas release due to xenon and kryton produced as by-products of fission.

Helium-injected copper was studied by R.W. Barnes, G.B. Redding, and A.H. Cottrel in 1958 as an alternative to examining fission gas bubbles in fuels. These studies led to viewing grain boundaries and free surfaces as sources of vacancies for bubble formation. These studies also led to the classic in situ TEM annealing work of R.S. Barnes and D.J. Mazey in 1960-64; they observed bubble formation on grain boundaries, dislocations, and other features as well as bubble migration and interaction.

Since that time many have contributed to observations of nucleation and growth of bubbles and their relationship at boundaries to helium embrittlement; some examples are: G.T. Martin (1961) and V. Levy (1964) with aluminum; P. Vela and B. Russell (1966) with copper; and A.F. Rowcliffe (1966), E.E. Bloom and co-workers (1967) and H.R. Brager and R.E. Robbins (1968) with various austenitic stainless steels. In parallel to the experimental efforts, theoretical work on bubble nucleation was done by G.W. Greenwood and co-workers (1959), and R. Bullough and R.C. Newman (1959); work on growth and swelling included G.W. Greenwood and M.V. Speight (1963), and various efforts by R.S. Barnes (1961-67). Gas release from nuclear fuels tended to focus on the diffusion and coalescence of bubbles and their migration to surfaces. An alternate approach has been to consider the atomistic reaction rates and formation of clusters for point defects after the work of A.C. Damask and G.J. Dienes (1963).

Helium studies also became important in fast reactor materials technology for embrittlement and, later, swelling. The earliest work on voids formed in fast-reactor-irradiated cladding by C. Cawthorne and E. Fulton (1966) led these authors to conclude that prior helium bubbles were somehow responsible for their formation, as Greenwood, et al., had predicted as early as in 1959. Since then, helium studies have been an intimate part of experimental and theortical void nucleation and growth theories, but not without controversy. The literature on void formation is vast, the reader is directed toward an excellent review by D.I.R. Norris (Rad. Effects 14(1972)1 and 15 (1972)1) and earlier conferences devoted to the subject in addition to work cited in this report. Examples are: (Voids Formed by Irradiation of Reactor Material, eds. S.F. Pugh, M.H. Loretto, and D.I.R. Norris (1977) and Radiation Induced Voids in Metals, eds., J.W. Corbett and L.C. Ianniello (1971).

The areas of helium diffusion and release have often been generally related to atomistic studies of the interaction of helium with point defects. Among the first atomistic studies was the work of D.E. Rimmer and A.H. Cottrell (1957) on copper. This work concluded that insoluble helium could be retained in "solution" by being strongly trapped in vacancies. Early experimental work by B. Russel and J.I. Hastings (1967) indicated that helium could exist and migrate interstitally before becoming trapped in lattic vacancies. Although much work had been done prior to 1966 on helium

diffusion, Blackburn noted that the diffusion behavior was uncertain at that time. A far more consistent picture of helium diffusion and release has been obtained from experimental work done by W.R. Wilson and C.L. Bisson (1971) nd E.V. Kornelsen (1972). Both have also developed theoretical atomistic pictures using the point defect interaction potential approach of R.A. Johnson (1964-66) to satisfactorily interpret their data. Their experimental and theoretical efforts are conidered the basis of expanded follow-on work today.

We conclude with more recent fusion irradiation damage studies, which until about 1973-74 considered surface effects like sputtering and blistering to be the primary modes of fusion first wall degradation. Theoretical studies by G.R. Odette and co-workers in 1974-76 and design-related work by G.L. Kulsinski and co-workers in 1974-76 indicated that the potential interaction between helium generation at higher than fast breeder rates together with displacement damage could result in both void swelling and helium embrittlement problems to limit fusion first wall lifetimes. Work by E.E. Bloom and F.W. Wiffen in 1975 on stainless steels irradiated in a high flux thermal reactor to contain a considerable amount of helium and d displacement damage supported the contention that swelling and embrittlement could be different, and posibly worse, for fusion conditions compared to fast reactor conditions (where very little helium is produced). The problem of studying radiation effects in a fusion environment does not exist, and irradiation effects must be simulated. Thus we must combine various experimental results together with comprehensive and detailed theoretical treatments in order to relate property changes in current irradiation environments to anticpated fusion conditions. This report testifies to considerable work in recent years related to achieve this goal.

## 5.3. A Perspective on Recent Work in the United States

Recently, there has been a great deal of progress in understanding helium effects, both on the theoretical and experimental sides. Work is developing fast, and it is difficult to be accurate in analyzing all contributions to this field. In the following, we restrict ourselves to the last few years, and give a brief account of investigators and their areas of interest. We attempt to do this only for investigations within the United States. However, future updates of this report will include a similar overview on similar efforts world-wide. First, a discussion on the theoretical efforts related to helium behavior in materials is presented. Following this, we give a description of ongoing experimental research activities.

### Theoretical Efforts

Theoretical efforts on helium behavior span a wide range of areas ranging from detailed atomistic calculations of helium-point defect congfigurations to more global methodologies using computer models of the microstructure. Institutions that are actively involved in these efforts are the following:

(1) Universities:

Massachusetts Insitute of Technology (MIT)
University of California at Los Angeles (UCLA)
University of California at Santa Barbara (UCSB)
University of Wisconsin (UW)

(2) Laboratories:

Oak Ridge National Laboratory (ORNL)
Sandia Laboratory (Sandia)
Westinghouse Research and Development Center
Argonne National Laboratory (ANL)

Baskes, Bisson, and Wilson (Sandia) are developing atomistic models for defect configurations including helium atoms. They base their work on the knowledge of the interatomic potentials and energy minimization for the studied defect-helium configuratons. Helium diffusion and interaction with small clusters of point defects under irradiation is studied by Mansur and Williams (ORNL), and by Ghoniem and Sharafat (UCLA). The nature of the pressure in a small helium-vacancy cavity is being investigated by Wolfer (UW) and the results of a real gas equation of state are used by Ghoniem and Sharafat (UCLA) to evaluate the radiation stability of these defects. Classical nucleation theory is extended by Russell and co-workers (MIT) to include helium effects. The bias of cavities to point defects and helium is investigated by Wolfer (UW). Cavity nucleation using kinetic theory is developed by Hall (Westinghouse) and Sharafat (UCLA). Mansur and co-workers (ORNL) are involved in developing analytical formulas to explain the critical cavity size and the bimodal cavity distribution. Global microstructural modeling including helium effects is being developed by Stoller and Odette (UCSB). Theoretical modeling of helium production under various irradiation conditions is being developed at HEDL by Johnson and Mann.

Experimental Investigations

Experimental efforts concentrate on the effects of helium on the development of various features of the microstructure. The effects of dose rate, dose, helium production rate, temperature, material conditions, helium pre-implantation and helium co-implantation are all studied. The most important aspects of such studies relate to the use of ion beams to understand fundamental mechanisms, since fusion conditions will be outside the experimental range given by current fission reactors. Dual ion beams are used to study microstructures by Packan, Farrell, Kenik, Lee, Horton, and Braski at ORNL. They are also used by Loomis, Ayrault, and Turner at ANL; and also by Spitznagel, Choyke, and Wood at Westinghouse and the University of Pittsburg. Other investigators using similar techniques are Van der Sande and Harling at MIT; Brimhall, and co-workers at PNL.

The effects of neutron-generated helium on the microstructure, swelling and mehcanical properties are investigated by the ORNL group (Masiasz, Grossbeck, Kleuh, Vitek, Wiffen, Horton, and Bloom), and also by the HEDL group (Garner, Brager, Gelles, Thomas, and Porter). Helium production measurements are performed by Rockwell International (Oliver, Kneff, Nakata, and Farrar IV). Jesser and co-workers are developing experimental techniques for understanding effects of helium on crack behavior.

An extensive list of investigators is not the purpose of this section. However, it is important to give a flavor of the directions of research and people involved in its implementation. It is to be realized that this is only a snapshot in time, and we will work on editing and updating the report as things change.

The cumulative number of publications on a particular research area is shown as a function of publication year. It is interesting to note the sharp increase in the interest in helium research during the past few years. However, areas such as cavity nucleation and growth have enjoyed the largest share of this interest. Also, relatively unexplored areas, such as precipitation or mechanical properties, need further efforts.

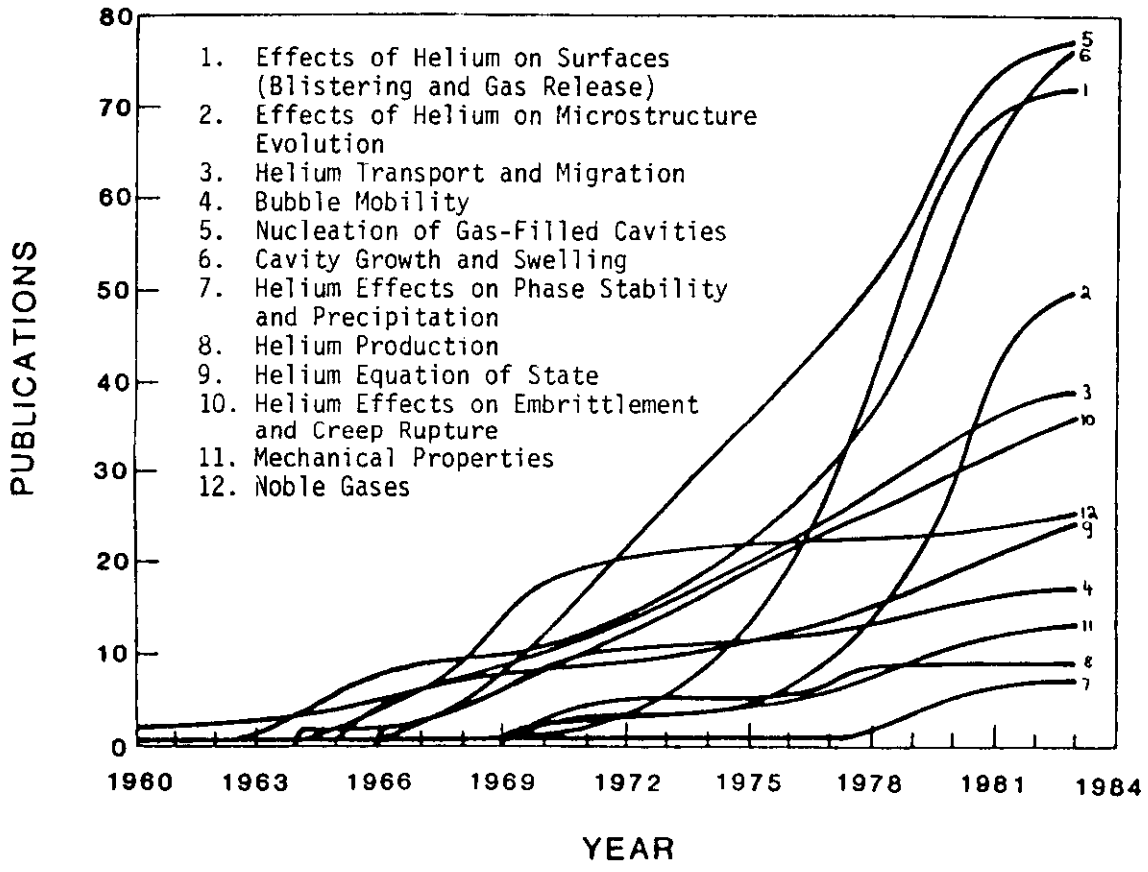


FIGURE 1. Cumulative Numbers of Publications in Various Research Areas.

## CROSS-SECTION TECHNIQUE FOR ION-IRRADIATED AISI 316 SS

R.L. Sindelar, G.L. Kulcinski, and R.A. Dodd (University of Wisconsin)

### 1.0 Objective

The goal of this program is to characterize the effects that dose rate and total dose have on the microstructural/microchemical evolution in a single sample of ion-irradiated 316 SS. The study will include both solution annealed and 20% cold-worked 316 SS.

### 2.0 Summary

A cross-section technique involving nickel plating on a 316 SS substrate has been deomonstrated for 14 MeV $^{58}Ni^{3+}$ irradiated 316 SS. Unlike a previous technique for cross-sectioning 316 SS,[1] this method does not rely on a high temperature diffusion bond between the nickel and the 316 SS.

### 3.0 Program

Title: Radiation Effects to Reactor Materials
Principal Investigators: G.L. Kulcinski and R.A. Dodd
Affiliation: University of Wisconsin

### 4.0 Relevant DAFS Program Task/Subtask

Subtask II.C.1.1 Phase Stability Mechanics
Subtask II.C.6.1 Effect of Damage Rate on Microstructural Evolution

### 5.0 Accomplishments and Status

Annealed and 20% cold-worked 316 SS prepared at Oak Ridge National Laboratory have been nickel plated by the procedure shown in Fig. 1 and chemically thinned to produce suitable TEM specimens which will show the entire damage

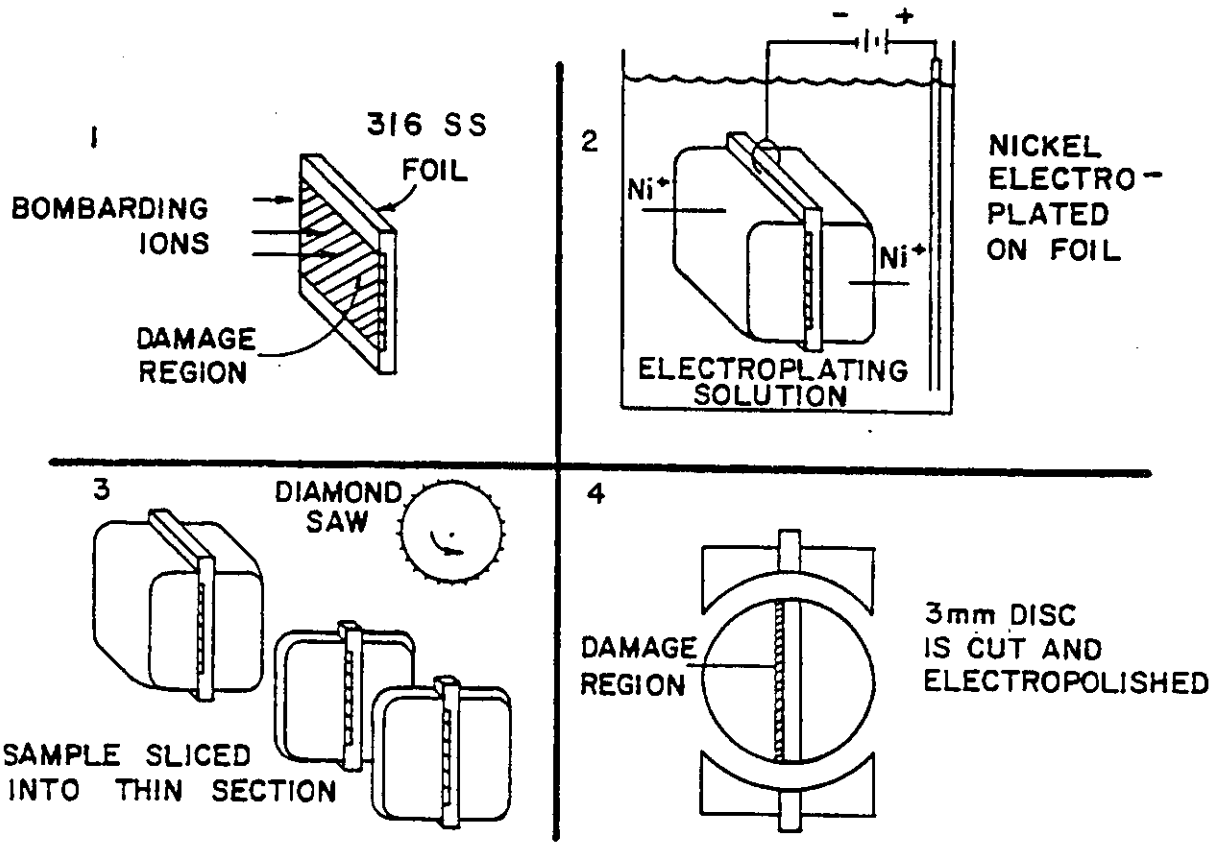


FIGURE 1. Preparing Foil in Cross Section.

region in a 14 MeV $Ni^{3+}$ ion irradiation for fusion environment simulation studies. Figure 2 reveals the nickel-316 SS interface for unirradiated cold-worked 316 SS.

Recent analysis has suggested an impact on the microstructure due to the addition of injected interstitials during an ion-irradiation of materials.[2,3] The utilization of 14 MeV $Ni^{3+}$ ions with subsequent employment of the cross-section technique will make analysis possible in regions free from surface effects and excess interstitial effects.

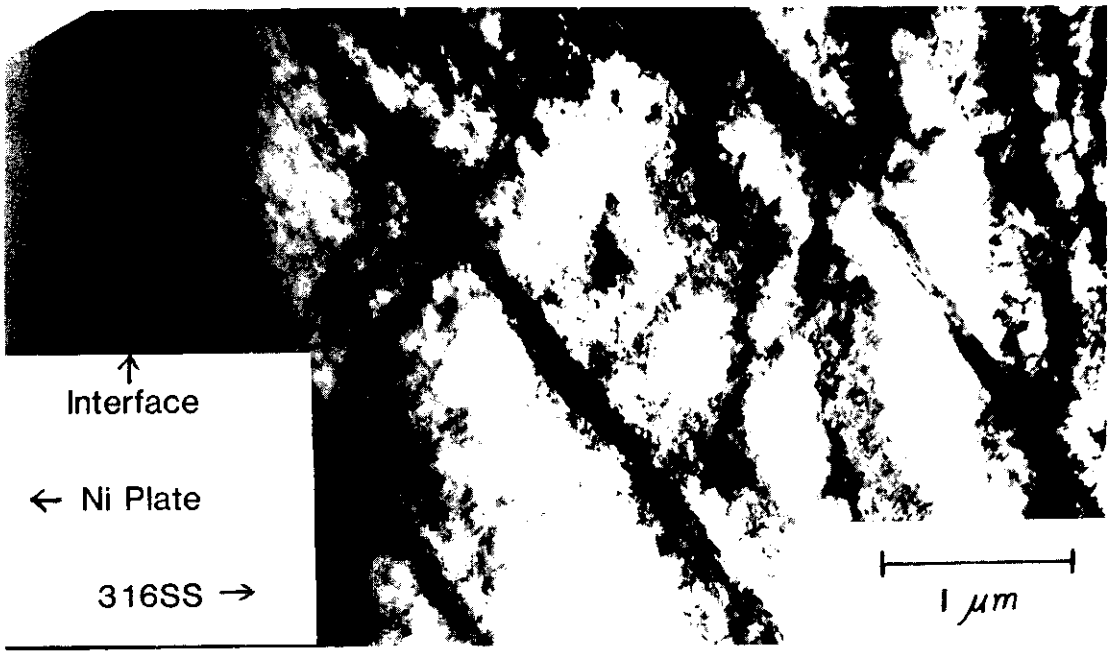


FIGURE 2. Unirradiated Cross-Sectional 20% Cold-Worked 316 SS.

## 6.0 References

1. R.A. Spurling and C.G. Rhodes, "A Technique for Preparing the Cross-Section of Proton-Irradiated 316 Stainles Steel Foils for Transmission Electron Microscopy," J. Nucl. Mater., 44, 341-344 (1972).

2. D.L. Plumton and W.G. Wolfer, "Suppression of Void Nucleation by Injected Intersitials," Damage Analysis and Fundamental Studies Quarterly Progress Report, DOE/ER-0046/12.

3. F.A. Garner, "Impact of the Injected Interstitial on the Correlation of Charged Particle and Neutron-Induced Radiation Damage," Proc. of TMS-AIME Symposium on Radiation Damage Analysis for Fusion Reactors, St. Louis, MO, October 24-28, 1982. To appear in J. Nucl. Mater.

## 7.0 Future Work

Irradiation and subsequent analysis of annealed and 20% cold-worked 316 SS is underway. The recent acquisition of a JEOL 200-CX 200 keV TEM with EDS facilities will allow a thorough microstructural/microchemical study to be undertaken.

# DISTRIBUTION

UC-20 (108)

UC-20c (75)

DOE-HQ/Office of Breeder
Technology Projects
NE-53
Washington, DC 20545

PB Hemmig, Asst Director,
Reactor Physics Tech

DOE-HQ/Office of Fusion Energy (2)
Washington, DC 20545

JF Clark, ER-70
JF Decker, ER-54, G-256

DOE-RL/Office of Asst Manager for
Projects & Facilities Management (2)
FMIT Project Office

GM Chenevert, Project Manager

DOE-RL/Office of Asst Manager
for Advanced Reactor Programs
Breeder Technology Division

KR Absner, Chief,
Technology Development Branch

Argonne National Laboratory (5)
9700 South Cass Avenue
Argonne, IL 60439

LR Greenwood BA Loomis
A. Taylor H. Wiedersich
RE Nygren

Battelle Memorial Institute (3)
Pacific Northwest Laboratory
P.O. Box 999
Richland, WA 99352

JL Brimhall
DA Dingee
TD Chikalla

Brookhaven National Laboratory
Associated Universities
Upton, Long Island, NY 11973

Chairman, Nuclear Energy Dept

Columbia University
Plasma Physics Laboratory
New York, NY 10027

RA Gross

General Atomic Company (2)
P.O. Box 81608
San Diego, CA 92138

GR Hopkins
JR Gilleland

INESCO
11011 Torreyana Rd
San Diego, CA 92121

RD Stevenson

Lawrence
Livermore National Laboratory (3)
P.O. Box 808
Livermore, CA 94550

WL Barmore
MW Guinan, L-396
CM Logan

Los Alamos National Laboratory (4)
P.O. Box 1663
Los Alamos, NM 87544

DJ Dudziak J. Fowler, E-546
CR Emigh G. Hurley, E-546

Massachusetts Institute of Technology (5)
77 Massachusetts Avenue
Cambridge, MA 02139

L. Lidsky I-W Chen, 13-5118
NJ Grant, 8-305 DB Montgomery, NW21
JB van der Sande, 13-5025

DISTRIBUTION (Cont'd)

Massachusetts Institute of Technology
Nuclear Reactor Laboratory
138 Albany St
Cambridge, MA 02139

OK Harling, NW12-204

McDonnell-Douglas Astronautics Co.
P.O. Box 516
St. Louis, MO 63166

D. Kummer

Mound Laboratory
P.O. Box 32
Miamisburg, OH 45342

Manager, Tech Appl & Dev

National Bureau of Standards
Gaithersburg, MD 20760

JA Grundl

Naval Research Laboratory (3)
Washington, DC 20375

I. Manning, Code 6672
JA Sprague, Code 6395
LE Steele, Code 6390

North Carolina State University
Department of Nuclear Engineering
Raleigh, NC 26707

JR Beeler, Jr.

Oak Ridge National Laboratory (12)
P.O. Box X
Oak Ridge, TN 37830

K. Farrell
ML Grossbeck
PJ Maziasz
LK Mansur
NH Packan
M. Roberts, Bldg 9204-1
Director, Bldg 9201-2
FG Perey
J. Sheffield
JO Stiegler
C. Weisbin
FW Wiffen

Princeton University (2)
Plasma Physics Laboratory
Forrestal Campus
P.O. Box 451
Princeton, NJ 08544

H. Furth
K. Wakefield

Rockwell International
8900 DeSoto Ave
Canoga Park, CA 91304

D. Kramer

Sandia National Laboratories (2)
P.O. Box 5800
Albuquerque, NM 87185

FL Vook, Org 5100

Sandia National Laboratories
Livermore, CA 94550

WD Wilson

Science Applications, Inc.
1200 Prospect
LaJolla, CA 92037

Dr. H. Gurol

University of California (2)
Los Angeles, CA 90024

RW Conn
NM Ghoniem

University of Michigan
Nuclear Engineering
Ann Arbor, MI 48109

T. Kammash

University of Missouri
Mechanical & Aerospace Eng
1006 Engineering Bldg
Columbia, MO 65211

M. Jolles

DISTRIBUTION (Cont'd)

University of Missouri
Dept of Nuclear Engineering
Rolla, MO 65401

A. Kumar

University of Virginia
Dept of Materials Science
Charlottesville, VA 22901

WA Jesser

University of Wisconsin
1500 W. Johnson Drive
Madison, WI 53706

WG Wolfer

Westinghouse
Advanced Energy Systems Division
Fuels Materials Technology
P.O. Box 158
Madison, PA 15663

A. Boltax, Manager

Westinghouse
Research and Development Center (2)
1310 Beulah Road
Pittsburgh, PA 15235

JA Spitznagel
S. Wood

Commission for the European Communities
200, rue de la Loi
B-1049 Brussels, Belgium

J. Darvas

Energieonderzoek Centrum Nederland
Westerdionweg 3
NL-1755 ZG Petten, The Netherlands

B. van der Schaaf

EURATOM
Joint Research Center Ispra
Materials Science Division
I-21020 Ispra, Varese, Italy

P. Schiller

Hahn-Meitner Institute für Kernforschung
Glienickerstrasse 100
D-1000 Berlin,
Federal Republic of Germany

H. Wollenberger

Hokkaido University (2)
Metals Research Institute
Kita-hu, Sapporo, Japan 060

Mihio Kiritani, Precision Eng
Taro Takeyama

Japan Atomic Energy Research Institute (2)
Physical Metallurgy Laboratory
Tokai Research Establishment
Tokai-mura, Naka-gun, Ibaraki-ken, Japan

Shuichi Iwata, Physics
Kensuke Shiraishi, Nucl Fuel Research

Kernforschungsanlage Jülich GmbH
Postfach 1913
D-517 Julich,
Federal Republic of Germany

H. Ullmaier

Kernforschungsanlage Karlsruhe
Institüt für Reaktorbauelemente
Postfach 3640
D-7500 Karlsruhe 1,
Federal Republic of Germany

K. Ehrlich

Kyushu University
Research Institute for Appl Mechanics
6-10-1 Hakozaki, Higashi-ku,
Fukuoka, 812, Japan

Kazunori Kitajima

National Research Council
Montreal Road
Ottawa, Canada

EV Kornelson

DISTRIBUTION (Cont'd)

National Research Institute for Metals
Nuclear Materials Division
1-2-1 Sengen, Sakura-mura,
Niihari-gun, Ibaraki 305, Japan

Naoki Kishimoto

Netherlands Energy Research Foundation
Materials Department
P.O. Box 1
NL-1755 ZG Petten, The Netherlands

W. Van Witzenburg

Osaka University
Dept of Nuclear Engineering
2-1, Yamada-oka, Suita,
Osaka, 565, Japan

Kenji Sumita

Science University of Tokyo
Engineering Dept
Kagurazaka, Shinjuku-ku,
Tokyo, 162, Japan

RR Hasiguti

Studiecentrum voor Kernenergie
Centre d'Etude de l'Energie Nucleaire
Boeretang 200
B-2400 Mol, Belgium

J. Nihoul

HEDL (37)

| | | | |
|---|---|---|---|
| SD Adkin | W/A-58 | WN McElroy | W/C-39 |
| TK Bierlein | W/A-1 | EK Opperman | W/A-58 |
| HR Brager | W/A-64 | NF Panayotou | W/A-65 |
| LL Carter | W/B-47 | RW Powell | W/A-64 |
| DG Doran (5) | W/A-57 | RJ Puigh | W/A-58 |
| EA Evans | W/C-23 | FH Ruddy | W/C-39 |
| FA Garner | W/A-57 | FA Schmittroth | W/A-4 |
| DS Gelles | W/A-64 | WF Sheely | W/C-62 |
| R. Gold | W/C-39 | RL Simons | W/A-57 |
| JW Hagan | W/B-41 | JL Straalsund | W/A-61 |
| HL Heinisch | W/A-57 | HH Yoshikawa | W/C-44 |
| DL Johnson | W/A-4 | Central Files (3) | W/C-110 |
| GD Johnson | W/A-65 | Publ Services (2) | W/C-115 |
| NE Kenny | W/C-115 | Document Services | W/C-123 |
| FM Mann | W/A-4 | Microfilm Services | W/C-123 |

Swiss Federal Institute
for Reactor Research
CH-5303 Wuerenlingen, Switzerland

WV Green

Tokyo Institute of Technology
12-1, 2-Chome, O-Okayama
Meguro-ku, Tokyo, Japan

Kensutaka Kawamura

United Kingdom Atomic Energy Authority
Atomic Energy Research Establishment
Metallurgy Division
Building 388
Oxfordshire, OX11 ORA, UK

DR Harries

University of Tokyo (3)
7-3-1 Hongo
Bunkyo-ku, Tokyo 113, Japan

Naohira Igata, Met & Mater Science
Shiori Ishino, Nuclear Eng
Taijiro Uchida